SYNTHESIS OF HIGHLY DENSE YTTERBIUM-DOPED LUTETIUM AND UNDOPED YTTRIUM OXIDE FOR HIGH POWERED LASING APPLICATIONS

A Thesis
Presented to
The Academic Faculty

By

Bryan Vitale

In Partial Fulfillment
Of the Requirements for the Degree
Doctor of Philosophy in Materials Science and Engineering

Georgia Institute of Technology

December 2015

SYNTHESIS OF HIGHLY DENSE YTTERBIUM-DOPED LUTETIUM OXIDE AND ZIRCONIA-STABILIZED YTTRIUM OXIDE FOR HIGH POWERED LASING APPLICATIONS

Approved by:

Dr. Robert F. Speyer, Adviser
School of Materials Science and Engineering
Georgia Institute of Technology

Dr. Thomas H. Sanders
School of Materials Science and Engineering
Georgia Institute of Technology

Dr. Rosario A. Gerhardt
School of Materials Science and Engineering
Georgia Institute of Technology

Dr. Angus Wilkinson
School of Chemistry and Biochemistry
Georgia Institute of Technology

Dr. Joe K. Cochran
School of Materials Science and Engineering
Georgia Institute of Technology

Date Approved:

October 16th, 2015

ACKNOWLEGDEMENTS

I would like to thank my family and friends who have supported me during my stay at Georgia Tech. Without their support, this project would not have been possible to complete. I would first and foremost like to thank my advisor, Dr. Robert Speyer, whose support and guidance allowed me to overcome many challenges during this work. I would also like to thank my brother and roommate, Adam Vitale, for his moral support and for allowing me to vocalize project ideas to him at any time. I would especially like to thank my parents, Stephen and Gail Vitale, who have always been highly supportive and emotionally nearby. I also express my great appreciation for the assistance of my lab partners Morris Satin and Joseph Eun as well as the various undergraduate research associates who contributed to the project in various ways for their numerous contributions and suggestions. Lastly, I thank the Air Force Office of Scientific Research, Contract FA9550-12-1-0219, for funding the project work, and I appreciate the helpful suggestions and support of the contract monitor, Dr. Ali Sayir.

TABLE OF CONTENTS

LIST OF TABLES

LIST OF FIGURES

SUMMARY

Utilizing polycrystalline transparent ceramics as laser host media offers many advantages over more conventional single crystal counterparts. Improvement in scalability, higher dopant concentrations, and lower cost is achievable through these materials, and equivalent lasing efficiency and transparency can also be obtained. The focus of this research is to sinter Yb^{3+}-doped Lu_2O_3 to high density and transparency and to analyze specimen density, transmissivity, microstructure, dopant distribution, and thermal conductivity with respect to processing parameters. The production of transparent polycrystalline Y_2O_3 for use as a ceramic substrate was also evaluated with an assessment of similar parameters.

Yb^{3+}-doped Lu_2O_3 and ZrO_2-stabilized Y_2O_3 disks were prepared by sintering and post-hot isostatic pressing (HIPing) mixed commercial and processed powders to produce dense ceramic bodies in both high vacuum carbon and tungsten furnace environments. The ZrO_2 additions to the commercial Y_2O_3 powder was stabilized with 3 mol% yttria, but for convenience, the ceramics processed in this manner will be referred to as ZrO_2-Y_2O_3. Processing techniques such as ball milling, chemical co-precipitation, and spray drying of the powders were evaluated, and sintering parameters such as soak temperature and dwell duration were assessed for the resulting powder compacts. Thermal treatments such as thermolysis of organic additives of as-pressed compacts and annealing of sintered bodies were additional studies performed in this work. By selecting optimized sintering environments, powder processing techniques, soak temperatures, and dwell times, post-HIPed specimens of near-theoretical density and up to 70% transmittance were obtained from commercial powder sources. This has not been previously reported via pressureless sintering using commercial-grade powders without initial processing of the powder

through chemical co-precipitation. Ceramic processing techniques such as the use of binder and plasticizing additives to aid in the fabrication of highly dense green bodies through the use of spray drying was evaluated in the production of theoretically dense ceramic samples from other commercial sources. Post-sinter heat treatment techniques were also used to maximize the optical qualities of the sintered and HIPed ceramics; discolorations and other dispersed defects were minimized using air or high oxygen atmosphere annealing treatments between sintering and post-HIPing heat-treatments and after post-HIPing. Determining the optimal sintering parameters in order to achieve a closed-porosity state of the ceramic specimens without large grain growth before post-HIP, along with optimized thermal treatment steps, were essential to achieving samples of maximum quality. X-ray diffraction (XRD) data, microstructure investigation through optical and electron microscopy, and elemental characterization through energy-dispersive x-ray spectroscopy (EDS) were performed to determine best process results, and lastly transmission and lasing data were acquired and analyzed for the resulting transparent and theoretically dense samples.

I. INTRODUCTION

High powered lasers are seeing an increasing number of applications in transformative medical, industrial, and military applications. Medical applications such as bloodless surgeries, like eye vision correction and kidney stone removal, are reliant on laser operation. Industrial applications like precision metal welding and cutting also utilize laser technology. Military applications such as target marking and guided munitions, missile defense, electro-optical countermeasures, and even blinding enemy troops grow (protecting the Geneva Convention) with the potential to increase power output of laser devices, specifically solid-state lasers which can more readily be produced with a limited space requirement. Rapid technological developments have led to high-power output from these devices, however, heat generated from continuous operation at higher output can degrade conventional lasers' efficiency over time. Temperature gradients that may form make it possible for thermal lensing to occur, and other optical distortions present from current production methods limit the capability of conventional lasing media[1].

The first step in further reducing the thermally-based limitations of the power output of solid-state lasers at lower costs would be to develop them out of high density polycrystalline ceramics as opposed to silicate glass or single crystals. The orders of magnitude higher thermal conductivity relative to glass provides significant merit to developing ceramic based laser hosts. The high cost of producing ceramic single crystals, along with the production limitations of crystal growth methodology, makes creating a polycrystalline ceramic an attractive alternative. For instance, single crystal growth of Nd-YAG, a common ceramic lasing material, can take 30-40 days at ~2000°C, with a yield of less

than 35% useable material for lasing media[2]. Additionally, higher powered lasers require comparatively larger lasing volume, meaning the technological limitations of forming larger single crystals becomes highly limiting[3]. Temperature fluctuations and segregation of laser-active ions at the solid-liquid interface during crystal growth are also issues yet to be fully resolved. High temperature phenomena such as chemical inhomogenity due to volatilization, cracking due to thermal gradients, and non-uniformities in dopant concentration can be mitigated by sintering polycrystalline ceramics of the same material at a significantly lower temperature. Along with benefits such as being able to achieve high dopant concentration in a more compact device, these advances allow the increase in the upper limit of power output of solid-state laser devices. Consequently, there is a definitive need to expand research into low cost production of sintered polycrystalline ceramics for lasing applications. One limiting factor in attaining continuous high power output in solid state lasers is removing the heat generated in the lasing medium which can cause beam degradation via thermal lensing if the host material is not adequately cooled during operation. For this consideration, polycrystalline sesquioxide ceramics offer an advantage of relatively high room temperature thermal conductivity over more conventional YAG lasers. Furthermore, Yb-doped sesquioxide crystals display wider emission bands than Yb:YAG and are thus ideal candidates for fabricating highly efficient pulse laser sources[4]. Thus, such a material is an ideal candidate for a highly doped solid state lasing medium for high powered laser operation with minimal effects of thermal degradation.

The breakthrough development of a polycrystalline neodymium-doped yttrium aluminum garnet (Nd:YAG) laser in 1995, with nearly the same optical characteristics of a

chemically equivalent single crystal, launched a worldwide research effort into the fabrication of transparent polycrystalline ceramics designed for laser oscillation[5]. Since then, cubic-structured (required for transparency in a polycrystalline dielectric) sesquioxides (Sc_2O_3, Lu_2O_3, Y_2O_3) have emerged as potentially better host candidates for high powered laser generation due to their higher thermal conductivity. Of these candidates, Yb^{3+}-doped Lu_2O_3 is potentially the most highly promising laser host due to maintaining a higher thermal conductivity relative to Yb^{3+} doped Sc_2O_3 or Y_2O_3, which see a significant decrease in thermal conductivity as the dopant is added due to solid-solution phonon scattering[4]; the closely matched atomic weights and ionic radii of Yb^{3+} and Lu^{3+} attenuate the phonon mean free path at the lesser extent compared to the other dopant ions, which can act as phonon scattering sites and reduce thermal conductivity.

The presence of second phases at grain boundaries as well as residual porosity act as optical scattering centers and inhibit transmission[3]. Powder and thermal processing methods must be employed which avoid trapping pores within individual grains, where they become difficult to eliminate with continued thermal and pressure treatments. For instance, the entrapment of coarse pores within the interiors of abnormally grown grains would prevent the removal of those scattering centers with further thermal processing. Phase purity must also be retained with respect to any dopant ions, sintering and pressing aids, or any other impurity sources such as milling media or wet synthesis chemistry components used to process the ceramic materials from the as-received powders to final ceramic parts. Specific material used for these processes must be carefully selected such that they are fully removed before processing of the final specimens (such as through a

low temperature thermolysis or calcination) or such that they do not enter into the ceramic powder in the first place or form complete solid solution.

Ceramics sintered directly from commercial powders have been shown to have impeded spectral transmittance, attributed to a higher impurity content relative to chemically synthesized powder[6, 7]. Chemical processing to form precursor powders has been shown to improve purity levels and form highly sinterable powders, resulting in higher transparency. Both combustion synthesis and powder co-precipitation have been used effectively[8]. Co-precipitation techniques are the most common method of powder preparation, and numerous variations in the processing parameters have been studied in order to maximize the quality of the final ceramic[9]. Fine sesquioxide powders have been also fabricated using combustion synthesis[8, 10-12] and flame spray pyrolysis[13].

The process for sintering the mixed commercial or chemically synthesized pressed powder compacts is typically either pressureless sintering[8, 14-21], hot pressing [6, 7, 22, 23], or a process of sintering to closed porosity, followed by hot isostatic pressing (HIP)[15, 18, 19]. Other methods such as laser-based sintering and spark plasma sintering have also been performed in order to fabricate fully dense ceramics of this type[24, 25]. While calcining chemically co-precipitated powders is necessarily performed in order to obtain sinterable oxide powders from methods involving ceramic fabrication from solution precipitates, annealing of fired ceramics themselves in an oxygen-containing atmosphere is another processing consideration that has begun to be investigated[14].

The primary goal of this work is to explore the sintering of Yb^{3+} doped Lu_2O_3 prepared by mechanically mixing commercial Yb_2O_3 and Lu_2O_3 powders and also by using ceramic processing techniques such as using organic binder and dispersant additives in

conjunction with spray drying of a well dispersed powder suspensions of $Yb3^{+}$-doped Lu_2O_3 as well as ZrO_2-Y_2O_3 in order to maximize the transparency of the final ceramics. Using an optimized pressureless sintering, air annealing, and HIPing process, this work sought to achieve transparencies significantly improved over those typically observed based on the use of commercial starting powders without undergoing any co-precipitation or similar process. This involved:

- Investigation of sintering parameters such as heating rate, soaking temperature(s), time(s), atmospheres, and cooling rate.
- Similar investigation of HIPing parameters.
- Annealing fired samples in air or other oxygen-containing atmospheres between and after sintering and HIPing to see effects on sample quality and clarity. Parameter testing on annealing atmosphere and dwell time.
- Analyzing x-ray diffraction data to examine phase purity of samples with respect to increased amounts of doping and other processing parameters.
- Microstructure examination of grain morphology and pore distribution of sintered ceramic bodies.
- Measure optical transparency of highly-dense samples over the solid solution range at near IR wavelengths, pertinent to the lasing wavelength.
- Elemental characterization of powders and ceramics to determine extent of milling or crucible contaminations in sintered or processed ceramic parts.
- Measuring properties such as fluorescence and lasing efficiency as a function of doping concentration and fabrication parameters.

A secondary goal of this work was also to investigate the fabrication of ZrO_2-doped Y_2O_3 for use as a transparent polycrystalline substrate in components such as transverse mode polarizers[26]. Y_2O_3 is also promising optical material due to its physical and chemical properties including high melting point, range of transparency (0.2–8μm), and resistance to corrosion. Yttria ceramics have also been developed for use in infrared-domes and components of semiconductor devices[27]. Many of the same parameter studies were conducted on these yttria based ceramics, with the notable difference that the ZrO_2 doping is acting as a grain growth inhibitor, instead of providing laser active ions for spontaneous/stimulated emission generation. The goals of high relative density and high transmittance remain the same, and processing parameters were studied and optimized in a very similar manner.

II. LITERATURE REVIEW

2.1 Material Data

2.1.1 Lutetium Oxide

Lutetium oxide (Lu_2O_3) has attracted interest as a candidate for scintillators and laser applications due to its broad range of transparency, low thermal expansion coefficient, high thermal conductivity, and low phonon energy[28]. Lu_2O_3 also has uses as catalysts in cracking, alkylation, hydrogenation, and polymerization. The theoretical crystal density of Lu_2O_3 is 9.42 g/cm^3, and it is insoluble in water but is soluble in many acids. It is also slightly hygroscopic. The room temperature thermal conductivity of Lu_2O_3 is 12.5 W/mK [4], and it also has a wide band gap of ~6.4 eV[21]. For comparison, undoped Yttrium-aluminum-garnet (YAG) has a room temperature thermal conductivity of 11.0 W/mK [4]. The structure of Lu_2O_3 is that of bixbyite, with space group $Ia\bar{3}$. This can be fully described as a body-centered lattice with a 40-atoms basis and is shown in with two representations in Figure 1[29, 30]. The unit cell can be thought of as a variation of the fluorite structure only with one fourth of the anions missing in order to correctly accommodate the trivalent lutetium cation. The unoccupied oxygen sites form nonintersecting strings along the <111> directions of the unit cell.

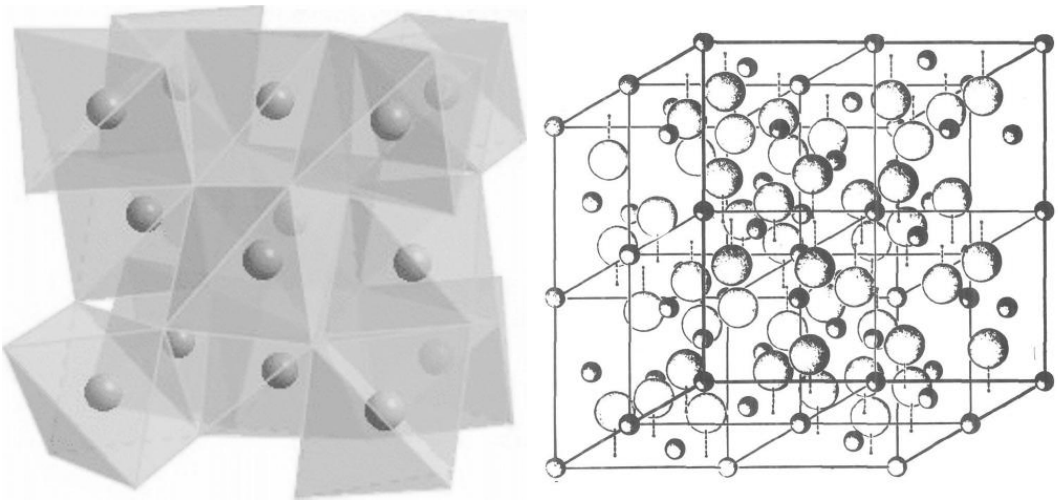

Figure 1: Graphical representations of the bixbyite structure[29, 30].

The primary lutetium oxide-containing commercial ore is the rare earth mineral monazite, which contains 0.0001% of the element. The crushed mineral is treated with concentrated sulfuric acid in order to produce sulfates of the rare earth elements contained within. The solution is then treated with ammonium oxalate to convert rare earths ions into their insoluble oxalates which are then calcined into an oxide form. The mixed rare earth oxide is dissolved in nitric acid to remove insoluble mineral components. Lastly the metal ions are separated into two-cation salts with ammonium nitrate by crystallization, from which lutetium can be separated via ion exchange. Lutetium salts are then selectively filtered out by a complexing agent and are then again calcined into the final pure oxide[31].

For many years, the understanding that Lu_2O_3 adopts the bixbyite structure was derived from results based on a Rietveld refinement or theoretical calculations of the structure based on diffraction data of Lu_2O_3 nanopowders, but never confirmed from a fully dense ceramic or single crystal. Guzik et al. were recently able to confirm this experimen-

tally using the micro-pulldown crystal growth method to form single crystal Lu_2O_3 structures which were then evaluated via XRD[32].

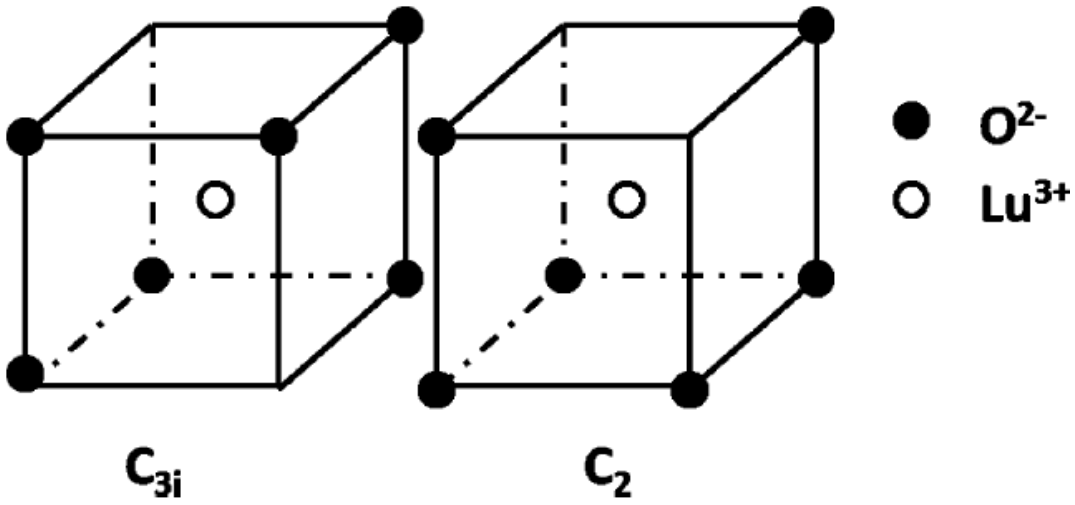

Figure 2: The coordination of the two types of lutetium sites in Lu_2O_3[32].

Lu_2O_3 was found in this way to have the same structure as Y_2O_3, where there are two independent cation sites with local symmetries C_2 and C_{3i}, as shown in Figure 2. The ratio of C_2 to C_{3i} is 3:1 with 24 C_2 site occupancies and 8 C_{3i} site occupancies in a single cell. This preserves the stoichiometry necessary with each Lu cation being coordinated with 6 O anions, shared amongst four cells. The simulated XRD spectra from these Lu_2O_3 single crystals was compared to that of the grinded compound and the transparent fully dense ceramic, showing good agreement with the bixbyite structure derived previously. Figure 3 contains the XRD spectra showing this matching.

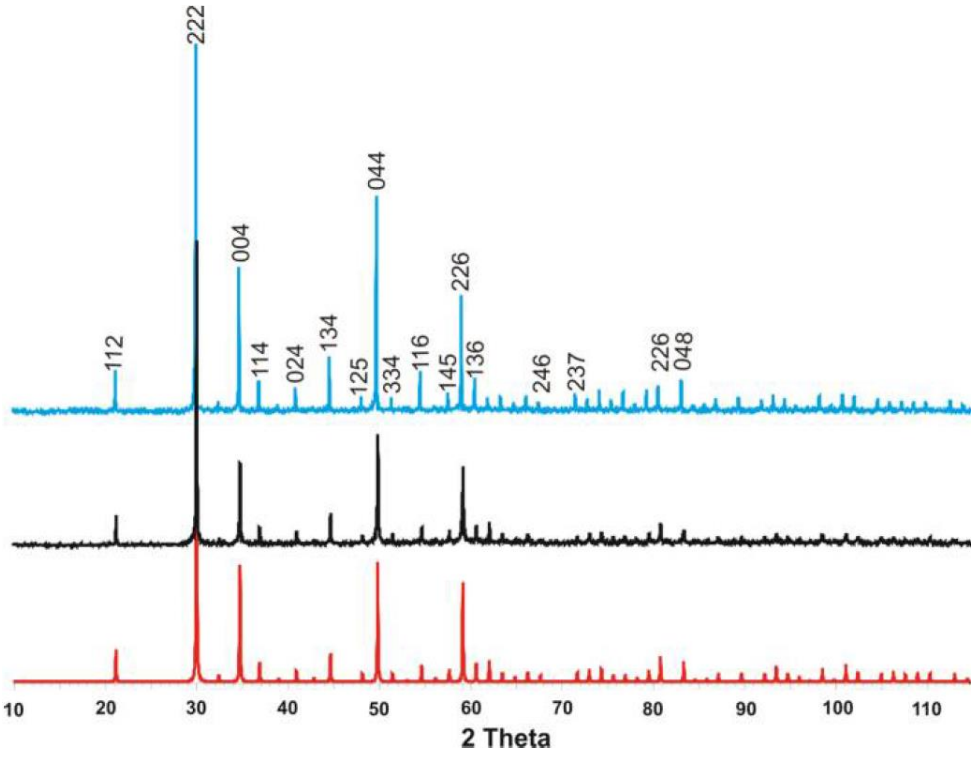

Figure 3: Simulated XRD pattern from micro-pulldown single crystal (bottom), experimental XRD pattern from grinded compound (top), and experimental XRD pattern from transparent ceramic (middle)[32].

2.1.2 Ytterbium Oxide

Ytterbium can act as a mixed-valence cation, meaning it can form both the monoxide YbO as well as the sesquioxide Yb_2O_3 [30]. The theoretical crystal density of Yb_2O_3 is 9.17 g/cm^3, and it is also insoluble in water but is soluble in many acids. Ytterbium is similarly obtained from monazite, though it is relatively more abundant than lutetium (0.1%), and it is processed in an identical fashion[31]. Yb_2O_3 shares the same bixbyite crystal structure as Lu_2O_3 and Y_2O_3.

Yb^{3+} was selected as the dopant for Lu_2O_3 based ceramics due to it exhibiting highly similar ionic mass and radii (173.05 g/mol and 0.101 nm) compared to Lu^{3+} (179.97

g/mol and 0.100 nm). The more identical these parameters, the higher expected solubility of the dopant and the lower the expected solid-solution-based decrease in thermal conductivity. A 2.7% Yb^{3+}-doped Lu_2O_3 ceramic maintains a thermal conductivity of around 11.0 W/mK, whereas a 5% Yb:YAG falls to 6.8 W/mK[4]. Due to the higher cation density of sesquioxides, doping levels of these two materials are comparable and show the benefit of a highly matched dopant and host matrix. Yb^{3+} shows stimulated fluorescence emission around both ~1030 [33] and ~1080 [34] nm.

2.1.3 Yttrium Oxide

While often grouped with the rare-earth elements, yttrium is actually more abundant than lead and is largely found in the mineral gadolinite[31]. The theoretical density of Y_2O_3 is 5.01 g/cm^3 and it is also insoluble in water. Y_2O_3 particles find a number of applications such as using its red light emission properties in making fluorescent lamps and television picture tubes as well as in plasma and flat panel displays. They are also used as coating additives used in high-temperature applications and also in plastics and paints for preventing UV degradation.

As a transparent polycrystalline ceramic, yttrium oxide is another material with the same bixbyite structure as Lu_2O_3 and Yb_2O_3 and is of interest to researchers due to its corrosion resistance, thermal stability, and transparency across a wide range of the electromagnetic spectrum. Similar to Lu_2O_3, if active rare earth ions are doped into polycrystalline Y_2O_3, it can be used as the active medium for solid state lasers. For instance, La^{3+}-doped Y_2O_3 is of great interest for many IR applications because of its position as one of the longest wavelength transmitting oxides[35]. Transparent Y_2O_3 is also an interesting

substrate material due to its wider range of transparency compared to sapphire[26]. It is this high degree of transparency over a wide range of wavelengths that makes transparent polycrystalline Y_2O_3 very promising candidate for use as a potential replacement for sapphire.

2.1.4 Zirconium Oxide

Zirconium is typically found in the mineral zircon, and is relatively abundant compared to the lutetium and ytterbium[31]. Zirconium oxide specifically has a theoretical density of 5.68 g/cm^3 and is remarkably chemically stable, being only slightly soluble in strong acids. While zirconium oxide has many traditional uses as a high temperature refractory, crucible, or milling media material, for the focus of this work it acts as a grain growth inhibitor for sintered Y_2O_3 ceramics. However, the phase transition from monoclinic to tetragonal at 1173°C means that the zirconia phase additions to any ceramic will undergo about a 9% volume change during this transformation. In order to prevent the accompanying stress fractures induced by this sudden volume change and maintain stability in elevated temperature processes, the zirconia must be stabilized with yttria, calcia, or magnesia[36] which allows the material to maintain a cubic structure and prevent the volume change induced via the phase transformation. For this work, ZrO_2-3Y (3 mol% Y_2O_3 stabilized ZrO_2) was used as the grain growth inhibitor for sintering Y_2O_3 ceramics.

2.2 Laser Fundamentals

In all states of matter, electron decay from discrete atomic energy states emits photons of characteristic frequencies. Figure 4 illustrates the basic setup of laser operation[37]. For

lasing to be possible, a population inversion of electrons into an excited state is required, facilitated through an external pump source[1]. A photon emitted from electron decay stimulates additional emissions, all coherent. Laser amplification occurs between opposing mirrors, with one side partially mirrored, from which the laser beam emerges. While such amplification can take place in a gas or liquid, the smaller footprint of solid state lasers make them an attractive option for numerous applications[22].

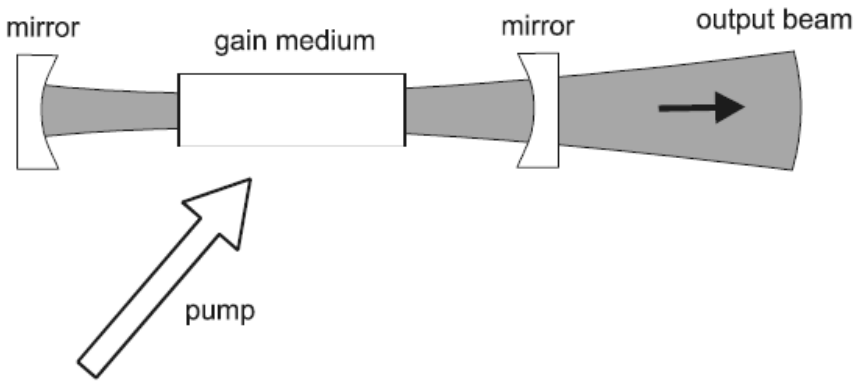

Figure 4: Basic illustration of laser light emission[37].

Laser emissions are invariably introduced from impurity cations doped into a host dielectric crystal. The most common population inversion to emission scenario is described by a four level system of energies: $E_3 > E_2 > E_1 > E_0$. The pump source excites electrons of the dopant from the ground energy to a wide absorption band E_3. Instantaneous decay to E_2 occurs by a radiationless process in which energy is given up to the lattice through the release of a phonon. After the desired radiative transition from E_2 to E_1, a final phonon emission returns the electron back to the ground state. Laser emissions involving decaying electrons to E_1 as opposed to the ground state is preferable since E_1 is not as heavily

populated, meaning a population inversion between these two energy levels is more easily sustained [38]. However, three level lasers are under development for specific purposes where continuous operation is not required[3]. Figure 5 illustrates both energy level schemes.

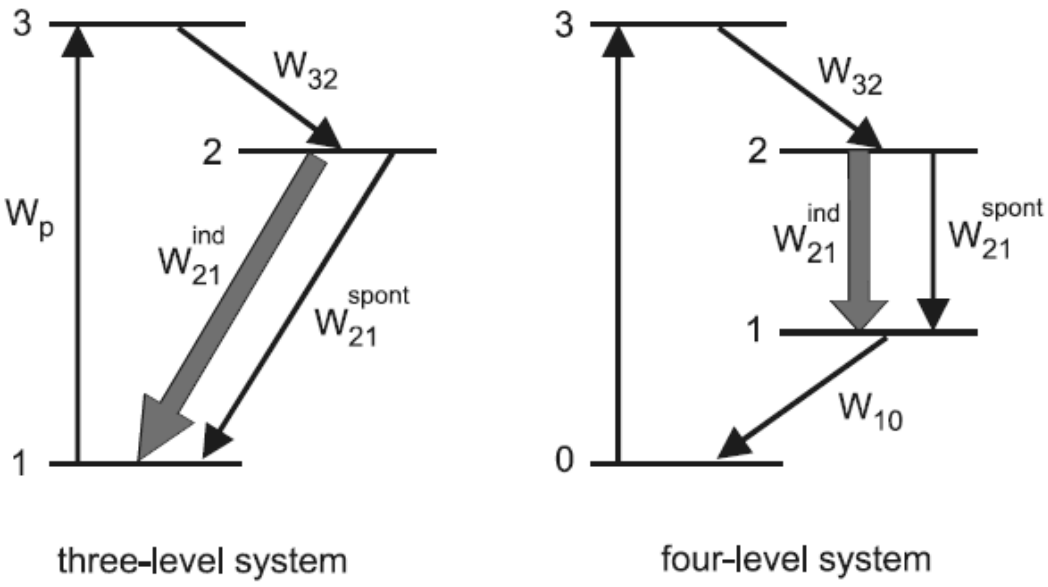

Figure 5: Two common energy level schemes for laser operation, the thick arrow illustrates stimulated emission, described below[37].

When an electron initially in the ground state absorbs a pump source photon and is raised to an excited state, it thereby has absorbed the incident photon and this process is named absorption. Afterwards, the inverse process occurs which is often called spontaneous emission, in which the excited electron falls back to a lower unexcited state, emitting a photon. In stimulated emission, an incident photon induces an electron already in an excited state to emit another photon. The emitted photons reinforce each other and the re-

sulting light is coherent, sharing the same polarization and phase[37]. This process is illustrated in Figure 6.

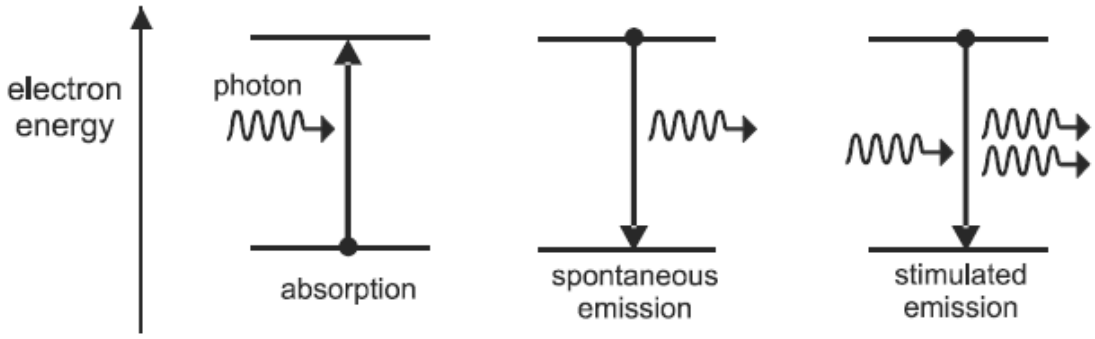

Figure 6: Diagram indicating the process of stimulated emission, resulting in optical amplification[37].

For absorption and emission phenomenon, transition cross sections quantify the probability of induced events such as stimulated emission of energetic photons or the absorption of a photon by a laser active electron. In general, for a laser ion electron in any electronic state the rate R in s^{-1} is

$$R = \sigma \frac{I}{h\nu} \tag{1}$$

where R is the transition rate, $h\nu$ is the photon energy with h being Planck's constant and ν being the photon frequency, σ is the general cross section which quantifies the likelihood of a transition event, and I is the optical intensity, which is measured in the power per unit area incident on a surface perpendicular to the propagation direction. For absorption cross section specifically, σ is closely related to the mass absorption coefficient and is

$$\sigma = \left(\frac{\mu}{\rho}\right) m_a / N_A \tag{2}$$

where: μ/ρ is the mass absorption coefficient (the attenuation coefficient μ over the density ρ), m_a is the molar mass, and N_A is Avogadro's number . This can be rewritten simply as

$$\sigma = \alpha / N \tag{3}$$

where α is the absorption coefficient and N is the atomic number density[39]. The cross section determination of stimulated emission is a little more complicated. As previously noted, stimulated emission photons share the same phase, direction of propagation, and polarization, which is distinct from light produced from conventional sources through spontaneous emission. Specifically, they share these characteristics with the incident photon inducing the stimulated emission and thus the photons involved are thus all mutually coherent. Therefore, in the presence of a population inversion, optical amplification of incident radiation takes place. Although light generated by stimulated emission is always at the exact frequency of the light which has stimulated it, this only refers the specific excitation corresponding to the energy of the transition. At frequencies slightly offset from the transition, the extent the emission will be slightly decreased according to the spectral line shape. While the specifics of this broadening are beyond the scope of this work, if one assumes only homogeneous broadening resulting from the finite lifetimes of the elevated energy levels as well as the interactions of the laser active ions with the crystal lattice phonons, the spectral line shape function is described as a Lorentzian distribution[40]

$$g'(\nu) = \frac{1}{\pi} \frac{(\Gamma/2)}{(\nu - \nu_0)^2 + (\Gamma/2)^2} \tag{4}$$

where Γ is the full width at half max, ν is the emission frequency, and ν_0 is the line center, or peak maximum. The line shape function is generally normalized so that its value at the peak maximum is one, and

$$g(\nu) = \frac{g'(\nu)}{g'(\nu_o)} = \frac{(\Gamma/2)^2}{(\nu - \nu_0)^2 + (\Gamma/2)^2} \tag{5}$$

is obtained as the shape function. Therefore stimulated emission intensities at frequencies away from the peak center are reduced by this factor. Experimentally there is likely also expected to be inhomogeneous factors broadening the line shape due to the fact that in a solid medium, the laser active ions can be in different sites where their ions experience different local electromagnetic fields. The attenuation due to these effects is Gaussian in shape and reduces the peak strength of the line shape function, but it is more likely to be a strongly contributing factor in glass or highly disordered materials[39]. The last factor needed to fully describe the stimulated emission cross section is to determine the likelihood of spontaneous emission initially. The Einstein A_{21} coefficient is related to the rate of spontaneous emission of light from some energy level $E_2 > E_1$ in the form

$$\varepsilon = \frac{h\nu}{4\pi} n_2 A_{21} \tag{6}$$

where ε is an emission coefficient, n_2 is the density of the upper energy state, *h* is Planck's constant, and ν is the emission frequency. Note that there can be many complicating factors convoluting determination of emission cross sections, such as reabsorption modifying the spectral shape of the emission and the possibility of spectral overlap of differing fluorescent transitions near a similar value. However, emission cross sections for rare earth ions can also be estimated from absorption cross sections[41]. While specif-

ics of the derivation are beyond the scope of this review, in conclusion, the stimulated emission cross section can be written in the form of a Fuchtbauer-Landenberg equation:

$$\sigma_{21}(\nu) = A_{21}\frac{\lambda^2}{8\pi n^2}g(\nu) \tag{7}$$

where A_{21} is the relevant Einstein coefficient, λ is the emission wavelength in a vacuum, n is the refractive index of the medium, and g(ν) is the line shape factor assuming homogeneous broadening only[42]. Note that the absorption cross section can also be written in terms of these Einstein coefficients.

The slope efficiency is widely used to measure the efficiency of a gain medium and gives the ratio of change in output power to a change in pumping power. It is dependent on many factors, including the pump source wavelength, doping cation, and the dopant concentration. This general relation is illustrated in Figure 7.

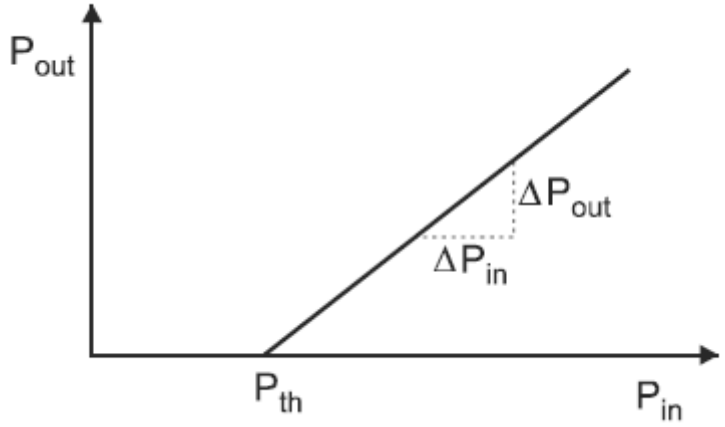

Figure 7: Output power P_{out} is shown to be dependent on both the input power P_{in} and a threshold power P_{th}[37].

It cans be seen from the figure above that the efficiency of the material is the slope of the P_{out} versus P_{in} curve. Thus the general equation

$$P_{out} = \eta_s(P_{in} - P_{th}) \tag{8}$$

can be used, where P_{out} and P_{in} are the output and input power, respectively, P_{th} is the threshold pumping energy, and η_s is the slope efficiency equal to $\Delta P_{out}/\Delta P_{in}$. It can be seen from this that in order to completely describe the efficiency of a laser, more than this information is required. The ratio $\Delta P_{out}/\Delta P_{in}$ alone cannot give the output power for a given pump power, since the threshold pump power P_{th} must also be known, Thus, both parameters are often given as figures of merit for measuring laser efficiency. The specifics of the systems determining the values of η_s and P_{th} manifest in the forms

$$\eta_s = \eta_q \eta_e \varepsilon_p \eta_p \frac{\ln R}{\ln R - L} \tag{9}$$

and

$$P_{th} = \frac{h\nu_e S}{2\eta_q \sigma_e \eta_e \tau_r \eta_r \varepsilon_p \eta_p} (L - \ln R) \tag{10}$$

for continuous (standing wave) laser operation where h is Planck's constant, R is the emission rate, S is the cross-sectional overlap of the pump and laser cavity, σ_e is the stimulated emission cross-section, and L is the round trip loss. The other efficiency factors have the following meanings: η_r is the radiative quantum efficiency equal to

$$\eta_r = \frac{\tau_f}{\tau_r} \tag{11}$$

where τ_f and τ_r are the fluorescence and radiative lifetimes. η_q is the quantum defect efficiency equal to

$$\eta_q = \frac{h\nu_e}{h\nu_p} \tag{12}$$

where ν_e and ν_p are the laser and pump emission frequencies, respectively. $\varepsilon_p\eta_p$ is the fraction of absorbed photons from the pump source, η_e is the effective stimulated emission efficiency equal to

$$\eta_e = \frac{\sigma_e^{eff}}{\sigma_e} \tag{13}$$

where

$$\sigma_e^{eff} = (\sigma_e + \sigma_a - \sigma_e^{esa}) \tag{14}$$

is the effective stimulated emission cross section, effected by the a reduced excited state absorption (ESA) factor. It can be seen from these expressions that in order to minimize p_{th} and maximize η_s, high pump efficiencies, large absorption cross sections, and long radiative lifetimes are desirable[43].

In order to meet these considerations, a solid-state gain medium must have a homogeneous index of refraction[38] and must be transparent to both the radiation of the pump source and the lasing radiation. It needs to be hard enough to withstand and sustain a high level of optical polish and must be chemically stable enough in order to not form color centers or have segregation of phases once optically active ion dopants are introduced into the host crystal matrix. The combination of dopant and host material must be selected to attain a long fluorescence lifetime, low lasing threshold, and high efficiency[3]. Polycrystalline ceramics laser media must be based on cubic symmetry so that there are not differing indexes of refractions at grain boundaries of grains of different orientation. These would act as scattering centers and would affect coherent beam generation. Small percentages of porosity imbue significant scattering, meaning near theoretical density is required[2].

It is important to recognize the difference between the spontaneous and the stimulated emission of laser hosts. The slope efficiency of the stimulated emission is what is critical for laser operation, while the spontaneous emission is of a much lower efficiency. The onset of laser activity can be identified by an increase in the output intensity once the

threshold pumping energy density required has been reached. Figure 8 illustrates this onset with different (red, green, and blue) colloidal quantum dot films[44].

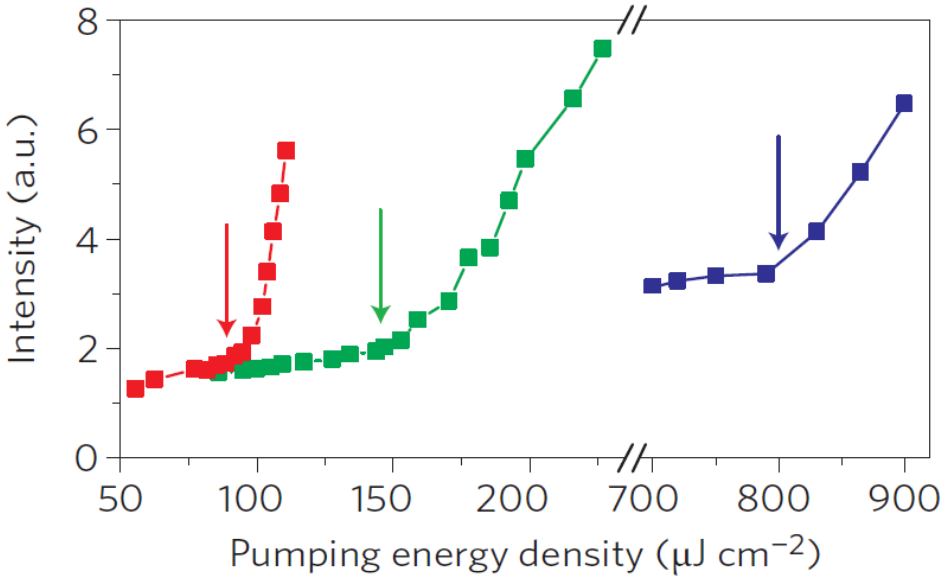

Figure 8: Example threshold pumping energies for various colloidal quantum dot films[44].

2.2.1 Rare Earth Spectroscopy

What is unique about rare earth ions doped into a crystalline matrix is that energy level structure is largely similar to those expected from quantum theory of atomic spectroscopy; that is, simple perturbations from the atomic structure can be collected into a small level of corrections generally summarized through crystal-field interactions[43]. With rare earth ions found in the $4f^n$ configuration, the partially occupied 4f shell electrons are shielded by the electrons in the 5s and 5p orbitals, and thus these electrons have very little interaction or bond formation effects with the crystalline lattice. Thus, 4f state transitions are expected to be sharp and have emission characteristics very similar to their pure atomic states. However, if a 4f electron is excited into the 5d or higher orbitals beyond

those shielded from the 5s and 5p shells, these interactions become more strongly influenced by the lattice and thus require a more significant degree of modification of the crystal-field theory to appropriately predict and model. However, for Yb^{3+}, these higher energy emissions are near UV and are not the focus of this study, which is instead focused on the emissions at around 1030 or 1080 nm. Thus one can largely treat the near-IR emissions from Yb^{3+} from the $4f^n$ orbitals as what would be expected from a free Yb^{3+} ion.

The usefulness of Yb^{3+} as a laser ion became evident with the development of high-powered InGaAs laser diodes in the 1990s[45]. It was found that Yb^{3+}, with respect to the near-IR emission, is effectively a quasi-three level laser system with a much lower stimulated emission cross section compared to Nd^{3+}. While these initially meant there were drawbacks of high lasing thresholds and heat generation, benefits become apparent when discussing high-powered operation. These include minimized losses due to ESA or to up-conversion and cross-relaxation energy transfers that can occur at high dopant concentrations of more complicated energy structures, such as with the Nd^{3+} ion[43]. The quasi-three level structure also means that the conversion factor η_q becomes a much higher value on the order of 90% for Yb^{3+} compared to ~75% for Nd^{3+}. It still remains imperative that these samples stay adequately cooled, but being able to fabricate a thin disk with a high dopant concentration along with the high thermal conductivity host material makes this easier to realize[46]. One small drawback of Yb^{3+} based lasers is that the extent of homogenous broadening due to electron-phonon coupling is slightly augmented compared to other rare earths such as Eu^{3+}[47]. Even though the emission cross section remains small compared to Nd^{3+}, its fluorescence lifetimes are longer and can be used to

produce higher peak output power. Thus, the value of the stimulated emission cross section cannot on its own be considered a figure of merit for determining the effectiveness of Yb^{3+} in various host crystals. Theoretical analysis of continuous wave operation of Yb^{3+} based lasers taking into account the ions long fluorescence lifetime, high P_{th}, and greater extent of heat generation had identified sesquioxide materials such as Y_2O_3 and Lu_2O_3 crystals as promising laser hosts as early as 2001 due to their high thermal conductivity and thus low sensitivity to high thermal loading at elevated pumping powers[48], but the general difficulty in producing high quality crystals of these materials meant they were not generally considered great candidates for the ion[43]. Fortunately, producing polycrystalline ceramics of the same material does not run into many of the same issues that work with single crystals involved at the turn of the century.

2.2.2 Emission of the Yb^{3+} ion

Reviewing quantum mechanics, the total angular momentum quantum vector **j** defines the angular momentum of any electron by combining its orbital angular momentum and its spin angular momentum. If an electron's spin angular momentum is described by the spin quantum vector **s** and its orbital angular momentum vector by the azimuthal vector **ℓ**, the total angular momentum **j** is defined as **j** = **s** + **ℓ** and it can take the following range of values in integer steps[37]:

$$|\ell - s| \leq j \leq \ell + s$$

For multielectron particles, L, S, and J are used instead, with the specific S value assumed by following Hund's rule of maximum multiplicity[49]. Using these terms, the energy levels taken by an atom or ion can be described by the free-ion term ^{2S+1}L, where

L takes the label S, P, D, F, or G for L = 0, 1, 2, 3, and 4 respectively and 2S+1 defines the spin multiplicity. For closed interior shells, the total orbital angular momentum L and spin angular momentum S quantum numbers are zero and thus the only transitions occur within electronic configurations at energy levels outside the optical range. For rare earth ions, the dominant +3 valence occurs when the atom gives up its outer 6s elections and one 4f electron, leaving the partially empty shell below the closed outer 5s and 5p shells. This allows for energy transitions on the order of 1000 cm^{-1}, within the optical range[50]. The ground electron configuration of $4f^{13}$ for Yb^{3+} thus contains the spectral term ^2F. By using

$$|L + S| \leq J \leq L + S$$

to account for spin-orbit coupling and explain the energy splitting, one labels the energy level manifolds as $^{2S+1}L_J$; this means that the ^2F term splits into $^2F_{5/2}$ and $^2F_{7/2}$ (since L is 3 and S is ½). The residual degeneracy within each of these splits is defined by 2J + 1 as based on the projection of the J quantum number, M_J, meaning the higher energy state of $^2F_{5/2}$ has a 3 way microsplit with 2 electrons in each, while $^2F_{7/2}$ has a 4 way split. This means there can be multiple detectable (and possible, as determined by selection rules) energy transitions between $^2F_{5/2}$ and $^2F_{7/2}$ energy states in the emission spectra of Yb^{3+} doped ceramics. The resulting energy gaps determine that the pumping energy for Yb^{3+} is about 970 nm, and the two primary IR emission wavelengths occur at about 1030 and 1080 nm [51].

2.3 Sintering and Ceramic Processing

Polycrystalline lasing media can be fabricated through a process called sintering. Sintering involves heat treating a pressed powder compact to induce atomic mass transport that densifies though solid bonding of particles and pore removal. The driving force for this process is the reduction in the total free energy (ΔG_{tot}) given by the equation

$$\Delta G_{tot} = \Delta G_v + \Delta G_b + \Delta G_s \tag{15}$$

where ΔG_v, ΔG_b, and ΔG_s are the free energy changes for the material volume, grain boundaries, and surfaces, respectively. The surface energy change is the controlling factor in this process and can be expressed as $\gamma_s \Delta A_s$ where γ_s represents the interfacial surface energy and ΔA_s represents the change in the surface area[52]. Thus, this interpretation of ΔG_s can be modified to give a representation for changes in interfacial energy related to the changing interfaces. Thus, the equation,

$$\Delta(\gamma A) = \gamma \Delta A + \Delta \gamma A \tag{16}$$

factors in both coarsening and sintering[53]. Densification occurs when solid bonds are formed between grains and grain centers are brought closer to each other to accommodate into an arrangement that reduces the solid-vapor surface energy area. The surface energy is a consequence of the fact that atoms on a particle's free surface have more energy than atoms within the bulk of the particle, since the interfacial atoms have broken interatomic bonds. Therefore, the reduction of the surface energy in order to arrive at an equilibrium state is the provided driving force for particle sintering.

2.3.1 Pressing and Powder Consolidation

The first step to sintering from ceramic powders is to consolidate the powders into a compact by means of pressing, molding, or casting. The focus of this work involves dry pressing, both through the means of a uniaxial single-action press as well as cold-isostatic pressing. In general, dry pressing is used in the production of refractories and tiles, due to it being relatively inexpensive yet still able to form shapes to close tolerances[54]. The stages in dry pressing include the loading of the pressing die, compaction of the powder or granular material, and ejection of the compact from the die. Good powder fill and flow is essential for a uniform density of the compact. Dense spherical granules of about ~20 μm size are preferred for this goal, and more than 5% fines of sizes below 20 μm can actually be a hindrance to achieving good flow during the compaction[52]. Fines may enter the spacing between the punch and die walls which can increase friction and impede the escape of air. In addition to this, extremely coarse granules can impede flow and restrict achievement of uniform bulk density, and should be removed by a sieve beforehand. Pressing problems such as decapping or dihedral cracking are reduced when the fill density is high, since it reduces the content of air in the powder as well as the distance the punch needs to travel. Powders containing dense granules will typically have a fill density of about ~30%, while granules containing large pores or a donut-shape will have a relatively lower packing density. Properly controlled granulation processes need to be utilized in order to maximize the fill density of the powders before compaction.

In dry pressing, pressure produced by the moving punches compacts with an initially high densification rate, but this decreases rapidly for pressures above 10 MPa. Granule rearrangement, often assisted by binder, occurs by the sliding and rearrangement of the

particles which reduces the intergranular porosity and increases the number of intergranular contact points. Air compressed in these areas migrate and escape through the spacing between the punch and die. The final compact density is less than the maximum packing fraction of the granules due to friction that prevents particle sliding as the number of intergranular contacts increase. The compaction rate CR is given by

$$CR = \frac{V_{fill}}{V_{pressed}} = \frac{D_{pressed}}{D_{fill}} \tag{17}$$

and is simply the ratio of the fill and pressed powder volume, or inversely, the ratio between the pressed and filled density. A low compaction ratio will reduce the amount of compressed air in the compact, and thus it is apparent why a high fill density is desirable. A binding agent is often used to increase the green strength of the granules and green density of the compact, while a plasticizer is used to ensure that the binder used is below its glass transition temperature.

The compaction of the powder through a pressing die generally occurs in three phases. In the initial phase, granules flow and rearrange into a more highly packed arrangement but do not deform. In the intermediate phase, the granules begin to deform and air trapped in intergranular pores beings to migrate away from the center of the compact; this occurs with the applied pressure begins to exceed the yield pressure P_Y of the granules, and is where the greatest extent of densification occurs. Lastly, the granules themselves begin to densify, leaving only small persistent intergranular pores between the now deformed spheres. Granules are expected to have a yield pressure of about 1 MPa, though if the binder content is high or poorly plasticized, a higher pressure is needed to compact to an equivalent density[52]. Generally, the dependence of P_Y can be qualitatively described by

$$P_Y = C\left(\frac{PF}{1-PF}\right)\left(\frac{V_b}{V_p}\right)S_0 \tag{18}$$

where C is a constant, PF is the packing fraction, V_b and V_p is the volume of the binder and plasticizer, respectively, and S_0 is the tensile strength. During the deformation of the granules, the achieved density can be estimated by

$$D_{compact} = D_{fill} + m\log\left(\frac{P_a}{P_Y}\right) \tag{19}$$

where $D_{compact}$ is the compact density, P_a is the applied pressure, and m is a compaction constant that depends on the deformability of the granules and takes the form

$$m = \left(D_{10P} - D_p\right)\log\left(\frac{10P}{P}\right) = D_{10P} - D_p \tag{20}$$

where 10P is a decade of applied pressures within the intermediate stage, and indicates the compactibility of the powder. It is noted that a high compact density can be obtained with a relatively low value of m if the granules are highly dense initially. But the elimination of intergranular pores is favored when moderately dense granules have an intermediate value of m of about 7-10%[52]. During the last stage of compaction, not much densification occurs due to concentrated stress at the growing number of intergranular contacts causing fracture of aggregates or anisometric particles that block densification. An illustration of these three general stages is given in Figure 9.

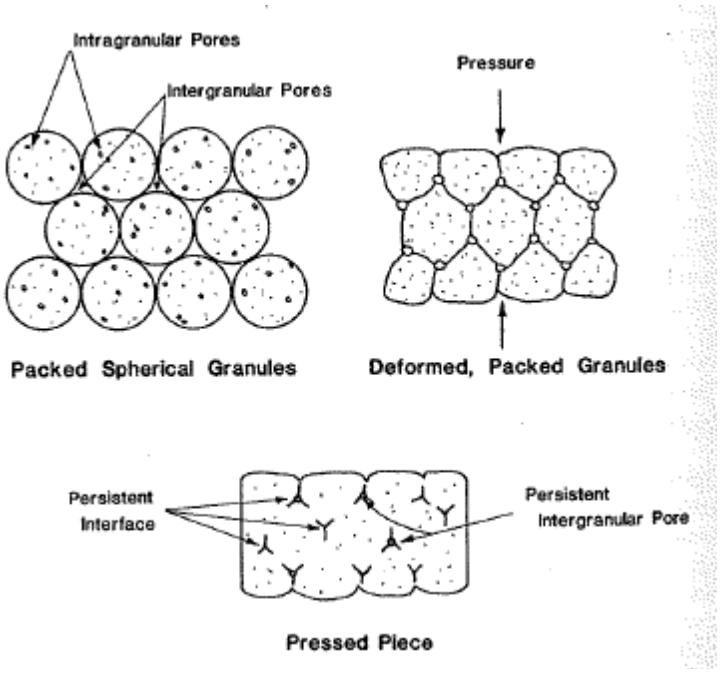

Figure 9: Illustration of the change of shape and pore distribution during powder compaction[52].

One limitation of dry pressing is that pressure gradients are invariably introduced, particularly at regions near the die walls, resulting in density variations throughout the part. This means that during firing of these pressed parts, variations in the amount of shrinkage will also vary as regions of inhomogenous densities are eliminated by material flow during sintering[54]. Movement of bulk powder decreases as distance from the moving punch increases, with the greatest resulting pressure occurring near the top corners, close to the punch and die walls. Pressure decreases as distance from the punch increases, though near the end of the intermediate phase of powder compaction a small region of low pressure can form right below the punch position. These pressure gradients are illustrated in Figure 10[52].

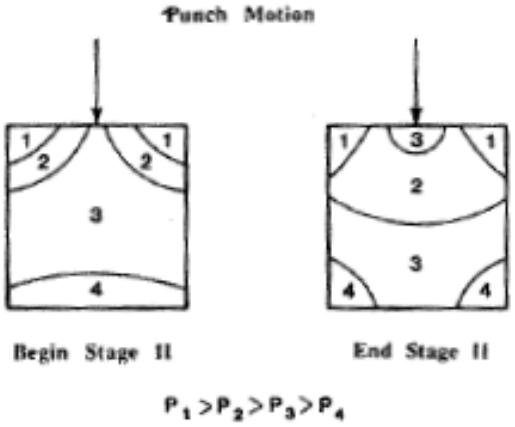

Figure 10: Pressure profile showing gradient of applied stress with a single-action press[52].

A well lubricated surface between the punch and die walls can reduce the amount of axial pressure gradients present in the powder compact before ejection. This is because a portion of the applied load is transferred to the die wall during compaction and die wall friction affects the shearing stress in the compact at the wall through the relation

$$\bar{\tau}_W = f K_{h/v} \bar{P} + A_W \tag{21}$$

where τ_W is the shearing stress at the wall, f is the wall friction, $K_{h/v}$ is the ratio of horizontal and vertical pressure, and A_W is the adhesion at the wall. While shear stress is thus always increased with increasing pressing pressure P, it can be reduced by sufficient lubrication, reducing the friction and thus the shear. For larger samples, the effect of the wall friction is notably lessened[55]. For uniaxial pressing using a single-action punch and die, the axial pressure P_H and depth H as a function of applied pressure P_a takes the form

$$P_H = P_a \exp - \left(\frac{4 f K_{\overline{h}} H}{\overline{v} \, Dia} \right) \tag{22}$$

where Dia is the diameter of the compact and 4H/Dia represents the ratio of the friction area to pressing area $A_{friction}/A_{pressing}$.

The density of the compact actually shows a small time-dependent relaxation as the powder is ejected from the die once the desired pressing pressure is reached. Differential springback occurs when the part is removed from the die due to the aforementioned pressure gradients that present themselves during the compaction process. Other factors include nonuniformities in compression of the compact due to variations in granule size or shape, surface roughness due to poor die lubrication, as well as the difference between ejected and unejected portions of the compact of the regions still constrained by the die walls before ejection is complete[52]. The amount of springback must be limited such that pressing defects such as delamination or endcapping do not occur.

The use of a polymer binder present in spray dried granules not only aids in the compaction process by allowing the granules to deform into each other during the intermediate compaction phases, but the presence of binder also provides green strength by limiting the amount of post-compaction dilation[55]. This is because elastic polymers can react to changes in the applied stress by short-range bending and stretching as well as by rearrangement of the molecular strands. These processes depend on the difference between the polymer's glass transition temperature T_g and the working temperature. If too far below the transition temperature, stress-induced rearrangement of the strands is slow but if working at or above the T_g of the polymer, there is enough random thermal motion of the strands to allow rearrangement under stress and the mechanical response of the

polymer will be more highly time-dependent. A general illustration of the compact density as a function of applied stress and time after ejection is show in Figure 11[55].

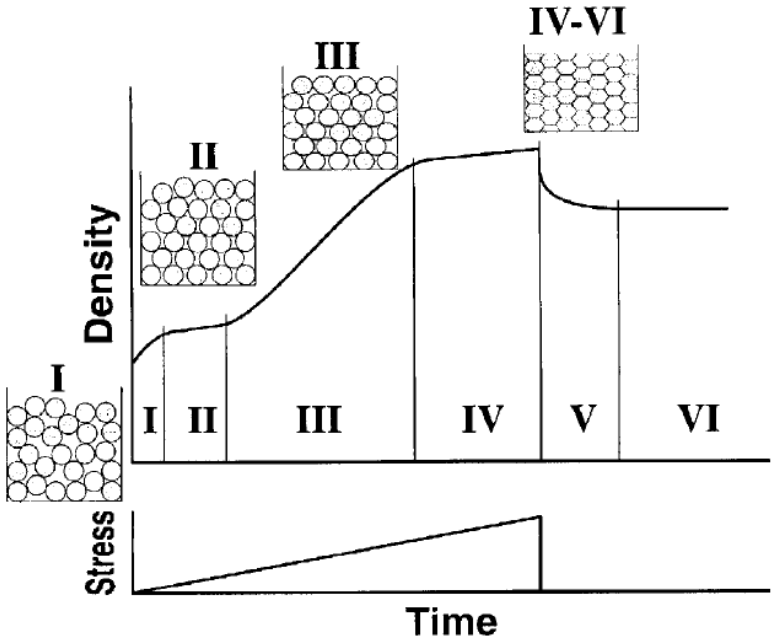

Figure 11: A qualitative illustration of $D_{compact}$ as a function of applied stress during pressing. I: Particle Rearrangement. II: Initial granule yielding. III: Large scale granule deformation IV: Compact compression. V: Ejection and accompanying instantaneous springback. VI: Final density[55].

The main defects that occur if the green strength of the compact is not high enough are delaminations, end capping, and ring capping. Other less common pressing defects include vertical cracking on the exterior of the compact, shape distortion upon sintering due to non-uniform shrinkage, and abnormally large pores formed from poorly formed granules[52]. Laminations appear as circumferential cracks on the frictional surface, perpendicular to the pressing direction, while end-capping is a shallow wedge shaped section which separates from the compact at an angle of ~15° from the end of the compact on ejection. Adhesion of the compact to the punch surface can aggravate this defect, and it is

more likely to occur if the compact strength is low. The presence of endcapping may indicate that the binder used was not properly plasticized. An illustration of these two common defects is given in Figure 12.

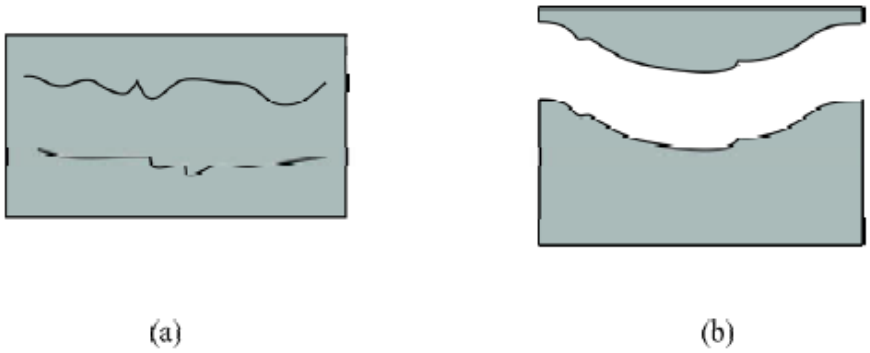

Figure 12: Defects of a.) delamination and b.) end-capping that can occur after ejection of a pressed powder compact.

Dry bag isostatic pressing mimics dry pressing except that the pressure is applied uniformly by means of pressurizing a low vapor pressure liquid medium with a flexible rubber or polyurethane shell between the pressing fluid and the powder or compact within, with the flexible mold often at least partially evacuated[52]. The result is that variations in sample density and resulting shrinkage are therefore diminished[54]. Operating pressures of as high as 345 MPa are can be achieved through isopressing, and shear stresses that can distort granules are found to be lower, though the granules must still be appropriately plasticized in order to remain deformable. Using an isostatic pressing process is a simple way to maximize the relative green densities of a powder compact, without changing its shape, while ensuring that the applied pressure is uniformly distributed over all surfaces of the samples.

2.3.2 Solid-State Sintering

In order to densify a powder compact, the specimen can be thermally treated through a process called sintering. In solid-state sintering, specifically, lattice (sometimes called volume) diffusion and grain boundary diffusion are the primary means of densification. Various other mechanisms can also occur that can result in coarsening of the ceramic. These mechanisms are summarized in Table 1.

Table 1: Transport mechanisms and the result of the microstructure of a ceramic during sintering[52, 54, 56].

Mechanism	Path of Atoms	Result
Viscous Flow	Lattice to neck	Densification
Evaporation-Condensation	Surface to vapor to neck	Coarsening
Surface diffusion	Surface to vapor to neck	Coarsening
Adhesion	Surface to lattice to neck	Coarsening
Volume diffusion	Boundary to lattice to neck	Densification
Dislocation climb	Dislocation to neck	Densification
Grain boundary diffusion	Boundary to neck	Densification

Solid-state sintering is not performed using a wetting liquid (liquid-phase sintering). This method is used to reduce adverse materials properties that could result from introducing the ceramic to a wetting agent, such as the formation of secondary phases. The process by which a ceramic undergoes solid-state sintering can be categorized into three stages. For an overview: In the initial stage of sintering, neck formation between particles occurs through surface diffusion or an evaporation-condensation process. The change in curvature caused by the neck formation gives rise to a sintering stress, which is modeled by the Laplace equation[56]

$$\sigma = \gamma\left(\frac{1}{R_1} + \frac{1}{R_2}\right) \tag{23}$$

where γ represents the surface energy as before, while R_1 and R_2 represent the radius of curvature for a each particle. A convex surface results in a positive radius of curvature with tensile stress while a concave surface results in a negative radius of curvature with compressive stress. A flat surface exhibits no curvature and therefore is stress-free. Thus, that is considered to be the stable geometric state and any surface irregularities will tend towards this flattened state in order to eliminate stress. The atoms at the particle surface require less energy for diffusion than the interior to undergo this process due to their excess free energy due to unfulfilled bonding compared to the interior, thus this process occurs first at the lower temperatures of sintering before particle grains begin to exhibit growth. During this period, pore volume decreases by ~10-12%[52], but particle centers do not approach. Since vapor-phase transport is the primary mechanism during this stage, pores do change shape during this stage which can have an appreciable effect on various properties, but density change is negligible[54].

In the intermediate stage, the necks between particles grow and lattice diffusion works to transport atoms from the interior of the grains to the grain boundaries. Thus, porosity is further reduced and the centers of the grains are brought closer together, resulting in densification. In this stage, multiple transport mechanisms can contribute to the microstructural evolution, and shrinkage modeling is complicated by the start of grain growth and changes in the overall pore geometry[52]. Solid-solid interfaces are created in the form of grain boundaries, which have lower free energy than the replaced solid-vapor interfaces at the former particle free surfaces. Vacancies in the grains are moved to the grain boundaries, and then collect as pores. Most of the shrinkage during sintering occurs

in this step. Densification continues until about 10% porosity is reached, at which point rapid grain growth occurs, which greatly reduces the densification rate[54].

The onset of this rapid grain growth indicates entrance into the final stage of sintering. The energetic favorability of reducing grain boundary energy area drives grains to grow, and diffusion of atoms across the grain boundary and the disordered regions between grains force the grain boundaries to be displaced. Densification during this phase is around 3-5%. Provided thermal energy causes some grains to grow at the expense of others, with the net effect as a reduction in total grain boundary area. Pores combine into the junctions at grain triple points, as shown in Figure 13. However, exaggerated grain growth during this stage can lead to the possibility of pores becoming entrapped within the grain interiors where removal becomes impossible and a lower extent of final densification results. Exaggerated grains can separate from pores in regions of the microstructure if the process is not carefully controlled. This becomes more likely if dense powder aggregates or coarse particles are present and the pore distribution remains inhomogeneous[52].

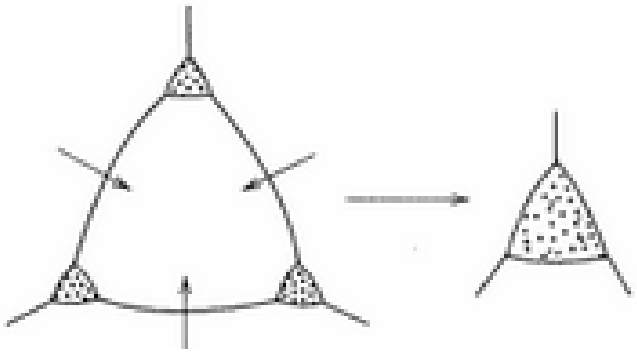

Figure 13: Pore agglomeration during grain growth in the final stages of sintering[54].

In more detail, Figure 14 shows the basic set up for a 2-sphere model for the neck formation that occurs at the initial stages of solid-state sintering, before densification occurs. Because of differences in chemical potential, the concentration of vacancies near a concave surface is higher than that at a convex surface. Consequently, evaporation-condensation transport will move material from out convex surfaces to the middle neck of adjoining particles due to the higher concentration of vacancies. Figure 15 summarizes the effect of surface curvature on vacancy concentration.

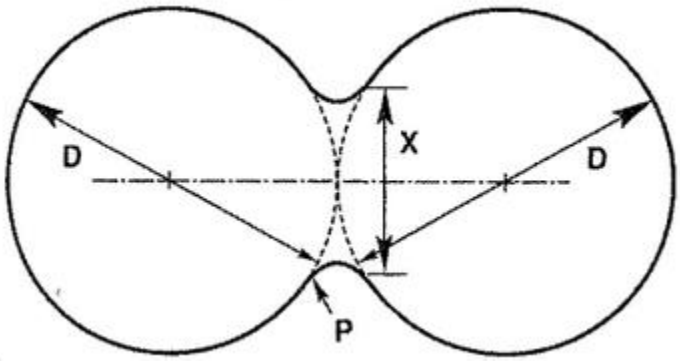

Figure 14: Two particles in contract during solid-state sintering[56].

Using the figure above and the Laplace equation, the stress of the area away from the neck is $\sigma = 4\gamma/D$, with D being the particle diameter. The stress at the neck is $\sigma = \gamma((2/X) - 4D/(X^2))$, where X acting as the neck diameter and X/2 being the effective particle radius. The transition from a convex (particles) to concave (neck) surface induces a sizeable stress gradient. This stress gradient provides the driving force for mass transport from near surface regions to the neck. However, as mass increasingly flows to the neck, the stress gradient is expected decreased as the curvature approaches a flat surface; thus the sintering process decelerates. Since during the initial stage of sintering largely involves

the mass transport from the highly curved particle surfaces to the neck, no appreciable densification is observed until other mass transport processes involving the particle bulk become energetically favorable at increased temperatures.

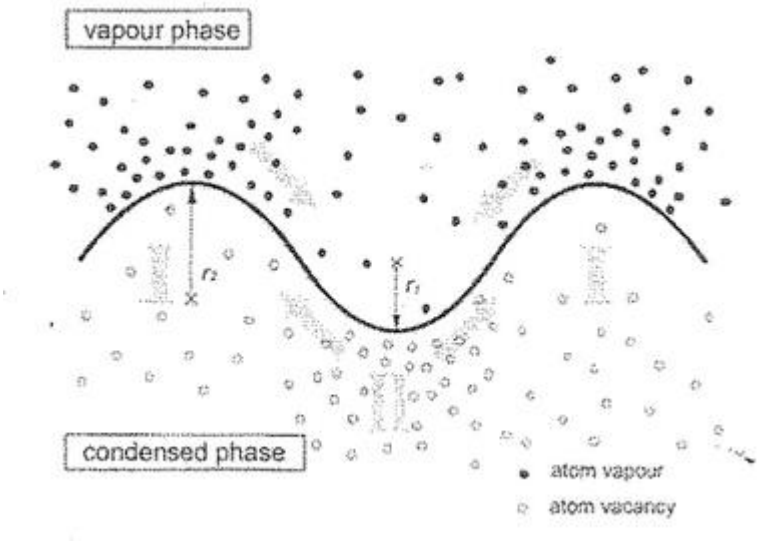

Figure 15: Effect of interface curvature on vacancy concentration and vapor pressure. Higher concentration of vacancies at the particle neck facilitates volume diffusion[53].

At the onset of the intermediate stage of sintering, particles begin to form grain boundaries between each other as they grow into contact due to the mismatch in the lattice orientation between them. A relatively high concentration of defects and vacancies at the grain boundaries lowers the energy needed for mass flow to occur, thus grain boundary diffusion occurs more rapidly than lattice diffusion at lower temperatures, with the grain boundary diffusion rate depending on the angle of misorientation between the grains. A lower grain boundary energy increases sinterability because high energy solid-vapor (pore) surfaces become replaced with these low energy grain boundaries since they are more energetically favorable. The higher the degree of misorientation initially present

between two particles growing into each other, the higher the energy of the resulting grain boundary. A high energy grain boundary can result in increased grain growth as a material is driven to reduce the overall energy of the system, by reducing the total grain boundary area, and thus grains begin to grow abnormally.

However, at higher temperatures lattice diffusion becomes more dominant than grain boundary diffusion. This is because increased temperature influences the rate of lattice diffusion due to the increase vacancy concentration C_v with increasing temperature, which follows the relationship

$$C_v = \exp\left(-\frac{Q_v}{RT}\right) \tag{24}$$

where Q_v is the activation energy for the formation of vacancies, R is the ideal gas constant, and T is the temperature. In addition, the resulting loss of grain boundary area as grains grow makes grain boundary diffusion less significant at this stage. In the ideal case, the particle/grain morphology during the intermediate stage of sintering changes from a sphere to that of a tetrakaidecahedron, a shape with 14 sides that will fill space with no porosity. Isolated pores are moved onto the grain edges and create a pore network that is interconnected throughout the microstructure.

Curvature can also affect the equilibrium concentration of vacancies in addition to temperature. The vacancy concentration for a curved surface is given by the Gibbs-Thomson equation

$$C = C_o\left[1 - \frac{\gamma\Omega}{kT}\left(\frac{1}{R_1} + \frac{1}{R_2}\right)\right] \tag{25}$$

where C_o is the equilibrium (temperature dependent) vacancy concentration, γ is the surface energy, Ω is the atomic volume, k is the Boltzmann constant, T is the temperature,

and R_1 and R_2 are the radii of curvature. Thus, in the early stages of sintering (before grain boundary and lattice diffusion begin the process of densification in the intermediate stage), the difference in the concentration of vacancies originates from the curvature mismatch between the particle bulks and the neck that forms between them. While the particles exhibit a convex surface; the neck has a concave surface. This mismatched vacancy concentration gradient leads to mass transport into the neck until grain boundary and eventually lattice diffusion takes over at higher temperatures in the intermediate stages when the curvature mismatch diminishes.

Grain growth occurs due to the movement of grain boundaries during the last stage of solid state sintering. The interconnected pores fix themselves in place and become isolated on grain corners and no longer pin grain boundaries. This results in the change in idealized pore microstructure shown in Figure 16. The ability of a pore to shrink is dependent on its size as well as the dihedral angle between pores and grains. A larger dihedral angle between the planes containing the grain faces and a smaller number of grains surrounding each pore will better result in shrinkage. Thus, it is generally beneficial to obtain the highest degree of packing and greatest relative density in the powder consolidation processes before sintering.

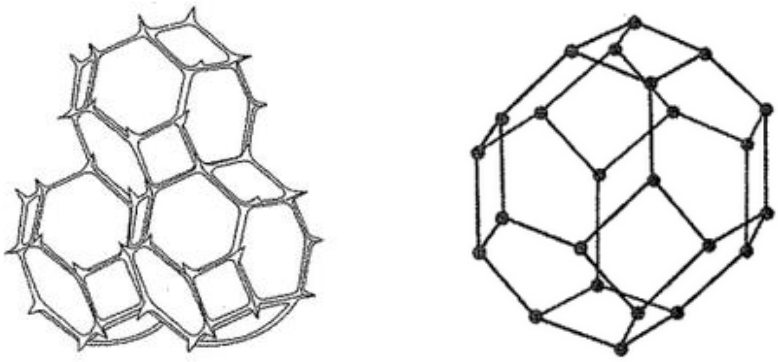

Figure 16: A representation of the evolution of interconnected pore structure during the intermediate and final stages of solid state sintering[56].

Continuing lattice diffusion can also contribute to the coarsening of pores near the end of the sintering process. This process results from the difference in equilibrium vacancy concentrations of pores of differing radii of curvature, similar to the discussion involving curved particles at the onset of sintering. Small pores with high curvature can act as vacancy sources whereas large pores with lower curvature act as vacancy sinks. The diffusion from the smaller pores to the larger pores results in coarsening of the surviving pores in a process known as Ostwald Ripening.

The effects of temperature, curvature, and grain boundary energy on mass transport, and thus sinterability, can be effectively summarized by Fick's first law

$$J = -D_V \frac{dC}{dx} \tag{26}$$

where J is the mass (or vacancy) flux, D_v is the diffusion coefficient, and dC/dx represents the concentration gradient. A higher degree of mass transport is expected from greater vacancy diffusivity due to higher temperatures and a larger vacancy concentration gradient due to mismatches in radii of curvature.

2.3.3 Chemical Co-precipitation

As high-performance applications for ceramic materials such as optical fibers and thick film electronic ceramics become of increasing interest in industrial processing, so too has the need for preparing ceramic powders with specific qualities, such as purity in excess of 99.9%, precisely controlled dopant distribution, consistent submicron particle size, and in some cases, even a particular particle shape is desirable. Chemical solution techniques such as co-precipitation are generally an easily implemented way for preparing particles of a fine size and high purity, making it a good match for achieving these desirable parameters. Co-precipitation is a process where a liquid solution containing the cations of interest is prepared, a solid particulate phase in the form of a salt is produced from precipitation, which is then decomposed without melting by calcining at a relatively low temperature[52]. While co-precipitation has been a studied process for many decades[57], the use of this method has recently become commonplace as highly pure nano-sized powders have become desirable for these emerging potential uses of ceramics fabricated from them. An example flow diagram for the formation of a pure precipitate from an ionic solution is given in Figure 17.

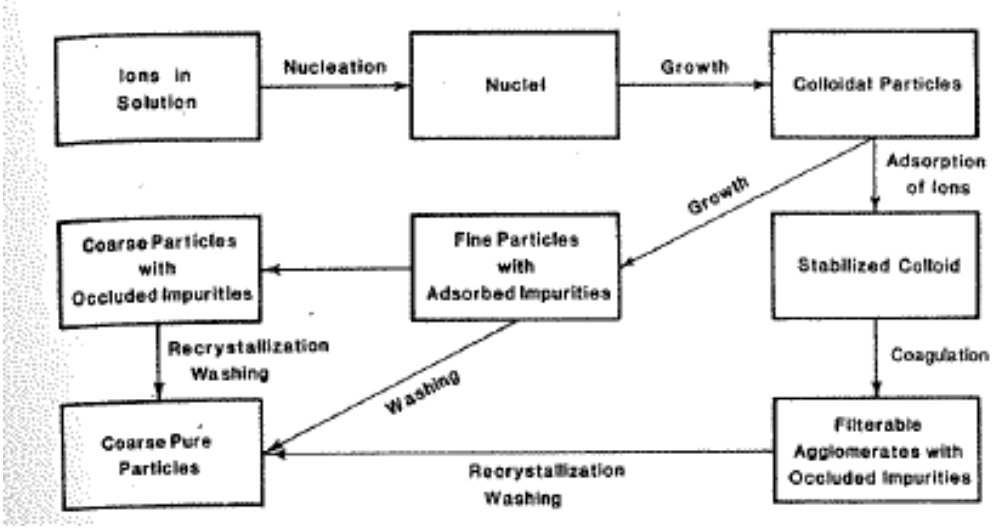

Figure 17: Flow chart for producing highly pure ceramic particles from precipitating ions from solution[52].

Precipitation occurs by nucleation and growth. A higher degree of supersaturation, such as forming the ionic solution at a higher temperature and then performing the precipitation at room temperature, may increase the nucleation rate and reduce the particle size, but the rapid rate of formation may cause foreign ions to end up occluded within the particles[52, 57]. While the formation of mixed crystals is desirable for applications such as providing a dopant material for the formation of laser-active ceramic media, occlusion may be any impurity in the solution being absorbed into the growing crystallite, which results in imperfections in the crystal lattice[57]. As shown in the figure above, occluded impurities can be removed through recrystalization washing, where dissolving and re-precipitating in a fresh solution may reduce the concentration of minor occluded impurities, though this could be time consuming due to the high nucleation of rate of supersaturated ion solution, requiring the precipitation rate to be well-controlled in order to prevent more occluded impurities from forming. However, adsorbed impurities on the

precipitate surfaces are still likely to form after that particle has nucleated, especially if the precipitate is micro-crystalline in character[57]. Washing of the precipitated powder many times will generally remove these impurities without the need for recrystalization. In either method of washing, generally many times the original solvent is needed to fully purify the samples, resulting in a large volume of dilute waste. Thus, optimizing initial precipitation parameters that avoid the need for recrystalization by preventing occluded impurity formation in the first place will greatly optimize the formation of highly pure nano-particles without undue time or yield costs[58].

One main limitation of the co-precipitation methodology is that upon calcination of the precipitate salt, the resulting powder is generally in the form of porous aggregates of agglomerated small particles which must be crushed or milled before sintering[52]. The agglomeration resulting from aqueous based co-precipitation and drying methods is caused by strong hydrogen bonding between hydroxide precursors and water molecules. The polar water molecules attract the precursors and cause them to pack together when dried[6]. The yield of chemically processed powder is limited by the extent of solubility of the ions in the solvent, and the rate of precipitation must be controlled to prevent occluded impurities from being entrapped in the nucleated crystallites. The extent of washing required to achieve the desired purity as well a proper method for crushing the final calcined agglomerates without unwanted impurity introduction must also be carefully considered. The method chosen must adequately reduce the agglomerates to a sinterable powder while not introducing new impurities that will hinder the qualities of the final ceramic and undo the timely processing of the nanopowders[59]. However, ball milling is an easy to implement way to reduce the extent of agglomeration and if it can be performed with-

out introducing impurities or if the impurity content is not of significance to the ceramic matrix (such as milling in media of the same material), it would be viable for producing ceramics from previously agglomerated powders with a high degree of flexibility for batch scaling.

2.3.4 Ball Milling

Sintering straight from agglomerated powders without milling, either as-received or post-calcination after chemical synthesis, will result in ceramics containing large grains and many structural and morphological defects[59]. While ball milling is widely used to reduce the average particle size of a material or modify particle size distribution, it is also used to effectively disperse and mix multiple components[52], which is useful when working with doped materials or organic additives used for pressing or spray drying of the milled powder once retrieved. Ball milling can also result in an increase in the sintering rate of ceramics produced compared to unmilled powders due to a smaller number of variations present in the original packing of particles in the powder compacts, such as voids between large agglomerates leading to variations in pore concentration upon sintering[54]. A ball mill is a rotating cylinder partially filled with hard wear-resistant media and either a dry feed material or a wet slurry that is exposed to the colliding media as they tumble on a rotating mill. A simple schematic of the setup is provided in Figure 18.

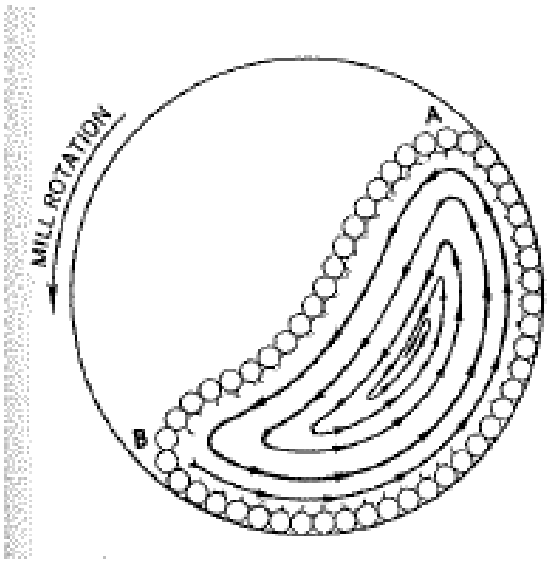

Figure 18: A schematic of a typical ball mill, showing spherical media cascading from A to B and the subsequent movement of the milled slurry feed[52].

Many factors determine the efficiency of ball mill operation, including the angular velocity of the mill, the size of the media relative to the size of the material, and the viscosity of the slurry. The collision of the media material produces both compressive and shear forces on the particles contained within the slurry. Shear occurs when a particle is caught between two surfaces moving at different velocities, and attrition is produced when by frictional stresses occur even as impact force decreases, as long as rubbing contact between media material occurs. The grinding energy produced during the operation of a ball mill is proportional the mass and change in velocity of the media on impact, meaning that the energy can be increased using media of a larger size or density, though the consideration of possible contaminants will also determine the density of the selectable materials that can be safely used with impurity considerations in mind. Larger media will also limit the fall distance of the material as constrained by the milling container.

If the feed slurry contains agglomerated powder, a dispersant must be used in order to maintain maximum milling effectiveness. Agglomerates end up absorbing some of the impact energy, reducing the energy remaining for particle fracture and thus size reduction[52]. Agglomeration also reduces the frequency of media impacts with free particles, which is directly proportional to the effectiveness of the mill. For efficient slurry milling, the solids content should be high enough such that the slurry has an adequate viscosity so that the media remains evenly coated in the contact zone, and media wear (and thus contamination) is minimized. Smaller media down to the size of 1 mm are used for milling micron sized particles or dispersing agglomerates because the rate of fine grinding is highly dependent on the collision frequency.

The grinding energy of a ball mill is proportional to the kinetic energy of the media on impact in the form

$$Energy = \Delta\left(\frac{1}{2}mv^2\right) \tag{27}$$

where m is the mass of the media and v is the velocity on impact. The critical angular frequency that can cause centrifuging, and prevent the proper cascading of the mill media, is given by

$$\omega_{cr} = 0.5R^{-1/2} \tag{28}$$

where R is the radius of the mill in meters, and ω_{cr} is the angular frequency in Hz. A mill should be operated at 0.65-0.85 Hz to produce a maximum media height of ~60° from the horizontal. A 50% mill volume of high solids-loading slurry is a good compromise of grinding efficiency and reduced media wear.

2.3.5 Sonication and Sedimentation

Sedimentation has long been a way to characterize a suspension's particle size distribution, and can also be used as a method to separate particles of different sizes based on the differing settling rates of large and small particles in a liquid of a specific viscosity. Gravitational sedimentation is useful for particles of larger size since small particles either settle too slowly for a practical analysis time, and also because particles affected by Brownian motion (collision with smaller fluid particles) preventing anything too small from effectively settling[60]. Stoke's law states that the sedimentation velocity depends on a particle's size, shape, and density. A settling velocity distribution can also be used to characterize inhomogeneous suspension without specific knowledge of these parameters[61]. Assuming spherical particles, at terminal velocity the downward force of a sphere in a viscous medium is

$$F_g = (\rho_p - \rho_f) g \frac{4}{3} \pi R^3 \tag{29}$$

where ρ_p is the density of the particle, ρ_f is that of the fluid, g is the acceleration due to gravity, and R is the radius of the spherical particle. Stoke's law states that the buoyant force acting on a spherical particle is

$$F_d = 6\pi\mu RV \tag{30}$$

where V is the flow velocity, R is the particle radius, and μ is the fluid viscosity. When the two compositing forces are equal, the terminal velocity of the particle becomes

$$V = \frac{2}{9} \frac{(\rho_p - \rho_f)}{\mu} g R^2 \tag{31}$$

which can then be used to determine the size of particles that have fallen a certain distance vertically as time elapses, at whichever desired height of the column used.

The two methods of sedimentation analysis or separation are integral and differential. In integral sedimentation, a specific distance from the surface of the column is monitored. A well-dispersed suspension is placed into the column (or centrifuge if accelerations of greater than *g* are desired) and particles are then allowed to settle from every point in the column at once. At the onset of the separation, the concentration of particles at this chosen height is maximized, but as time elapses, particles of a certain size will have fallen past the marked point, leaving only a less concentrated suspension of smaller diameter particles remaining at and above a certain settling distance. In differential sedimentation, all of the particles are placed into the column at once, and they are assumed to settle at different rates according to their size. At any particular time only particles of a certain size or higher have passed the desired marked point in the column, and smaller particles above that point can be filtered out. A schematic of both sedimentation methods is given below in Figure 19[60].

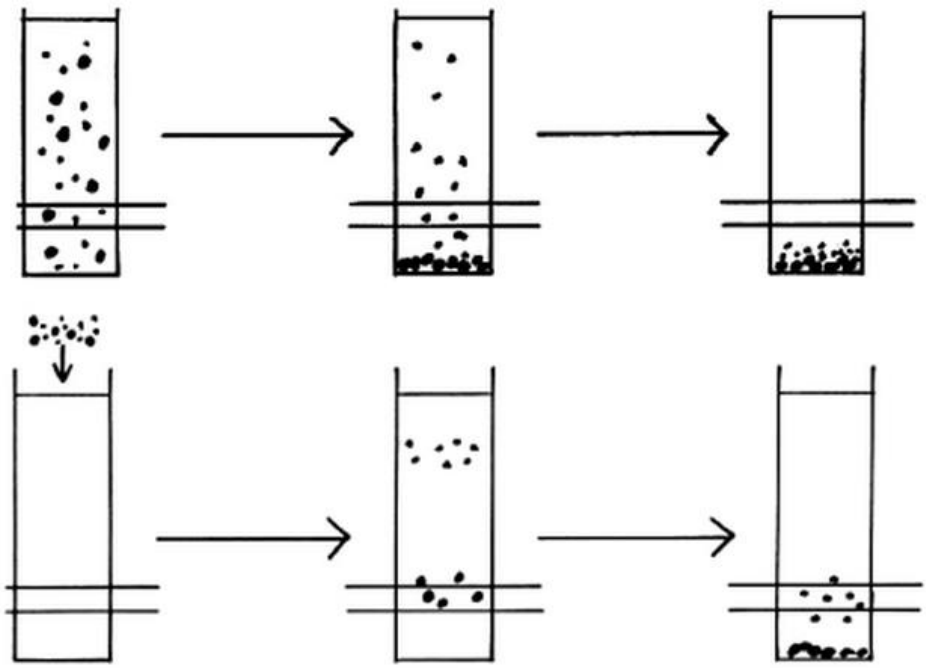

Figure 19: An illustration of integral (top) and differential (bottom) sedimentation columns. The arrow represents either a point of analysis (using an x-ray source and detector) or a marked point for particle separation[60].

Neither method of sedimentation is without drawbacks. In integral sedimentation, the initial conditions of the suspension are hard to characterize and turbulent mixing may have already occurred as the suspension enters the column. In differential sedimentation, placing all of the particles at the top of the column at the onset can result in the particles not settling individually according to Stoke's law, but rather as a homogeneous dense liquid settling as a bulk fluid. This can be prevented by only placing a very small amount of the suspension at the surface of the fluid and by providing a density gradient in the column fluid before sedimentation begins. This means that particles at the surface and just under the surface will each have a different drag force and the tendency to bulk settle is greatly reduced. However, this process can be much more involved to set up and maintain a con-

sistent fluid density gradient from trial to trial as different powders are separated or analyzed.

Sonication is also a related method for dispersing and deagglomerating particles in suspension. This is especially important if the goal is to separate particles of particular individual sizes without convoluting agglomerate factors limiting the extent of particle reduction possible (such as settling full agglomerates). When sonicating suspensions in liquids, a transducer horn converts the energy from an ultrasonic generator into mechanical energy in the form of ultrasonic vibrations. From this horn, the sound waves then propagates into the suspension, resulting in alternating high-pressure and low-pressure cycles, producing mechanical shear forces that can result in breaking apart agglomerated particle aggregates[62]. The resulting high speed jets of liquid can become pressed between the particle agglomerates and separate them from each other. The resulting smaller particles can then even become accelerated within the suspension jets and collide with each other at high speeds, further reducing their size.

In order to generate sufficiently high amplitudes, the transducer must be equipped with an acoustic horn which increases the vibrational amplitude delivered to the suspension. One limitation of this method is that conventional high-gain converging horns are limited to having small output diameters in order to provide high enough sound amplitudes. If the output diameter of the horn is increased (in order to investigate the possibility to scale up a certain sonication process, for example), its maximum vibration amplitude becomes significantly lower and the effectiveness of the process is greatly reduced. Another important potential area of concern when using these ultrasonication horns is possible contamination by metal particles during sonication. For instance, the tip surfaces

of titanium alloy based horns can undergo erosion over time, resulting in Ti metal contamination of the suspension being sonicated[63].

2.3.6 Spray Drying

Dried agglomerated and bulky powders do not flow well for considerations of pressing[52] or sinter well for considerations of having a uniform green ceramic, and these issues can be resolved by means of a granulation process such as spray drying which results in homogenous spherical granules of high uniformity. Spray drying is a method where dry solid granules are obtained by evaporation of the carrier liquid in a suspension. Spray drying involves of feeding a suspension containing the particles to be granulated through an atomizer that divides the stream into droplets as they enter a drying chamber. They then come into contact with a dry hot inlet gas and convert into granules as they undergo evaporative cooling, and are collected in either a cyclone or filter bag[64]. Atomization is the controlling factor of the spray drying process since the formation of small droplets through an atomization nozzle greatly increases the surface area to for the liquid solvent to evaporate, which improves the efficiency of heat transfer from the drying gas to the droplets. This means that tuning of the atomization process enables control of the droplet size and consequently, the final size and characteristics of the dried granules.

There are many different types of atomizers that are used to produce the droplets from the suspension as they begin to dry. Two main nozzles types are rotary nozzles which use centrifugal energy to disperse the droplets and mixed-flow pressure nozzles which use

acoustic energy. A diagram of these types is given in Figure 20[52]. Atomization nozzles and two-fluid nozzles are also sometimes used[64].

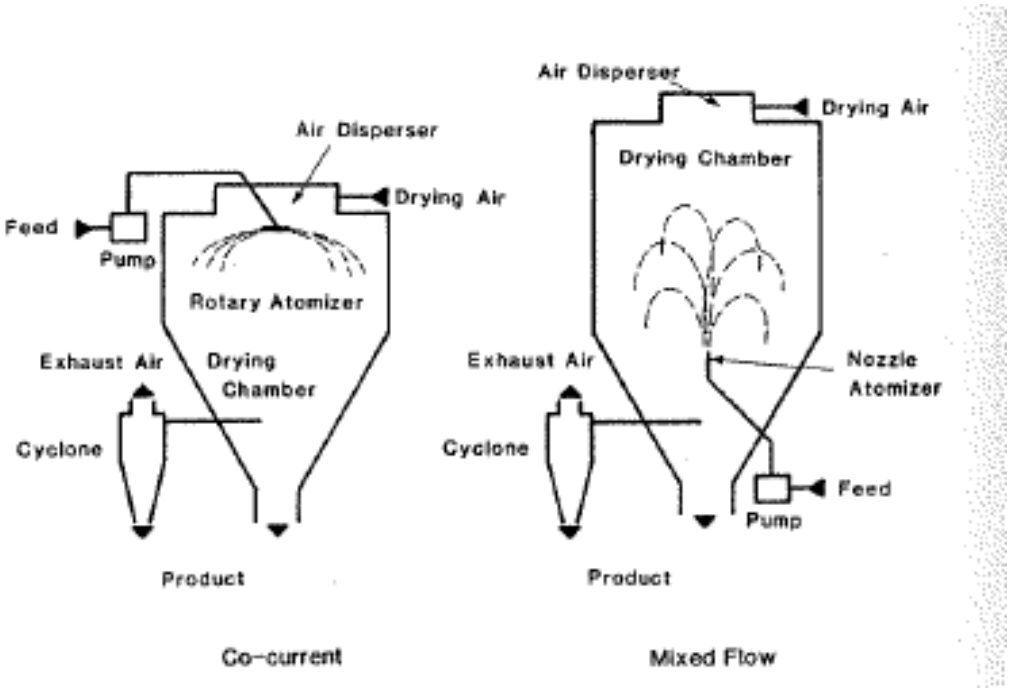

Figure 20: Schematic of co-current (left) and mixed flow (right) spray driers, with a centrifugal atomizer and a nozzle atomizer, respectively[52].

In the figure above, it is shown that the primary components of any spray dryer are the pump and feed inlet, the atomizer exposed to the drying chamber with an inlet for a dry hot air (usually nitrogen) and a cyclone (or filter bag) used for collecting the dried granules. For the mixed flow atomizer, ultrasonic nozzles use acoustic energy to cause the tip to vibrate, and this is where the droplet formation takes place. Tuning of the specific ultrasonic frequency used will affect the final droplet size[65]. Ultrasonic nozzles are typically used for laboratory scale spray driers due to their low droplet velocity and limited spray throughput[64]. A primary limitation of ultrasonic nozzles is that the drying temperature is often limited to only about than 110°C. This means that ultrasonic nozzles are

highly compatible with slurries based on a ketone solvent; ketones such as acetone are popular for processes that require very low temperatures in the drying condenser due to their high vapor pressure. This is also convenient for rapid drying when the drying chamber is limited in size. The low drying temperature is also useful when there are organic binders and additives within the slurry that would be susceptible to thermolysis at the 250-600°C range of other spray dryer types[52]. Spray drying at a low temperature means that the organic binder additives can coat each granule evenly for subsequent pressing processes.

Gas dispersers are the second important component in a spray drying unit because they define the pattern of air flow inside the chamber, usually near the nozzle and slurry input, and impact the drying efficiency, particle residence time, and droplet-particle collisions[64]. The disperser is generally located just at the location where the drying gas enters the, where it is critical to have a consistent circulation of the dry gas flow in the chamber to such that all droplets are homogenously dried. A poorly dispersed air flow could result in a greater amount of wall deposits and captured wet particles, lowering the process yield.

2.3.7 Sintering of Traditional Nd:YAG Ceramics

The first Nd:YAG polycrystalline laser ceramics were developed by Ikesue et al. in 1995. The method of forming a transparent YAG ceramic was based on in-house synthesis of Al_2O_3, Y_2O_3, and Nd_2O_3 powders prepared by alkoxide precipitation, pyrolysis of $Y_2(OH)Cl_5 \cdot nH_2O$, and oxalate precipitate, respectively. They demonstrated a sub-micron particle size and an impurity content of less than 100 ppm by weight [3, 5, 66]. The ce-

ramics were vacuum sintered at 1750°C for 20 h using an ethyl silicate sintering aid. Without this sintering aid, an optically anisotropic phase would segregate out of solid solution and hinder transparency. Ceramic samples (3 mm in thickness) achieved a transmittance of ~80%, and the oscillation threshold (pump power required to induce the threshold population inversion) and slope efficiency (ratio of output to input power) were 309 mW and 28%, respectively , almost equivalent to those of an Nd:YAG single crystal[5]. This was a breakthrough result that spearheaded decades of further research into studying polycrystalline gain media as alternatives to single crystals for laser output generation.

Nd:YAG nanopowder production has also been studied by Liu et al. Nd-doped YAG powders were developed by co-precipitation, using MgO as a dopant. This, acting a dispersing agent, resulted in a reduced particle size of ~100 nm [67]. Arabgari et al. prepared a similar nanopowder via nitrate solutions mixed together at an appropriate molar ratio. A 2 M ammonium hydrogen carbonate solution was added drop-wise, acting as a precipitant. At three specific pH values, yttrium, aluminum, and neodymium hydroxides are precipitated out of solution. The hydroxides were then washed multiple times and calcined at 1000°C for 5 h. It was shown that increasing the precipitant concentration improved the crystalline structure and resulted in a smaller final particle size. Adding a surfactant was also shown to decrease the extent of agglomeration [68].

Ikesue et al. were unable to see a benefit in HIPing their sintered ceramics. The optical transmittance of HIPed samples was inferior to those sintered under vacuum. The authors argued that the argon gas present from the HIP treatment was soluble at the silicate grain boundaries present from their used sintering aid. This gas would then evolve as

pressure was released, degrading the ceramic and introducing optically scattering porosity[69]. Ikesue also demonstrated the ability to produce a Nd:YAG single crystal from a sintered ceramic[2]. To do this, a powder compact was pre-sintered at 1550°C for 3 h and was polished to a mirror finish and bonded to an undoped YAG crystal. The bonded sample was then heat treated at ~1800°C, allowing continuous grain growth to occur from the seed crystal through the polycrystal[66]. The result was a formed Nd:YAG single crystal. This resulted in a small improvement in lasing efficiency due to the lack of grain boundaries. With this it has been shown that sintering fabrication technology is not only limited to fabricating polycrystalline cubic laser gain media but can also be utilized to produced heavily doped single crystals as well.

The effects of oxygen annealing have also been investigated for optical YAG ceramics by the physics department of Sichuan University and the opto-functional laboratory of the Shanghai Institute of Ceramics. W. Zhang et al. investigated air and vacuum annealing and their respective effects on transmittance results. Nd:YAG nanopowders were synthesized using a co-precipitation method of neodymium and yttrium nitrate, along with ammonium aluminum sulfate and precipitating with ammonium bicarbonate. The samples were vacuum sintered for 20 h and then annealed under different conditions before being mirror polished on both faces for transmittance data [70].

The authors argue that vacuum sintering creates a slightly reducing atmosphere that results in a ceramic with a greater number of oxygen vacancies that acts a grey impurity that negatively affects transmittance, with the color center formation equation shown in Figure 21. Both vacuum and air annealing for 20 h after sintering were shown to slightly increase transmittance, with air annealing being effective up to 1450°C. The slight im-

provement in transmission is shown in Figure 22. Air annealing is argued to reduce the level of oxygen vacancies in the sample. The calculated lattice parameter is shown to decrease up until this point, which argued as the result of oxygen diffusing back into the vacancies. At 1500°C, the lattice parameter increases and transmittance is lessened, argued as indeterminate high temperature defects. The lattice parameter of similarly annealed samples at 1450°C in vacuum maintain an even higher value, due to not extinguishing oxygen vacancies, but likely still slightly improve transmittance by removing other vacancies, such as antisite defects where cations will occupy an oxygen sites in the lattice[71]. The pumping efficiency of similar ceramics were shown to have the highest slope efficiency at an annealing temperature of 1450°C by Fu et al., argued to be an unsurprising consequence of a greater level of transmittance observed at this temperature[72]. It is discussed that remnant color centers in the ceramic will act as absorbers of the incoming light, and thus lead to less of the desired absorption by the laser active ions, such as Nd^{3+} in this case. However, Fu et al. determined that post-sinter annealing of longer than 8 h were actually damaging to the ceramic's slope efficiency, suggesting the 20 h by Zhang was too extensive.

$$O^{2-} \rightarrow O^{-} + e^{-}$$

$$V_O^{\bullet\bullet} + e' \rightarrow V_O^{\bullet}(F^{+})$$

$$V_O^{\bullet\bullet} + 2e' \rightarrow V_O^{\times}(F)$$

Figure 21: Mechanism of oxygen vacancy-induced f-centers (color centers) in a vacuum sintered optical Nd:YAG ceramic[72].

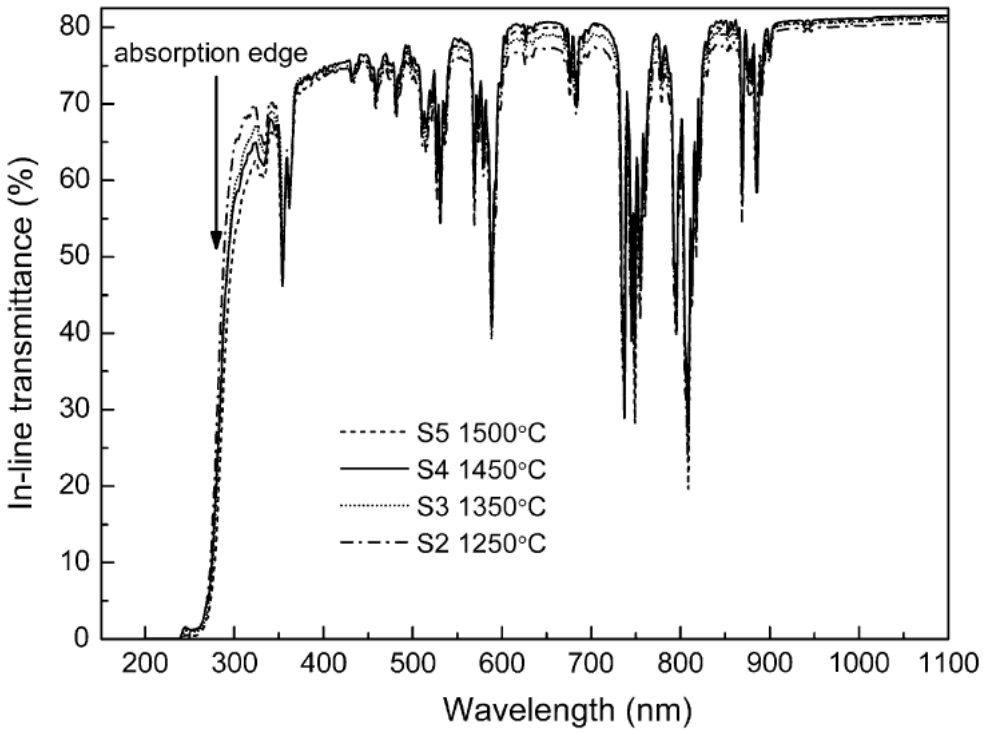

Figure 22: Transmission data of optical Nd:YAG ceramic and effect of air annealing between 1250-1500°C [70].

W. Zhang et al also analyzed the effects of post-HIPing of sintered samples and re-annealing to further remove defects affecting the transmittance of the ceramics. The samples were sintered at the same temperature and annealed at 1450°C in air. They were HIPed at 1700°C, just under the sintering temperature, for 2 h. The post-HIP anneal was performed between 1250-1450°C for 10 h, a shorter duration than the initial anneal[73]. While transmittance values show marked improvement, some other aspects such as the initial absorption edge shift back to pre-annealed values. The HIP result on transmittance is shown in Figure 23. The HIP is argued to also have a slightly reducing atmosphere, so while it is effective at removing intergranular pores, a subsequent annealing step was also identified as possibly being beneficial.

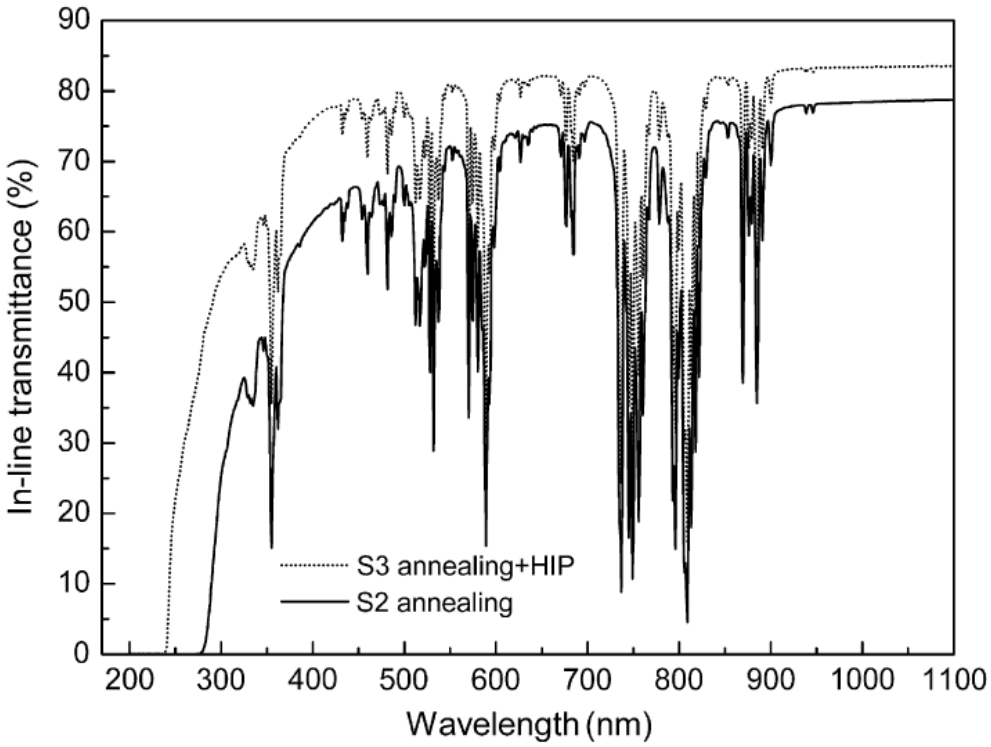

Figure 23: Transmittance data of optical Nd:YAG ceramic with and without HIPing[73].

Re-annealing at 1250°C was shown to be the most effective at maintaining the high transmittance of HIPed samples. 1350°C and up was shown to decrease transmittance, arguing that air annealing after HIP with too high a temperature would end up resulting in pore expansion. So the post-HIP anneal was found to be best implemented at a temperature lower than the post-sinter anneal to maintain the decreased size of any small amount of remnant intergranular pores.

The implementation of a post-HIP treatment on optical Nd:YAG ceramics was also investigated by researchers at the Laboratoire Science des Procédés Céramiques, with a focus on comparing conventionally vacuum sintered optical Nd:YAG to post-HIPed ceramics produced by pre-sintering for a shortened duration before exposing the samples to

a high pressure (150 MPa) argon atmosphere. An additional focus of that work was to evaluate the optimal amount of SiO_2 sintering aid needed with respect to the processing method used[74].

While relative density was shown to increase via traditional solid-state reaction sintering (SSRS) with increased sintering temperature and also increased silica content[75], it was also identified that regardless of the silica content used, at high sintering temperatures SSRS sintering was shown to increase grain size and also the propensity for pores to separate from grain boundaries resulting in lower quality samples and decreased transmittance. The formation of intragranular pores in this manner once relative density of the samples exceeded 99% means that the residual porosity can no longer be removed via further sintering or by hot isostatic pressing.

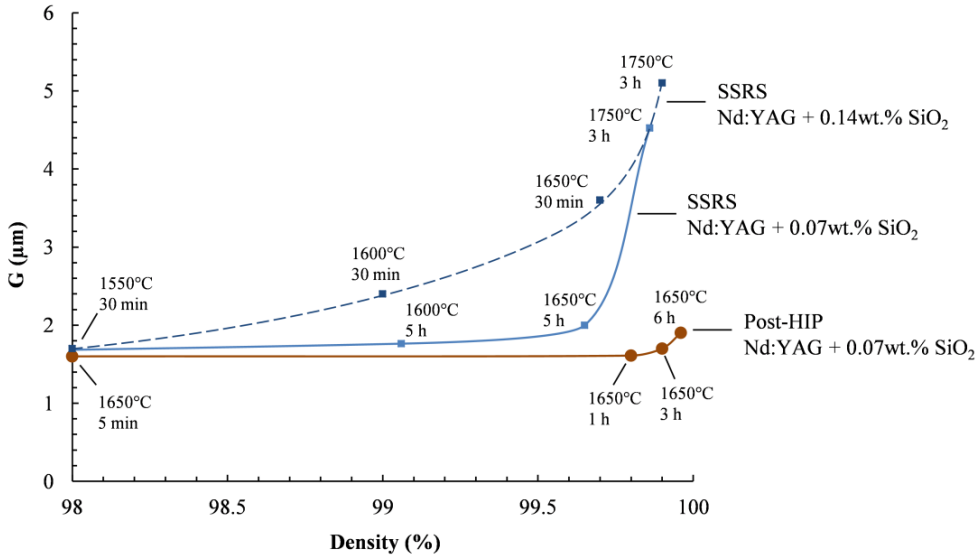

Figure 24: Grain size comparison between samples prepared entirely by solid-state reactive sintering (SSRS) and those produced through post-HIP. Samples were etched by heat treating them at 1000°C[74].

It can be seen from Figure 24 that the level of grain growth seen from processing the samples using post-HIP instead of strictly through SSRS is much further reduced, in addition to less sintering aid needed to achieve high relative density. The decreasing extent of the formation of intragranular pores also resulted in more transparent samples once they were polished, as shown in Figure 25. There are no disparate absorption peaks in either spectrum, indicating that the only difference between the two methodologies in the extent of intragranular porosity, which acts as a grey impurity across all wavelengths.

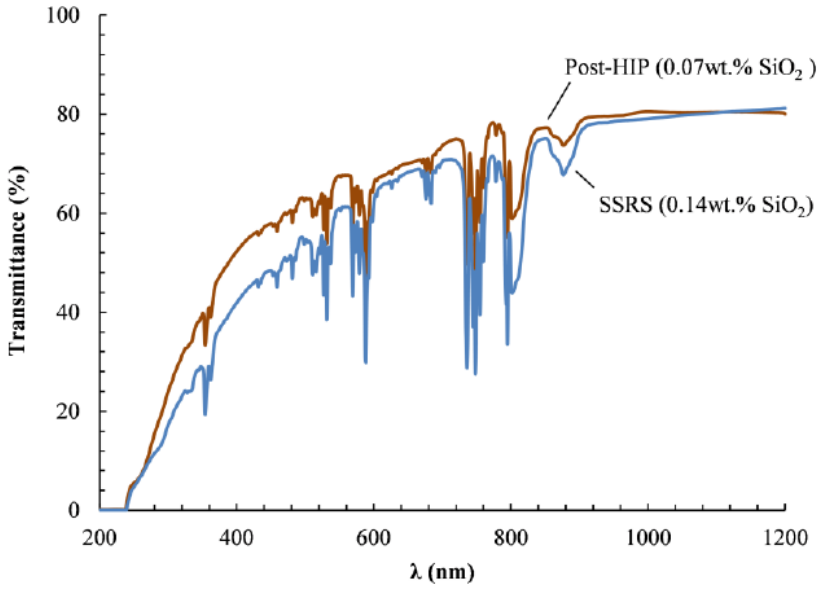

Figure 25: Transmittance comparison of solid-state reactive sintered (SRSS) samples at 1750°C for 3 hours to post-HIPed samples prepared at 1650°C for 6 hours[74].

This work also has a great review of the kinetics of pressure induced densification according to the Nabarro-Herring model. The model states that the densification rate can be enhanced by increasing the isostatic stress, increasing the temperature, and decreasing the grain size (by decreasing the starting particle size).

$$\frac{d\rho}{dt} = \frac{A}{kTG^n} D_0 \exp\left(-\frac{Q_D}{RT}\right)\sigma \quad (32)$$

Where ρ is the relative density, G is the mean grain size, Q_D is the activation energy of densification based on lattice diffusion, and σ is the applied isostatic stress. Since the densification rate increases directly with applied stress, the temperature required to reach theoretical density can be reduced while also limiting grain growth and in turn reducing the amount of irremovable intragranular porosity.

2.4 Sintering of Sesquioxide Ceramics

While polycrystalline YAG ceramics were the first to be studied as potential laser host media, more recently sesquioxide ceramics such as Y_2O_3, Sc_2O_3, and Lu_2O_3 have become attractive candidates for that purpose as a result of their high thermal conductivity and scalability[2]. Melt grown crystals of sesquioxides are difficult to fabricate, requiring temperatures at 2400°C, plus many sesquioxides exhibit a stress-induced phase transition at 2200°C. This means that both extensive high temperature crucible interactions an well and strain induced cracking of the cooled crystal become issues for producing high quality single crystals of sesquioxides[2, 22]. Thus, fabrication of polycrystalline sesquioxide laser hosts through sintering becomes an attractive alternative. Additives such as ThO_2, La_2O_3, and HfO_2 are sometimes used in these systems to enhance densification[19] while additives such as ZrO_2 are often used as grain growth inhibitors[27] and Er_2O_3, Nd_2O_3, and Yb_2O_3 are typical laser active dopants compatible with a sesquioxide matrix.

While the previously-mentioned recent information reported by W. Zhang et al. do investigate the effects of annealing on optical YAG ceramics, similar data regarding ses-

quioxides is much more limited. However, some initial results have been reported by the Shanghai Institute of Ceramics. Chen et at. produced Eu^{3+}- and Nd^{3+}-doped Lu_2O_3 ceramics (which lase at 611 and 1080 nm, respectively). They were sintered in dry flowing H_2 gas at 1850-1880°C for 6-8 h; relative densities of ~99.8% were achieved. Both compositions were fabricated by dissolving the corresponding metal nitrate into solution and precipitating using a mixed ammonium hydroxide – ammonium bicarbonate precipitant, and then calcining between 600-1200°C[20]. Nd^{3+}-doped samples with a grain size of ~50 μm, and of 1.4 mm thickness, achieved a transmittance of 75.5% at 1080 nm[21]. Eu^{3+}-doped samples of 1 mm thickness with a grain size of 50-60 μm achieved a transmittance of 80.3% in the region of 600-800 nm. Subsequent annealing of fired Eu^{3+}-doped Lu_2O_3 samples in an oxygen-rich atmosphere at 1200°C for 2 h was performed in order to establish a well-defined oxidation state and minimize lattice imperfections. This annealing was shown to decrease the photoluminescence intensity as shown in Figure 26, which was attributed to the possibility of absorption of the interstitial oxygen created in the annealed ceramic[14]. This is a noticeably different result compared to the annealing results of Zhang and Fu regarding the annealing of Nd:YAG optical ceramics, where annealing was shown to increase transmittance and thus emission. The take-away here is that vacuum sintered parts show a benefit for post-sinter annealing, while the study in which a hydrogen environment was used during sintering showed the opposite result.

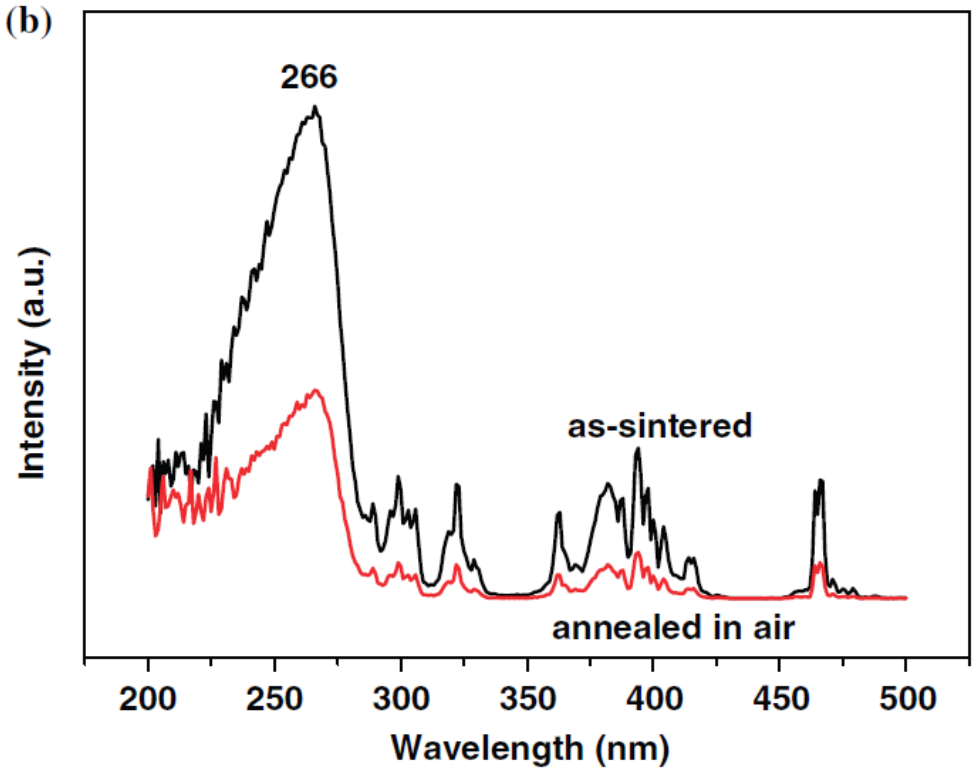

Figure 26: Comparison of optical Eu^{3+}-doped Lu_2O_3 before and after annealing, showing lower luminescence after the additional heat treatment[14].

As identified in Nd:YAG based optical ceramics, the formation of F-centers in a vacuum sintered sesquioxide ceramic can also affect the optical properties of the laser-active dopant if there is one present. Tel'nova et al. at the Moscow Institute of Physics evaluated the optical properties of Yb-doped Y_2O_3 ceramics with respect to the presence of oxygen vacancies. The electrons present in vacancy induced f-centers can compete with the divalent Yb^{3+} cations and reduce them to the bivalent state. However, as expected, the f-center decay after annealing the sintered ceramics returns the samples to transparency and returns the absorption spectra to that matching Yb^{3+} instead of Yb^{2+}[76]. Since the unannealed ceramic contains Yb^{2+}, the sintered lattice forms either vacancies or ionic intersti-

tials, resulting in either a substitution solid solution or an interstitial solid solution independent of the anionic lattice. In either case, no unwanted absorption peaks are found. So there is some conflicting information about the benefit of annealing sesquioxide ceramics, depending on the material and sintering method used.

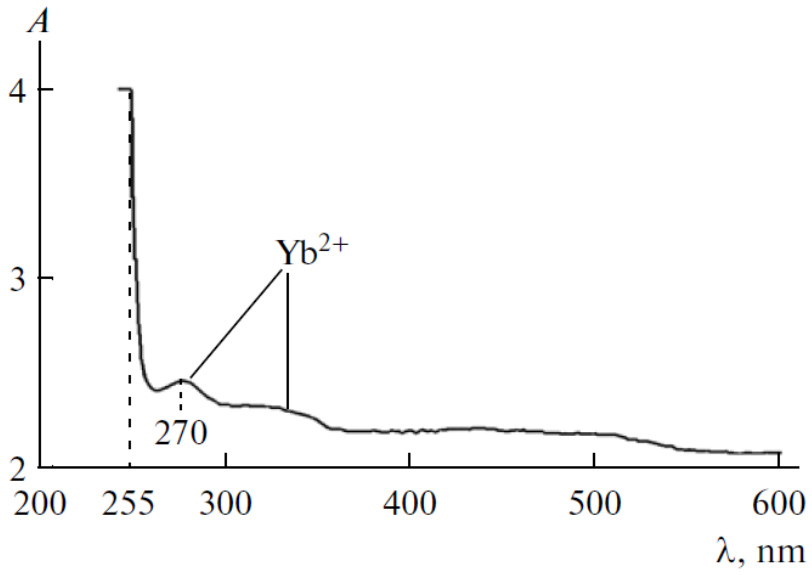

Figure 27: Absorption spectrum showing Yb^{2+} in Yb:Y_2O_3 ceramics after vacuum sintering without annealing[76].

2.4.1 Hot Pressing of Y_2O_3 and Lu_2O_3 Ceramics

Sanghera et al. have developed Yb^{3+}-doped Y_2O_3 and Lu_2O_3 ceramics (which lase at 1080 nm) of varying doping levels. These were densified by hot-pressing precipitated powder compacts between 1300-1700°C for 2-6 h at a pressure of 50 MPa. The starting powder to be hot-pressed was fabricated via co-precipitation synthesis by adding ammonium hydroxide to a mixed nitrate or chloride solution of the relevant cations and then calcining at 600°C. These samples contained a small amount of LiF sintering aid that was

argued to have been extracted via evaporation during heat-treatment[6]. The hot-pressed specimens were then HIPed between 1300-1800°C, under an argon pressure of ~200 MPa, yielding relative densities of 99%[34]. A 2 mm thick 10% Yb:Lu_2O_3 ceramic with a maximum slope efficiency of 74% was fabricated in this way[23]. These Yb:Lu_2O_3 ceramics maintained a grain size of 20-50 μm, which is larger than generally demonstrated for laser-quality ceramics[7]. Sample fluorescence lifetime was relatively insensitive to doping concentrations between 2-8% with a measurable decrease at higher concentrations[23]. Yb:Y_2O_3 samples with 2% dopant, also 2 mm thick, were produced in a similar manner. Slope efficiencies varied between 36-44%, depending on the output coupler[22].

Sanghera et al. also found that producing powders via co-precipitation synthesis sometimes resulted in the formation of large (>100 μm) agglomerates which makes the fabrication of larger optical parts from these powders often containing large structural defects. While ball milling has been used to break up powder agglomerates, there is concern that it will introduce the milling media material into the milled oxide powder. Thus, Sanghera et al. evaluated jet milling as a way to remove these hard agglomerates from their synthesized powder[59]. A simple jet milling schematic is given in Figure 28.

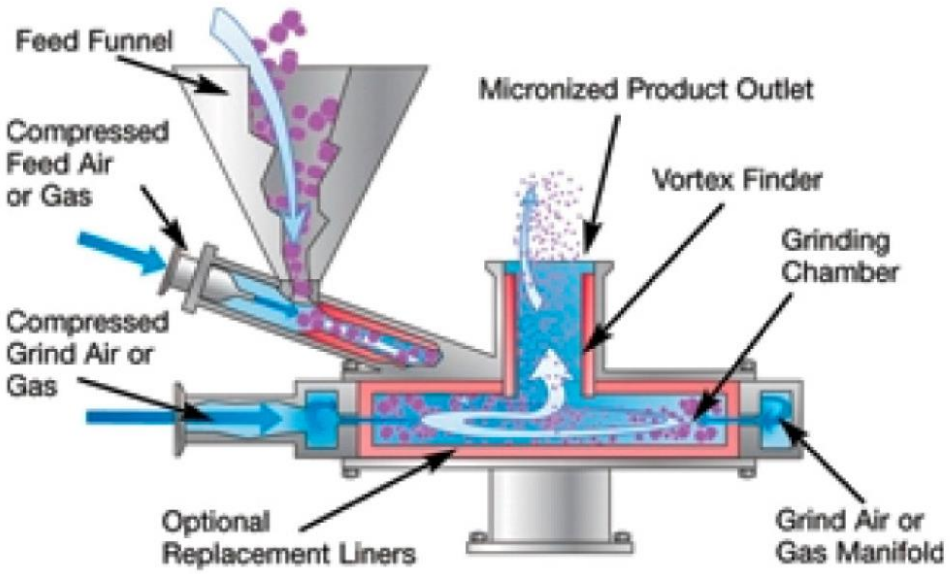

Figure 28: Schematic of a jet milling system for breaking up agglomerates of oxide powders prepared via chemical co-precipitation.

Jet milling forces the feed powder to collide with itself at high velocities using high pressure gas, thus does not have the potential to introduce impurities through the use of any media. However, abrasion with the liner material may still cause contamination of the feed material, so a tungsten carbide liner was used since it has relatively high hardness and abrasion resistance. Hot pressed powders prepared in this way again reached near theoretical transmission of ~80%.

2.4.2 Laser Synthesis of Y_2O_3 Ceramics

Similar Yb^{3+} and Nd^{3+}-doped Y_2O_3 ceramics were produced by Bagayev et al. at the Russian Institute of Electrophysics. Instead of using chemical co-precipitation synthesis, a laser synthesis method developed by Osipov et al. from the Russian Academy of Sciences

was used to produce high purity, low agglomeration nanopowders[77, 78]. In this method, Osipov argues that nanopowders produced in this was have a lower size distribution with a d_{50} of about 100 nm and a lower extent of agglomeration compared to chemically synthesized powders, but at the cost of a higher production price. This is because the high powered pulsed CO_2 lasers (continuous wave lasers have been shown to be less effective[79]) used to irradiate the target in this sort of method are still commercially unavailable. In this method, a laser target is produced from coarse commercial powder of 1-20 μm, which are dry mixed, pressed, and sintered into cylindrical disks. The target is then irradiated with the pulsed CO_2 laser while a drive or motor spins the surface so that it is uniformly processed. The vapor is then condensed under a carrier gas and then collected through filtration. Figure 29 provides a schematic for this setup.

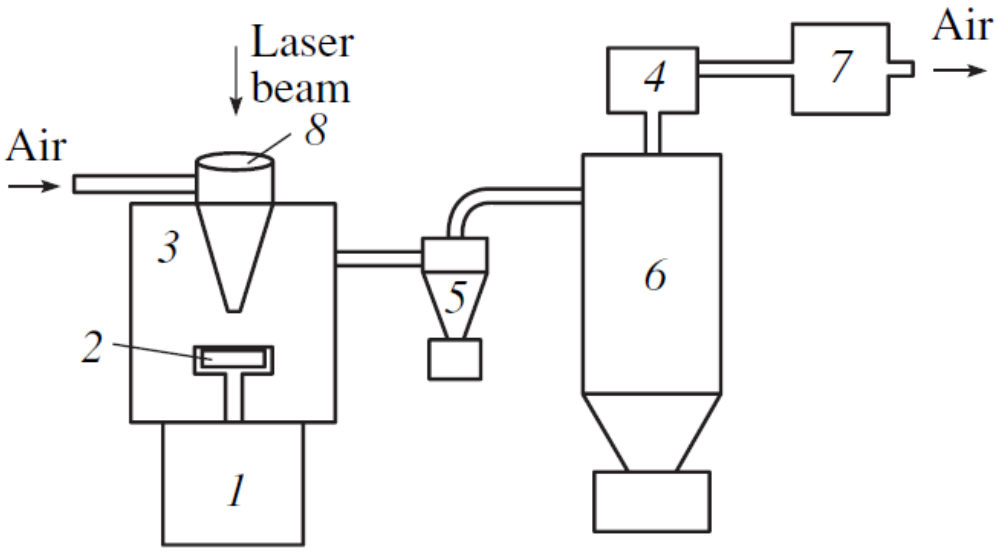

Figure 29: A schematic of the laser processing setup for forming nanopowders from ceramic targets. 1: Drive. 2: Target. 3: Evaporation Chamber. 4: Fan. 5: Cyclone. 6: Filter. 7: Filter. 8: Lens.

After the laser synthesis of the Y_2O_3 nanopowders, that particles are found to be in a metastable monoclinic phase, and are thus annealed for 3h in air at 800-1100°C before vacuum sintering for 20 h at 1700°C and 1900°C. The sintered samples were then annealed in air at 1350°C for 5 h to eliminate the oxygen vacancies. The final polished samples were shown to achieve a maximum transmittance of 81.3% and a maximum slope efficiency of 29%, while maintaining a grain size of less than 10 μm for the 1700°C samples and 50-130 μm for the 1900°C samples, though it was found that these could be reduced to 20-90μm with 12 mol% ZrO_2 additives. Thus, it was found that ZrO_2 as an additive for Y_2O_3 ceramics acts as a promising grain growth inhibitor. The Russian Institute of Electrophysics also evaluated using an attrition mill on commercial Y_2O_3 powders in order to find a way to process non-agglomerated nanopowders for use in sintering optical ceramics without resorting to methods that are difficult to scale up for manufacturing. While it took many evaluations of various commercial sources that worked, the authors were able to find that in one case, where the Y_2O_3 powder consisted of agglomerated nanopowders on the order of 100 nm in size. By de-agglomerating the powder via grinding, they were able to sinter YAG ceramics using the commercial Y_2O_3 powder and achieve a transmittance of greater than 80%[80].

In addition to the formation of nanopowders, laser processes have also been used to sinter bulk doped Y_2O_3 ceramics. In this method, a laser is targeted onto the ceramic sample as the heating source for sintering. The advantage of this method is that heating rates of 2000°C/min can be achieved without crucible contamination. By using a continuous wave CO_2 laser at a power density of about 2.1 W/mm^2, researchers at the University of Sergipe were able to fabricate ~98% dense Ca-doped Y_2O_3 ceramics[25]. The pow-

ders were made using a typical chemical co-precipitation method similar to as described earlier and were preheated to 300°C before laser sintering. However the densities achieved were not suitable for optical transparency, and this method is similar to vacuum sintering in that it results in the creation of oxygen vacancies. Near identical radioluminescence spectra of undoped and Y_2O_3 ceramics doped with Ca, Mn, and Zn suggest that oxygen-related defects actually became the dominating feature in these spectra.

2.4.3 Microwave and Combustion Reaction Sintering of Y_2O_3 Ceramics

Luo et al. at Nanchang Hangkong University have recently shown that microwave sintering is an effective processing method for creating optical Y_2O_3 ceramics, while maintaining a fast heating rate[81]. Microwave sintering is a technique where samples positioned in a microwave field can convert the microwave energy into heat to provide volumetric heating. This provides advantages of rapid and uniform heating and also a greater degree of densification because of a reducing in the activation energy needed for sintering, resulting in a lower required sintering temperature[82]. A general comparison of the differing results between microwave and vacuum sintering is given in Table 2[81].

Table 2: Comparison of microwave and vacuum sintering methods[81].

Processes and properties	Microwave sintering	Vacuum sintering
Heating rate (°C min^{-1})	150–250	15–20
Temperature (°C)	1500	1700
Holding time (min)	30	240
Relative density (%)	99.5	99.1
Microhardness (*hv*)	11.82	10.15
Bending strength (MPa)	255	110
Fracture toughness (MPa $m^{1/2}$)	3.56	1.27
Transmittance (%)	80.5	78.5

The major disparity between the two methods of microwave and vacuum sintering appears to be the rapid heating rate utilized by microwave sintering, and a much longer dwell time needed in conventional sintering. Luo et al. fabricated Y_2O_3 with better mechanical properties, transmittance, and even a smaller, more uniform grain size. This is in contrast with the negative results shown by the fast sintering rate of University of Sergipe's laser sintering result. Regardless, even in the use of a vacuum sintering technique, minimizing sample exposure to the vacuum furnace environment through the use of rapid heating rates and minimal holding time might improve optical and structural properties, even if the aforementioned annealing process described previously becomes necessary due to the formation of oxygen vacancies. Using a two step sinter and then HIP process may also be used to minimize time in a vacuum sintering environment, where a long holding time can be reduced to a much shorter hold time by then processing a short-fired closed-porosity body via a HIPing step afterwards.

Liu et al. at Wuhan University of Technology also investigated the use of an ultra high heating rate for use in sintering Y_2O_3 ceramics. By developing a pressure-assisted

sintering method termed as CR-QP (combustion reaction plus quick pressing), ultra-high heating rates exceeding 1600°C/min can be used along with a short soak duration limited to several minutes[83]. A Y_2O_3 compact wrapped in a thin layer of graphite foil and placed in an air atmosphere furnace environment using a CR-QP die along with Nickel and Aluminum metal powders as combustion reactants lining the sample. The resulting exothermic reason results in very rapid heating, which helps to limit the particle coarsening seen in the early stages of sintering, which is based on time-dependent surface diffusion. An external pressure is applied to help enhance the extent of densification over a limited period of time. A brief soak time helps prevent abnormal grain growth that can occur at higher sintering temperatures without the use of sintering aids or other grain growth inhibitors, which can negatively affect properties such as optical transparency.

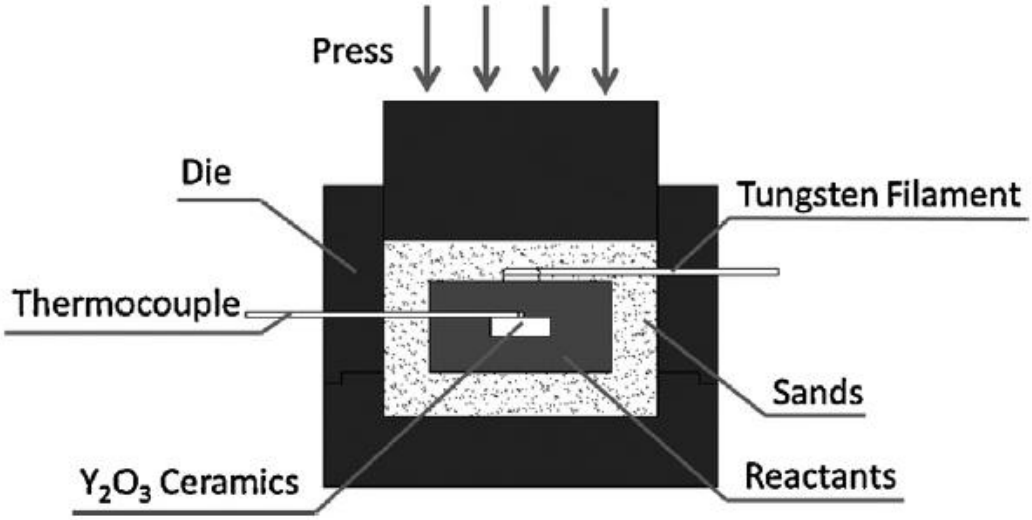

Figure 30: Schematic of a Y_2O_3 sample prepared by CR-QP [83].

Utilizing this method, a Y_2O_3 ceramic sintered at 1620K of 98.5% relative density with a grain size of 50 nm was obtained, but no optical data is provided. Similar ceramics fired

at higher temperatures saw larger grain size with many interior pores and lower relative density, suggesting that the competing relationship between densification and grain growth is highly dependent on the target temperature, which can be difficult to control in this method[83].

The Shanghai Institute of Ceramics has also vacuum sintered Y_2O_3 to transparency through the use of ZrO_2 additives acting as grain growth inhibitors[27]. After slip casting Y_2O_3 green bodies and sintering at 1730-1900°C for 5-15 h, Jin et al. found that a 5 mol% doping of ZrO_2 into their Y_2O_3 ceramics produced optimal microstructure with minimal remaining porosity resulting in much greater transmittance measurements for the doped samples, with a maximum transmittance occurring at 5 mol% doping, as shown in Figure 31.

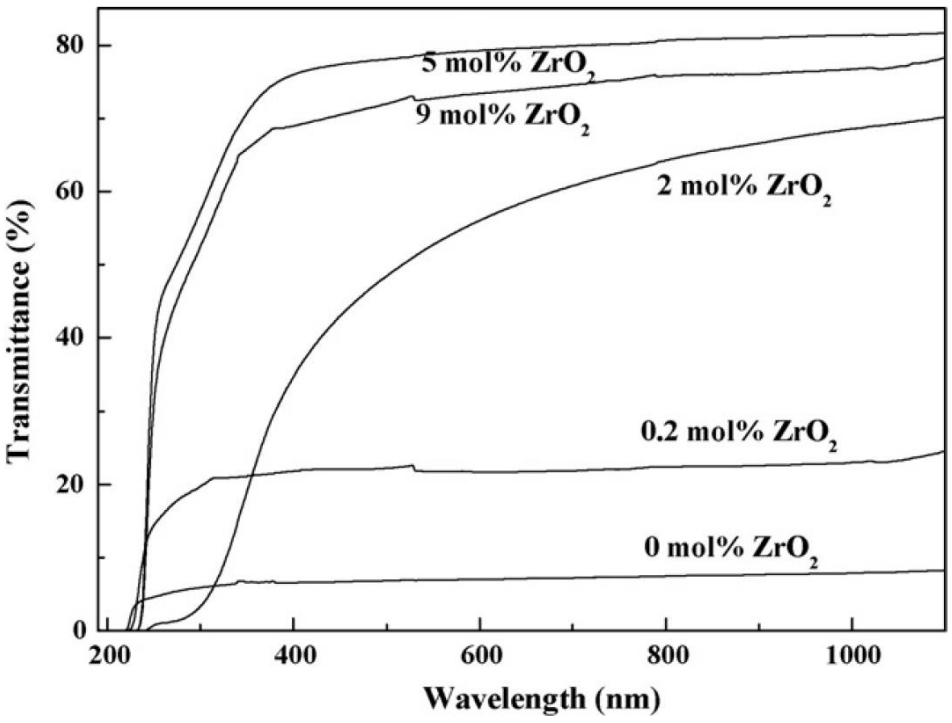

Figure 31: Transmittance measurements of Y_2O_3 ceramics with respect to different ZrO_2 concentrations, sintered at 1860°C for 8 h[27].

All samples were shown to be phase pure via XRD, and diffraction data shows the expected decrease in lattice parameter due to the smaller size of Zr^{4+} to Y^{3+}. Since ZrO_2 is soluble in Y_2O_3, the presence of Zr^{4+} increases the concentration of oxygen interstitials which greatly reduces the Y^{3+} diffusivity, which is turn reduces the grain boundary mobility of Y_2O_3. The effect of reduced grain size with ZrO_2 additives is quite dramatic, as illustrated in Figure 32.

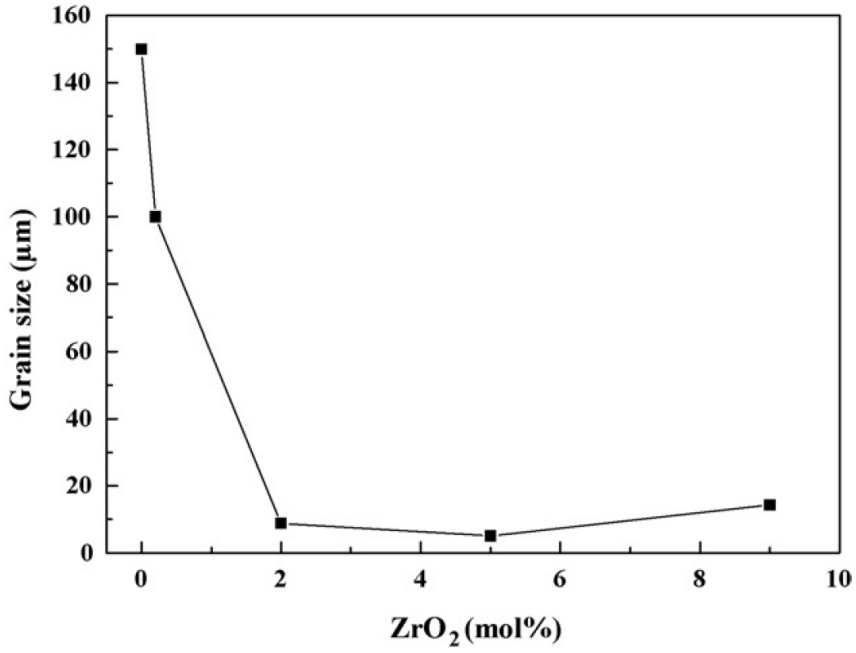

Figure 32: Effect of ZrO_2 concentration and grain size of Y_2O_3 ceramics sintered at 1860°C for 8 h[27].

From these two sets of data, a strong correlation is implied between the decreased grain size and increased transmittance, likely due to the absence of larger grains sweeping in pores from the boundaries to where they can no longer be removed via further sintering and densification.

2.4.4 Spark Plasma Sintering of Sesquioxide Ceramics

Additionally, spark plasma sintering (SPS) has been used to fabricate optical doped Lu_2O_3 ceramics by French researchers at both the Laboratoire Science des Procédés Céramiques[84], the Institut de Chimie de la Matière Condensée de Bordeaux[85] and also by researchers at Tohoku University[24]. Spark plasma sintering is a technique distinctly different from traditional vacuum sintering in that a uniaxial pressure is applied to the ceramic at some or all points during the firing while a DC current is used to heat the sample. It is generally similar to hot pressing with respect to the applied pressure and the use of a graphite die, but the use of current incident on the sample allows for higher heating rates. Usually, a lower pre-loading pressure is used at low temperatures, followed by increasing to a higher pressure when the soak temperature is reached[86]. At room temperature, An et al. tested uniaxial pressures ranging from 10 to 1000 MPa at room temperature, with 100 MPa being the applied pressure at the final temperature of 1723K, which is notably low compared to the temperatures generally needed to vacuum sinter Lu_2O_3 conventionally. The densification of a ceramic via SPS usually takes place within a few minutes, and SPS can support heating rates of over 1.67 Ks^{-1}. However, previous work has suggested that for optical ceramics, a much slower heating rate, as low at 0.17 Ks^{-1} is conducive to achieving high transparency, due to resulting in fewer pores seen via FE-SEM[24].

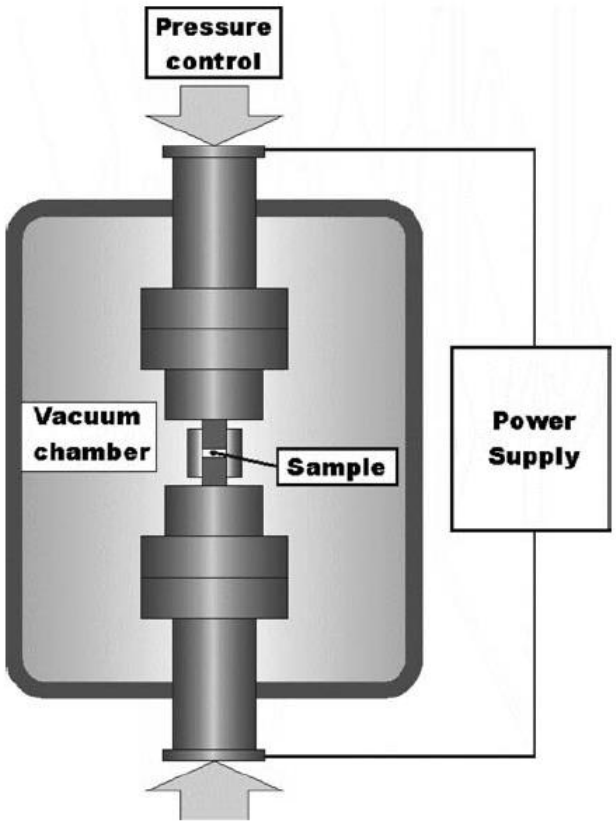

Figure 33: A schematic of a basic SPS set up[87].

The applied pressure at the initial stages of sintering can directly affect compaction through particle rearrangement. It continues to aid in densification through plastic deformation, particle sliding, and the destruction of agglomerates. At higher temperatures, densification is attributed mostly to grain boundary diffusion and is largely independent of the initial pressure applied. Since the SPS process is performed in vacuum, the formation of oxygen vacancies is still a defect phenomenon that can occur, and the defect concentration seems to be higher when a higher initial uniaxial pressure was used. 30 MPa was found as an optimal first pressure with respect to ceramic transmittance.

Boulesteix et al. found during their efforts in using SPS to sinter Nd^{3+}-doped Lu_2O_3 that remnant porosity could be reduced based on the shaping process used to prepare the green body before undergoing sintering. Using a combination of chemical co-precipitation and ball milling in ethanol, Lu_2O_3 green bodies were prepared either by placing the powder in the mold without pre-shaping or via suspension slip casting. These samples were heated to 900°C in order to determine basic porosity characteristics of the resulting compacts via mercury intrusion[84]. Not only did the pre-shaped bodies have the expected higher relative density (44% compared to 39% for unshaped), but also showed a much more uniform pore size distribution and smaller pores in general. After reaching just 1400°C at 130 MPa, comparable to the work done by An et al., all of the sintered samples achieved a relative density of >99.9% but samples prepared via pre-shaping slip casting showed significantly improved transmittance compared to unshaped powder. Microstructural inhomogenity can lead to differential sintering if different regions of the compact begin with better packing than others, leading to additional stresses on other regions of the part, resulting in more pores than a pre-shaped part[88].

Using SPS to produce Yb^{3+}-doped Lu_2O_3 at 10% doping has also been investigated by Prakasam et al[85, 89]. Also utilizing a relatively low heating rate, an optically transparent ceramic was able to be produced, with heating rates in excess of 50°C/min resulting in opaque samples. It was later found that increasing the heating rate above 50°C/min resulted in increased grain size and pore formation[89]. Samples produced this way were initially black in color due to the reducing nature of the vacuum atmosphere. The highly reducing atmosphere of the SPS method also resulted in colored samples for Futami et al. at Tohuku University[90], who only achieved a maximum of 40% transmittance for

Sc_2O_3, Y_2O_3, and Lu_2O_3 samples. However, the post annealing at 1200°C performed by Prakasam helped to remove this discoloration in SPS Yb^{3+}-doped Lu_2O_3. After annealing for 1 h in air and mirror polishing, the final ceramics were obtained. Similar to the Nd:Lu_2O_3 ceramics produced by SPS, maximum density was achieved at around 1400°C at a final pressure of 100 MPa, though transparency of samples produced at 1700°C was improved[85]. So even though the density appeared constant past a certain sintering temperature, it was found that after annealing, the higher soak temperature ceramics achievement higher transmittance, but still. Annealing above 1200°C was also found to be damaging to the transmittance of the samples, but still only managed to reach a maximum of about 60%, as shown in Figure 35.

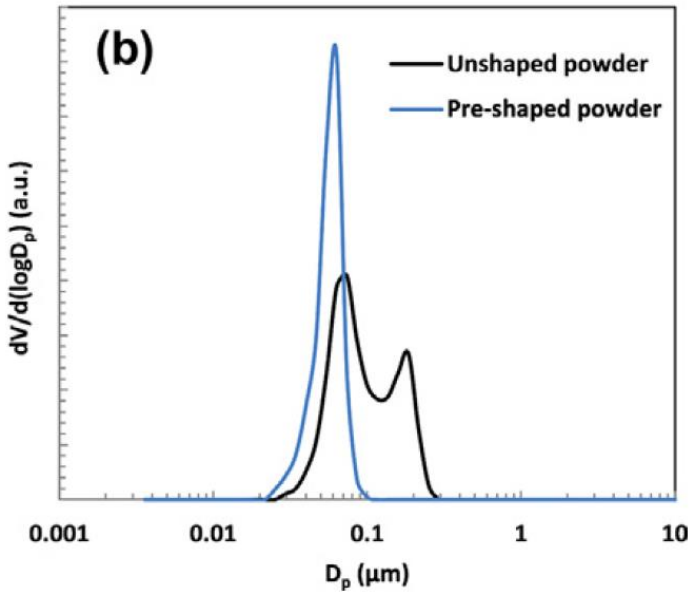

Figure 34: Cumulative pore volume versus pore size of partially SPS sintered slip-cast and unshaped Lu_2O_3 ceramics, as determined by mercury intrusion[84].

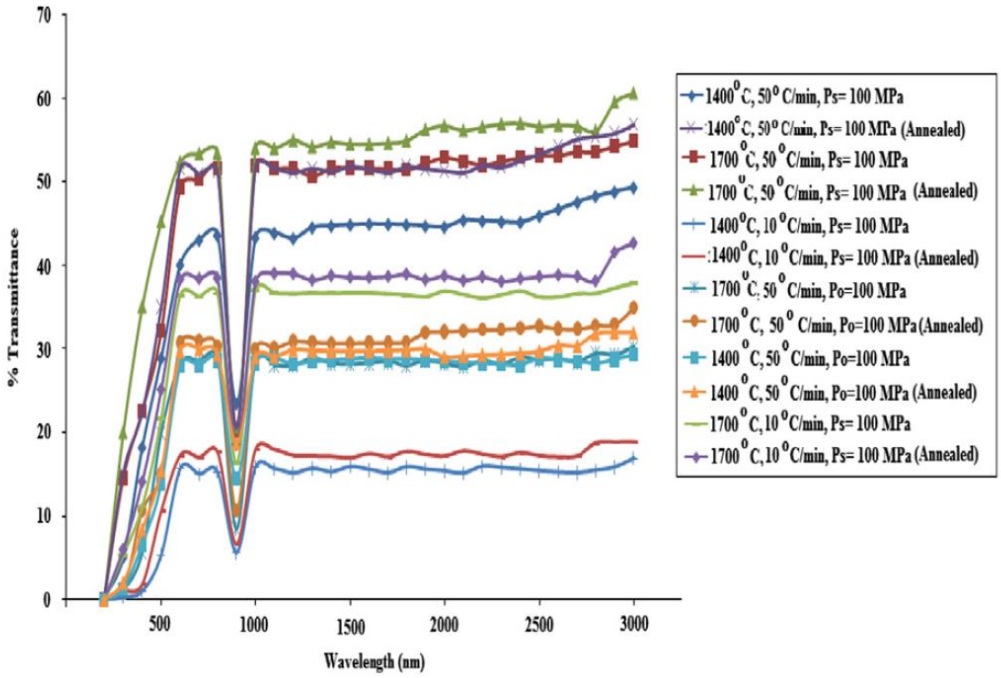

Figure 35: Transmission Spectra of various SPS sintered Yb^{3+}-doped Lu_2O_3, showing the effect of annealing and soak temperature[85].

2.4.5 Traditional Sintering of Sc_2O_3, Y_2O_3, and Lu_2O_3 ceramics

Conventional vacuum sintering has still managed to produce fully dense sesquioxide ceramics of very high transparency. Ballato et al. have developed numerous Er^{3+}-doped Sc_2O_3, Y_2O_3, and Lu_2O_3 ceramics (which lases at 1530 nm) which were densified via two-step sintering between 1500-1600°C in vacuum, followed by a HIPing at ~1600°C under an argon pressure of 206 MPa for 8 h[15]. Er^{3+}-doped Sc_2O_3 powders were fabricated by adding ammonium hydroxide to a mixed nitrate solution and then calcining at 1100°C in flowing oxygen. Grain sizes of under 500 nm were obtained and showed a maximum transmittance of 80% at 1530 nm[18]. Such nano-grained ceramics have shown enhanced hardness and better thermal shock-resistance compared to coarser grained ceramics or

single crystal counterparts[2]. Maintaining nano-grain size during sintering also further prevents pores from ending up entrapped within the limited grain bulk, meaning the this can facilitate sintering such ceramics to a transparent state[15]. Er^{3+}-doped Y_2O_3 was produced in a highly similar manner and also maintained an average grain size below 500 nm and ~80% transmittance at the lasing wavelength. These two-step sintered Y_2O_3 specimens were compared to conventionally sintered Y_2O_3, which maintained an average grain size of ~330 μm. The submicron grained ceramics demonstrated significantly better microhardness and fracture toughness[19].

Ballato's use of two-step sintering was the key determinant of limiting the final grain size of these sesquioxide ceramics while still using a traditional sintering environment. Using dilatometry, Ballato et al. have shown a maximum shrinkage rate at ~1400°C. The average grain size increased slowly with increasing sintering temperature up to 1500°C, but significantly more rapidly at higher temperatures[19]. Above a relative density of ~95%, the transition from the intermediate to the final states of sintering is also accompanied by a rapid increase in grain size. Since the temperatures of most rapid densification and most rapid grain growth were distinct, it was decided that by initially sintering up to 1500°C and then dwelling the ceramic at 1400°C, it would be possible to obtain a fully dense ceramic without promoting significant grain growth.

For the Lu_2O_3 ceramics, a more intricate co-precipitation methodology was required. Er^{3+}-doped Lu_2O_3 was fabricated using an extended co-precipitation process with hexamethylenetetramine (HMT) acting as an assisting ligand. Precursor oxides or nitrates are dissolved into nitric acid and ammonium hydroxide is added drop-wise at the base precipitant. This dried precipitate is then dissolved into sulfuric acid and again precipitated,

using an HMT containing base. The resulting sediment is then calcined at 1100°C for 4 hours to produce the sinterable nanosized oxide powder, which is then fired using a similar two-step sintering schedule. The Er^{3+}-doped ceramic exhibited an optical transmittance of 78% at 1550 nm, with lower values at shorter wavelengths. A grain size of ~16 μm was identified in the final ceramic[28].

The Shanghai Institute of Ceramics' work with Nd^{3+}-doped Lu_2O_3 mentioned previously has also evaluated a two-step sintering process for fabricating fine grain ceramics via conventional sintering techniques[91]. Zhou et al. found that by dropping the sintering temperature from 1720°C to 1620°C after 15 minutes and holding at the lower temperature for 10 h, they could produce sub-micron grained samples of Nd^{3+}-doped Lu_2O_3 with much greater photoluminescence when pumped at the same wavelength of 808 nm. By using EXAFS, they found that the Nd coordination number is much higher in the fine grained ceramics compared to the coarse grained material, leading to a higher local effective concentration of Nd ions. The resulting boost in photoluminescence is shown in Figure 36.

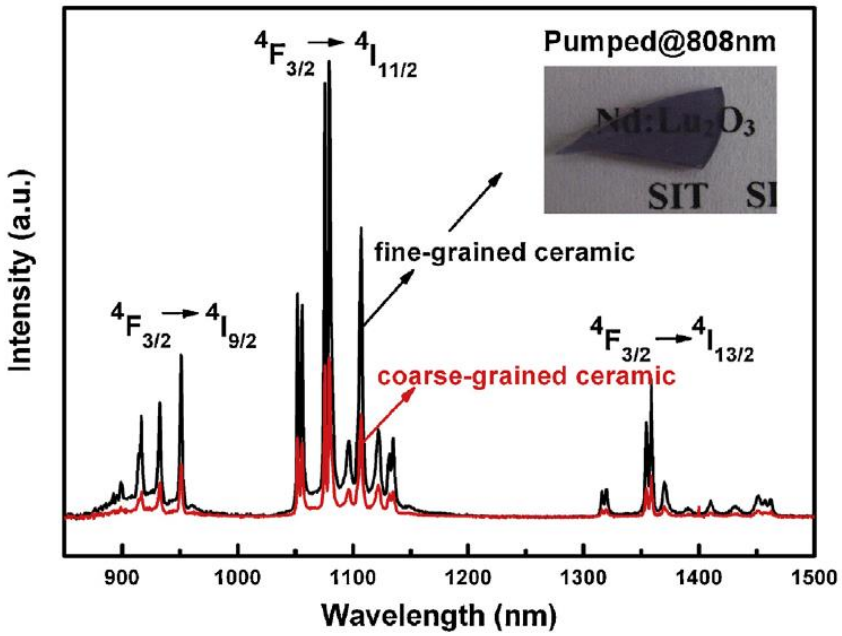

Figure 36: A comparison between coarse and fine-grained samples' photoluminescence with fine grain samples between fabricated via two-step sintering[91].

Seeley et. al at the Lawrence Livermore National Laboratory investigated two interesting parameters in the fabrication of transparent Eu^{3+}-doped Lu_2O_3 optical ceramics. Starting with nanopowders fabricated through flame spray pyrolysis, an aqueous suspension was made with polyethylene glycol and polymethacrylate organic additives. The suspension was spray dried in flowing nitrogen, sieved, and then pressed and CIPed into green bodies before finally heat treating at 900°C to remove the organics[13]. From this point the ceramics were conventionally vacuum sintered and HIPed, but the use of spray dried powders for use in producing optical ceramics seems unique to this research. The researchers noticed through HRTEM analysis of focus ion beam cut sections that HIPing the sintered samples resulted in a second, Eu-rich phase appearing at the triple point of the cubic primary phase grains, as shown in Figure 37. Greater extent of phase segrega-

tion was given as the reason for decreasing transparency with higher HIP temperatures (1900°C), while remnant porosity was given as the reason for sample cloudy-ness at lower HIP temperatures (1750°C). Previous work done by Wu, Y. et al and also by researchers at the Laboratoire Chimie de la Matière Condensée de Paris [92, 93] have identified Gadolinium doping as a solution for preventing this phase separation.

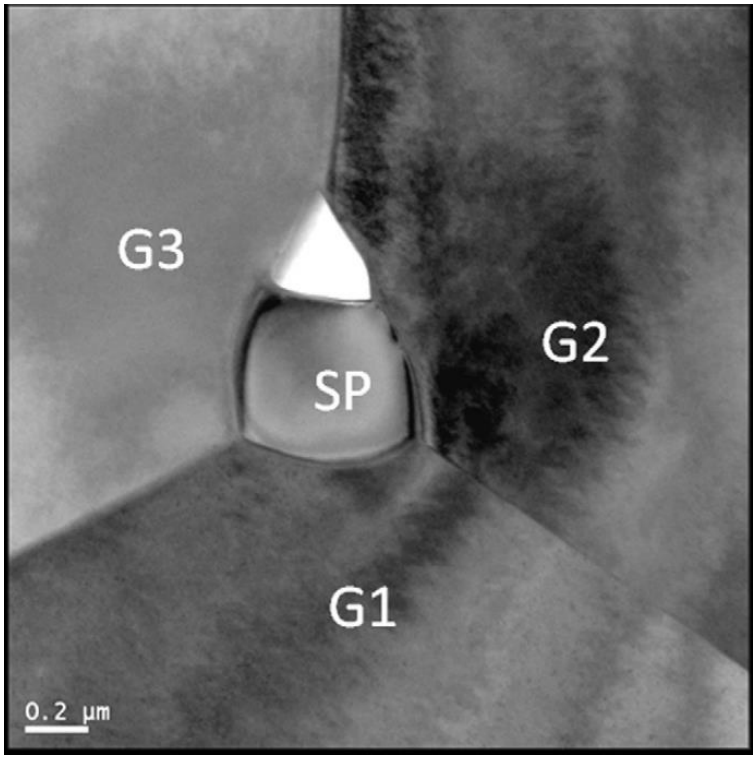

Figure 37: An HR-TEM image of a second phase (SP) at the triple point of three cubic Eu:Lu_2O_3 grains (G1, G2, G3).

$Gd_xLu_{1.9-x}Eu_{0.1}O_3$ at a composition of X = 0.6 was found to be the optimal doping for Gd additives. With this amount of Gd dopant, the HIP conditions were assumed to be close to the extent of phase transformation to from cubic to monoclinic, improving the ionic mobility without forming new phase boundaries. However, past X = 0.9, significant sec-

ond phases were formed and transparency was lost. Unfortunately, while optical scatterometry data was given to support these claims, no transmittance data is provided to easily compare the effects of Gd-doping and spray drying compared to other literature in the fabrication of optical Lu_2O_3 ceramics. However, it does provide incentive to try to minimize HIPing temperatures in order to not segregate out the laser active ions in the first place, as long as near theoretical relative density can still be achieved.

As for conventional sintering of the specific doped ceramic of interest, Yb^{3+}-doped Lu_2O_3, work has been done at Shanghai University where 5 at.% Lu_2O_3 was fabricated by sintering in hydrogen for long soak times (~ 45 h)[51]. The starting nanopowders were mixed in ethyl alcohol with zirconia media before being processed into green bodies and undergoing thermal processing. The samples reached 99.4% relative density and only 60% transmittance, which is not of high enough quality for laser experiments. This is indicative of a grey impurity caused by the scattering of light by remnant porosity. Absorption and emission spectra of the ceramics was still analyzed with no undesirable peaks, suggesting that poor microstructure is the culprit of lower optical properties as opposed to impurity. While these samples may have been improved with a post-sinter HIP to remove remnant porosity, no grain size is reported, and likely the long sinter duration resulted in good relative density but poor microstructure where abnormally grown grains may have prevented interior pores from being removed. While the optical or microstructural data here is less useful, emission and energy data is provided for the 5 at.% ceramic showing the absorption and emission peaks resulting from the measured energy splitting. The fluorescence spectrum was measured at room temperature after exciting the sample using a 940 nm Xe lamp.

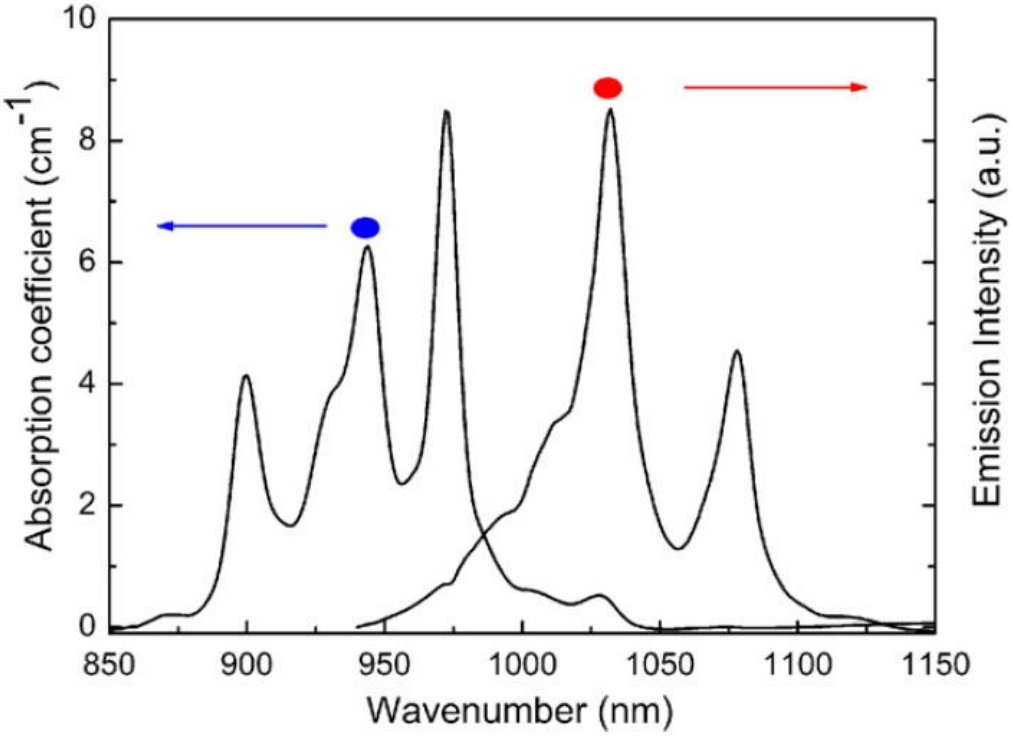

Figure 38: Absorption and emission spectra of 5 at.% Yb:Lu_2O_3 transparent ceramics sintered in hydrogen for 45 h[51].

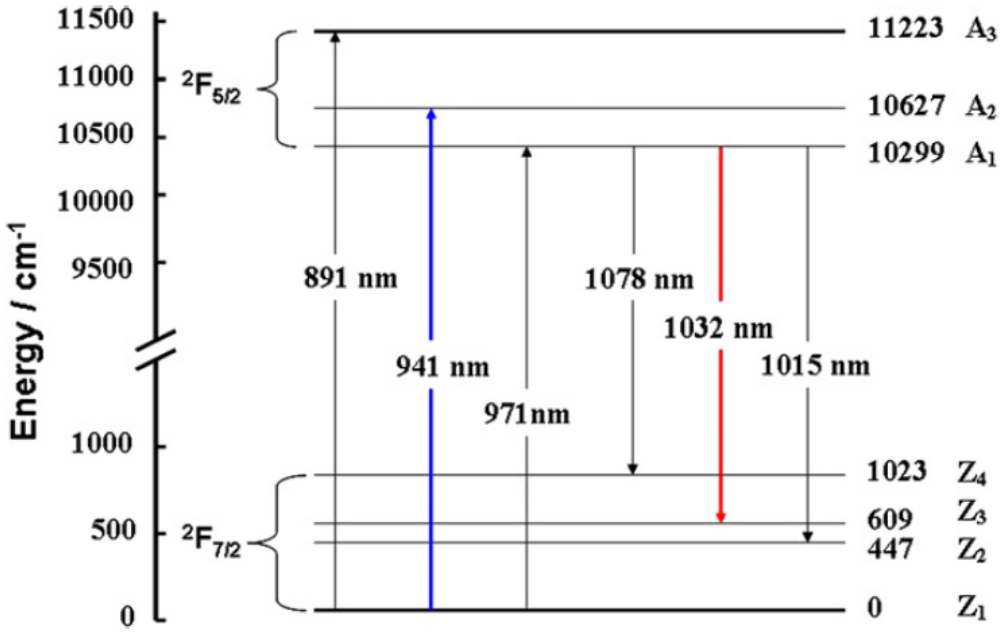

Figure 39: Energy level diagram of Yb^{3+} in Lu_2O_3 transparent ceramics, calculated from emission spectra in Figure 38[51].

Table 3: Comparison of fluorescence spectra between YAG[94], single crystal Yb:Lu_2O_3[95], and polycrystalline Yb:Lu_2O_3[51].

Results of the Yb^{3+} energy level schemes and measured $^2F_{5/2}$ decay time. The samples were 5 at.% Yb-doped.

Parameters energy (cm^{-1})	Transparent ceramics YAG [11]	Host crystal Lu_2O_3 [10]	Transparent ceramics Lu_2O_3 (this work)
$^2F_{5/2}$	10930	11071.7	11223 (A_3)
	10624	10528.5	10627 (A_2)
	10327	10243.8	10299 (A_1)
$^2F_{7/2}$	785	980.7	1023 (Z_4)
	612	561.8	609 (Z_3)
	565	414.5	447 (Z_2)
	0	0	0 (Z_1)
τ (ms)	0.95	1.29	1.31

Figure 38 show three broad absorption bands and three emission bands as described previous for the Yb^{3+} ion. The splitting of the energy manifolds are affected by the crystal matrix the active ion is placed in, but the emissions between different materials can still be compared reasonably easy. Specifically, energy level assignment was assisted by comparing this data to work done on transparent YAG ceramics and Lu_2O_3 single crystals and is illustrated in Figure 39. The direct comparison of this work to others is shown in Table 3. The polycrystal shows a slightly higher splitting in the ground state $^2F_{7/2}$, resulting in a fractional thermal population which is beneficial to obtaining laser output due to an electronic population inversion being more achievable. The decay time of the $^2F_{5/2}$ excited state was measured and was approximated to be 1.31 ms, and while some reabsorption at 1032 nm may result in the actual lifetime to be a bit shorter, ~1 ms is advantageous for high power laser output.

III. SINTERING OF AS RECEIVED COMMERCIAL POWDERS

3.1 Experimental Procedures

3.1.1 Consolidation and Sintering Procedure

Lu_2O_3 (Alpha Aesar, 99.99% pure, d_{50} = 4.06 μm) and Yb_2O_3 powders (Alpha Aesar, 99.99% pure, 325 mesh) were used to form compositions ranging from 0 to 10 mol% Yb_2O_3. For Yb_2O_3-Lu_2O_3 mixtures, powders were mixed in ~38 mm diameter polyethylene vial placed on milling rollers for 15 min. Powders were uniaxially pressed into cylindrical pellets at ~100 MPa. For initial tests, 40 mg of powder was pressed into compacts of 6.3 mm in diameter (~5.2 mm diameter after sintering and post HIPing) and ~2.4 mm in thickness. In subsequent tests, 2 g of powder were pressed into compacts of 11.6 mm in diameter (9.8 mm diameter after sintering and post-HIPing) and ~3.4 mm in thickness. The walls of the dies and punches were coated with steric acid as a lubricant to prevent ejection stresses from damaging the compacts as they were removed from the die. The powder compacts were then sealed into evacuated latex bags and cold isostatically pressed (CIPed) at 345 MPa. After a 30 second hold, the pressure was slowly released to prevent springback.

Dimensional relative densities were determined based on caliper and analytical balance measurements, using the rule of mixtures for calculating theoretical density. Based on this, green relative densities averaged ~58%. Powder compacts were sintered in graphite crucibles in a graphite element vacuum tube furnace (Model M11, Centorr Vacuum Industries, Nashua, NH). Using a mechanical vacuum pump, pressure was maintained throughout firing at ~3 Pa. Specimens were heated at 50˚C/min to selected dwell tem-

peratures in the range 1600-1850°C with durations of 2-4 h. The furnace was then allowed to cool with no power applied to the elements to less than 80˚C before being re-pressurized and opened.

3.1.2 Archemedes Density Measurements and Open/Closed Porosity

Relative densities of the sintered samples were measured using the Archimedes method. Dry, submerged and saturated weight measurements were performed at least three times and averaged. Submerged weights were taken after boiling in deionized water for ~5 min and allowing the water to cool back to near room temperature. This was done to ensure that no air entrapment kept gaseous bubbles within the sample bulk to affect the subsequent weight values. Saturated weights (or soaked weights) were taken by drying off the surface of the submerged specimens with a laboratory task wipe. Theoretical densities were determined based on the rule of mixtures using crystallographic densities of and relative percentage of commercial powders used for each specimen. A ceramic's relative density ρ can be calculated through the relation

$$p = \frac{W_{sat} * p_{fluid}}{W_{sat} - W_{sub}} \tag{33}$$

where W_{sat} is the saturated weight of a ceramic sample soaked in a fluid of density ρ_{fluid} (usually water) where all open pores are assumed to be filled, W_{dry} is the sample's dry weight, and W_{sub} is the weight of the sample when submerged underneath the fluid and acted upon buy a buoyant force. This density value can then be divided by the expected theoretical density to determine the specimen's relative density, ρ_r as a percentage of the

theoretical density. A ceramic's extent of open porosity P_{open} can then be determined by the relation

$$P_{open} = \left(\frac{W_{sub} - W_{dry}}{W_{sub} - W_{sat}}\right) * 100 \quad (34)$$

where the open porosity is also reported as a percentage, and it then follows that the ceramic's extent of closed porosity is simply

$$P_{closed} = 100 - \rho_r - P_{open} \quad (35)$$

and the percentage of porosity remaining in the sample of open character is then

$$Percentage\ of\ Open\ Porosity = \left(\frac{P_{open}}{100 - \rho_r}\right) * 100 \quad (36)$$

and the closer this value is to zero, the more effective a HIPing step will be since the pressing gas will not be able to enter closed pores and prevent densification.

3.1.3 Air Annealing and Polishing of Ceramic Samples

After sintering, many of the specimens had visible colorations, varying from red to yellow, which were successfully removed via annealing in static air by heating at 5˚C/min to 1100°C with a dwell at that temperature of 2 h. Specimens in the annealing furnace were then allowed to cool overnight with the elements turned off. These pellets were HIPed (Model AIP6-30H, American Isostatic Press, Columbus, OH) in argon at 1700°C at 206 MPa for 1 h. In some cases, the pellets were then again similarly annealed in static air at 1100°C for 4 h. After each thermal processing step, Archimedes densities were measured. Images of the primary furnace equipment used in the fabrication of these samples is shown in Figure 40.

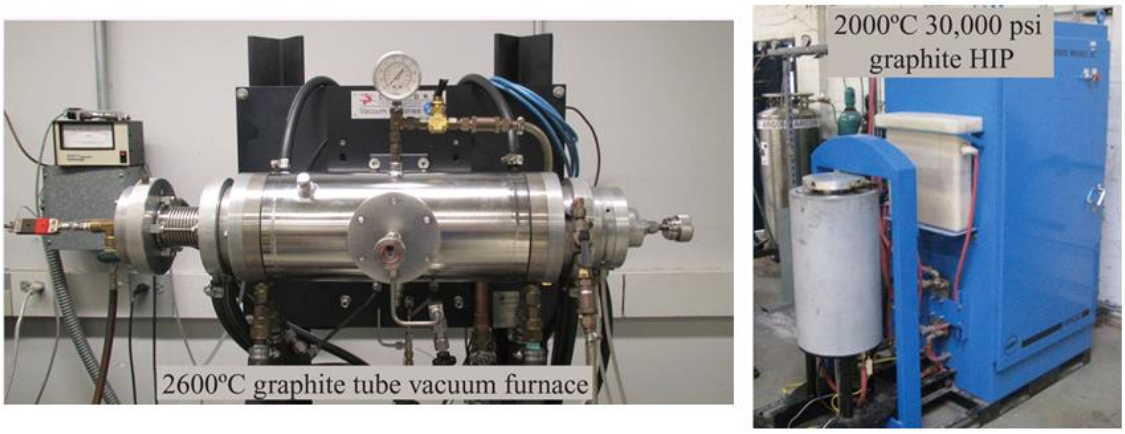

Figure 40: Graphite element vacuum sintering furnace and hot isostatic press.

For transparency and microstructure characterization, specimens were ground and polished. They were affixed (CrystalBond 509 mounting adhesive, Structure Probe Inc., West Chester, PA) to aluminum mounts and ground using 45 μm and 15 μm embedded diamond grinding disks (Buehler Apex series, Buehler, Lake Bluff, IL). The sample faces were then polished in diamond suspension (Buehler MetaDi series) coated fiber disks (Buehler TexMet) to a finish of 1 μm. Samples tested for transmission and emission characteristics were further polished to a finish of 0.5 μm. The ceramic specimens were then removed from the mount and the process repeated on the other face to ensure an equivalent finish on both sides. The final polished ceramic was then washed in acetone followed by DI water to remove the remnant bonding adhesive. Powder and ceramic imaging was done using a FE-SEM (Zeiss Ultra60, Carl Zeiss AG, Jena Germany) or a FIB/SEM (FEI Nova Nanolab 200, FEI Company, Hillsboro, Oregon).

3.1.4 X-ray Diffraction Analysis Methodology

Polished specimens were sputter-coated with a gold surface film for x-ray diffraction (XRD) analysis. The surface coating was estimated to be ~1 μm thick. The coated samples were subsequently heat-treated in static air at 2°C/min to 400°C with a 2 h dwell for the purpose of growing the nano-scale gold grains to sizes which would yield less broadened XRD peaks. Diffraction data (X'Pert PRO Alpha-I, PANalytical, Almelo, The Netherlands) was collected using Cu Kα radiation at a 0.084 °/s scan speed, a step size of 0.017°, and 2θ range of 10° to 85°. The scan was repeated 3 times and the intensities summed. Soller slits corresponding to 0.04 radians were installed in the incident and diffracted x-ray beam pathways in order to produce scans with minimal background interference relative to the intensities of the diffraction peaks. Additionally, a 10 mm mask was installed in the incident beam pathway, and a 5 mm mask was installed in the diffracted beam pathway.

The gold XRD peaks were used as an internal standard in order to correct for small shifts in specimen height as mounted in the diffractometer. The scattering angles of four gold peaks, with ICDD values of 38.184, 44.392, 64.576, and 81.721° 2θ were used to shift by linear interpolation 2θ data values of experimental XRD patterns, based on the 2θ positions of the gold peaks to their ICDD values. The peak 2θ positions of the gold internal standards were determined by fitting to best-fit Gaussian functions (Kalidagraph 4.0 software, using the Levenberg-Marquardt iterative numerical optimization algorithm) initiated from user-entered seed values.

3.1.5 Optical and Spectroscopic Analysis

Spectral transmittance was measured for samples with varying Yb_2O_3 doping levels over the spectral range of 900 to 1200 nm. An ionically colored glass neutral density filter was used to calibrate transmittance (Schott, NG11). The filter data sheet provided internal transmittance data as a function of wavelength (62-67%), which does not include reflection from the front and back surfaces. Orthogonal reflectance is given by:

$$R = \left(\frac{n_a - n_f}{(n_a + n_f)^2}\right) \tag{37}$$

where n_a is the index of refraction of air (1.00) and n_f is the index of refraction of the filter (1.49 at 1014 nm). To convert the internal transmittance to transmittance (which includes reflections), an incident intensity I_0 of 1.0 is assumed, and the intensity entering the filter I_1 is determined as $I_1 = I_0(1 - R)$. The intensity reaching the back face is then calculated as $I_2 = I_1 T_i$, where T_i is the wavelength-dependent internal transmittance. The intensity emerging from the filter I_3 is then $I_3 = I_2(1 - R)$. The transmittance is thus calculated as I_3/I_0. Data sheet internal transmittance, calculated transmittance, and measured transmittance are shown in Figure 41. The measured transmittance followed the same trend with wavelength as the manufacturers' data, but was lower in value. The difference between measured and calculated transmittance (~3% shift) is treated as a zero offset, and the differences between these data as a function of wavelength was added to spectral transmittance data of Lu_2O_3 specimens with varying Yb_2O_3 doping levels.

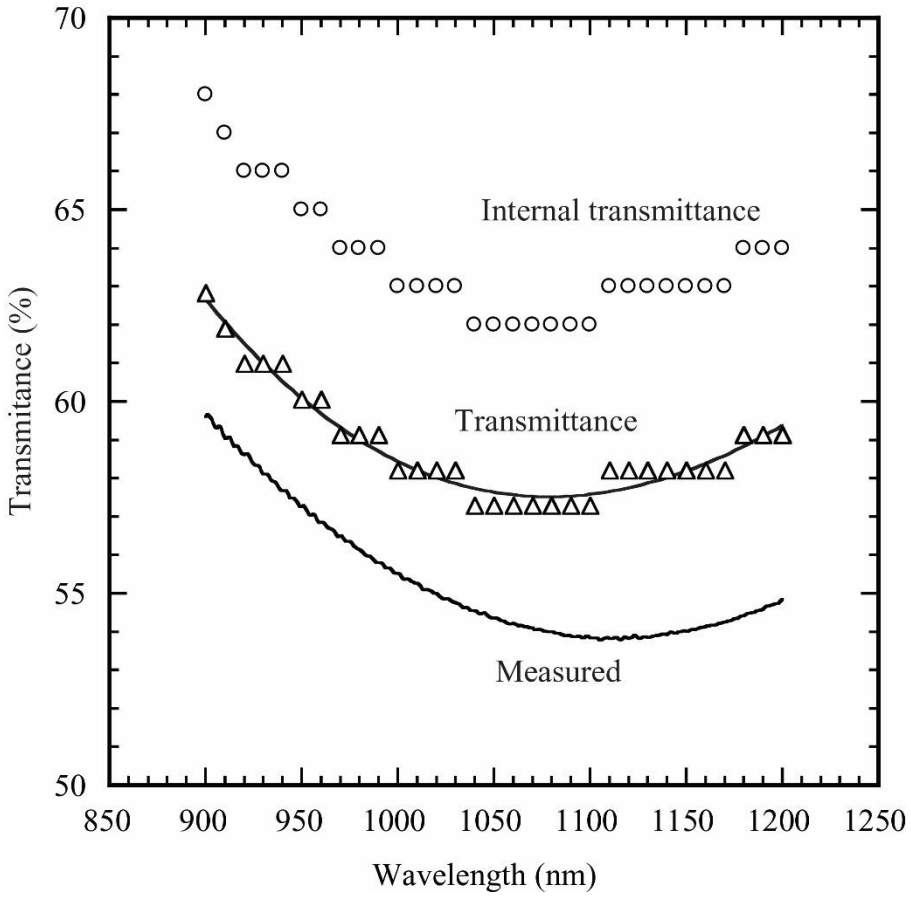

Figure 41: Internal transmittance from the data sheet for a glass transmission calibration filter, along with the calculated transmittance accounting for surface reflection. The curve through the calculated transmittance is a 3rd order polynomial fit (λ in nm, T_i in percent: T_i = -1.1737 x 10^{-7} λ^3 + 5.2017 x 10^{-4} λ^2 – 0.71252 λ + 368.17). Also shown are experimental transmittance data for the calibration filter.

Transmittance data were collected for Lu_2O_3/Yb_2O_3 specimens of varying thickness: (Yb_2O_3 mol% / thickness in mm: 0/1.52, 2/1.99, 4/1.02 6/1.36, 8/1.42). They were normalized to the average thickness of 1.462 mm by calculating the absorption coefficient α in the Beer-Lambert expression

$$T_i = \exp(-\alpha x) \tag{38}$$

where x is the specimen thickness. The transmittance is then re-calculated based on x = 1.462 mm.

To calculate the theoretical maximum transmittance, the wavelength-dependent indices of refraction for pure Lu_2O_3 and pure Yb_2O_3 were obtained from the literature as coefficients to the dispersion formula

$$\frac{1}{n^2 - 1} = \frac{-A}{\lambda^2 + B} \tag{39}$$

where for Lu_2O_3, A = 66 x 10^{-4} and B = 0.3833, and for Yb_2O_3, A = 68 x 10^{-4} and B = 0.3778. The rule of mixtures was then used to calculate the indices of refraction for the various compositions. The difference in index of refraction between Lu_2O_3 and Yb_2O_3, and the variation in reflectance with wavelength, turned out to be negligible. Assuming an incident intensity I_0 of 1, the intensity entering the sample $I_1 = I_0((n_a - n_s)/(n_a + n_s))^2$ where n_s is the index of refraction of the sample. The sample is assumed to be perfectly transmissive. At the back surface, the intensity exiting the sample is $I_2 = I_1((n_a - n_s)/(n_a + n_s))^2$. Thus, the theoretical maximum transmittance is given by I_2/I_0.

3.2 Sintering Results

The as-received Lu_2O_3 and Yb_2O_3 powders were analyzed via FE-SEM (Figure 42). Angular Lu_2O_3 and rod-like Yb_2O_3 particles were identified of particle sizes in the range 2-10 μm.

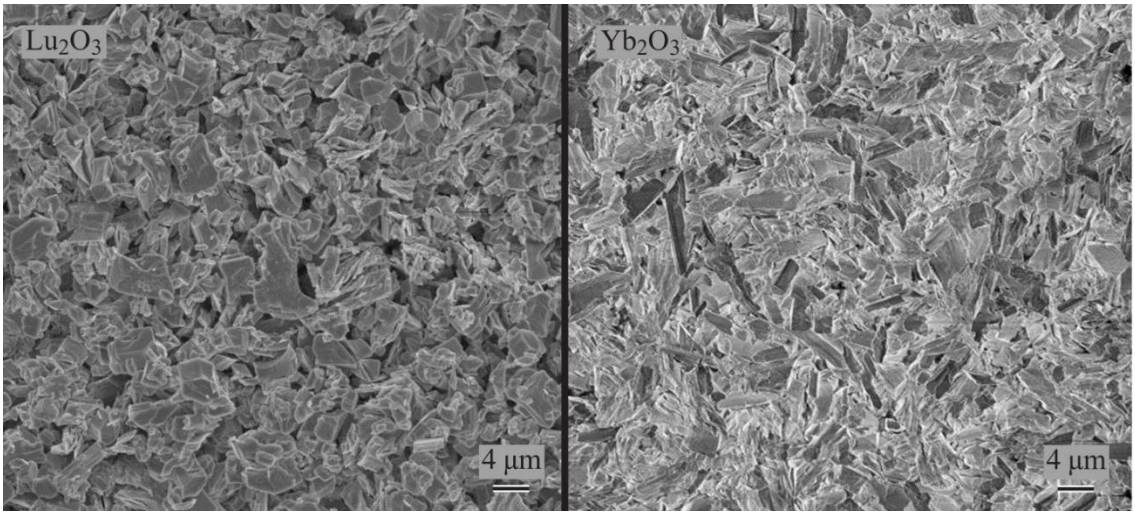

Figure 42: SEM image of commercial Lu_2O_3 (left) and Yb_2O_3 (right) as-received powders.

An initial set of sintering heat-treatment tests was performed for 6 mm diameter pure Lu_2O_3 samples. As shown in Figure 43, although sintered relative densities of these powder compacts generally increased with increasing sintering soak temperature, a peak post-HIPed relative density was reached when specimens were sintered in the soak temperature range of 1650-1725°C. Specimens exposed to sintering soak temperatures above 1800°C gained no apparent relative density benefit from post-HIPing. After post-HIPing with a sintering soak temperature of 1700°C, compacts soaked for 4 h had higher relative densities than compacts soaked for 2 h.

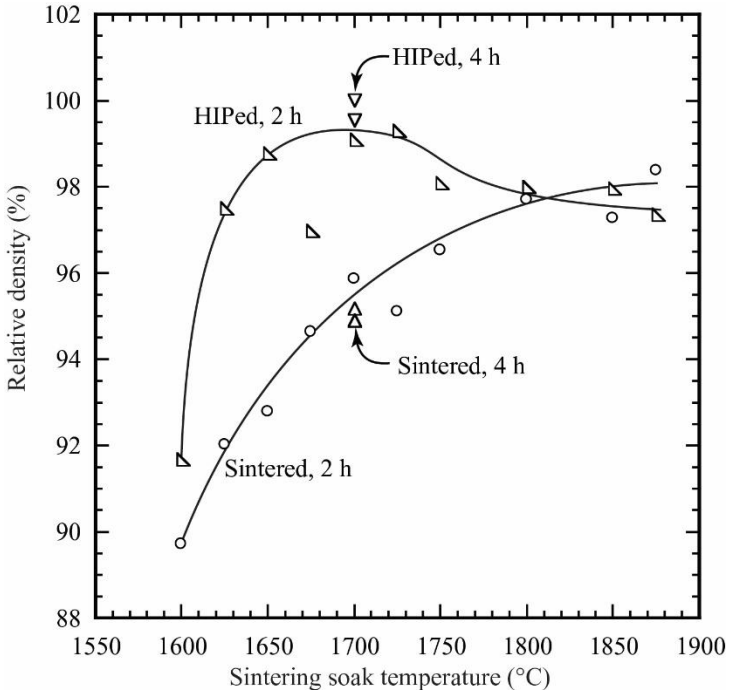

Figure 43: Relative density of 6 mm diameter pure Lu_2O_3 specimens after sintering at the indicated soak temperatures and air annealing. Also shown are results after these samples were post-HIPed and air annealed.

Figure 44 shows the relative densities of 11.6 mm diameter, 5 mol% Yb_2O_3-doped specimens exposed to various sintering soak temperatures for 4 h, followed annealing in static air at 1100°C, post-HIPing at 1700°C for 2 h, and another air anneal at 1100°C for 4 h. Air annealing had little measurable effect on relative density. Relative densities increased with increasing sintering soak temperature. Sintering to soak temperatures in the range of 1650-1725°C resulted in ~100% relative density after post-HIPing. Sintering at 1750°C or above appears to have produced microstructures with porosity which could not be removed by post-HIPing.

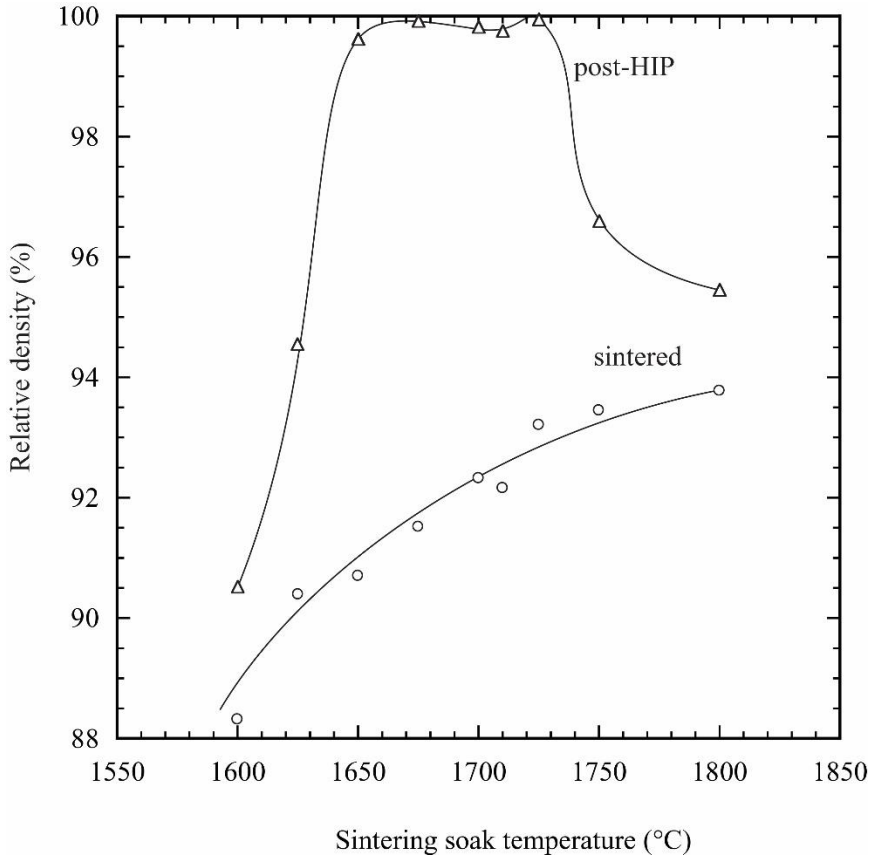

Figure 44: Relative density of 11.6 mm diameter 5 mol% Yb2O3-doped specimens after sintering and air annealing, and after post-HIPing and air annealing as a function of soak temperature.

Certain 5 mol% Yb_2O_3 doped specimens were deliberately not annealed in static air either after sintering or after post-HIPing to evaluate the effects of those processes (Figures 45 and 46). Annealing after sintering was found to improve the visual transparency of the pellets. A yellow tint was observed in the absence of the air anneal after sintering, most notably for specimens exposed to a sintering soak temperature of 1650°C. Annealing of pellets after post HIPing which were not near 100% relative density was found to often result in fractured specimens retrieved from the furnace. For those samples which remained intact, there was no apparent advantage resulting from this annealing step. In some specimens, e.g. the one exposed to a 1700°C sintering soak temperature and no air

anneals (Figure 45), opaque grey spheres are observed dispersed within. Figure 47 shows the microstructure of a 1725°C sintered and post-HIPed specimen, showing grains in the range of 50-80 μm.

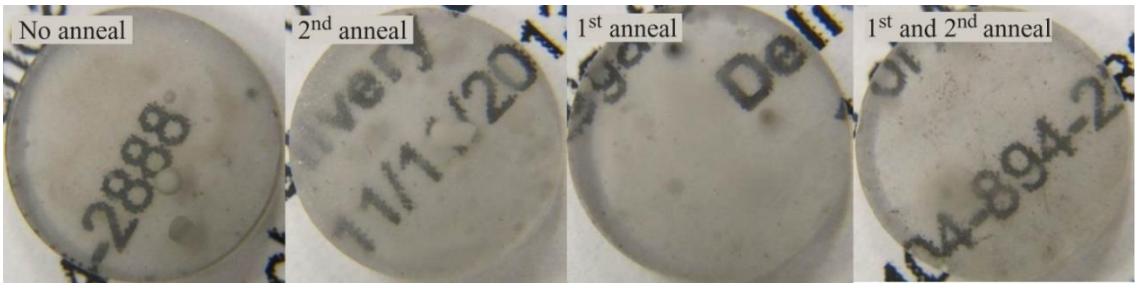

Figure 45: Appearance of 5 mol% Yb_2O_3 samples exposed to a sintering soak temperature of 1700°C for 4 h and then post-HIPed. Labels indicate annealing steps used or not used during thermal processing.

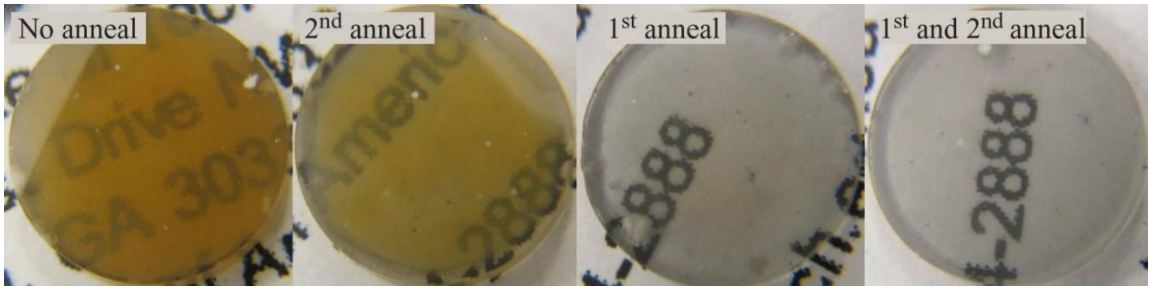

Figure 46: Appearance of 5 mol% Yb_2O_3 samples exposed to a sintering soak temperature of 1650°C for 4 h and then post-HIPed. Labels indicate annealing steps used or not used during thermal processing.

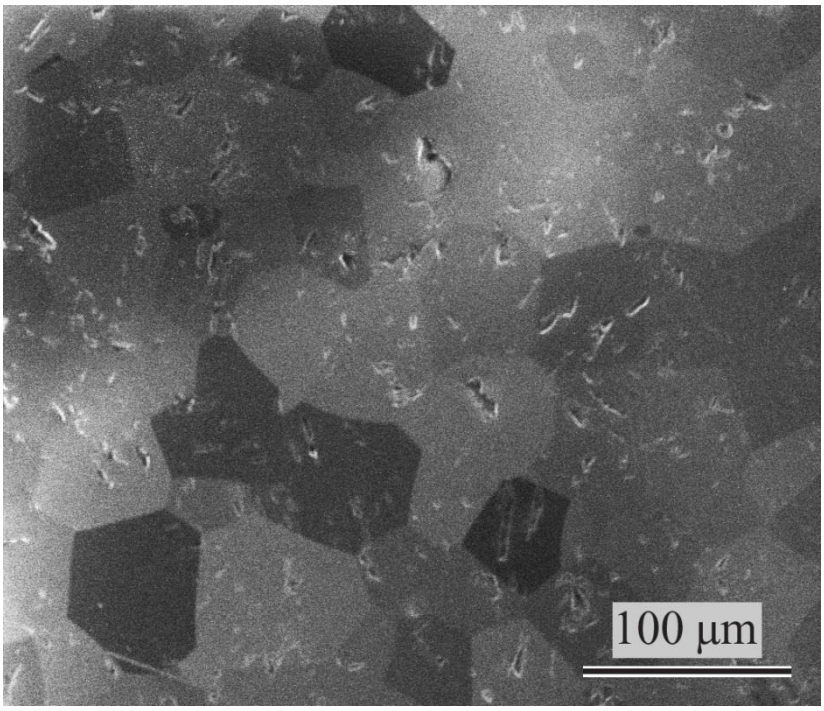

Figure 47: FIB-SEM micrograph of a polished section of a 5 mol% Yb2O3 specimen exposed to a soak temperature of 1725°C for 4 h, followed by post-HIPing. The polished specimen was sub-sequently thermally etched at 1000°C for 2 h. Grain sizes in the ~50-80 μm range. In a phase-pure sample, grain orientation contrast is caused by channeling of the field ion beam (FIB) incident gallium ions between lattice planes of the individual grains. As a result, different crystal orientations generate a different density of secondary electrons escaping the specimen, yielding contrast between the grains

Grain imaging of sintered ceramics can also be performed through thermal etching, allowing grains to be views until an optical microscope. Thermal etching was performed by mirror polishing a face of a highly dense sample and then HIPing the sample in 206 MPa of argon for 1 h at ~1700°C. It was found that thermally etching under high pressure was preferable since lower quality samples could degrade if elevated in temperature, allowing entrapped gas to expand and fracture the ceramic. Under the high argon pressure, this tendency is less likely to damage the sample, and allows for microstructural analysis of porosity containing samples, even those with entrapped argon gas from a previous HIP

treatment. Figure 48 shows an optical micrograph of a 12% Yb^{3+}-doped sample with very little apparent porosity.

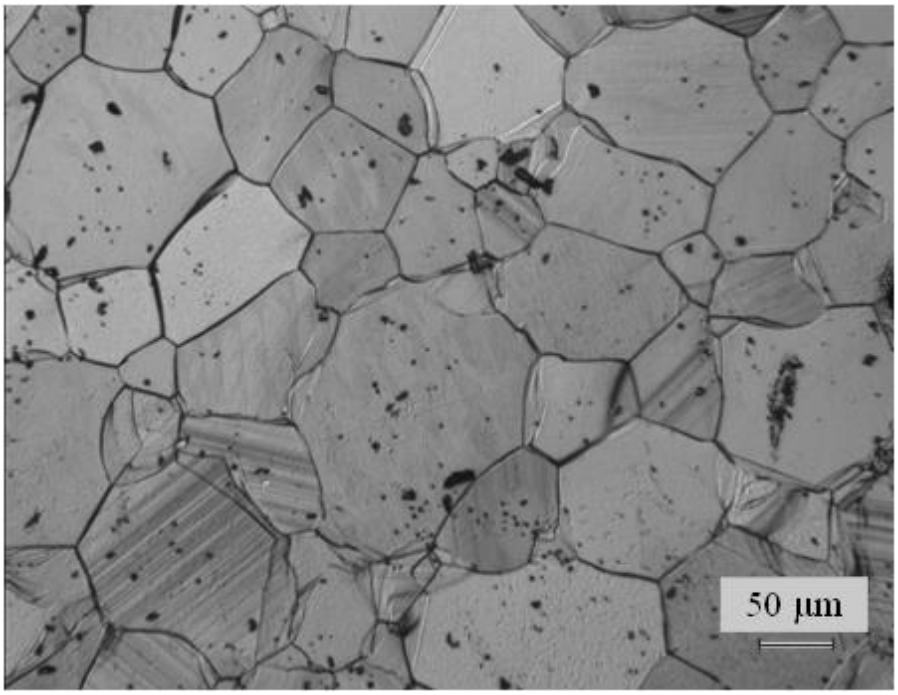

Figure 48: Micrograph of a 12% Yb:Lu_2O_3 ceramic viewed under optical microscope at 100x. While opaque, the ceramic does not show a high extent of porosity.

Relative density data for 0-10 mol% Yb_2O_3 doped specimens, using a fixed sintering soak temperature of 1700°C are shown in Figure 49. All but the 10 mol% Yb_2O_3 doped samples post-HIPed to near theoretical density. However, the undoped, 0 and 2 mol% Yb_2O_3 specimens showed relatively degraded transparency, as did the 10 mol% Yb_2O_3 sample (Figure 50). Subsequent heat treatments for 0 and 2 mol% Yb_2O_3 with sintering soak temperatures below 1700°C resulted in lower sintered relative densities, but higher post-HIPed relative densities in the case of a sintering soak temperature of 1625-1650°C. Those specimens in turn displayed very good transparency, as can be seen in Figure 51.

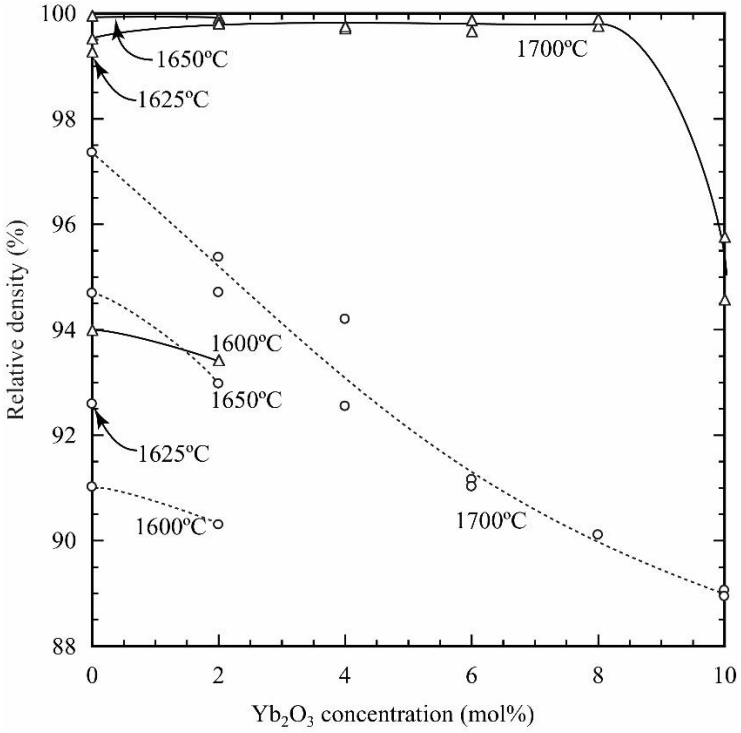

Figure 49: Relative density of Yb_2O_3-doped specimens after sintering and air annealing, and after post-HIPing (no air annealing after post-HIPing). Soak temperatures are indicated. Circles correspond to sintered relative densities and triangles correspond to p post-HIPed relative densities.

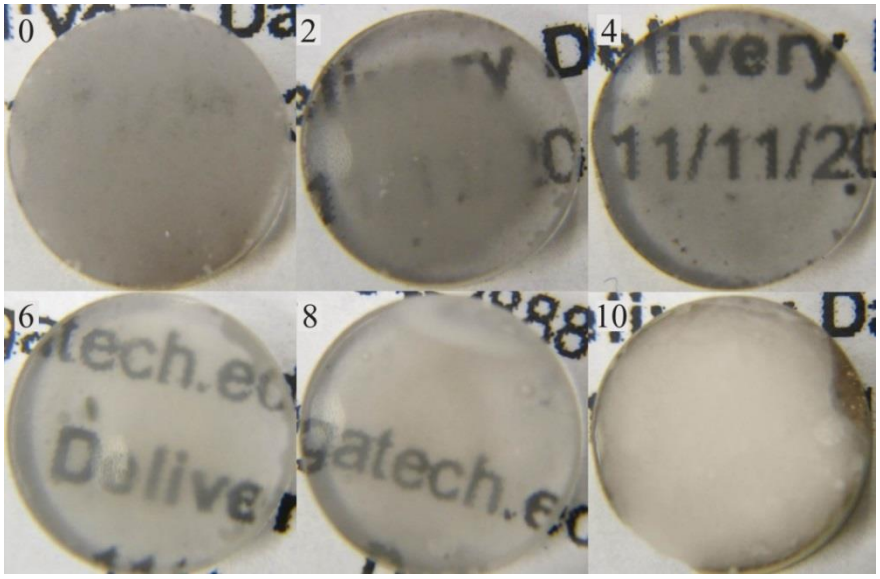

Figure 50: Appearance of polished specimens after exposure to a sintering soak temperature of 1700°C for 4 h, followed by post-HIPing. Numbers in the figure indicate the mol% Yb_2O_3.

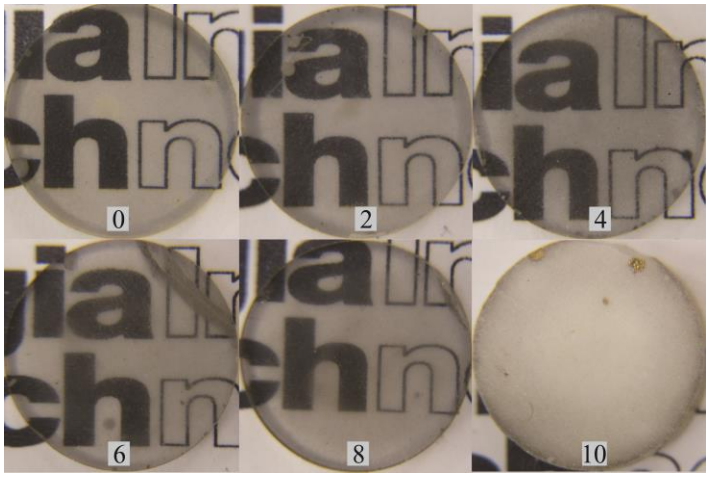

Figure 51: Appearance of polished specimens after exposure to a sintering soak temperature of 1625-1700°C for 4 h, followed by post-HIPing. Numbers in the figure indicate the mol% Yb_2O_3.

The as-received powders were relatively mono-modal in size, so a green relative density of 58% without use of binder or other organic pressing agents was quite acceptable. For post-HIPing to be effective, specimens must be sintered to a closed porosity state, which was demonstrated to be as low as 90.5% in relative density. Sintering soak temperatures above 1725°C result in degraded post-HIPed relative densities, likely from rapid grain growth during sintering which allowed pores to be swept into the grains where they were not effectively eliminated by post-HIPing. Typically, post-HIPing is performed 100-200°C below the sintering soak temperature, so that porosity can be eliminated without additional grain growth. For the laser host application; however, grain growth is not a negative so long as it does not affect pore removal. Thus, in this work, there were cases in which the sintering soak temperature was 1650°C, which was followed by post-HIPing at 1700°C; this heat/pressure-treatment resulted in fully dense and transparent post-HIPed

specimens. Grain sizes in post-HIPed specimens were approximately an order of magnitude larger than the starting particle size.

For specimens in the range 0-8 mol% Yb_2O_3, higher Yb_2O_3 content appears to require higher sintering soak temperatures. For this series of specimens, lack of transparency appears in three forms: a general grey haze, isolated grey spheres, or a yellow appearance. A sintering soak temperature of 1700°C for 0 and 2 mol% Yb_2O_3 yielded the general grey haze, which was completely eliminated by lowering the sintering temperature to 1650°C: The relatively high sintered relative densities of the 0 and 2 mol% Yb_2O_3 samples exposed to a sintering soak temperature of 1700°C (97.5% and ~95%, respectively), are interpreted to have forced pores into the grain interiors where they could not be eliminated via post-HIPing. This porosity scatters light and resulted in the grey haze.

3.3 X-ray Diffraction Results

Calculated differences between ICDD and best-fit specimen sputter-coated internal standard gold peak 2θ scattering angles are shown in Figure 52. A decreasing difference is seen with increasing 2θ values. All XRD data 2θ values sets were shifted using linear interpolation, based on the four internal standard gold peaks. The Lu_2O_3 peak at 79.2335° 2θ (the ICDD Lu_2O_3 peak position) was selected to evaluate solid solution 2θ shifts with increasing Yb_2O_3 concentration. As can be seen in Figure 53, the shift is roughly linear up to 8 mol% Yb_2O_3. This shift deviates from Vegard's law based on the ICDD 2θ location of pure Yb_2O_3, as indicated in the figure. The 10 mol% Yb_2O_3 data is significantly offset from the trend, with a shift comparable to 0-2 mol% Yb_2O_3. A sec-

ond 10 mol% Yb_2O_3 specimen was prepared, and as may be seen in the figure, showed a similar 2θ shift.

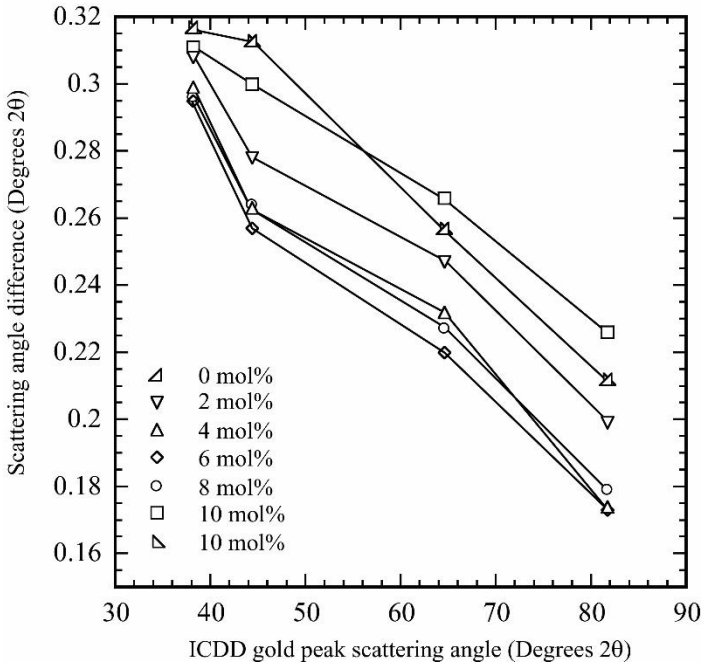

Figure 52: Difference in 2θ positions of ICDD gold peak positions and those of gold coatings on specimens (peaks fit to Gaussian functions to determine peak positions). Differences calculated as gold coating angle minus ICDD gold scattering angle data.

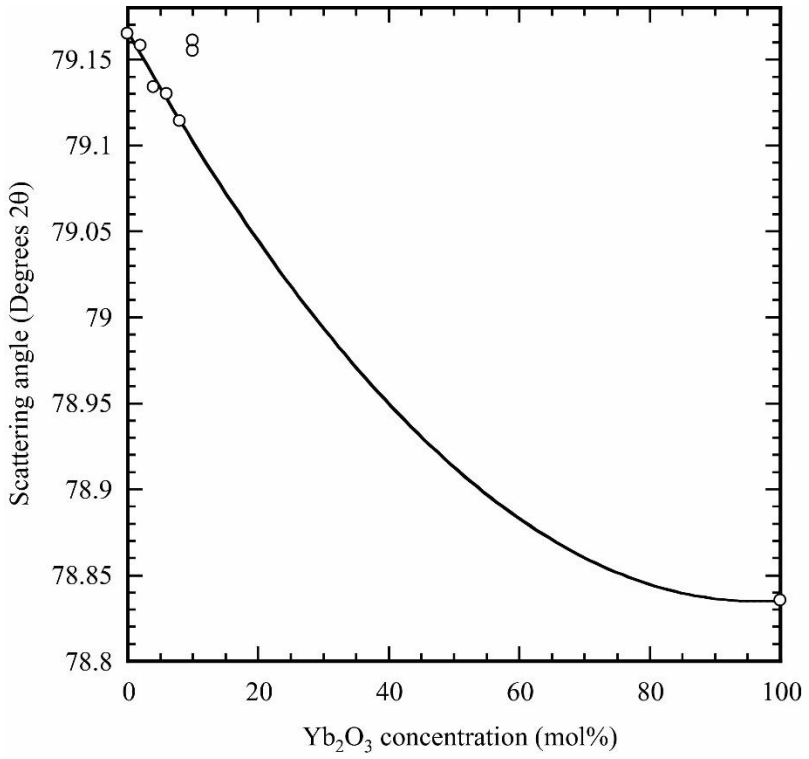

Figure 53: X-ray diffraction patterns of pure and mixed oxide powders are compared to a sintered pellet of pure Yb_2O_3 composition. A high 2θ peak with a large degree of positional shift was used to identify the extent of Yb_2O_3 in solid solution.

Specimens exposed to sintering soak temperatures of 1650°C with no air anneal showed a yellowed appearance that was uniform throughout the specimen. This was fully removed via air annealing only when the specimen sustained porosity, i.e. after sintering. It is interpreted that yellow color comes from a reduced state of Lu_2O_3/Yb_2O_3 on particle surfaces, which is then trapped in the sintered and post HIPed body. Subsequent oxidation during air annealing of the porous sintered body removes it. The porosity (even if closed) facilitates adequate oxygen diffusion into the specimen interior for this purpose.

Post-HIPing specimens which have limited open porosity may facilitate trapping compressed gases in what subsequently become closed pores. A subsequent air anneal permits the expansion of these gases to in turn fracture the parts. The isolated grey

spheres appear to be present in a higher volume percentage in the specimens exposed to a sintering soak temperature of 1700°C, as compared to 1650°C. These regions appear to be diffusional agglomerations of a second phase. Its greater presence at higher sintering soak temperatures is interpreted to imply nucleation and growth of a reduced species, which would be favored by higher temperatures in a vacuum environment.

Solubility of Yb_2O_3 in Lu_2O_3 appears to be continuous up to 8 mol% Yb_2O_3. At 10 mol% Yb_2O_3, a critical state appears to have been reached in which a second phase, rich in Yb_2O_3 nucleates and grows, drawing Yb_2O_3 out of Lu_2O_3 grains, causing the 2θ peak positions of the main phase to be close to phase-pure Lu_2O_3. At this concentration of doping, the two phases have likely never formed a complete solid solution, as indicated by the peak position remaining at near pure Lu_2O_3 values. This second phase may be the cause of the visible opacity via scattering at phase boundaries. Unique peaks in the XRD pattern, implying a second phase, were not observed--perhaps because its volume percentage was below the detection limit.

3.4 Transmission and Emission Results

Transmission properties of the Yb:Lu_2O_3 ceramics were analyzed using a Shimadzu UV-3101PC UV-Vis-NIR Spectrophotometer using the experimental configuration details explained previously. Transmission and absorption results for samples ranging from 0 to 8 mol% doping in the near IR range are shown in Figure 54. A theoretical maximum transmission value is also given, which assumes perfect transmission through the sample and only accounts for surface reflection due to the difference in index of refraction. The 10% Yb:Lu_2O_3 samples were not of optical quality worth measuring.

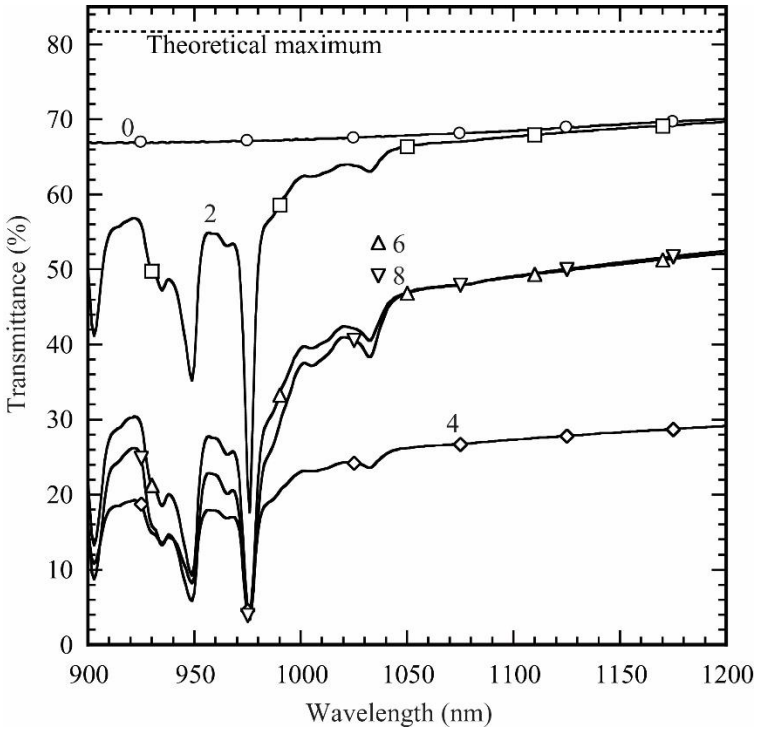

Figure 54: Transmittance spectra. Numbers in the figure indicate Yb_2O_3 concentration in mol%. The theoretical maximum accounts for top and bottom surface reflections.

Generally good optical properties are seen for undoped and 2%-doped Yb:Lu_2O_3, with the primary absorption peak of the doped specimens occurring at ~976 nm, which matches the typical pumping wavelength used for Yb^{3+} -doped lasing ceramics in the literature [4, 33, 96]. The peak at ~1032 nm provides a larger re-absorption loss for emission at that wavelength, so for optically thick ceramics or the case of using a low output coupling resonator, lasing will occur at the smaller emission peak of ~1080 nm instead[33]. Figure 55 gives the expected absorption and emission data from a Yb^{3+}-doped Lu_2O_3 ceramic, showing good match with the absorption peaks seen in the measurement of these specimens. A green glow suspected to be an upconversion or impurity was also identified, which has been seen in similar Er^{3+}-doped and Er^{3+}/Yb^{3+} co-doped Lu_2O_3 optical ceramics[97, 98], but this emission assumed to be around 550 nm was outside of the detectable range of our spectrophotometer. So while no impurities were detected via EDS, this glow

slows that possibility of Er^{3+} contamination. This emission does not seem to be recorded in research about pure Yb^{3+}-doped Lu_2O_3.

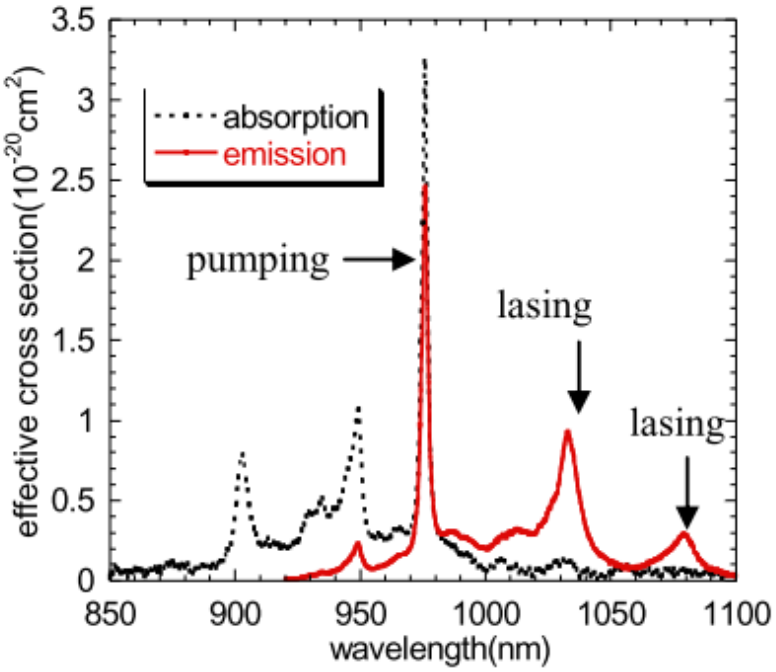

Figure 55: Absorption and emission spectra of a typical Yb:Lu_2O_3 ceramic[33].

Lower transmittance and generally poorer performance is seen for samples above 2% doping. This could be because of an increased impurity level due to requiring higher firing temperatures required to achieve theoretical density from these specimens. Sintering parameters and HIPing processes likely have to be adjusted for samples of high Yb^{3+} content. However, no new absorption peaks are seen, indicating that it could just be an issue with remnant porosity, pore coarsening, or larger grain size as well. Microstructural analysis will also aid in identifying the cause of the decreasing extent of transmittance with increasing dopant percent.

To test for emission characteristics, the samples of varying ytterbium ion content were pumped at 976 nm with a laser diode (premiScan optical parametric oscillator) on a

five nanosecond pulse and measured using an iHR320 spectrometer. The pumping laser was changed into a column used for stripe pumping of the specimen, with slit control to manage the power incident on the sample. A polished face oriented at 90° to the axial surface was ground into a radial edge of the cylindrical specimens in order to position the InGaAs photodiode at 90° with respect the emission detector, such that the incident and fluorescence emission are isolated. Data collection was synchronized to the laser pulse, with a fixed delay to acquire at maximum signal possible. The monochromator was scanned from 1000 to 1100 nm at 1 nm step, 1s per acquisition. Figure 56 shows a schematic illustrating this stripe pumping setup[44].

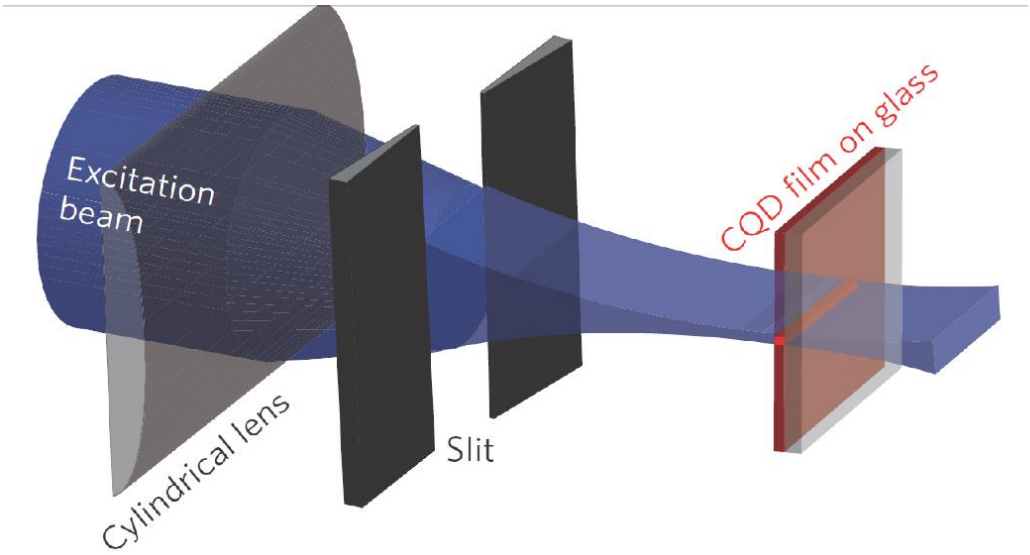

Figure 56: Schematic of a excitation source for a stripe pumping setup[44].

Figure 57 shows the orthogonal nature of the incident pumping stripe and the emission from the edge of the sample. Figure 58 shows the specific geometry used on the Yb:Lu_2O_3 samples with the orthogonal sample edge polished identically to the other faces of the sample to a 0.05μm finish.

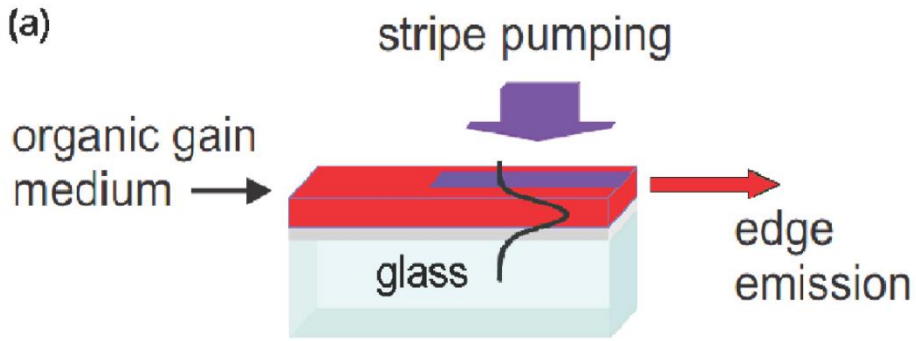

Figure 57: An example stripe pumping configuration highlighting the incident and emitted light are oriented at 90° to each other. [99]

Figure 58: A transparent Lu_2O_3 sample prepared for stripe pumping analysis, with a small section of the radial edge polished to allow emission of the $Yb^{3}+$ fluorescence.

The relative emission intensity of the peaks at ~1030 nm and ~1080 nm was determined to be constant regardless of incident pumping power. This is consistent with the literature which suggests that the selective emission is determined based on either the output coupler used [33] or the fabrication method [23]. Since these factors are constant for this

analysis, the matched relative intensities with the peak emission at ~1030nm normalized to 1 at each incident power is justifiable. Figure 59 shows the increasing intensity of both emission peaks with increasing incident power. Figure 60 shows that the relative intensity of these peaks is constant. This was found to be the case for each sample.

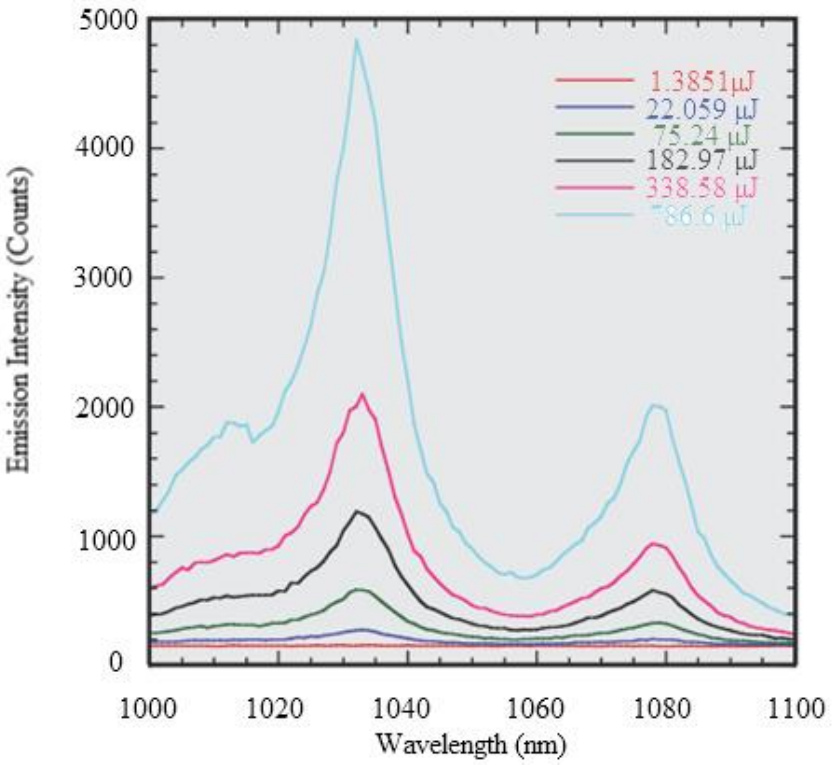

Figure 59: Relative intensities of ~1030 nm and ~1080 nm emissions for the 4 mol% Yb:Lu_2O_3 sample with increasing incident pumping power.

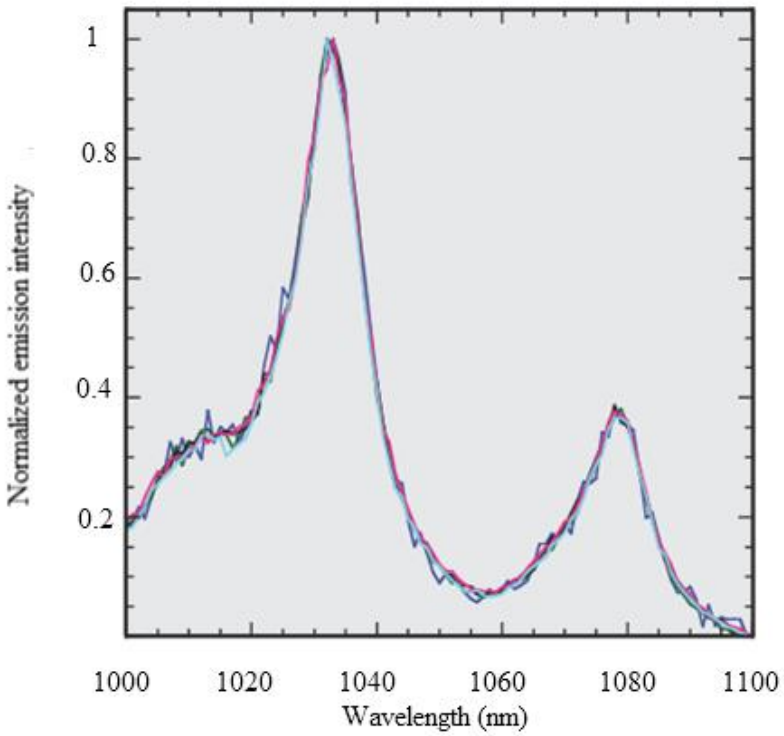

Figure 60: Normalized emission peaks showing matched relative intensity for each emission.

To test for sample homogeneity, data was collected three times from each sample to compare the emission slope intensity for different locations on the sample. The slope efficient (output intensity over incident pumping power) was used as the metric to compare the emission characteristics from each sample. While this measurement does not allow one to get an actual efficiency percentage since our output emission is measured in general intensity counts, it does allow for the testing both the relative efficiency of the multiple locations on each sample as well as the relative efficiency of each sample with respect to increasing Yb^{3+} content. Figure 61 illustrates the idea of spot checking each sample for homogeneity using multiple stripe locations.

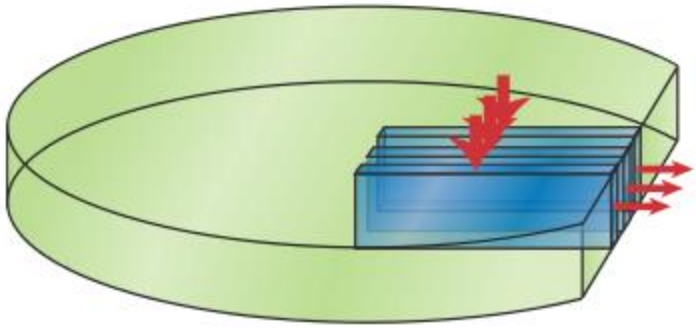

Figure 61: Graphic illustrating testing each sample at multiple locations for optical homogeneity using the stripe pumping methodology.

Figure 62 shows the ~1030 nm emission results for the 4 mol% sample, showing very good, but not perfect, match with three test locations on the sample. The presence of locations within the sample of remnant high porosity manifesting in the form of small white specks within the transparent matrix is the likely cause of the minor differences seen between the individual test locations. The possibility of impurity phases within the samples is another potential contributor to the variations of emission slope, but the lack of phase impurities shown in XRD suggest that isolated areas of high remnant porosity is the more likely contributor. Figure 64 shows the slope results for the samples from 0 to 8 mol% Yb^{3+} content. While the variation in sample thicknesses do account for some of the trends seen in the figure, the relative results are still indicative of increasing emission efficiency with increasing concentration of Yb^{3+} laser-active ions in the samples.

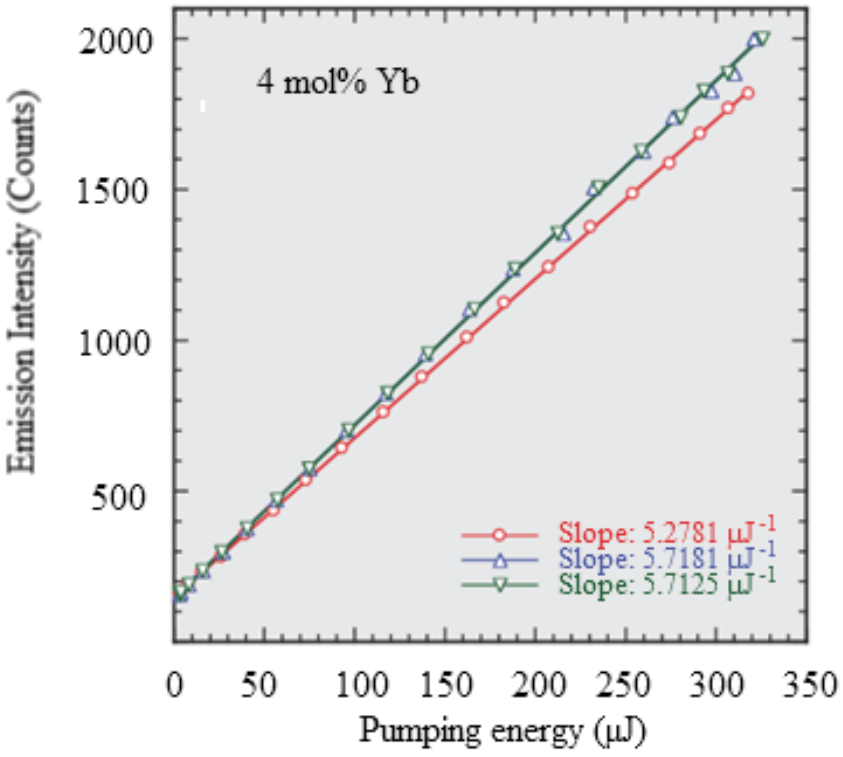

Figure 62: Slope efficiency for three random locations on the 4 mol% Yb:Lu_2O_3 sample with respect to the ~1030nm emission. Very minor dependance of location is identified, indicating a generally consistent quality throughout the sample.

A very important thing to note is that one does not see any increase in the slope at any of the utilized incident pumping energies, indicative of a threshold pumping energy not being reached characteristic and thus no stimulated emission being achieved, at least for the expected emission at ~1030 nm. However, for these samples, the unexpected green emission at ~550 nm was recognized at the same location of the incident 976nm pump laser stripe. This is likely either indicative of a Er^{3+} impurity or some upconversion phenomenon that can occur with quasi three-level lasing ions, which Yb^{3+} can behave as[43]. A threshold of 100-200 μJ was found for the ~550 nm emission, and since one can know that the threshold for higher order process such as excited state and multi-photon absorp-

tion is typically much higher than emission from the lower excited states (such as 1030 and 1080 nm emission)[100], then this indicates that perhaps the threshold pumping energy for the infrared emissions expected from the Yb^{3+} ion is simply below the detectable range of the equipment. Further, the fitted slope measured is significantly higher for the 1030 nm emission than for the slope for the lasing in the potentially upconverted emission. A visual of this green-yellow emission is shown in Figure 63.

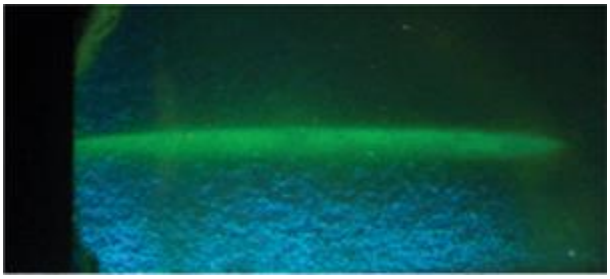

Figure 63: Impurity or upconverted green emission from samples during stripe pumping analysis.

If the phenomenon is indeed a lasing from a more energetically unfavorable upconversion process, then it's likely that the 1030 (and 1080 nm) bands are also lasing and actually showing stimulated emission but the equipment used simply doesn't detect low enough, or perhaps the samples are simply too small to result in an appropriately low incident power density. As mentioned, these measurements are performed with a pulsed laser, so the number of incident photons is much greater than continuous wave laser used in some of the literature. Starting with 99.99% pure commercial Lu_2O_3 and Yb_2O_3 powders suggests that whatever potential Er^{3+} impurity must either be accordingly small or becomes present in the sample at some other point in its fabrication. In either case, the appearance of this green emission phenomenon will have to be further investigated.

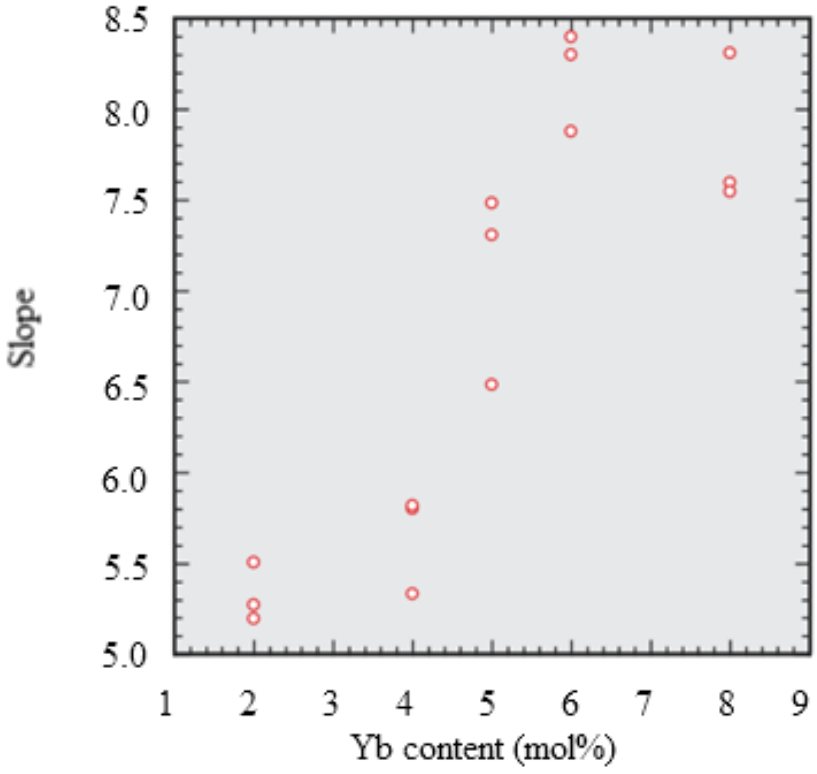

Figure 64: Slope efficiency of ~1030 nm emission of 0-8 mol% Yb:Lu_2O_3 ceramics. A maximum slope is identified at ~6 mol%.

One sees the general expected increase of slope efficiency of the ~1030 nm infrared emission with increasing Yb^{3+} content, though this does not account for slight variations in the sample thicknesses based on variations in the initial dimensions of the green bodies from the commercial powders and also grinding and polishing duration to ensure a flat and fully polished surface. For instance, the 4 mol% sample, while still a higher overall emission efficiency than the two percent sample, deviated further below from the average thickness of the 5 mol% doped samples than the rest. It is also important to note that it had a much lower measured degree of transparency than the 2 mol% as shown in Figure 54, though the increased degree of emission despite the lower thickness and transparency

indicates that achieving the maximum doping percent of Yb^{3+} is the most critical component of achieving high output from these materials.

Surprisingly, the 6 and 8 mol% samples appear to have about the same slope efficiency, despite being nearly identical thickness (less than 0.1 mm difference) and transparency (as indicated in Figure 54). The XRD experiments done previously, as well as other information in the, literature suggests possible reasons for this plateau in emission despite expecting a greater concentration of laser active ions in a near-identically sized samples. The first reason is that at some concentration between 6-8 mol%, the Yb^{3+} ions are failing to go into solution, though not to the extent that one could clearly see in the opaque 10 mol% Yb:Lu_2O_3 samples. A more likely explanation is that there could be a lower degree of reabsorption or other higher order process like the stated upconversion that could affect the lower energy transition that is being monitored, or a concentration quenching effect preventing Yb^{3+} ions past a certain concentration from emitting properly[23]. Further analysis of the ~550 nm signal could give a better picture as to a potential decay pathway that is present in the system. Sanghera et al. suggest that at higher Yb^{3+} ion doping levels, the energy associated with an excited ion can keep transferring to others until it transfers to a quenching site, such as an impurity or grain boundary. One key qualifier that Sanghera identifies is that this decay transfer process would also result in shorter fluorescence lifetimes, which makes that measurement a possible indication of whether this quenching effect is actually occurring. Figure 65 shows that for Yb-doped Lu_2O_3, the fluorescence lifetime can start decreasing as early as 3 mol% and as late as past 10 mol%. This is even shown to occur in single crystals, suggesting that Yb^{3+} clustering or other

impurities could decay the lifetime of the fluorescence in addition to grain boundaries[23].

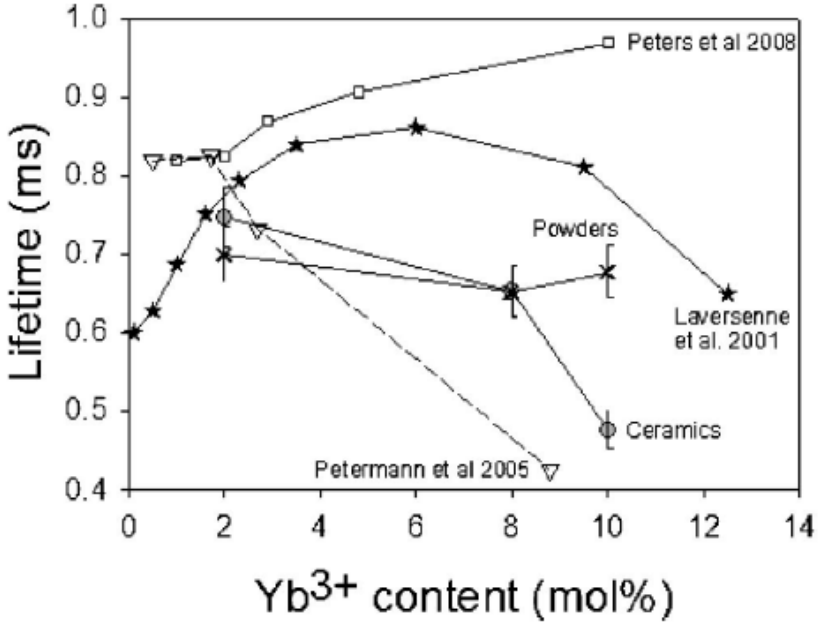

Figure 65: Varying fluorescence lifetimes of Yb:Lu_2O_3[23], with data sets from multiple sources[101-103]. While the results show that it seems to be typical to see a decrease in lifetime with high Yb^{3+} content, even in single crystal, the onset of this phenomenon can vary widely.

Further study of the fluorescence lifetimes of our samples could provide insight to whether concentration quenching is the cause of the flat-line slope efficiency of emission between 6 and 8 mol% Yb^{3+} doping, but the capability and equipment (access to a fluorometer) for the optics lab to make such measurements was not available at the time of this study.

IV. SINTERING OF PROCESSED COMMERCIAL POWDERS

It was found that the using the methods identified in the processing of the samples produced earlier in this work that the sintering behavior of our Yb:Lu_2O_3 ceramics was highly dependent on the specific commercial powder lot used, even with powders of the same identified purity and of similar apparent particle size. A second powder lot from the same initial source, Alfa Aesar, started displaying much different sintering characteristics and it became a lot more difficult to sinter samples to transparency using the same methods as before. This was later determined to be likely because of the course macro-particles of the various commercial powder sources were actually soft agglomerates of a much smaller particle size that varied much more widely. Higher sintering temperatures were required to reach equivalent levels of transparency, and greater degree of annealing out of sintering-related coloration became necessary, accomplished through annealing with a higher concentration of oxygen present in the annealing atmosphere. Another lot from HEFA Rare Earth with identical purity and similar agglomeration was tested to check the extent of vendor-specific behavior, but sintered similarly poorly. At that point it became crucially imperative to being to utilize further ceramic processing techniques to increase the sinterability of the ceramic powders while not compromising the purity or other properties that would adversely affect the optical properties of the final ceramics.

The focus of the work became to identify the appropriate processing technique to reduce the sintering temperature required to reach a state of closed porosity, to minimize the extent of furnace-induced impurities, and to improve on the microstructural properties seen from the samples produced from unprocessed commercial powders. Candidate tech-

niques for this goal included ball and jet milling, chemical co-precipitation, sedimentation of the powder agglomerates, sonication of an aqueous powder slurry, and spray drying into spherical granules. Since processing technique such as ball milling and spray drying are also conducive to the possibility of scale-up for the production of larger or a more numerous amount of samples, along with the possibility of imperfect yield from these processes, the HEFA Rare Earth commercial powder ended up being the primary sample material used due to its relatively lower cost-to-buy compared to re-sellers such as Alfa Aesar. SEM micrographs of the various commercial powder lots before any processing are shown in Figure 66.

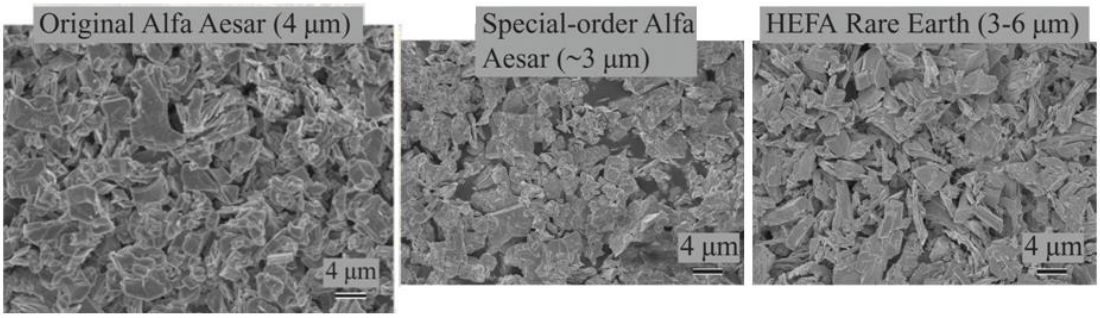

Figure 66: SEM micrographs of candidate commercial powder lots. Disparity in sintering behavior could not be correlated to apparent particle size, due to the particles shown being agglomerates of smaller particles.

In addition to assessing various ceramic powder processing techniques, a tungsten element vacuum furnace (Model M60, Centorr Vacuum Industries, Nashua, NH) was evaluated to test if removing the presence of carbon from the sintering environment of the ceramic samples would result in specimens of improved optical quality. This layout of the hot zone of this furnace is given in Figure 67.

Figure 67: Tungsten element sintering furnace rebuilt to test for the effect of eliminating the carbon sintering environment.

4.1 Experimental Procedures

Initial commercial powder sintering experiments mimicked those of the first study, with the same details found at the beginning of Chapter 3 regarding 2 g Lu_2O_3 ceramic samples. Pressed powder compacts were formed in the same way, with relative density of the green bodies remaining near 59%. Once uniaxially pressed and CIPed, 0-10 mol% Yb:Lu_2O_3 specimens were sintered in the graphite element furnace between 1700-1900°C for 4 h. A greater extent of darkening and coloration was noticed with these samples due to the elevated sintering temperature, so the 1100°C 2 h static air anneal performed after sintering was replaced with a flowing oxygen-rich annealing atmosphere with the same

schedule. The post-HIP was performed identically, at 1700°C for 2 h with the same pressurization schedule. A 1800°C HIP schedule was evaluated, but results on the sample were highly negative and imbued a large degree of coloration from the HIP.

Replacing the mechanical pump on the sintering furnace with a turbomolecular pump (Edwards T-Station 75) seemed to improve sample results sintered at these elevated temperatures (see Figure 70). After HIP, samples were annealed again in the flowing oxygen-rich atmosphere at 1100°C for 4 h and polished as before. Samples formed from 1800°C HIP required elevated temperature (1400°C) high-oxygen annealing, which while effective at removing coloration, hindered transparency on the edges of the samples though otherwise provided the best results. Sintered and HIPed relative densities were measured using the Archimedes density as described in Chapter 3. While modest transparency was achieved with these samples otherwise, they were clearly not of identical quality to earlier produced samples from commercial powders. It was evident that some method of either particle size reduction or purification was going to be needed to reduce the necessary sintering temperature of the Lu_2O_3 ceramics in order to prevent the higher temperature-induced defects that degrade the samples formed from as-received commercial powders.

4.1.1 Sintering of Co-precipitated Lu_2O_3 Powders

The first processing method implemented to improve the sintering behavior of the commercial oxide was to implement a precipitation methodology before pressing into green body compacts. To achieve this, 10 grams batches of as-received (Aesar Aesar) Lu_2O_3 powder were dissolved in ~300 mL of warm 2N nitric acid (Avantor/JT Baker, reagent grade) while stirring. Once fully dissolved by visual inspection, 50 vol% ammonium hy-

droxide solution (VWR) was added dropwise to the stirred acid solution. The solution was under constant pH monitoring using a Hanna Piccolo pH meter which was two-point calibrated using 4.01 and 7.01 pH buffer solutions (Hanna Instruments). A color change was noticed at ~6 pH with the onset of precipitate formation. The precipitate suspension was allowed to homogenize at a pH of greater than 7. A buechner funnel setup using ash-less filter paper (Whatman, grade 42) was implemented to collect the precipitate and filter it from the now-neutralized acid solvent. Under light suction using an aspirator, the filter paper was wetted with DI water to ensure a good seal between the filter and the funnel before separating the suspension. The collected precipitate was transferred into a weighing tray and allowed to dry in a warming oven overnight, where it formed a dried precursor cake. The dried precipitate was then calcined between 500-1000°C for 6 h in static air to form the final Lu_2O_3 oxide powder.

The calcined Lu_2O_3 was highly agglomerated and was hand-crushed using an alumina mortar and pestle. Crushed calcined powders were also milled using either tungsten carbide or boron carbide media for ~100 h in HDPE bottles. They were milled as a low wt% (<10%) aqueous slurry. Crushed and milled powders were analyzed via x-ray diffraction and scanning electron microscopy. While an array of green-body samples were formed from the crushed calcined powders in the same manner as stated in Chapter 3, milled powders were not formed into compacts due to a high extent of impurity present from the media contamination. Dimensional relative densities of the pressed samples averaged around ~53%, notably lower than those formed from as-received commercial powders. Specimens formed from the crushed calcined powders were sintered under vacuum between 1700-1750°C for 4 hours, annealed in static air at 1100°C for 2 h, and HIPed at

1700°C for 2 h. Densities after sintering and HIPing were measured using the Archimedes density method as before.

4.1.2 Sonication and Sedimentation of Lu_2O_3 and Y_2O_3 Powders

Due to the negative results from chemically co-precipitated powders, whether crushed or milled, media-less methods of particle size reduction such as sonication of agglomerates and separation of large particles through sedimentation were evaluated. As-received (Alfa Aesar) 99.99% purity Lu_2O_3 powders were suspended in DI water and sonicated using a ½ inch Ti6-4 sonication probe (Cole Parmer) attached to a Vibracell VC600-2 600W ultrasonic processor. The sonicator was allowed to run at full power for 15 minutes on a 2 second pulse with the sonication probe submerged into the Lu_2O_3 suspension in a glass beaker while stationed on top of stir plate. The sonicated powder suspension was then allowed to dry in a warming oven overnight before being pressed and CIPed into compacts as before.

Relative densities of the powder compacts formed from sonicated powder were notably higher than those of commercial powders, measuring at around ~64%. However, the samples were also notably darkened, potentially from impurities due to being in contact with the sonication probe. Samples were vacuum sintered at 1700°C for 4-6 h, and then HIPed at 1700°C for 2 h. Lu_2O_3 powders from HEFA Rare Earth were also similarly sonicated and sintered at 1700-1800°C for 4 h. Ceramics formed from HEFA powders were not HIPed, due to the high sintering temperature still required to reach acceptable relative densities from sintering. Densities were again measured using the Archimedes method.

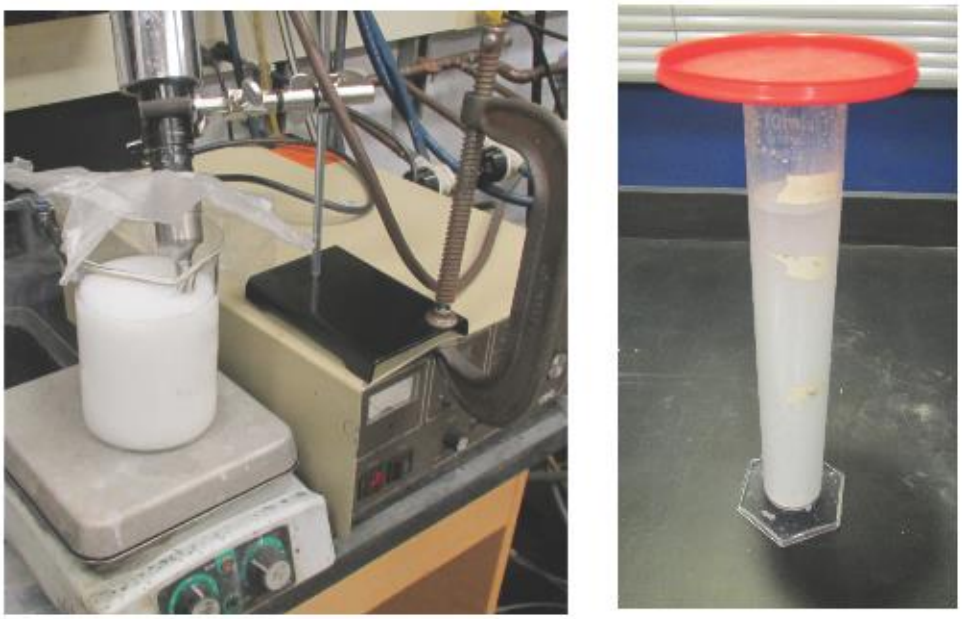

Figure 68: Sonication and sedimentation setups for particle size reduction of agglomerated as-received powders.

For sedimentation, the less expensive commercial powder (99.99% purity, HEFA Rare Earth) was used due to considerations of low yield as a result of filtering out larger agglomerates from the as-received powder. A mixed slurry of the commercial Lu_2O_3 powder and water was poured into a 1 liter plastic column and allowed to settle for ~140 minutes. Based on Stokes' law, the height of the column, and the viscosity of the fluid, this would result in all particles of 2 micron diameter or more to be collected in the bottom half of the column, assuming spherical particles. The finer particles from the top of the column were collected using a large syringe, and the remaining suspension was remixed and allowed to resettle 2-3 times before drying the fines-containing suspension in a warming oven. CIPed powder compacts formed from filtered sediment powders were vacuum sintered at 1700-1800°C for 4 h.

4.1.3 Sintering of Jet and Ball Milled Lu_2O_3 and Y_2O_3 Powders

The final attempt at media-less particle size reduction was to use either a jet-milling process, similar to that identified by Sanghera et al[59], or otherwise use a more conventional ball mill. Using a toll milling service provided by Powder Technology Inc, 100 g of Lu_2O_3 was sent to be milled to a target d_{50} of 1 µm. While the less expensive HEFA powder was used in this test, it was still critical to maximize yield from the process due to the generally high cost of the oxide compared to other typically milled powders.

In addition to the toll jet milling attempt, ball milling was revisited, using 3 mm spherical 3 mol% yttria-stabilized ZrO_2 media (Inframat Advanced Materials). While the initial attempt to revisit wet milling was specific to the secondary focus of this work regarding ZrO_2-Y_2O_3 due to the impossibility of ZrO_2 media contaminating the matched material powders, it was also evaluated for the milling of Lu_2O_3 powders as well. Lu_2O_3 (HEFA Rare Earth, 99.99% pure), Y_2O_3 (Skyspring Nanomaterials, 99.99% pure), and 3 mol% YSZ (Skyspring Nanomaterials, 99,99% pure) were the commercial powders used at this point of study. A 50 wt% aqueous slurry of each oxide was prepared without any organic additives. The slurries were milled in HDPE jars, with the YSZ media filling ~50% of the jar volume and the slurry slightly exceeding the void space in the media. The mill was allowed to run for several days, with samples extracted for analysis via SEM to determine the extent of particle size reduction with milling time for each oxide. Media was filtered from the slurry by using a Buchner funnel and rinsing the slurry through with DI water into a glass beaker. The collected milled yttria powder slurry was dried in a warming over before being prepared into CIPed powder compacts as before.

Specimens prepared from milled Y_2O_3 were vacuum sintered at 1625-1675°C for 2 h. Initial results were followed by the preparation of more samples uniaxially pressed at a slightly higher initial pressure (~150 MPa) and these samples were sintered at 1650°C for 2 h. Resulting cracking of sintered samples and high degree of open porosity prevented subsequent HIPing of milled Y_2O_3 samples. Due to the difficulty of achieving high quality samples from the Y_2O_3 batch, no specimens were attempted to be fabricated from Lu_2O_3 powder milled in this way.

The viability of milling of Lu_2O_3 and Y_2O_3 oxides was reevaluated using an acetone based slurry instead of the previous aqueous slurry. It was reasoned that oven drying of the milled powder was reagglomerating the reduced size particles, resulting in the poor sinterability. The goal of using a more volatile solvent was to eventually be able to spray dry the de-agglomerated powder slurry from the mill. This allows a more rapid drying of the slurry for smaller scale batches compared to water-based suspensions. Additionally, the use of a dispersant was investigated to assist in the de-agglomeration of the commercial powders through ball milling. An acetone-soluble low molecular weight polymethylmethacrylate polymer (PMMA) was added to the slurry as a dispersant (Elvacite 2008, Lucite International). PMMA is a thermoplastic with a glass transition temperature well above room temperature at roughly 100°C. This resin attaches on the powder surfaces and disperses by steric hindrance, physically keeping particles isolated from each other. The addition of PMMA is also conveniently used as a binder to improve the strength of resulting spray dried granules and subsequent pressed powder compacts[104]. 3 g of PMMA were added for every 100 g of oxide powder. This ratio was determined by

visual inspection of dispersion characteristics of small slurry volumes that were allowed to settle in conical vials.

HDPE milling jars were loaded with ZrO_2 media as before and the powder slurry was ball milled for ~72 h with the PMMA additive. After the milling duration had finished, the media was again collected from the milling jars using a Buchner funnel and rinsing the slurry through, this time with acetone. The milled powder slurry was collected into a plastic bottle for transferring to disposable syringes for charging the spray dryer. No samples were sintered from the acetone wet-milling process without also spray drying. In the process of sintering powder compacts formed with the aid of PMMA, the high glass transition temperature of the polymer meant that the use of a plasticizer became crucially imperative. The use of the acetone-soluble plasticizing agent dibutyl phthalate (DBP), which has been used as the plasticizer for PMMA polymers, was evaluated[105, 106]. Powder slurries containing 12:1 to 3:1 plasticizer-to-binder ratio by weight were identically milled, spray dried, heated to 400°C in oxygen-rich atmosphere and then sintered to test for the effect of plasticizer content on the densities of the sintered samples.

4.1.4 Sintering of Spray Dried Lu_2O_3 and Y_2O_3 Powders

Spray drying was evaluated as a processing method due to the capability to get the milled oxide particles into a pressable form without the re-agglomeration that oven drying would induce. Additionally, spherical granules flow better than the agglomerated powder and improve the uniformity of die fill when producing green bodies by uniaxially pressing and CIPing. Using spherical granules produced in this was would also be expected to reduce the potential density gradients in the pressed powder compacts, which would vary

with the extent of agglomeration as-received. A prototype spray dryer unit designed by the late Dr. Robert Snyder (Georgia Institute of Technology) and manufactured by Glatt Air Technologies (Ramsey, NJ) used for this operation is shown in Figure 69. The operation of the spray dryer involves atomizing the oxide slurry into a heated cylindrical drying chamber. A vent extends from the bottom of the chamber through the top lid to expel acetone vapor and nitrogen while the dried granules are caught on a lined tray at the bottom. A viewport is monitored from the side to ensure proper atomization of the slurry. The slurry was atomized using an ultrasonic nozzle (Sono-Tek, Milton, NY), where a piezoelectric crystal vibrates the nozzle at a frequency of 48 kHz. At some critical amplitude, droplets of liquid are released from the atomizing surface. Manual tuning of the power input to the nozzle and viewport monitoring are used to ensure fine droplet generation.

Figure 69: Laboratory scale spray dryer used for drying milled powder-acetone slurry into spherical granules.

For a 48 kHz nozzle, 38 μm is expected to be the median droplet size with 99% of the droplets falling within a the range of 10-150 μm[65]. The droplets leave the ultrasonic atomizer with a velocity of ~1cm/sec, and the low velocity along with the relatively large size of the drying chamber prevents partially dried droplets from sticking to the walls of the chamber. This maximizes yield of granules from the slurry. Additionally, the use of ultrasonic atomization ensures that the dispersion of the products in the spray dried granules is highly uniform. A syringe pump was used for fluid delivery (New Era Pump Systems, Wantagh, NY). The pump is calibrated to the syringe diameter and pushes the slurry-load syringe at a linear rate. The slurries were spray dried at ~500 mL/h and the drying chamber was maintained at ~70°C. The powders collected on the tray liner at the bottom were filtered through a 60 mesh sieve to remove any large improperly dried flakes before being collected to be pressed into powder compacts.

Once powder compacts formed from these spray dried granules were CIPed, the PMMA polymer was removed from the specimens by heat treating them at 1°C/min to 400°C and holding for 2 h under a flowing oxygen-rich atmosphere. The slow heating rate was chosen to prevent bloating of the parts due to too-rapid combustion of the organic components. This heat treatment also removed any DBP from the compacts, if present, which has a boiling point at around ~360°C so that any unreacted organic would otherwise be volatized away when exceeding this temperature. The resulting 4-5% weight loss suggests a complete burnout of the binder polymer with this schedule. The measured weight loss of ceramic compacts after undergoing this thermolysis process slightly exceeded the expected weight of the mass content of plasticizer and binder, with the excess

being attributed to water loss. After this low temperature thermolysis, the samples were found to have a green relative density of ~59%. Lu_2O_3 compacts formed from spray dried granules were vacuum sintered in a graphite element furnace between 1500-1800°C for 2-16 h. Similar Y_2O_3 compacts were sintered in the graphite element furnace at 1625-1750°C from 2-16 h. Lu_2O_3 compacts were also sintered in the tungsten element vacuum furnace (settered on ZrO_2 or buried in loose Lu_2O_3 powder) at 1500-1850°C from 0-20 h. Sintered samples were annealed in a flowing high-oxygen atmosphere at 1100°C for 2 h before being HIPed between 1500-1800°C for 2-8 h. Samples that were buried in loose Lu_2O_3 in the tungsten furnace during sintering were not annealed before HIPing due to the lack of apparent coloration. Samples of sufficient HIPed density were annealed at 1100-1200°C for 4 h before being polished in the same manner as stated in Chapter 3.

Lastly, an additional HIP parameter adjustments were made for spray dried Lu_2O_3 by elevating the applied pressure to 310 MPa in an attempt to receive samples of near theoretical density at potentially lower sintered temperatures. Alongside this study, purity analysis of the spray dried powder, sintered samples, and HIPed specimens was performed using XRD phase analysis as before, and also via EDS (INCA Microanalysis Software, Oxford Instruments).

4.2 Sintering Results

The switch to a turbomolecular pumping station improved the vacuum levels of the graphite element sintering furnace to ~ 0.5 mtorr (from about 20 mtorr.) While it was not possible to see the results of this change on the initial lot of powder due to exhausting that supply, it did manage to achieve modest levels of transparency on the new commer-

cial powder lots that required much higher sintering temperatures in order to achieve an appropriate level of relative density. To get a rough idea of the transparency improvement using the higher level vacuum pump, three samples were processed and polished identically other than vacuum level used, and the results are shown in Figure 70.

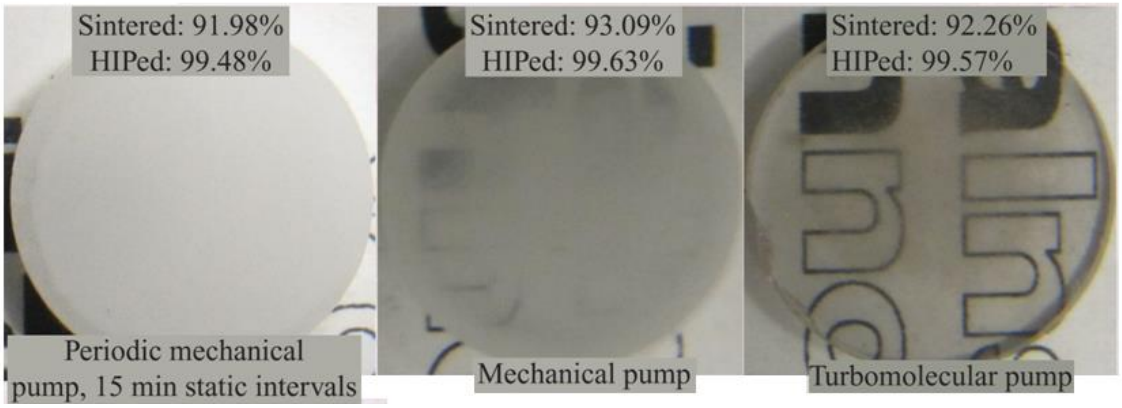

Figure 70: Generally improved optical quality with increasing vacuum level, seemingly independent of relative density. Samples were vacuum sintered at 1800ºC for 4 h and HIPed at 1700°C for 2 h, with oxygen-rich annealing before and after HIP.

An interesting result of this short study is the clear difference in apparent transparency independent of similar levels of final relative density. This suggests that the remnant white haze present in the middle and left samples could actually be some carbon based impurity, if one expects lower-vacuum sintering environments in the graphite element furnace to allow more carbon to enter the samples. This also gives motivation to lower the sintering temperature as far as possible in order to prevent furnace-based impurities from entering the samples in the first place, or to sinter in an environment without any carbon containing components.

4.2.1 Elevated Graphite Element Furnace Sintering Results

Below 1750°C, the relative density of the undoped Lu_2O_3 samples was not high enough to be able to effectively HIP to a highly transparent state. However, comparison of samples fired at these two temperatures confirms the general trend of higher sintering temperatures ending up with samples of poorer apparent optical properties. Since these samples are undoped and it was previously noted that samples of increasing Yb^3+ content required higher sintering temperatures in the first place, this study really made it apparent that the commercial powder lot was not going to be sinterable in the as-received form. The initial results of undoped samples formed from this commercial powder are given in Figure 71.

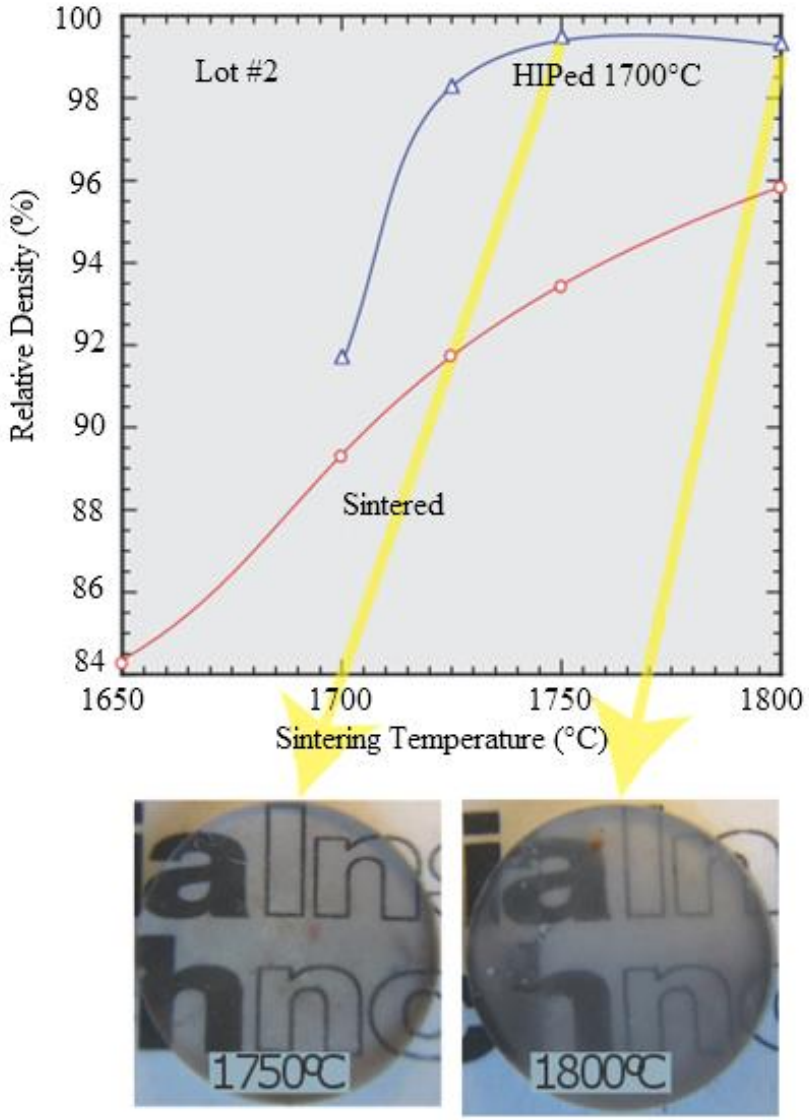

Figure 71: Density results of second ALFA powder lot, illustrating higher sintering temperatures required, leading to poorer quality samples. A greater degree of haze is present in the sample sintered at 1800°C.

Results of higher temperature sintering of samples doped with 2-8 mol% Yb^{3+} content is given in Figure 72. To reach any degree of transparency with up to 8 mol% as before, sintering temperature as high at 1850°C was required. Samples were marred with various cloudy spots and general haze, even though final relative densities were generally good,

especially for samples of 4 mol% and below. Also, as before, an apparent limit was reached at 10 mol% Yb^{3+}, where increasing the sintering temperature was not sufficient to achieving any extent of transparency at that level of dopant concentration. This limit reappearing despite the shifted sintering temperatures required suggests that the opacity reached at this point, even in the first sample study, is not temperature dependent, but rather a solubility or segregation issue of the Yb^{3+} ions. In the initial study, 8 mol% samples of high relative density was achieved at 1700°C, while the study with the second set of commercial powder showed that this was generally still achievable at 1850°C. This suggests that the opacity of 10 mol% Yb:Lu_2O_3 initially indentified could not possibly have been solved by simply increasing the sintering temperature.

It is also interesting to note that the HIPing temperature required to achieve these generally high relative density samples was unchanged from the initial study. This suggests that there is still enough driving force for densification at this temperature according to the Nabarro-Herring model, despite apparently needing higher sintering temperatures to reach a state where HIPing becomes effective to the sample such that the model can be appropriately applied. It became a greater degree of focus to identify the porosity profile of sintered samples; specifically, the extent of remaining open and closed porosity.

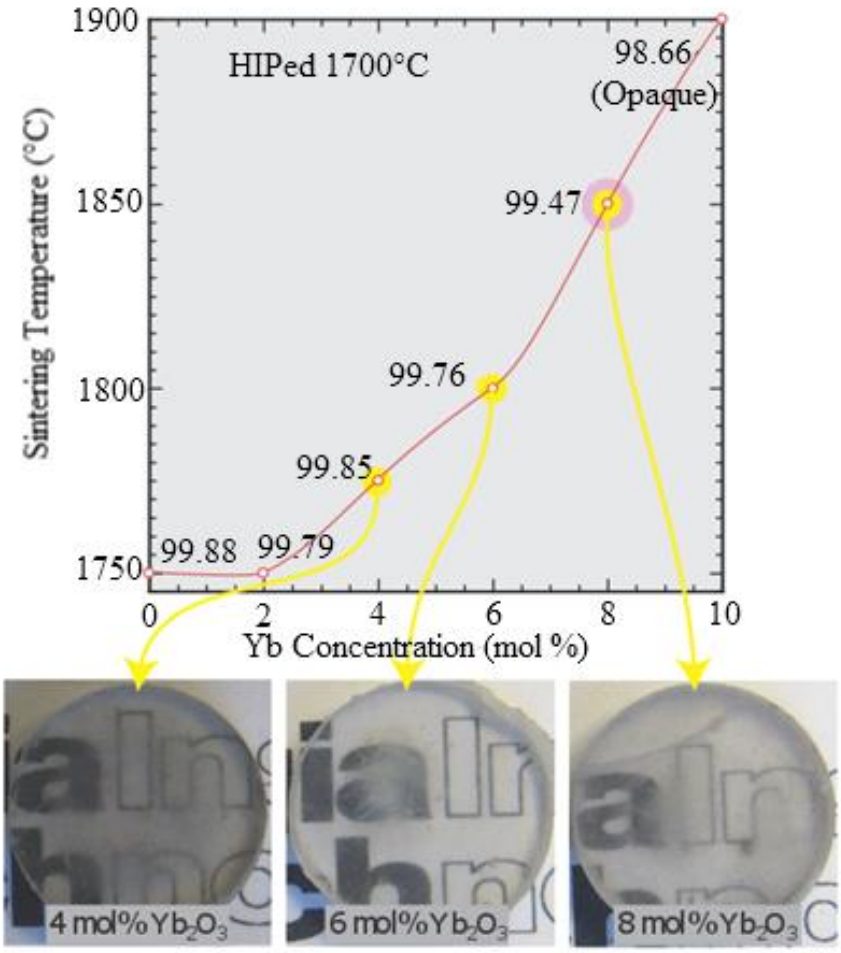

Figure 72: Expected increase in required sintering temperature with increasing dopant concentration led to sintering temperatures of greater than 1800°C, leading to very cloudy samples. Values show relative densities of specimens after HIPing.

Generally poorer relative densities are seen with increasing sintering temperature, indicating a greater extent of remaining porosity in these samples contributing to their lack of transparency. This is in addition to the contribution of transparency-preventing carbon impurities resulting from the increased sintering temperature as well. And optical micrograph of an undoped sample is shown in Figure 73.

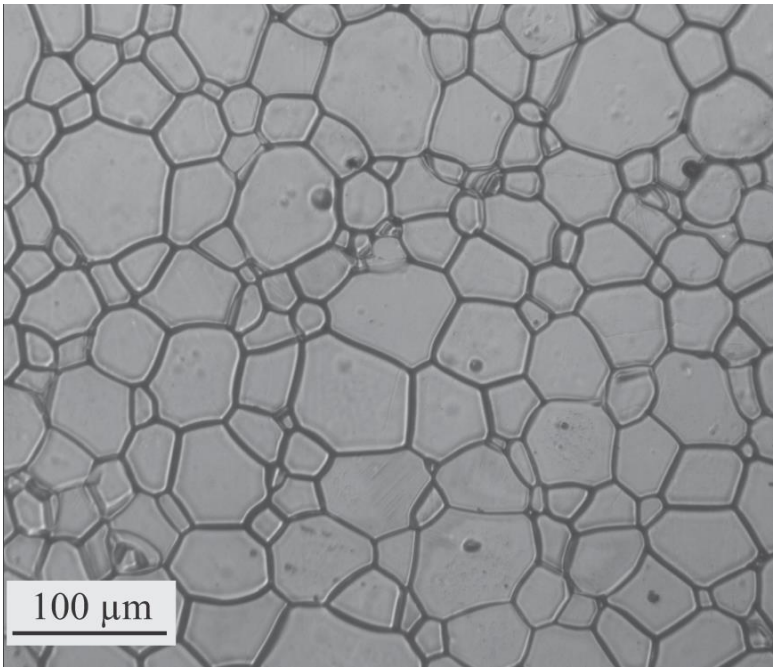

Figure 73: Optical micrograph of undoped Lu_2O_3 ceramic sintered at 1800°C for 4 h and HIPed at 1700°C for 2 h. Sample was thermally etched in the HIP at ~1000°C. Grains are moderately large, varying from 40-100 µm in size.

Grain sizes of up to 100 µm are present, which is generally larger than what is reported in the literature. One sees that the grain boundaries are entirely pore free, but the presence of remaining pores in the grain interiors is very notable. This means that HIPing of these sintered samples will not be able to remove these pores or improve density above a certain limit for as long as they remain. The onset of rapid grain growth that sweeps pores into the grains is much harder to prevent at these temperatures, at least with the extent of agglomeration present in the new commercial powder. This gives yet another incentive to reduce the sintering, and if possible, HIPing, temperatures of these ceramics so that issues of pore-entrapment and furnace contamination can be avoided and optical properties improved.

4.2.2 Processed Powder Graphite Element Sintering Results

While sintering at higher temperatures allowed samples from as received powder to achieve high relative density and moderate transparency, it had become clear that additional processing needed to be undertaken in order to reduce the sintering temperatures and improve the sample quality. Based on the initial literature review, co-precipitation has been established as an extremely common method of powder purification and nanopowder synthesis, and was evaluated as a solution to the issues that had presented themselves from the results of sintering as-received powders at higher temperatures. Being able to sinter lutetia nanopowders instead of commercial agglomerates would hopefully lower sintering temperatures back into a range where both furnace impurities are minimized and grain growth is controlled such that pores are not swept into abnormally grown grains. The extent of literature present utilizing this method made it a promising candidate for being able to sinter powders regardless of commercial source and potentially purify it further than the commercial certification. Lu_2O_3 based nitrate precipitates were filtered from a neutralized acid solution and dried in the method described previously. To ensure that the precursor nitrates were fully converted back to pure Lu_2O_3 from the dried and calcined powder precipitates, x-ray diffraction was performed on powder samples that had been calcined between 500-1000°C for 6 h, using the same scanning rate describe in Chapter 3. The results are given in Figure 74.

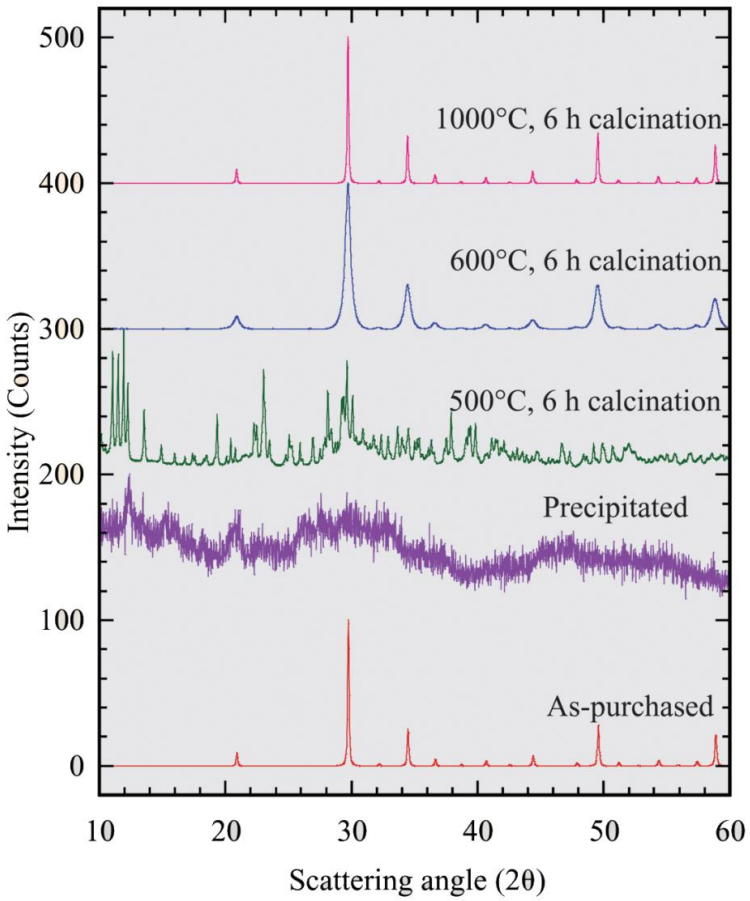

Figure 74: X-ray diffraction data of calcined Lu_2O_3 powders formed from chemical co-precipitation.

The precipitated nitrate precursor shows very little crystallinity, as-dried. With increasing calcination temperature, the peaks approach the XRD spectra given from the initial commercial powder used. At 500°C, the calcined powder is clearly not fully returned to its initial oxide state. At 600°C and up, the peaks match the commercial XRD pattern perfectly. One result that was motivating about the success of this process was the apparent peak-broadening of the Lu_2O_3 diffraction given for the samples calcined at 600°C. According to the Scherrer equation, this suggests that successful nanoparticle synthesis had been achieved through this method. The equation states

$$\tau = \frac{K\lambda}{\beta \cos \theta} \tag{40}$$

where τ is the average crystal (grain) size, K is the shape factor, with a value close to unity (usually 0.9), λ is the wavelength of the x-rays used, β is the full width at half maximum as a metric of the broadening of the diffraction peaks, and θ is the Bragg angle. After heat treating at 1000°C, the peaks again become notably narrow, nearly matching those of the commercial powder; this potentially indicates a pre-sintering effect at this temperature had coarsened the particles out of nano-scale dimensions. 600°C was thus decided on as the calcination temperature for sintering samples from precipitated powders.

Confirmation of nano-particle synthesis was attempted to be confirmed via SEM. However, the extent of agglomeration upon drying and calcining made this difficult. While the resultant oxide retrieved from the calcination crucible was manually crushed with a mortar and pestle, the extent of agglomeration still present in the samples became readily apparent once viewed under the microscope. Agglomerates as large as 50 μm were identified, much larger than those even present in the commercial powder as-received. Due to what was learned from previous results, the sinterability of these powders was immediately put into question. Further beneficiation of the powder was going to be necessary before attempting to sinter these agglomerates. The extent of agglomeration is given in Figure 75.

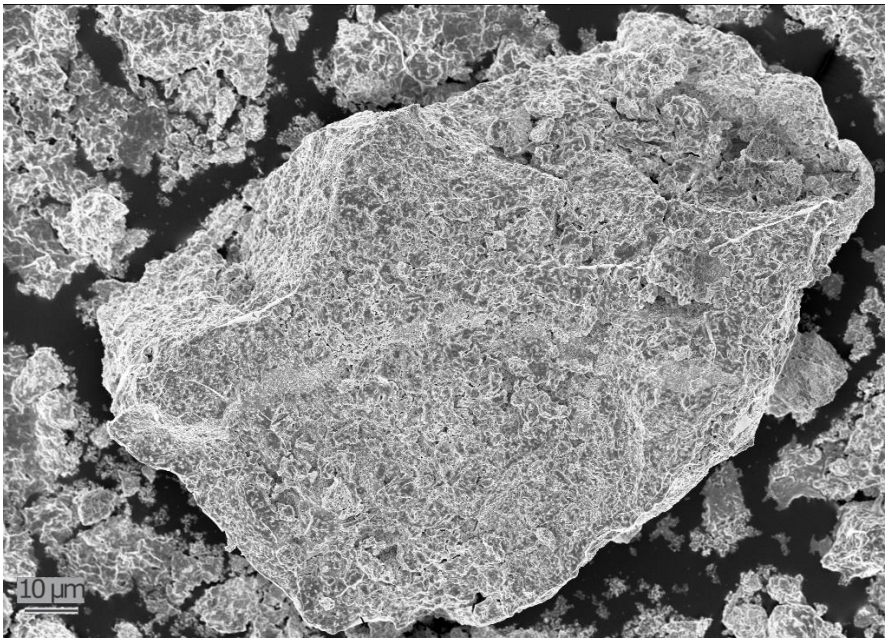

Figure 75: A Lu_2O_3 powder agglomerate post-calcination at 600°C. Sub-micron particles become packed into very large agglomerates not favorable to sintering.

In order to more evenly break up agglomerates of the calcined powder, samples were wet milled with both B_4C and WC. The high hardness of these materials compared to that of Lu_2O_3 made them appear as good candidates for easily crushing the packed particles without an extended milling duration. The B_4C and WC milling batches were processed identically as described earlier and SEM micrographs were taken from droplet samples of the slurry once milled for ~100 h. The resulting images show highly effective crushing of the large agglomerates, as apparent in Figure 76. Milling with the WC media seemed to be slightly more effective, but both methods reduced the agglomeration and resulted in particles well under 1 µm. However, once dried, both milled slurries were highly discolored, with impurities from the milling media coating the crushed particles.

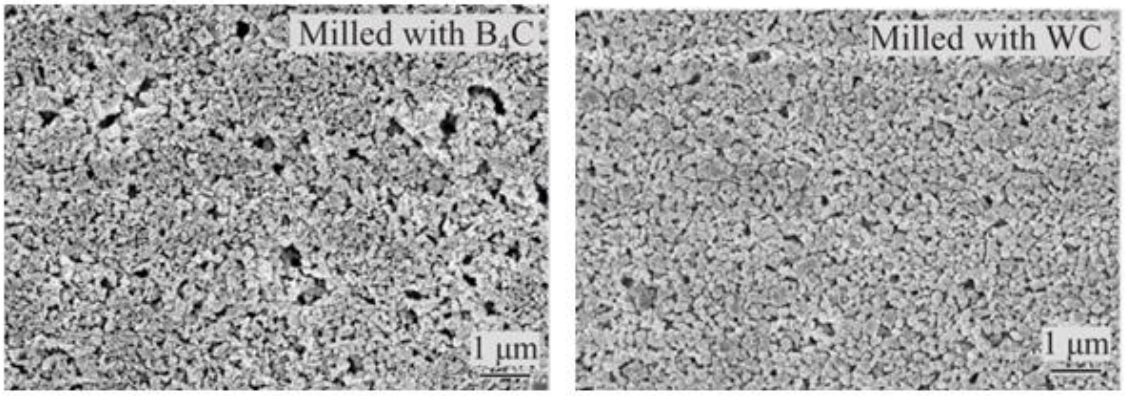

Figure 76: SEM micrographs showing highly reduced particle size after milling with either B_4C or WC.

To analyze the extent of contamination from the milling process, the dried milled powder was analyzed via x-ray diffraction and compared to the commercial powder. To attempt to recover from the impurities that presented themselves from the milling, the B_4C milled powder was again heat treated in air to oxidize via the reaction:

$$B_4C_{(s)} + 4O_{2(g)} \rightarrow 2B_2O_{3(s)} + CO_{2(g)}$$

and then washed in methanol in an attempt to remove the boron oxide from the samples. Methanol was expected to dissolve the boria and form a volatile gas phase via the reaction

$$B_2O_{3(s)} + 6CH_3OH_{(l)} = 2BO_3(CH_3)_{3(g)} + 3H_2O_{(l)}$$

in which the volatile component would evaporate away. However, this ended up proving to be unsuccessful, as the washed powder would end up reagglomerating slightly upon again drying in a warming oven, and thus needed to be re-crushed via mortar and pestle before pressing into powder compacts. Historically, work done using this washing meth-

od also involved many repetitions of the methanol rinse and gas volatilization, indicating that is would be very difficult to adequately remove the boron-oxide impurity entirely. A test sample of the washed B_4C milled powder ended up highly darkened and clearly of very poor purity. While further tests of contaminant removal were tentatively planned, it became clear that a cleaner particle size reduction method would have to be discovered. XRD spectra of the two milled batches is given in Figure 77.

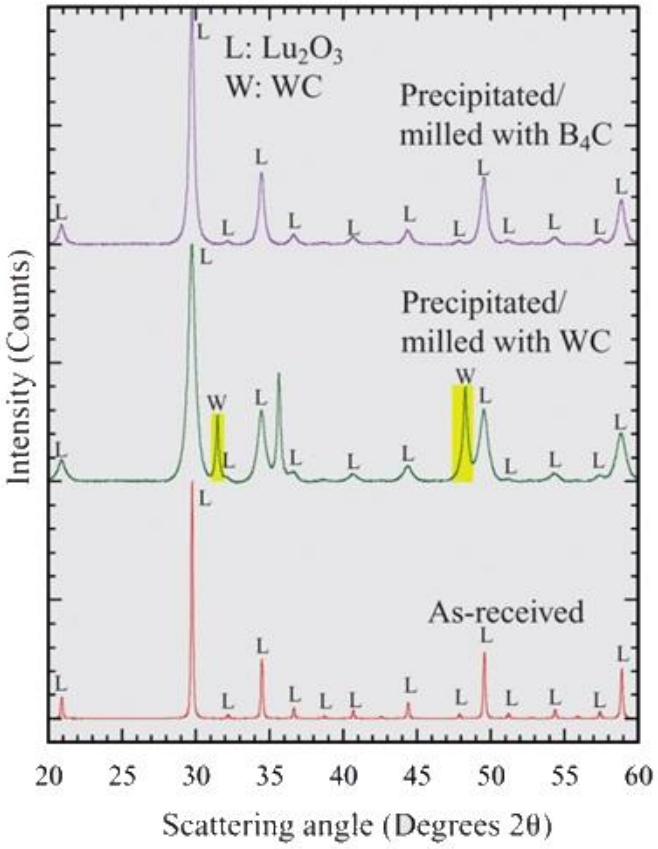

Figure 77: X-ray diffraction data of precipitated Lu_2O_3 powders after ~100h milling with B4C (oxidized and methanol washed) and WC media.

Both milling with B_4C and WC resulted in maintaining the degree of peak broadening present from precipitated powders, compared to the narrow peaks of the as-received

powders. However, WC impurities were highly present after the extended milling duration. While the methanol wash attempt of the B_4C milled powder seemed initially successful due to the lack of impurity phases present in the accompanying XRD spectra, the poor sintering result of this powder suggests that remnant B_2O_3 was present in the sample, but was not obvious due to its similar white coloration of Lu_2O_3 and its amorphous nature making it undetectable in the diffractometer.

Because of the negative results of milling the precipitated powder agglomerates, sintering tests were performed using hand-crushed calcined powders via a mortar and pestle. The results are given in Figure 78.

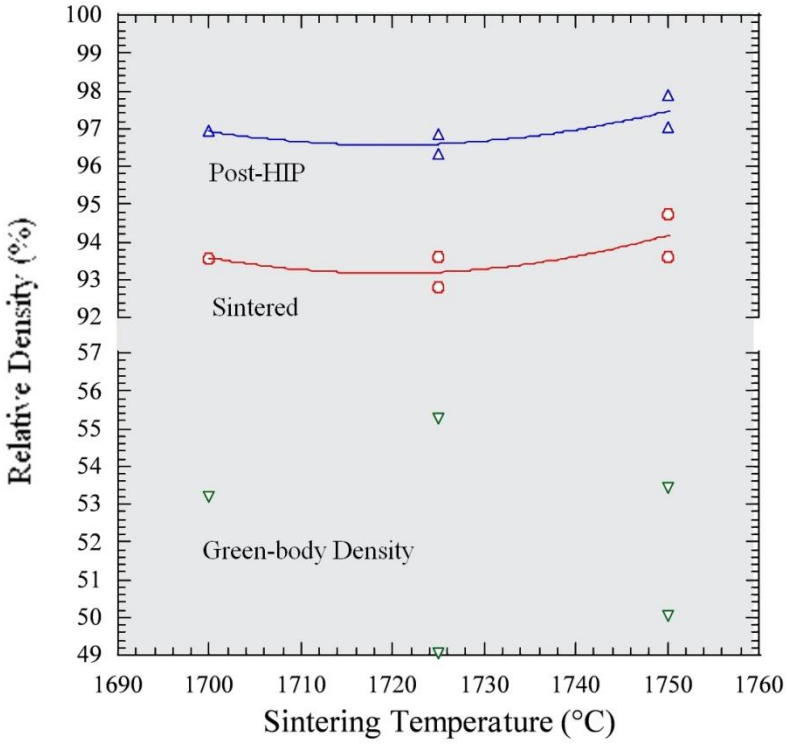

Figure 78: Density results of sintered samples (4 h hold) formed from crushed precipitated Lu_2O_3 powders. Remnant agglomeration led to low and erratic green-body densities and poor post-HIP results (1700°C 2 h).

While green body relative densities of as-received powders typically averaged about ~58%, the same values for those pressed from these precipitated powders is ~5% lower, indicating relatively poor packing of the particle agglomerates post-calcination. While sintered densities were generally good compared to the elevated temperatures required for the as-received powders, post-HIP densities at the same schedule failed to achieve anything near theoretical density. Samples were very opaque and spotty. Due to the difficulty of processing the precipitated powders as well as these poor sintering results, co-precipitation of Lu_2O_3 was dropped from consideration as the particle size reduction method for the production of these ceramics. An additional consideration that led to this decision was the throughput issue of the co-precipitation methodology that made this process unsuitable to scale-up; hand crushing of calcined precipitate powders becomes increasingly costly with larger batch sizes.

A potentially more suitable process for the breaking of the large agglomerates present in the as-received powder was the use of a sonication probe on aqueous suspensions of Alfa and HEFA powders. While this was not expected to reduce the minimum particle size of the as-received powders, the goal was to break apart the macro-particle agglomerates without exposing the entire slurry to a contaminating milling media. While dried powders from the sonicated slurry still needed to be crushed via mortar and pestle, the presence of large particle agglomerates seemed highly reduced compared to those produced from calcined powders from the co-precipitation process. Without an elevated temperature calcination step required, only minor re-agglomeration of dried powder from aqueous suspension was observed. Powder compacts formed from this process were high-

ly improved compared to the co-precipitation process as well, averaging much greater than 60% relative density. Results of the attempts to sinter these compacts formed from sonication powders is shown in Figure 79.

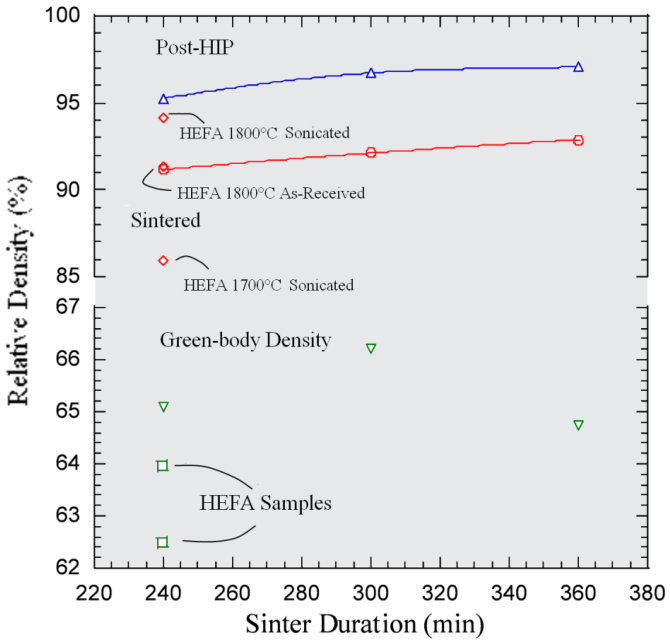

Figure 79: Relative density results from 1700°C sintering of Alfa Aesar (second lot) and 1700-1800°C sintering of HEFA (marked on plot independent of Alfa Aesar) powders after ~15 min of sonication using a Ti alloy probe. Post-HIP performed at 1700°C for 2 h. Sonication of powders improved green relative densities as well as sintered density values, but post-HIP density values still far too low for achieving transparency. HEFA powders still required elevated temperatures for appropriate sintered density values.

Alfa powders formed from this method sintered to very similar densities as before. Increasing the sintering duration to attempt to bump up the as-sintered relative density without exposing the sample to the elevated furnace temperature did trend to appropriately higher values, but none of these samples came close to HIPing to suitable densities at the same HIP schedule. HEFA samples formed from this method required 1800°C sintering temperatures in order to exceed even 90% relative density after a 4 h dwell. The

HEFA samples were not HIPed due to the extent of coloration present from their elevated temperature processing.

However, the sonication of Y_2O_3 powders in this way was markedly more successful. While the as-received agglomeration of commercial Y_2O_3 powders was highly similar to those of commercial Lu_2O_3 powders (shown later in Figure 92), the sintered densities of sonicated Y_2O_3 reached very high relative densities (compared to Lu_2O_3) even with very short sinter durations. One key difference is that the sonication here was also responsible for the compositional mixing of ZrO_2 and Y_2O_3 powders, where only undoped Lu_2O_3 was evaluated otherwise. This was done since literature suggests the high importance of ZrO_2 content for sintering Y_2O_3 ceramics to high relative density and transparency. Sintering results of 5-9 mol% ZrO_2-Y_2O_3 is provided in Figure 80.

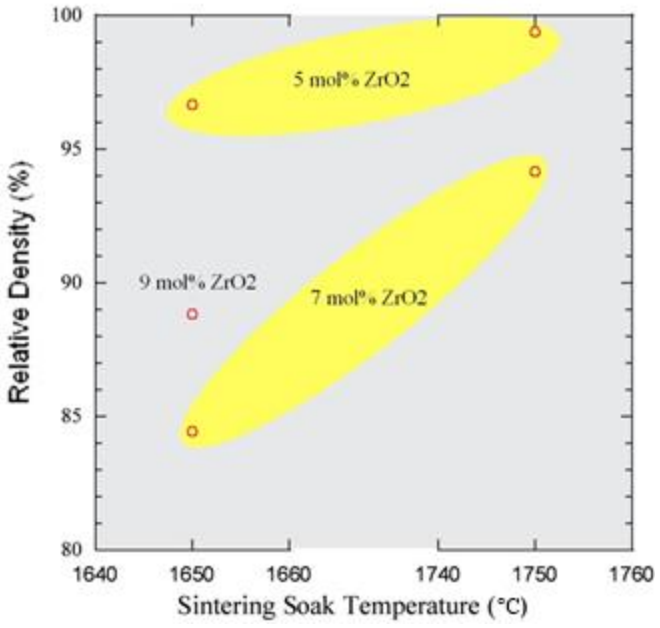

Figure 80: Density results of sonicated Y_2O_3 ceramics after sintering for 2 h. 5 mol% ZrO_2 additives show clear improvement over higher zirconia amounts, even reaching close to theoretical density without HIPing.

Samples sintered from sonicated Y_2O_3 powder batches show that ZrO_2 content greater than 5 mol% was highly damaging to the sintered relative densities of these specimens, which is consistent with the literature. 5 mol% ZrO_2-Y_2O_3 samples sintered at 1750°C even exceeded 99% relative density, much higher than any sintered density result from Lu_2O_3 powders. While samples of greater than 5 mol% ZrO_2 content did suggest a high degree of temperature dependence on sintered relative density, the extent to which 5 mol% outperformed these suggested that the sintering schedule be optimized with that content fixed. Further sintering results of 5 mol% ZrO_2-Y_2O_3 are summarized in Figure 81.

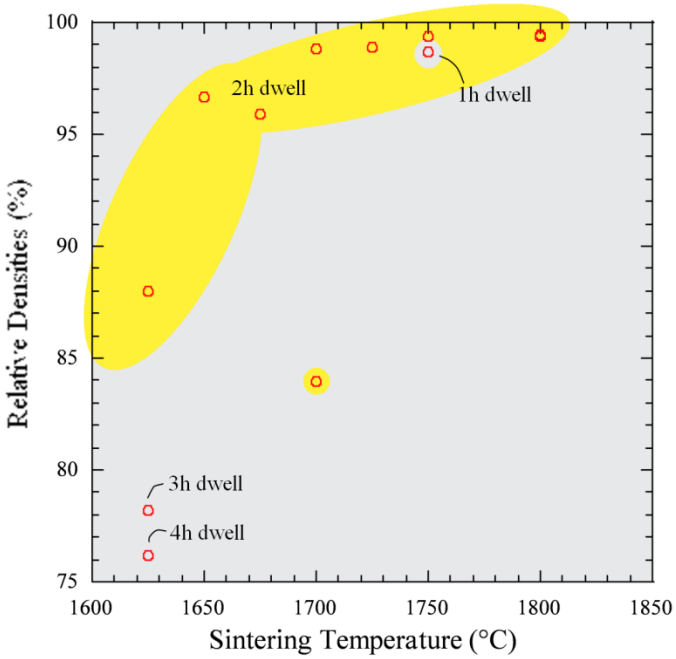

Figure 81: Density results of sonicated 5 mol% ZrO_2-Y_2O_3 samples, showing that samples quickly reach very high relative densities even with very short dwell durations.

5 mol% ZrO_2-Y_2O_3 appears to be highly sensitive to both the sinter soak temperature as well as the dwell duration at lower sintering schedules. However, past 1700°C, the relative densities all approach near theoretical values even for a sinter soak duration as low as 1 h. While the likelihood of easily achieving high relative densities is promising, there was also a slight erratic nature to the results shown. This includes the noted damaging results to sintering beyond 2 h at low temperatures, as well as a lot of variability in the sintered density for two samples processed in the same manner. This is likely due to inhomogeneities remaining in the sonicated powder, or potentially from sonication impurities present from the Ti alloy probe. For the best results achieved, though, samples did manage to arrive at the onset of transparency for sintering temperatures as low at 1650°C and only HIPing at 1600°C. Initial promising results of achieving transparency with Y_2O_3 samples are shown in Figure 82.

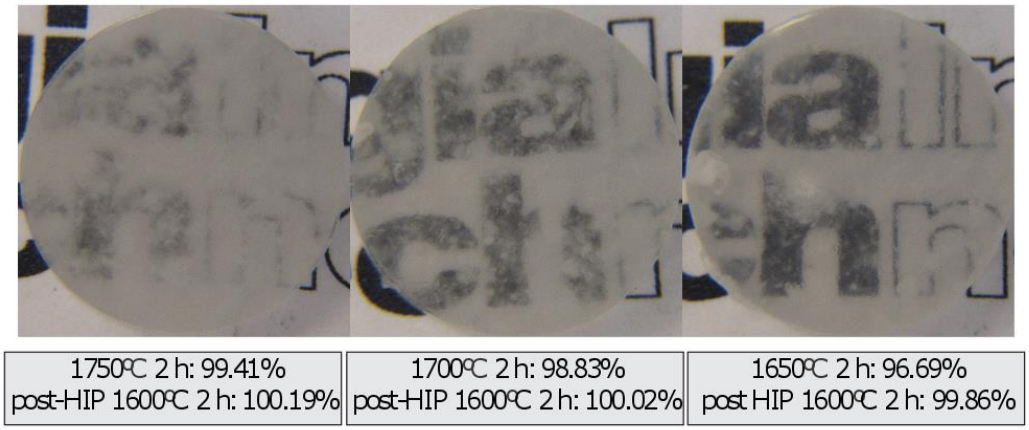

Figure 82: Initial 5% ZrO_2-Y_2O_3 samples using sonicated aqueous slurry.

As with earlier results regarding Lu_2O_3 specimens, the lowest sintering temperature able to be HIPed up to theoretical density seems to give the best result with respect to trans-

parency, even though the HIPed relative densities of all three samples is near the theoretical limit at similar values. Unlike Lu_2O_3, however, the hazy white fog is less uniform and is discreetly located within spotted sections of the samples. This suggests that inhomogeneities either in remnant porosity or deposition locations furnace-induced carbon impurities are caused by the sonication process compared to sintering of as-received powder, though a direct comparison for sintering of as-received Y_2O_3 based ceramics is not present.

Sedimentation would be a way to only sinter the smallest commercial agglomerates without any possible impurities from milling media or a sonication probe. Due to the low yield expected from sediment powders, due to removal of agglomerates of larger than 2 μm, only HEFA powder was tested for this study, due to the relative low cost compared to powder from Alfa Aesar. It was understood when initiating this study that this would not break up any of the commercial agglomerates into the smaller submicron particles that comprised them, but it was hopeful that this would get the powders to behave more similarly to the first powder lot, where the degree of initial agglomeration did not prevent samples from sintering to transparency. However, having to dry the sediment powders from their aqueous suspension from the sedimentation column in a warming over induced the same type of agglomeration that had hurt the samples from sonication experiments, where the dried powder retrieved from the oven was found with a greater extent of re-agglomeration than expected. The results are shown in Figure 83.

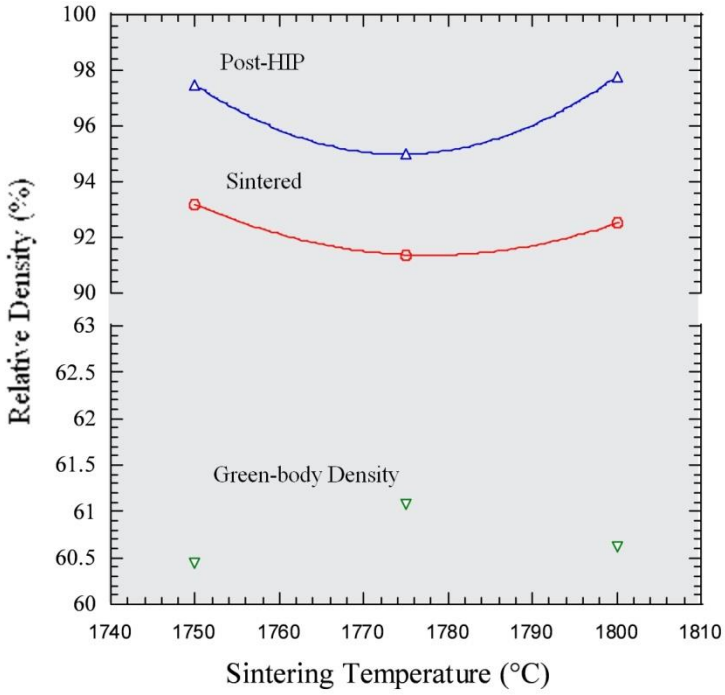

Figure 83: Density results of HEFA powder specimens sintered (4 h) after undergoing sedimentation. No real improvement was noticed over as-received HEFA powder, indicating that the extent of agglomeration was too high for filtering out large agglomerates to be effective.

The sediment HEFA powder did not sinter much differently than the commercial as-received powder, and increasing temperature of the sintering dwell did not yield improved relative density. Likely, the lack of improvement from the base commercial powder is due to the ineffectiveness of sedimentation with respect to a flocculated suspension of powder agglomerates; that is, the particles would have to be broken out of their agglomerated clumps in order for Stokes' law to effectively apply. It is also likely that the chosen target agglomerate size of 2 μm was still too large relative to the sub-micron particles that comprised the powder agglomerates. Poor yield and long time periods required

for further sedimentation tests meant that it was not a good candidate for processing the commercial powder for improved sintering results.

The negative results from chemical co-precipitation, sonication, and sedimentation suggested that for Lu_2O_3 powders, the agglomerated extent of the commercial powders was the chief hindrance to successful sintering results. The previous best-result method for removing the agglomerates from the as-received powders was the milling tests regarding the calcined powder precipitates. Thus, milling was revisited as the candidate method, only it was apparent a better milling media would be needed to prevent a high degree of contamination from the milling jar. Both a toll jet milling service and a new attempt at ball milling of the oxide powders were evaluated.

Unfortunately, this attempt at jet milling was not a success because the material simply would not mill appropriately. The oxide powder ended up recirculating in the mill for approximately 1 h and not enough material exited the mill to appropriately measure any resulting particle size. The small amount of milled powder recovered appeared coarse to the eye. The mill interior was carefully cleaned out in order to recover as much of the powder material as possible, and it was noted upon cleaning that most of the build-up was in the mill body. Roughly 70 g of powder remained in the mill, with other powder deposits found in the classifier and the cyclone. It appeared that the impact of the material with itself caused clumping and stickiness, potentially due to both the agglomerated nature of the commercial as-received powder, as well as the hygroscopic nature of Lu_2O_3; successful jet milling of this oxide could require a pre-processed powder either through chemical co-precipitation or some other method, but this result suggested that jet milling as a substitute for such processes was not something that was worth investigating further.

Previous results showed a high degree of contamination from milling with B_4C and WC media. Milling with ZrO_2 media was tested since zirconia has been successfully used as a grain-growth inhibitor in producing transparent oxide ceramics in the literature, and thus it was hopeful that a potential impurity of this material would not be as detrimental to the fabrication of ceramics media from this powder as the non-oxide media contaminants. ZrO_2 also is a great match for producing ZrO_2-Y_2O_3 ceramics since the extent of contamination possible there would not change the composition of the powders retrieved from the mill. Similarly, using Lu_2O_3 material as the crushing media for the Lu_2O_3 powder milling process would be a way to prevent contamination of any sort for that process, but the lack of available commercial Lu_2O_3 ceramics and the relative high cost of producing custom Lu_2O_3 media compared to inexpensive and relatively available ZrO_2 made that option not viable. Figure 84 shows the initial results of ball milling the commercial HEFA powder for an extended duration in a 50 wt% aqueous slurry.

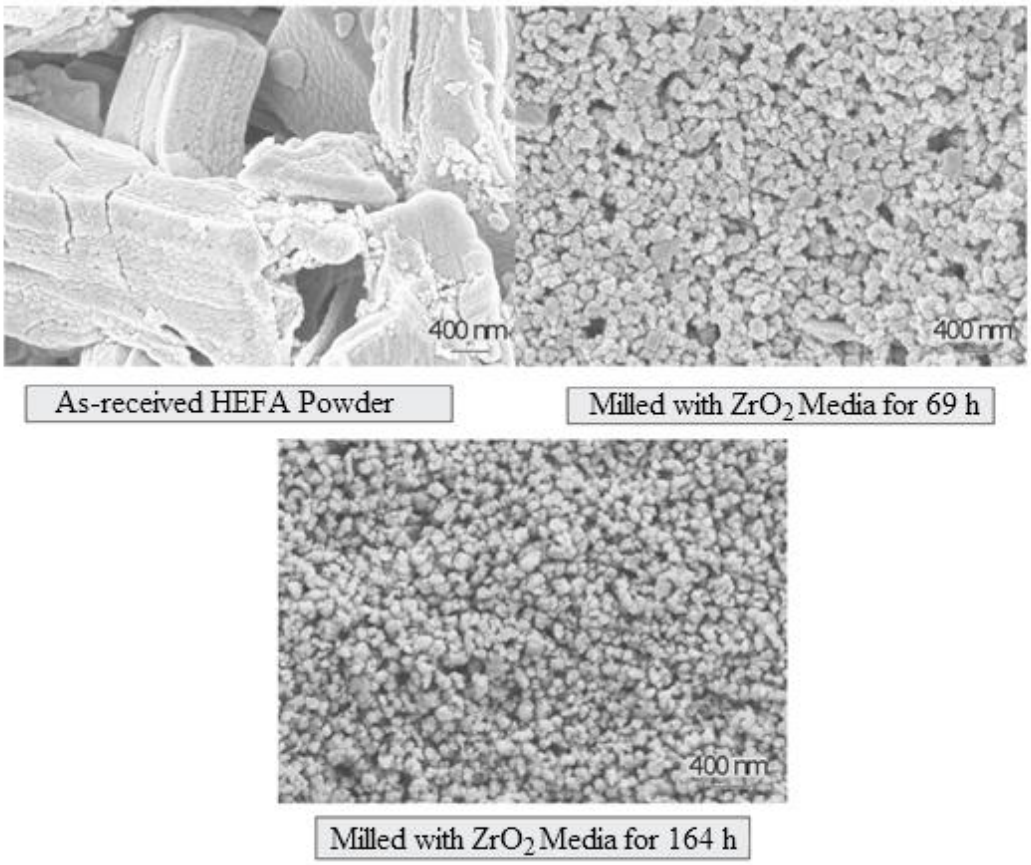

Figure 84: Comparison of as-received and ball milled Lu_2O_3 (HEFA) powder, showing great improvement in the degree of agglomeration. Diminishing returns in size reduction identified past ~72 h.

It is evident, as before with the other media experiment, that ball milling of the commercial powder results in a huge reduction on the extent of agglomeration present as-received, reducing the ~4 μm agglomerates into particles of well below 400 nm. A similar result was obtained from milled Y_2O_3 powders (as shown later in Figure 92). The diminishing returns of particle size reduction noted past ~72 h suggested that extended duration on the ball mall would not be highly beneficial. Initial sintering results of Y_2O_3 compacts created from dried milled powder from the mill is given in Figure 85.

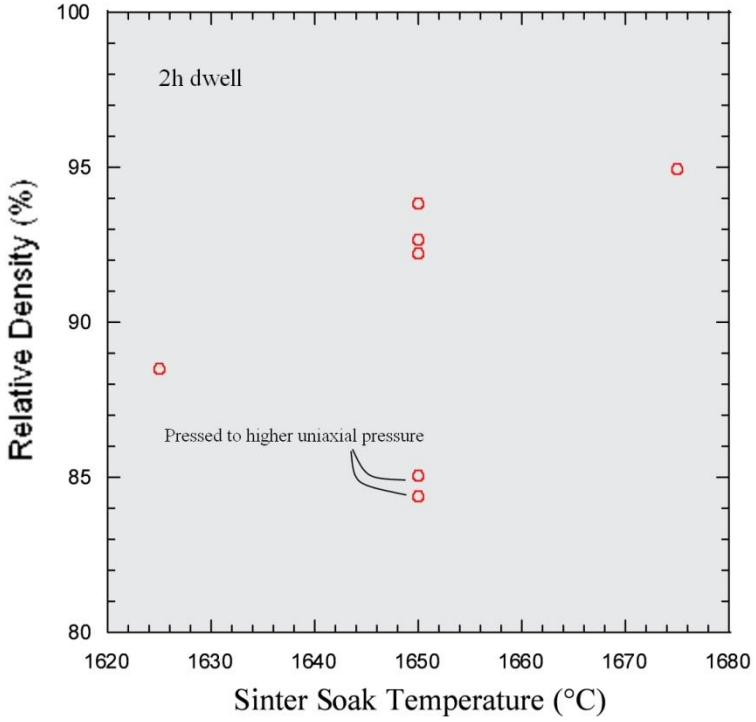

Figure 85: Density results of samples produced from ball milled Y_2O_3 powder. Samples were of very poor quality with a high degree of cracking resulting in relatively low sintered relative densities.

Samples produced from the milled Y_2O_3 powders showed much lower sintered densities compared to sonicated yttria specimens sintered earlier. Samples were highly cracked and the relative density could not be easily measured due to the fragile nature of these specimens. An example of such is given in Figure 86.

Figure 86: Sample formed from milled Y_2O_3 powder shows high degree of cracking, not suitable for HIPing to high relative densities.

Attempts to press the powders with higher uniaxial pressure actually degraded the quality of the sintered samples, likely due to a greater amount of instantaneous springback damaging the already fragile green-body yttria compacts. Efforts to slow the heating and cooling rates of the sintering schedule did not improve any of the sample qualities or prevent the cracking from occurring. While the reasons for the sudden fragility of the oxide compacts is likely multifaceted, it is probable that the compaction of de-agglomerated powders without any pressing additives (other than die lubricant) resulted in compacts not achieving the green strength required to survive the release of the uniaxial load or the ejection from the die. The earlier pressing of agglomerated oxides without pressing additives were likely of sufficient strength to survive the ejection process due to most of the sub micron particles already being strongly bound into relatively large packed agglomerates, as shown in any of the SEM micrographs of the commercial powders. The as-received packed nature of particulates into these agglomerates likely kept the relative density of the compacts sufficiently high for successful sintering as well. However, due to the highly negative results of attempting to sinter the milled Y_2O_3 powders without

pressing additives, no attempt was made to form powder compacts or sinter milled Lu_2O_3 powders produced in the same manner.

It became clear that some sort of pressing additive would now be needed to get green compacts comprised of de-agglomerated powders to press appropriately and improve the green strength of the compacts so that they would be able to survive the springback between being uniaxially pressed and before being CIPed into their final compact density before thermal processing. However, it order to solve the issue of re-agglomeration upon drying, it also became apparent that a non-aqueous wet milling solution as well as a new drying solution of the milled suspension would also need to be implemented. Thus, an identical set of milled suspensions was produced using acetone and PMMA binder. Instead of drying in a warming oven, the milled suspension was spray dried into granules. To test for the extent of ZrO_2 or YSZ phase contamination from the mill, the spray dried Lu_2O_3 were analyzed via x-ray diffraction with several repetitions of the scan schedule given in Chapter 3 and compared with the ICDD data for ZrO_2 and YSZ crystals. The results are shown in Figure 87. For Lu_2O_3 samples, all acetone-based ball milling and spray drying was performed with the HEFA commercial powder lot.

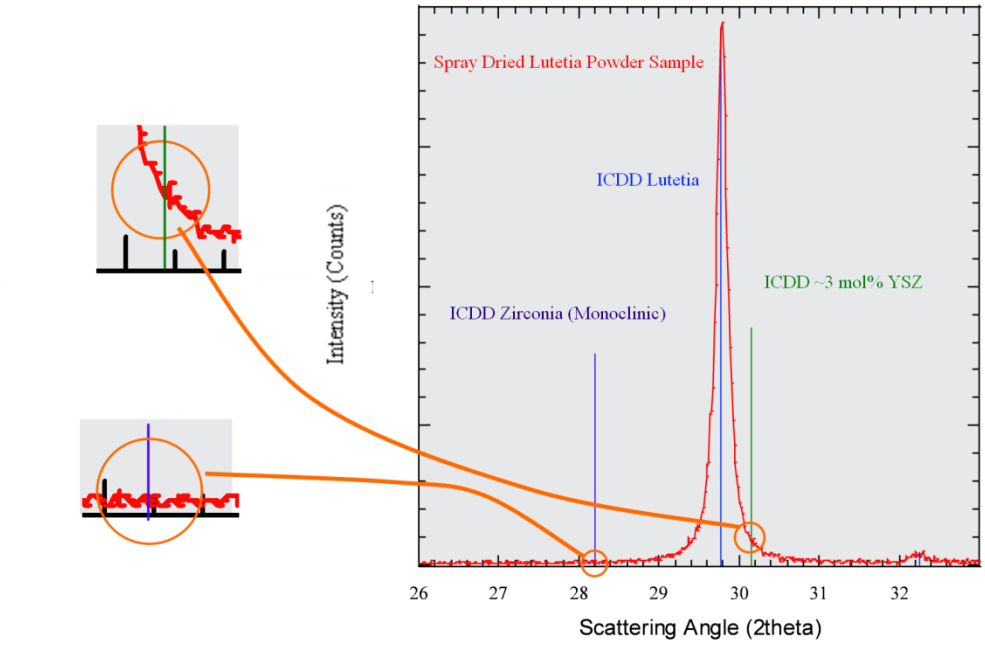

Figure 87: X-ray diffraction analysis shows no ZrO_2 contamination of Lu_2O_3 spray dried powders formed from ball milling Lu_2O_3 agglomerated powder using ZrO_2 media. Height of the vertical ICDD data lines is arbitrary, due to the different files being normalized to different peak values.

The primary ICDD peak of ZrO_2 at ~28.18° as well as the primary peak of YSZ at ~30.15° are not present in the sample of Lu_2O_3 granules, and no other extraneous peaks were identified in the spray dried powder, indicating no discreet phase contaminants present. A similar test was done with ZrO_2-Y_2O_3 ceramics. Note that since both the milling media used in the ball mill as well as the ZrO_2 additives to the yttria powder are in the form of 3 mol% YSZ, a sintered and polished sample needed to be used to test for phase purity, since otherwise the matching diffraction pattern of the ZrO_2 media and the ZrO_2 powder added as a grain growth inhibitor would overlap. So the focus of this was less to confirm the lack of mill contamination (which is impossible due to the matched batch and

mill materials), but rather to confirm phase purity after HIPing. The result is shown in Figure 88.

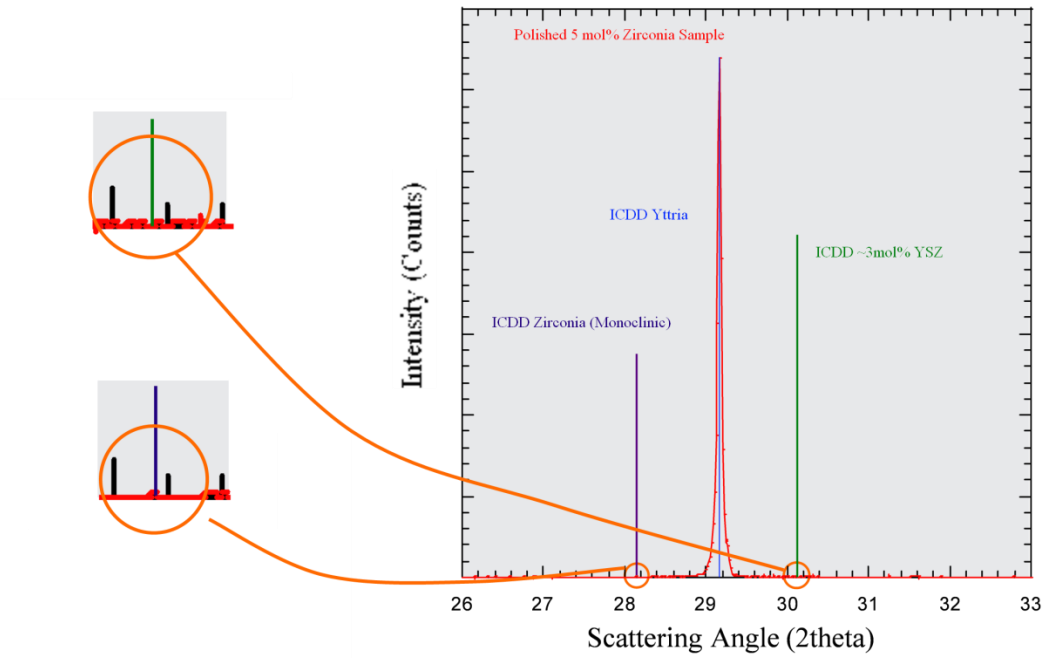

Figure 88: 5 mol% ZrO_2-Y_2O_3 ceramic shows no extent of ZrO_2 phase present, indicating all zirconia from both initial mixture and potentially the ball mill media are in solution with Y_2O_3 matrix. Height of the vertical ICDD data lines is arbitrary, due to the different files being normalize to different peak values.

The extinguishing of either zirconia peak (monoclinic or tetragonal) in the final sample suggests that all ZrO_2 content, both added from commercial powder or possibly from the milling process, goes into solid solution with the Y_2O_3 matrix, which is necessary for obtaining optical transparency, due to the scattering that remnant phase boundaries would induce.

To confirm the successful processing of spray dried granules, samples were analyzed via SEM. An example Lu_2O_3 granule is shown in Figure 89, and granules for Y_2O_3 sam-

ples are shown in Figure 92. While a small portion of granules show some damage, most are of good quality, without large voids in the interior of the spheres, which would have indicated the formation of vapor bubbles during the drying process. Granules appear to vary from 5-50 μm.

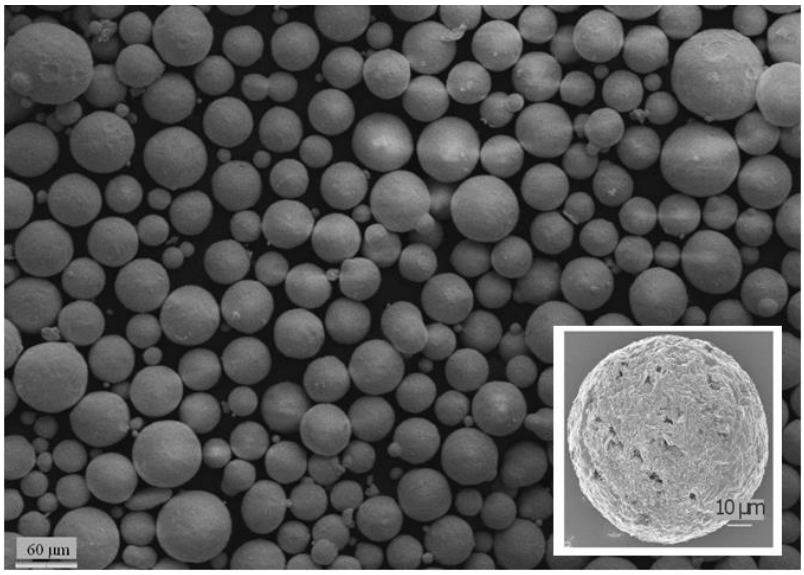

Figure 89: Example Lu_2O_3 spherical granules formed from spray drying a ball milled Lu_2O_3 acetone slurry.

Lu_2O_3 compacts pressed and CIPed from spray dried powders did not show the same fragility and cracking issues present from the milled Y_2O_3 powders (without spray drying). Green densities of the powder compacts averaged around 59%, roughly the same as those produced from as-received commercial powders, but higher than those from milled powders dried in a warming oven, which was ~55%. After undergoing thermolysis to remove the PMMA binder content from the Lu_2O_3 compacts formed with the spray dried powder, they were sintered and HIPed to the results shown in Figure 90.

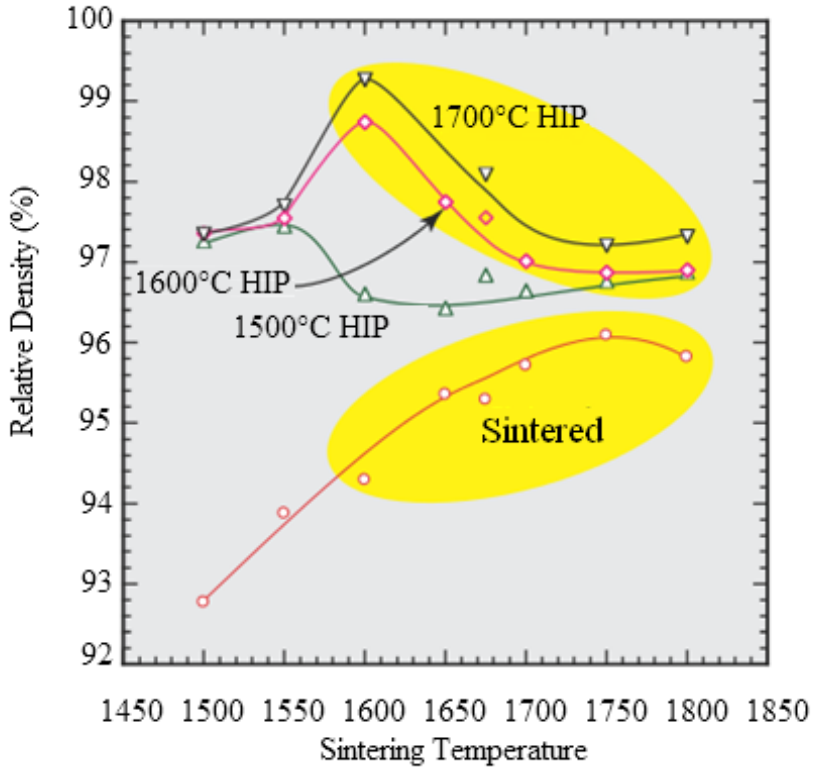

Figure 90: Initial sintering results (4 h) of spray dried Lu_2O_3 powders, showing 1600°C as new optimal sintering temperature. Only marginal improvement shown from increasing the HIP temperature from 1600°C to 1700°C (2 h).

Sintered densities at relatively lower temperatures between 1500-1700°C are greatly improved compared to previous sintering attempts using commercial or otherwise processed oxide powders. Increasing the sintering temperature past 1600°C is shown to be detrimental to the final relative densities of the samples upon HIPing. A greater degree of improvement is observed by increasing the HIP temperature from 1500°C to 1600°C compared to the elevated 1700°C process. Due to the increased coloration seen from elevated temperature HIPing, from this point, an extended HIP duration of 4 h was identified as a solution to further densifying the ceramic samples, rather than increasing the temperature past 1600°C.

Evaluation of the porosity profile of the sintered ceramics gave insight as to why 1600°C was identified as the optimal sinter soak temperature before HIPing the ceramic samples. Information about the porosity of these samples is given in Figure 91.

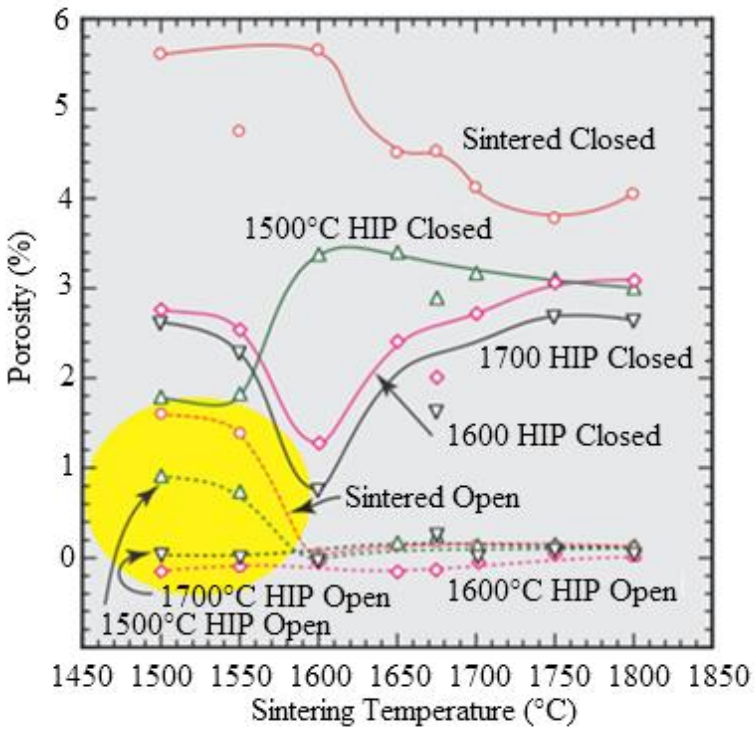

Figure 91: Porosity results of sintered Lu_2O_3 specimens formed using spray dried powders. 1600°C is shown as the limit of achieving a state of closed porosity.

Sintering below 1600°C is shown to allow the samples to maintain a small level of open porosity of 1-2%, or roughly a quarter of the remnant porosity of the samples remaining open. This explains the ineffectiveness of HIPing samples sintered at these lower temperatures, due to the argon gas being able to pressurize within these open pores, preventing densification. However, at 1600°C and beyond, the extent of open porosity within the

samples is effectively zero, and remains this way upon HIPing. While the extent of closed HIP porosity is minimized at 1600°C, the closed porosity of sintering past 1600°C continues to trend downward. However, the lack of improvement noted by sintering or HIPing beyond this temperature suggests that remnant porosity, though closed, is of an arrangement where it cannot be eliminated during the HIP process. Thus, it is reinforced that a sintered state of maximum density is not necessarily of the optimal microstructure necessary for being able to HIP to highest relative density. Instead, the extent of closed porosity should be reached without far exceeding this point in order to minimize both grain growth and the accompanying sweeping of coarsened pores into the grain interiors. However, HIPed densities of these samples still only achieved a state of translucency rather than transparency, likely due to the relative densities only just exceeding 99%, rather than beyond 99.5% or higher as in the initial study of transparent ceramics formed from commercial Lu_2O_3 powders. However, these densities along with the translucent resulting samples were still much improved compared to any other evaluated methodology of ceramic processing and sintering schedule, giving an avenue forward for eventually achieving transparency.

Despite this promising initial result for Lu_2O_3 ceramics, Y_2O_3 ceramics appeared to display much different sintering behavior after being milled and spray dried. The milling of Y_2O_3 powders was similarly successful at breaking up of powder agglomerates from the as-received commercial source, as identified via SEM. Spray dried powders formed from milled Y_2O_3 suspension were of similar size and quality as Lu_2O_3 samples. Comparison of powder agglomerates before and after milling, as well as the spray dried granules

of Y_2O_3 powders, are shown in Figure 92. A similar point of diminishing returns in particle/agglomerate size reduction is shown past ~72 h.

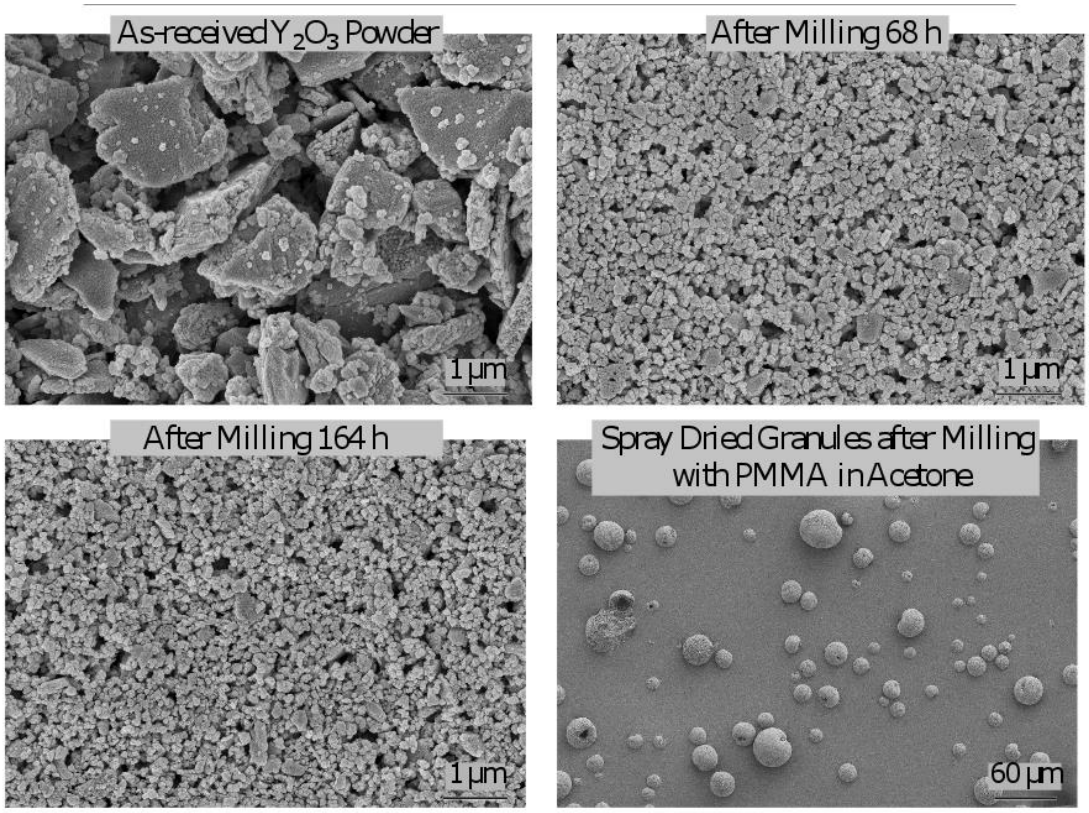

Figure 92: Progression of Y_2O_3 powder, from as-received commercial agglomerates to spray dried granules after milling for ~72 h.

As with the initial results of sonicated Y_2O_3, sintered relative densities of Y_2O_3 samples formed from spray dried powders showed the capability to reach high sintered densities even with sinter durations as short as 2 h. However, the sinter soak temperature required to reach these densities was slightly elevated compared to those of the sonicated powder. The high degree of dependence on sinter duration on sintered relative density remained.

A summary of the initial sintering results of Y_2O_3 samples formed after spray drying is shown in Table 4.

Table 4: Initial sintering results of spray dried 5 mol% ZrO_2-Y_2O_3. While samples were not of good quality, high sintered densities were identified with high dependence on sinter duration.

Sample	First Sintering	Second Sintering	HIP				
			1450 2h	1500 2h	1550 2h	1600 2h	1600 2h, 1650 2h
1	1650, 2h: 88.23	1650 4 h: 93.81	97.08	98.83	98.36	N/A	99.08
2	1650, 6h: 96.09	N/A	N/A	99.32	98.77	N/A	99.27
3	1625 6h: 87.36	1650 4h: 93.98	N/A	98.12	98.09	N/A	N/A
4	1650, 4h: 93.60	N/A	N/A	N/A	96.75	N/A	N/A
5	1650, 5h: 94.98	N/A	N/A	N/A	97.87	N/A	98.31
6	1650 2h, 1625 3h: 89.99	N/A	N/A	N/A	N/A	N/A	N/A
7	1700 2h: 97.79	N/A	N/A	N/A	N/A	99.38	N/A
8	1700 4h: 99.08	N/A	N/A	N/A	N/A	99.64	N/A

Unlike Lu_2O_3 samples, which seem to show a plateau of sintered densities where increasing the sintering duration is relatively ineffective at increasing the relative density, Y_2O_3 samples achieved sintered densities as high as 99% by simply increasing the duration of the sintering step. Also unlike Lu_2O_3, the relative densities of HIPed ZrO_2-Y_2O_3 samples seemed to only improve with increased sintered density. This suggests a lower propensity of Y_2O_3 ceramic to sweep pores into the grains, maintaining a favorable microstructure for samples to be successfully HIPed. This was most readily apparent with samples 7 and 8 in the table above, where increasing the sintered relative density by increasing the duration of the sinter resulted with a higher HIPed relative density at the same schedule. A subsequent set of samples was sintered beyond 6 h in this temperature range to test the extent of this behavior. The results are given in Figure 93.

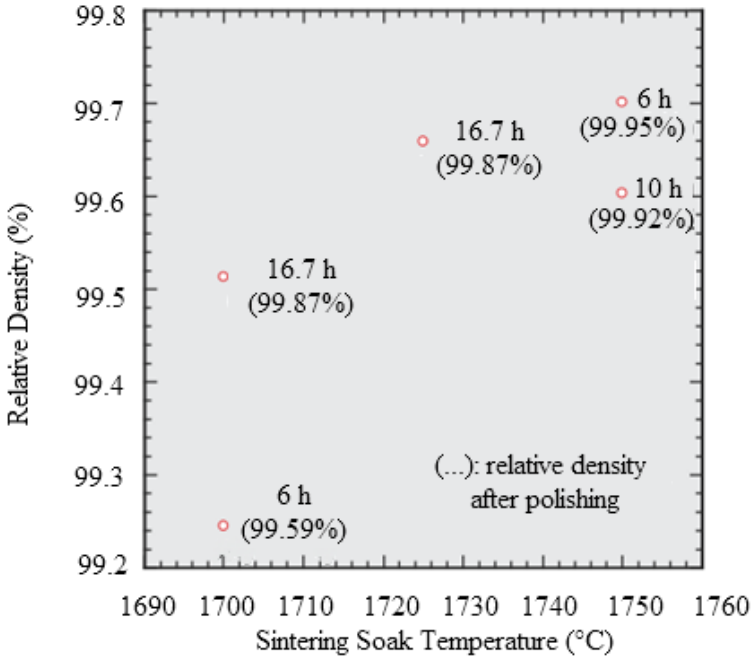

Figure 93: Relative density of HIPed (1600°C, 2 h) and polished 5% ZrO_2-Y_2O_3 after extended duration sintering.

Sintered relative densities of as high as 99.7% were achieved by this increase in sintering duration. However, the extended time within the graphite element sintering furnace did increase the level of coloration noted upon retrieving the samples from the furnace. Fortunately, the annealing schedule used to remove the coloration did not need to be adjusted, resulting in translucent samples post-anneal. The notable aspect of this result was the direct comparison of achieving translucency from sintered samples of Y_2O_3 without HIPing, where Lu_2O_3 samples required the HIP process in order to approach similar relative density values. To achieve the final transparent state of these samples, the translucent yttria specimens were HIPed at 1600°C, reannealed, and finally polished. The progressing

from sintered bodied to polished specimen is given in Figure 94 for the extended duration sample sintered at 1725°C.

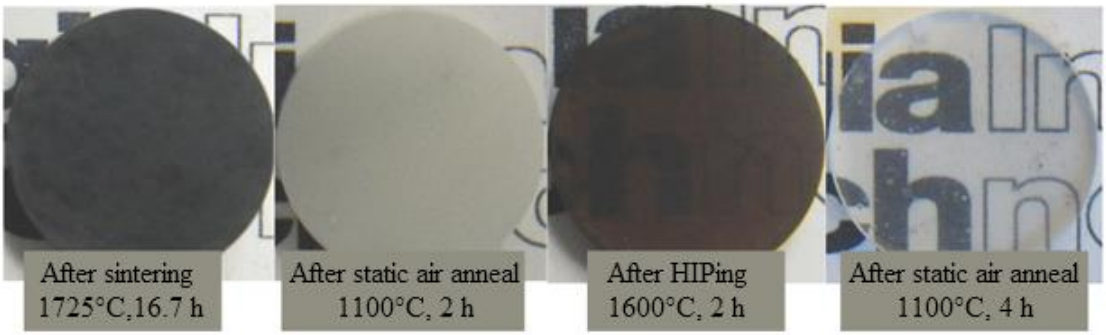

Figure 94: Progression of 5 mol% ZrO_2-Y_2O_3 samples showing vacancy-induced coloration, subsequent air annealing to translucent state, post-HIP transparency and final anneal to transparent state.

While the extent of coloration apparent for these samples is higher than what is typically noticed for sintered ceramics in this study, all of the coloration is removed upon each anneal in the presence of static air. The final sample shows a good degree of transparency, though with isolated minor white blemishes. An added improvement from sintering to high relative density before undergoing a HIP step is that it minimizes that grain growth possible, partially due to being able to HIP well below the sintering temperature (1600°C, compared to 1700-1750°C) for the last fraction of a percent of relative density to reach the theoretical limit. The added zirconia content also seems to succeed as a grain growth inhibitor, as designed. A thermally etched optical micrograph of the sample above is shown in Figure 95.

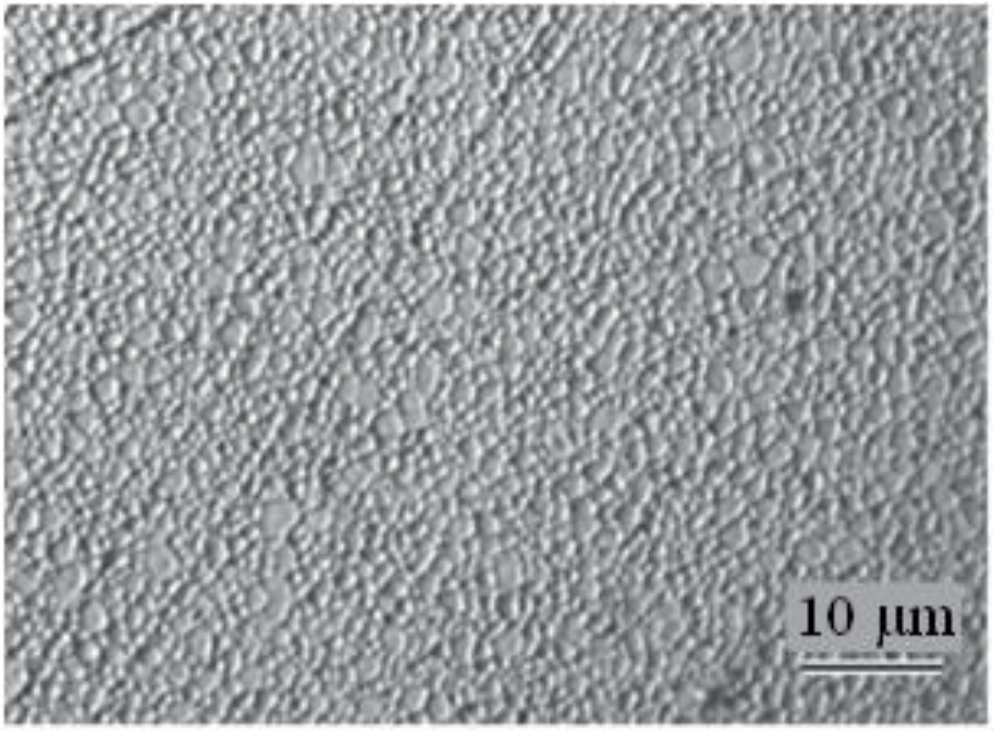

Figure 95: Optical micrograph of 5% ZrO_2-Y_2O_3, thermally etched in HIP, showing a relatively modest extent of grain growth.

Grain size well below 10 μm is noted for these highly dense yttria samples, a huge improvement over the much higher grain sizes for any samples previously fabricated. The sintering behavior of the Y_2O_3 as well as the ZrO_2 content additions are highly likely to both be contributors to this result. The micrograph above shows a nearly entirely pore free microstructure, and the x-ray diffraction results discussed previously suggests an entirely phase-pure sample with respect to ZrO_2 content. This makes identification of the small amount of remaining white specs difficult. Likely, they are either oxidation impurities of carbon content that enters the sample from the graphite element sintering furnace; otherwise they may simply be remnant porosity or discreet phases that are simply below the ability to be determined by density measurements or below the detection limit of the

diffractometer. In any case, while the cause of these white specs needed to be further investigated, a more pressing issue was to achieve a comparible level of transparency from the Lu_2O_3 samples produced from spray dried powders.

4.2.3 Processed Powder Tungsten Element Furnace Sintering Results

To eliminate the potential for carbon based impurities to enter the samples during sintering, a set of experiments was performed in a tungsten element vacuum sintering furnace. Sample processing was otherwise performed identically as in previous experiments. Due to the relative success of sintering Lu_2O_3 samples at 1600°C, that was the chosen temperature for most of the experiments done with the new sintering environment. Some tests were fired at 1500°C for an extended duration as an attempt to reduce sintered grain size without the use of a grain growth inhibitor.

As an initial test, samples were sintered at the chosen 1600°C soak temperature for increasing durations up from 0 h. Despite 1600°C soak temperatures, most all of these samples still showed some extent of open porosity, whereas before, 1600°C was noted as the threshold of removing most of the extent of open pores. While the extent of some open porosity present at low sinter durations is unsurprising, the way in which they manifested was unexpected. SEM micrographs of fracture surfaces of samples sintered for 0-2 h are given in Figure 96.

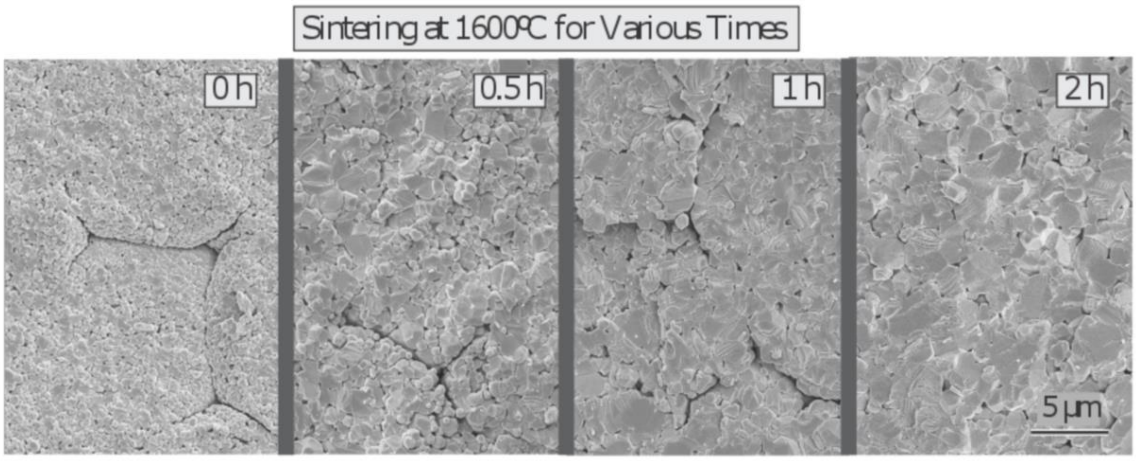

Figure 96: SEM Micrographs of Lu_2O_3 specimens formed with spray dried powder sintered in tungsten element furnace at 1600°C, showing decreasing extent of granule edges with increasing sintering duration, along with accompanying grain growth.

Not only does one see rather large grains relative to the successfully sintered Y_2O_3 samples from earlier, but a propensity for samples to retain characteristics of the spray dried granules remains present, even after sintering for 1 h. This suggests that the spray dried powders were not properly deforming during the compaction process due to being below the glass transition temperature of the PMMA binder. However, one does see the general extent of this series of open channels to be reduced with increased sintering duration. The general reduction of open porosity with increased sintering duration is shown in Figure 97. Note that while the sintered density does increase with increasing duration, the increase remains modest compared to the sort of increase identified with sintered Y_2O_3 ceramics. Not only does this mean that increasing the sinter duration of these Lu_2O_3 samples wouldn't greatly benefit our relative densities, the accompanying grain growth of increasing the sinter duration at this temperature was thought to be too risky due to in-

creased grain size potentially leading to lower quality of the final HIPed samples regarding their transparency.

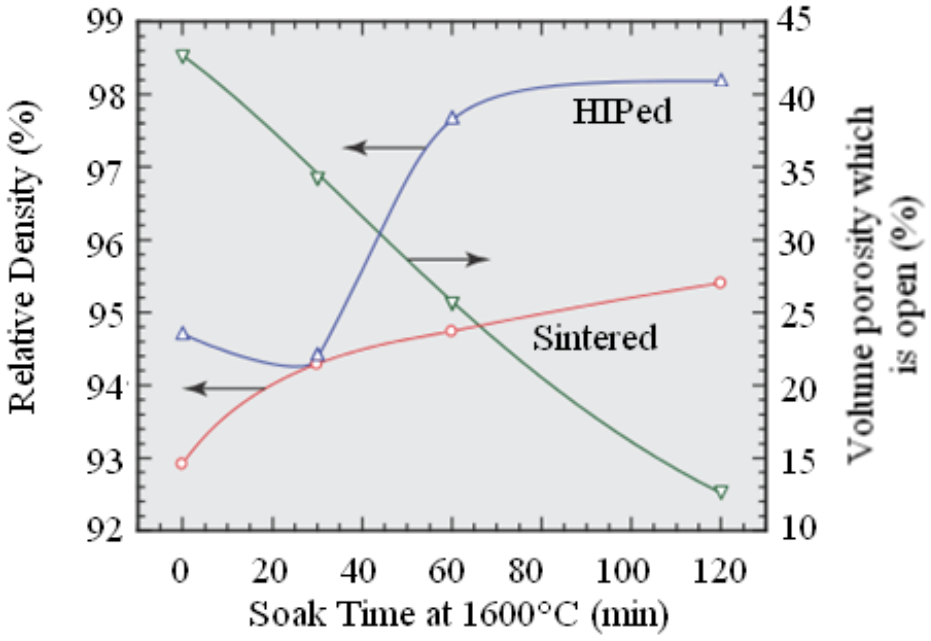

Figure 97: Density and porosity results of initial Lu_2O_3 samples formed using spray dried powders and sintering in tungsten element furnace. Even with extended sinter duration, a detrimental amount of open porosity remained in the samples. Samples were HIPed at 1500°C for 4 h.

One also sees a general improvement in HIPed density with decreasing extent of open porosity, relative to the total remaining porosity, though the final relative density never exceeded 99% so the samples remained opaque. Samples were re-HIPed at 1600°C with negative results, likely due to the repeated release of the argon pressure at elevated temperatures. To try to maintain modest levels of grain growth and match the sinter and HIP temperatures, an extended duration sintering test was done at 1500°C to further analyze the porosity behavior of Lu_2O_3 ceramics sintered in the tungsten element furnace. The

sinter soak was extended to 20 h to attempt to closely match sintered relative density compared to the shorter 1600°C sintering schedule, as well as close up the open channels between particle granules as identified in SEM, where increased sintering duration was shown to reduce the level of porosity. Initial results of this series of tests are summarized in Figure 98.

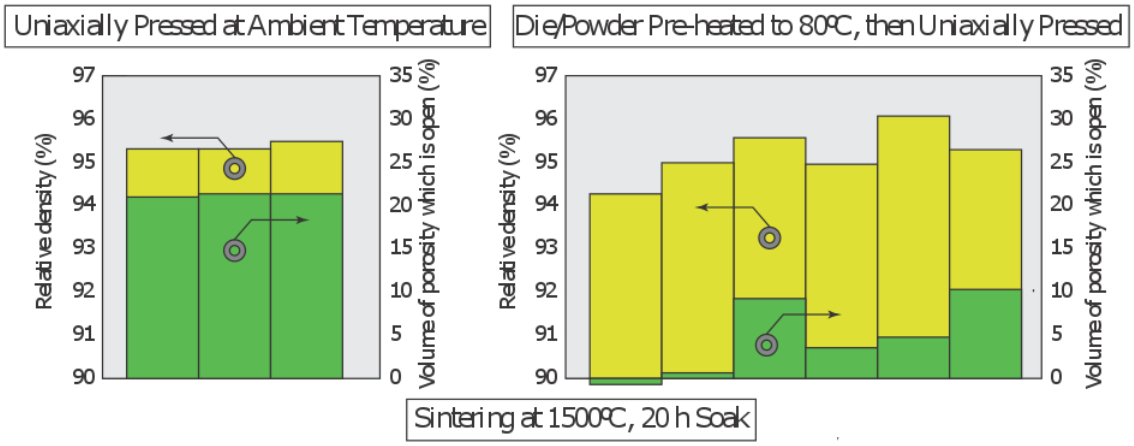

Figure 98: Increasing the uniaxial pressing temperature about the glass-transition temperature of PMMA plasticizer showed general trend towards decreasing open porosity.

While sintered relative densities of these samples (left) remained in the mid 90% range, the extent of open porosity did not improve with the increased sinter duration. However, a quick test of uniaxially pressing powder compacts at a temperature approaching the glass transition temperature of the PMMA binder did generally show that densities of ceramics sintered at this schedule could be maintained while the extent of remnant open porosity could be significantly improved. For some cases of identically sintered samples, the remnant open porosity was eliminated completely (right), but results were erratic, likely due to not being able to identically heat the pressing die in a warming oven and

pour and press the powder compacts for each produced sample. Another limitation of this method was that the CIPing process of the powder compacts could not be performed at the elevated temperature. Samples were again imaged under an SEM for visual confirmation of reduction in open channels with the elevated temperature uniaxial pressing methodology. The results are shown in Figure 99.

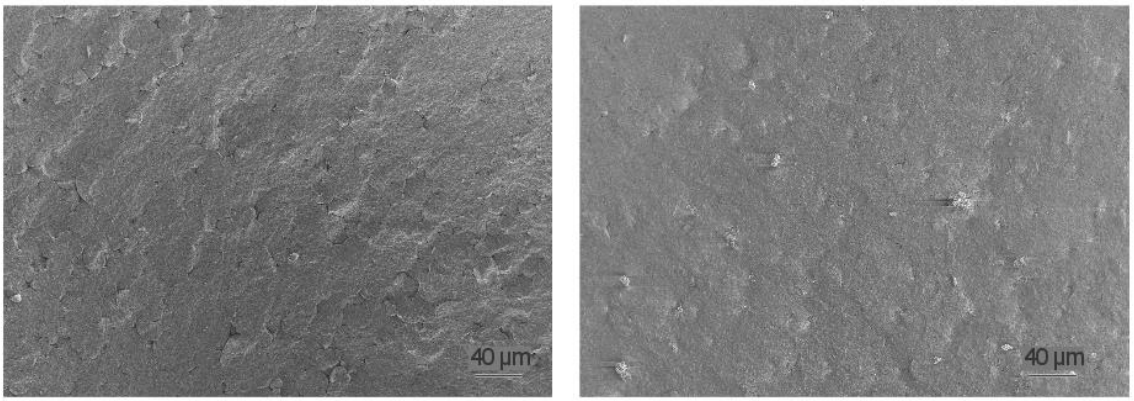

Figure 99: SEM Micrographs of Lu_2O_3 samples sintered in tungsten element furnace (1500°C 20 h) showing decreasing extent of remaining visible granule edges from normally pressed samples (Left) and samples pressed at an elevated temperature (Right).

The great reduction of the channel “triple points”, areas where three particle granules in plane are shown to have remnant open regions between them even after sintering, is greatly reduced in samples produced with the introduction of the warm-pressing process. However, it became clear that while the warm-pressing process appeared as general direction needed for producing samples with limited open porosity, the lack of reliability of the method meant that other measures of preventing the presence of open-channel porosity needed to be considered.

Extending the sintering duration past 2 h for samples sintered at 1600°C seemed to show a plateau in the level of sintered relative density achieved (in fact the density was slightly less). The next attempt as reducing the residual open channels was to use dibutyl phthalate as the plasticizing agent to hopefully reduce the transition temperature of the PMMA polymer to below that of the ambient conditions used to press the Lu_2O_3 powder compacts. A general increase in the relative green densities to ~60% up from ~58% (even after organic removal) of the CIPed compact was an initial indication that this attempt to more easily deform the granules during compaction was a success. Results of sintering these samples in the tungsten element furnace between 1500-1600°C is given in Figure 100.

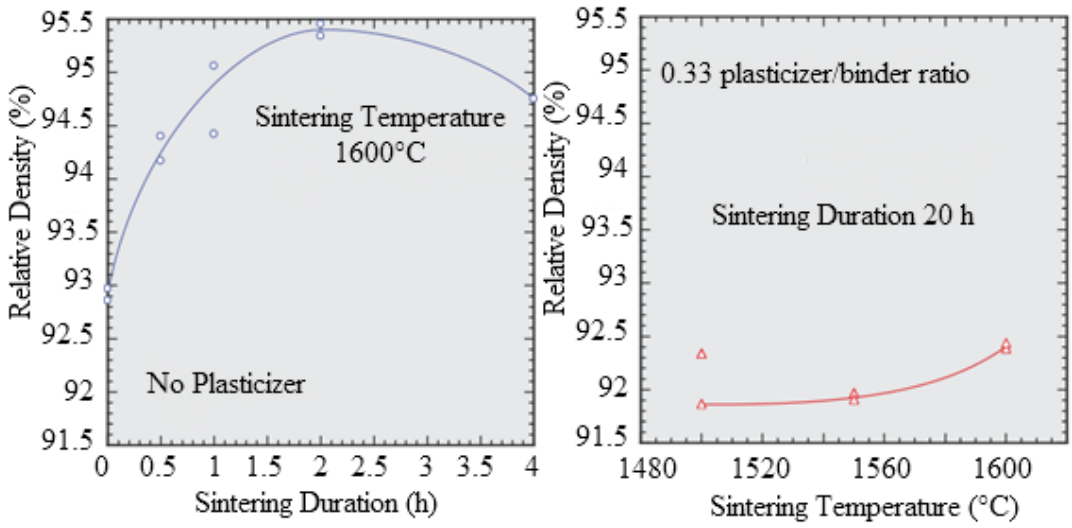

Figure 100: Comparison of sintered density of samples with no plasticizer content and samples with a 1:3 plasticizer to binder ratio, sintered in the tungsten element furnace. Presence of this plasticizer content has a negative effect on sintered density.

The immediately obvious result is a much lower sintered density compared to that of the samples produced without plasticizer, even with extended sinter soak durations of 20 h at the 1600°C dwell temperature. However, despite the much lower values, the open porosity of these samples were much improved, remaining at values near 0%. To test for the extent of open porosity being reduced being due to the extended sinter duration, a sample was sintered at 1500°C for only 4 h and still maintained less than 1% of its porosity remaining open, though the density was too low for further tests to be done. Unfortunately, samples HIPed between 1500-1600°C for 4 h on these samples sintered in the tungsten element furnace were found to often break and were not able to be retrieved from the press to be further measured. This result coupled with the poor sintered relative densities suggested that the plasticizer content needed to be reduced in order for samples to survive the HIPing process.

4.2.4 Optimizing Plasticizer Content in Graphite/Tungsten Sintering Environments

To compare to previous spray dried results sintered in the graphite element furnace, samples of varying plasticizer content were sintered between 2-16 h in the older furnace. The results of testing for the extent of sinter dependence on plasticizer content is given in Figure 101.

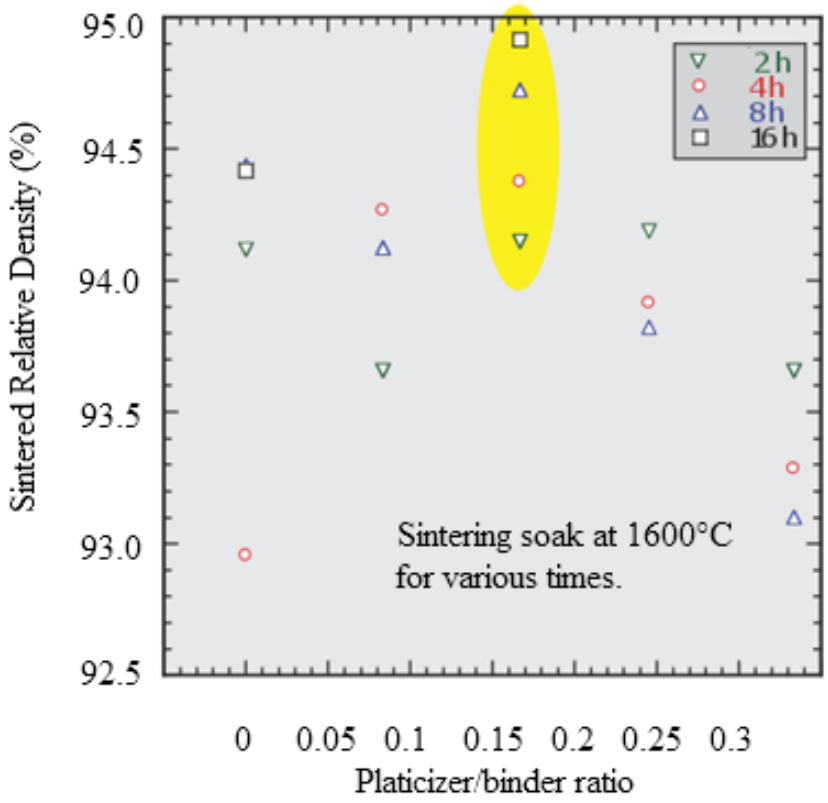

Figure 101: For samples sintered in graphite element furnace, a 1:6 plasticizer to binder ratio was found to have the highest sintered density. It held that 1:3 plasticizer to binder ratio had the lowest sintered densities.

Sintered densities maintained better relative percentage with increasing plasticizer content, though a decrease was still noted with the previous full plasticizer to binder ratio of 1:3. While sintered densities seemed relatively independent of plasticizer content up to the 0.25, samples formed from a ratio of 1:6 showed generally the best relative densities. No general trend was noticed by increasing the sinter duration past 2 h. The extent of remaining open porosity for these samples all remained very low, even at the low sinter durations. However, upon HIPing, samples sintered for only 2 h showed complete opacity (as well as generally appearing very damaged after HIPing) while samples sintered be-

tween 4-8 h HIPed to much higher relative densities. Sintering beyond this point showed a negative result on samples upon HIPing. A visual comparison of these samples is given in Figure 102.

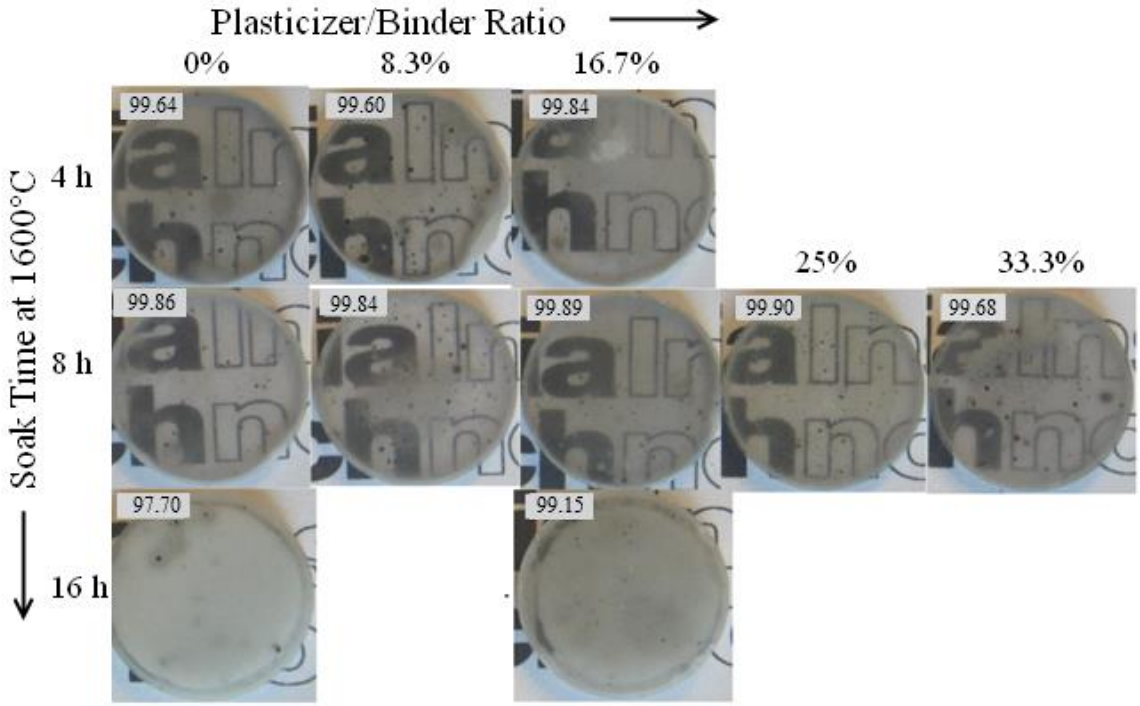

Figure 102: Camera images of Lu_2O_3 samples sintered in graphite element furnace as a function of sinter duration and plasticizer content and HIPed at 1600°C for 4 h. 8 h duration shown to have best general result, with longer durations hindering transparency. Remnant black specks remain present in all samples.

It is apparent that the final HIPed relative density and the resulting degree of transparency is dependent on more than just the relative density of the samples upon sintering, as well as the porosity profile of the sintered samples. Samples sintered for 2 h or 16 h, as well as samples sintered with higher plasticizer content at 4 h, did not reach an appropriately high density upon HIPing to achieve transparency, despite similar densities upon sinter-

ing. Samples sintered for 8 h showed generally the best results with samples of the entire range of plasticizer content exceeding 99.6% relative density. However, these samples were marred with black specks within the bulk of the samples and final quality was determined to be independent of the plasticizer content. While previous general coloration of ceramics sintered in the graphite element furnace was able to be removed by annealing samples before and after sintering, as discussed in Chapter 3, these speckled defects appeared to be irremovable through this process. Attempts to anneal out the coloration mid-sinter by interrupting the soak after 0-1 h and then allowing the samples to finish sintering the full 8 h duration and otherwise processing normally did not improve the extent of speckling of the samples. SEM micrographs of fracture surfaces of these samples containing the 1:6 plasticizer to binder ratio sintered at these schedules are given in Figure 103.

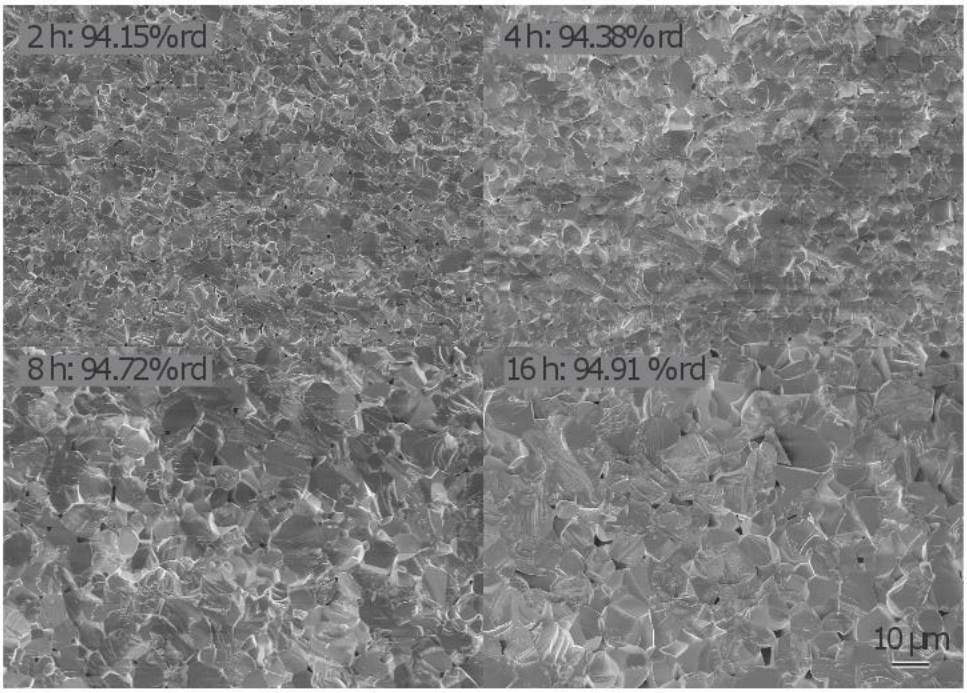

Figure 103: SEM micrographs of Lu_2O_3 fracture surfaces showing increasing extent of grain growth with increasing sinter duration. While pores remain at grain boundaries, 16 h sample shows a high extent of grain coarsening, which may hinder post-HIPing to theoretical density.

While the relative densities of these samples are all within the range of 94-95%, an increasing extent of grain growth is notable for extended sinter durations. Pores also appear coarsened, which may be preventing the samples from proper densification in the HIP at the 16 h sinter duration. It is also possible that due to the large grain sizes, pores were swept into the grains such that the fracture surface is unable to expose such voids if the grain bulks were not cleaved during the fracture. It is not clear from the fracture surface why samples sintered for 2 h could not properly HIP to high relative density.

Since an 8 h sinter soak duration was identified as the optimal schedule for producing highly dense Lu_2O_3 ceramics upon HIPing, identical samples were sintered in the tungsten element furnace for 8 h, but the relative densities were notably lower. It was found

that comparable relative densities could only be achieved in the tungsten element furnace by increasing the sintering temperature to 1800°C. Fracture surfaces of these samples are given in Figure 104.

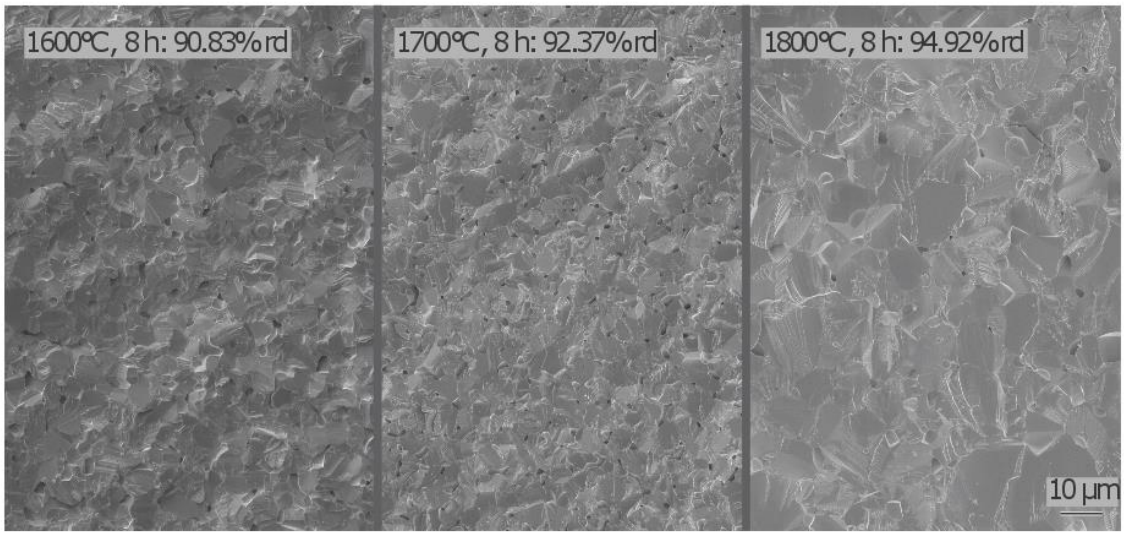

Figure 104: SEM micrographs of Lu_2O_3 samples of the 1:6 plasticizer to binder ratio sintered for 8 hours in tungsten element furnace. Similar sintered density to graphite furnace is reached only at 1800°C, resulting in large degree of unwanted grain growth.

As expected, the higher temperature sintering required to reach similar relative densities as the samples produced in the graphite element furnace also results in much larger grain sizes, some larger than 10 µm. Despite the low relative densities noted for samples sintered at 1600-1700°C, the extent of open porosity for all of these samples was near zero percent. Attempts to HIP many these samples at 1600°C for 4 h failed due to the specimens exploding, likely during the depressurization. While this was initially thought to be due to the lower sintered densities achieved in the tungsten element furnace, the same

result for the ~94% dense samples sintered at 1800°C suggest that some other phenomenon specific to this sintering environment is the culprit.

4.2.5 Impurity Determination of Sintered Ceramics

While some samples sintered in this manner were able to HIP to high relative density (~99.5%), if they were undamaged in the HIPing process, it was later discovered that samples sintered in the tungsten element furnace resulted in a thin layer of a tungsten containing deposit appearing on the sample surfaces. This impurity could be the root cause of the lowered sintered density values in comparison to identical samples prepared in the graphite element furnace. The presence of tungsten on these samples was first identified via EDS on a contaminated Lu_2O_3 sample compact, and the presence of a non-pure-lutetia phase was confirmed via XRD on a darkened powder. Samples sintered in the tungsten element furnace while buried underneath loose Lu_2O_3 powder were shown to have a much higher degree of general sample clarity (by remaining white) and showed improved sintered densities along with no unwanted phases appearing present as measured via x-ray diffraction and no W signature. The EDS spectrum showing W contamination of these samples is presented in Figure 105.

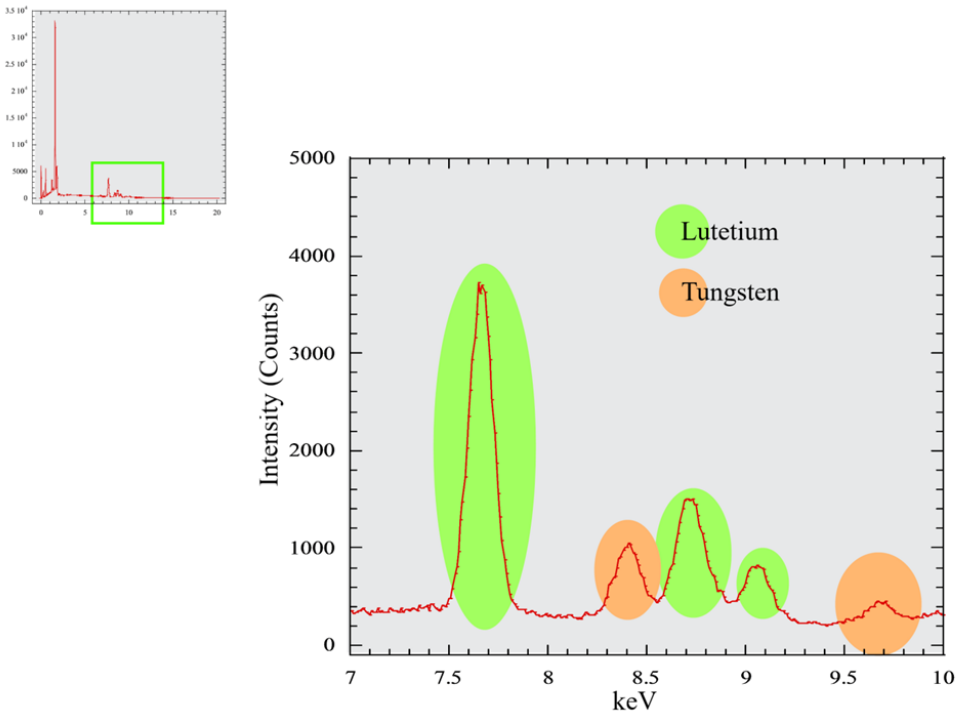

Figure 105: EDS Spectrum of darkened sample showing clear W impurities on sample surface.

The EDS spectra also showed the presence of carbon in these samples, but the regularity of the carbon peak appearing in every EDS scan (even on blank sample stubs) and the low detectability of the light element suggests the possibility that the detection of the element is an artifact of the measurement, though this did merit further investigation. The Lu peaks were easily identified as the element's characteristic $L_{\alpha 1}$ (7.655 keV), $L_{\beta 1}$ (8.709 keV) and $L_{\beta 2}$ (9.049 keV) emissions. Clear presence of W $L_{\alpha 1}$ (8.396 keV) and $L_{\beta 1}$ (9.672 keV) indicate that the surface interaction of Lu_2O_3 and the tungsten environment needed to be avoided in future processing. Lastly, the O signature peak of $K_{\alpha 1}$ at .525 keV was also present[107, 108]. XRD analysis showed evidence of monoclinic Lu_2WO_6 (ICDD 00-026-0870), as shown in Figure 107.

The layer of this tungsten-containing phase was found to be never more than just on the very surface of the sintered samples, identified when they were fractured for microscopic analysis, revealing a clean and unreacted (white) bulk. The solution identified was to bury the specimens to be sintered underneath Lu_2O_3 commercial powder inside an alumina crucible, such that only the surface of the loose powder getter would react with the tungsten impurity phase, leaving pure lutetia underneath. The result was samples of much higher sintered density and with no visible extent of impurity deposition in the samples. In addition to this, despite the low densities of the sintered samples relative to HIPed, they were found to be somewhat translucent, displaying a characteristic glow when illuminated. This was not something that had been achieved during this project work outside of sintering highly dense Y_2O_3 with extended dwell durations. Extending the dwell duration of these buried Lu_2O_3 samples seemed to result in a greater extent of translucency, but without a notable increase in sintered density. Visual representations of sintered samples produced both settered on top of ZrO_2 stands (with the W deposit darkening the sample) and translucent samples produced from burying the specimens underneath Lu_2O_3 powder in an alumina crucible are given in Figure 106.

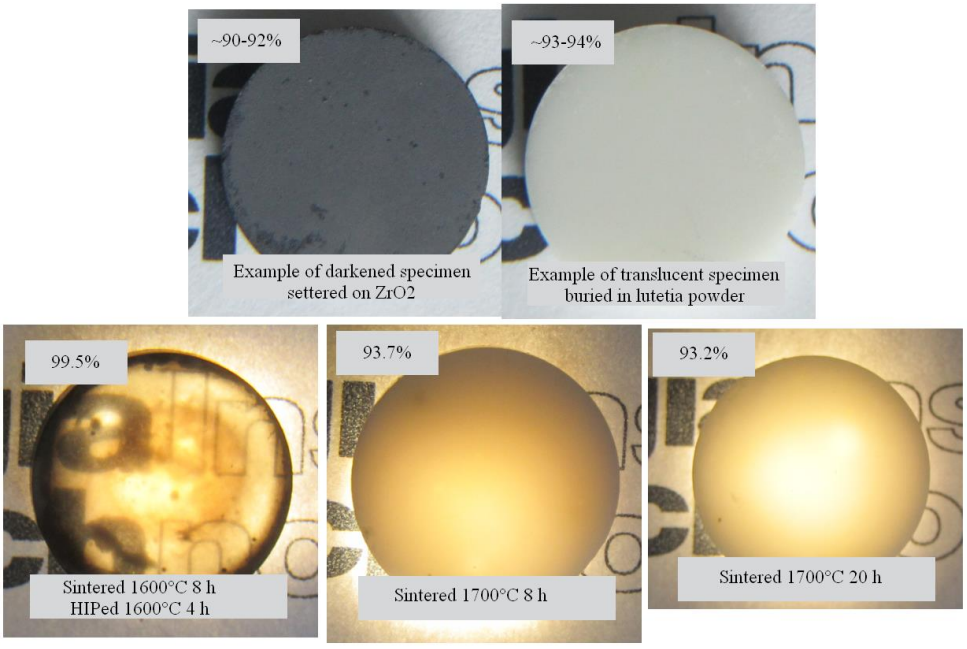

Figure 106: Top Left: A representative impure sample from vacuum sintering in W element furnace. Top Right; A representative sample sintered underneath loose powder showing no visible extent of contamination. Bottom Left: A darkened sample HIPed to high relative density but marred by W impurities. Bottom Middle: A 8 h duration buried sample showing translucent property. Bottom Right: A longer-duration buried sample showing a higher extent of translucency but without increased density. Samples in bottom row illuminated with backlight.

While the W-containing surface of the darkened samples could be effectively polished off before or after HIPing, the radial tungsten contamination of these samples is apparent in the figure above. Polishing of this surface did not greatly affect the measured density of the coated samples, suggesting that the presence of the W-containing layer altered the sintering behavior of the bulk of the sample, even if it remained uncolored. The ~2% increase in sintered density of buried samples suggests that the removal of this layer's presence improved the sinterability of the specimens. Phase purity of these various sample

types was confirmed via x-ray diffraction, as shown in Figure 107. However, only certain specimens of high sintered density fired for 8 h were able to HIP effectively.

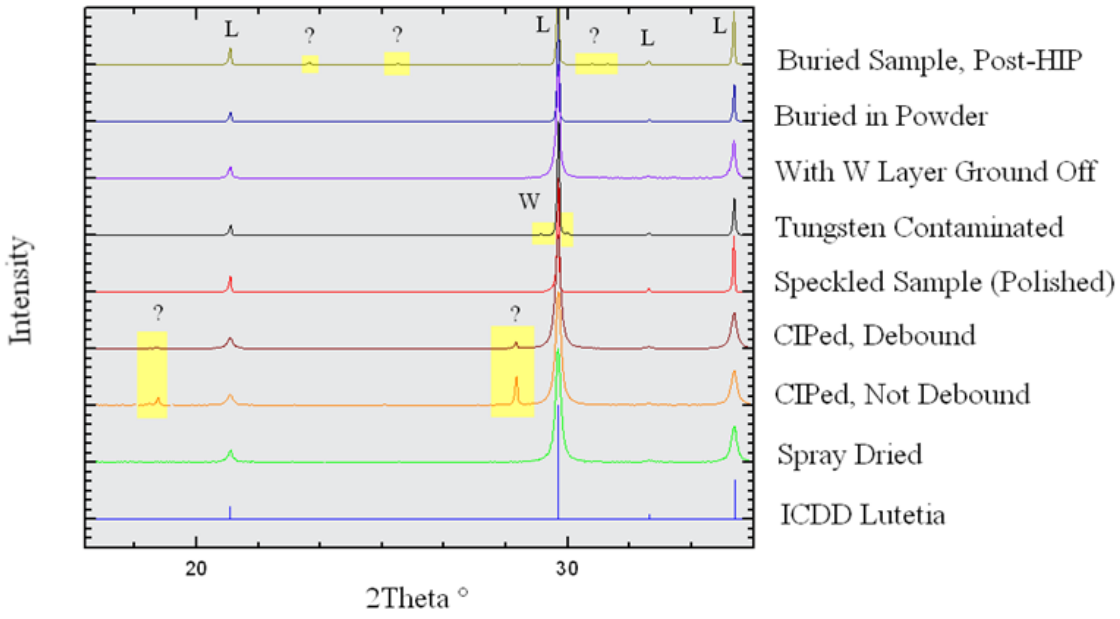

Figure 107: X-ray diffraction spectra for specimens at various points of processing. Phase contaminants are shown in yellow.

It appears that contaminants phases become present both after CIPing (orange) and HIP-ing (dark green), however these appear to only be at the surfaces of the samples. The extent of impurity seems to decrease in the debound sample after undergoing thermolysis (brown) but grinding down the surface shows the complete removal of these peaks, as shown in Figure 108, for both the CIP and HIP imbued impurity phases. Speckled samples from the graphite element furnace (red) appear in the diffractometer as phase-pure Lu_2O_3, suggesting that the visual spots in these specimens are amorphous in nature, or are below the detection limit of the diffractometer. Lastly, samples sintered in the tungsten

element furnace without being buried in loose Lu_2O_3 powder (black) show a phase impurity matched to Lu_2WO_6, while samples sintered identically in loose powder (blue) do not show these impurities. The contaminated surface of loosely packed powder was used for this spectrum. Contaminated samples can be ground to remove this impurity from the faces of the samples (violet), but the radial faces cannot be processed in this way. This information is summarized and illustrated in Figure 108.

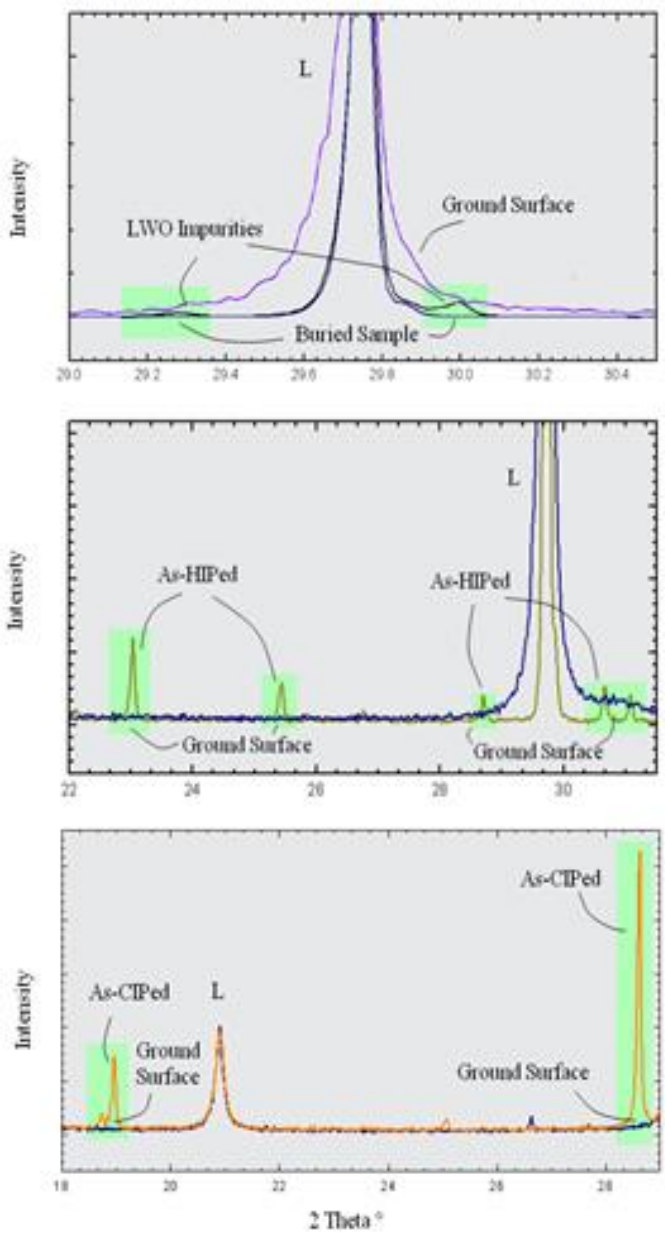

Figure 108: XRD spectra showing decreased impurity extent for ground sample surfaces of CIPed, tungsten-sintered, and HIPed samples, as well as no impurity phases for samples sintered while buried in loose Lu_2O_3 powder.

While the impurity phases present in CIPed and HIPed specimens could not be strictly identified, they appear only at the surfaces of the samples, as evidenced by their removal

upon grinding of the sample faces. This suggests that the contamination is from the sample being in contact with the evacuated latex bags or graphite crucible during CIPing and HIPing, respectively. While HIPed samples are often ground and polished regardless, CIPed samples show a diminishing extent of impurity content once exposed to a thermolysis heat treatment, where the organics present from pressing are removed via a low temperature thermolysis, and do not appear in any of the remaining sintered sample spectra. The tungsten phase impurity present can be ground off the flat faces of the samples as well, but to prevent the impurity from forming at the radial edges of the sample, it must be buried in Lu_2O_3 powder before thermal processing, which was also shown to be effective at removing this impurity. Lastly, it is evident in both the sintered and HIPed spectra above that grinding of the sample surface results in broadening of the primary Lu_2O_3 peak at 29.74°, suggesting that the grains found at the surface of the samples are much larger than those found in the bulk, resulting in peak broadening once these are exposed to the diffracting x-rays.

Translucent samples that were buried in powder and sintered in the tungsten element furnace between 1600-1700°C were HIPed in the same range of temperatures. Of these, only samples sintered at 1650°C and HIPed at 1700°C showed promise for achieving high relative density. Many of the other samples showed only a minor increase in density upon HIPing, as shown in Figure 109.

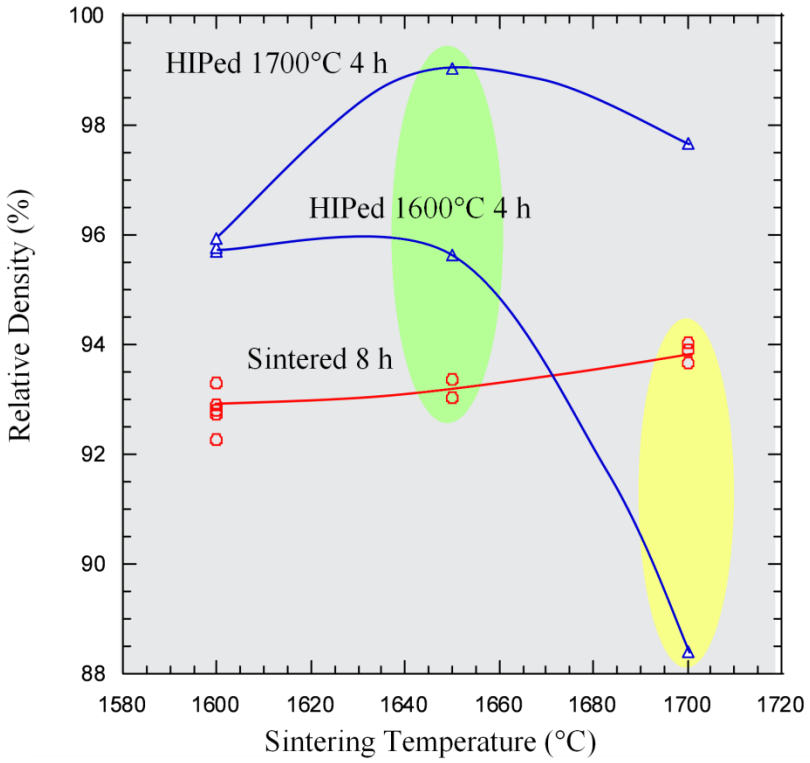

Figure 109: Relative densities of buried samples sintered for 8 h and HIPed at 1600-1700°C for 4 h.

Sample densities were relatively insensitive to temperature changes with respect to relative density achieved through sintering. Extending the dwell duration to 20 h was also ineffective at increasing the sintered density past the threshold identified at ~94% (see Figure 106.) Samples HIPed at 1600°C did not exceed 96%, and samples sintered at 1700°C showed adverse effects relative to those sintered at 1650°C and HIPed at either temperature. Electron micrographs shown in Figure 110 do show an increasing extent of grain growth past 1650°C, though no indication of pores becoming swept into grain interiors is noticed.

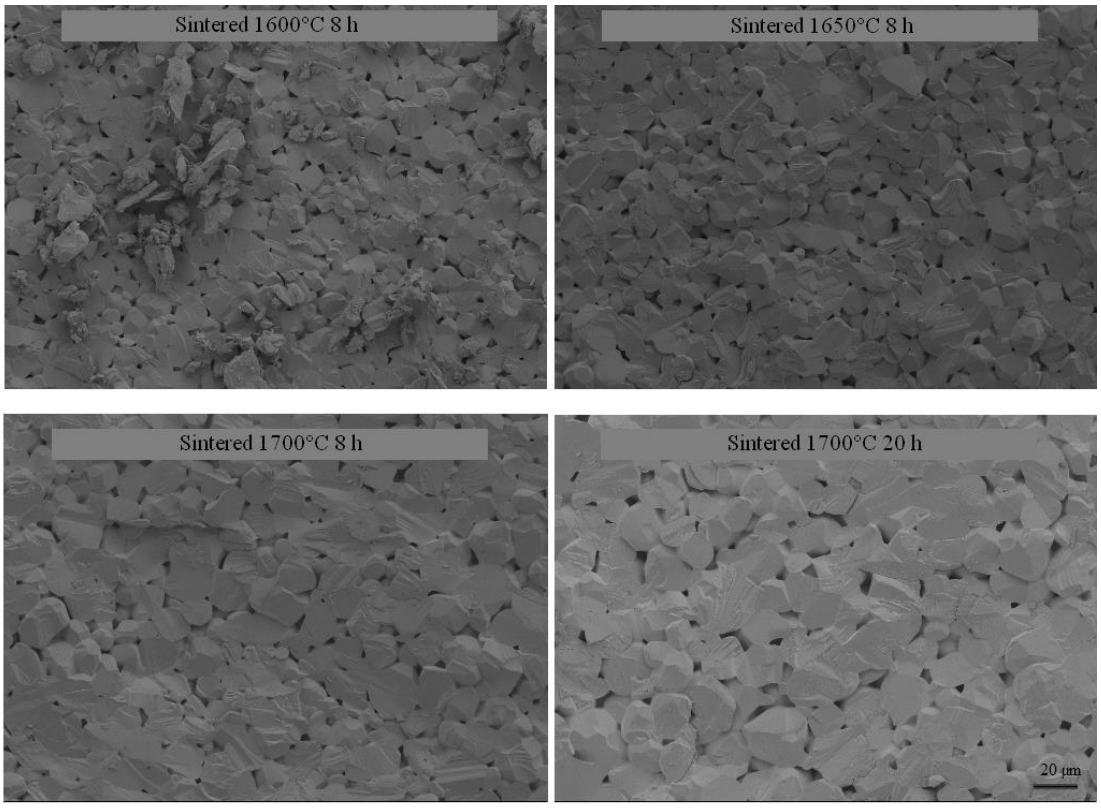

Figure 110: SEM micrographs of buried samples sintered in the tungsten element furnace.

Grain sizes begin to exceed 20 µm when sintered at 1700°C, especially if for the extended duration of 20 h. However, pore distribution does not seem to change, and there is no visible extent of pore coarsening or entrapment, and the pores remain at the grain boundaries and triple points. Upon HIPing, however, it was noticed that near the surfaces of the sample faces, the microstructure appeared to be pore free, while the bulk interiors of the samples still maintained a high degree of porosity. While the extent of this divide was dependent on the total relative density of the sample, it was consistent regardless of the final density or processing parameters. This phenomenon is shown in the micrographs given in Figure 111.

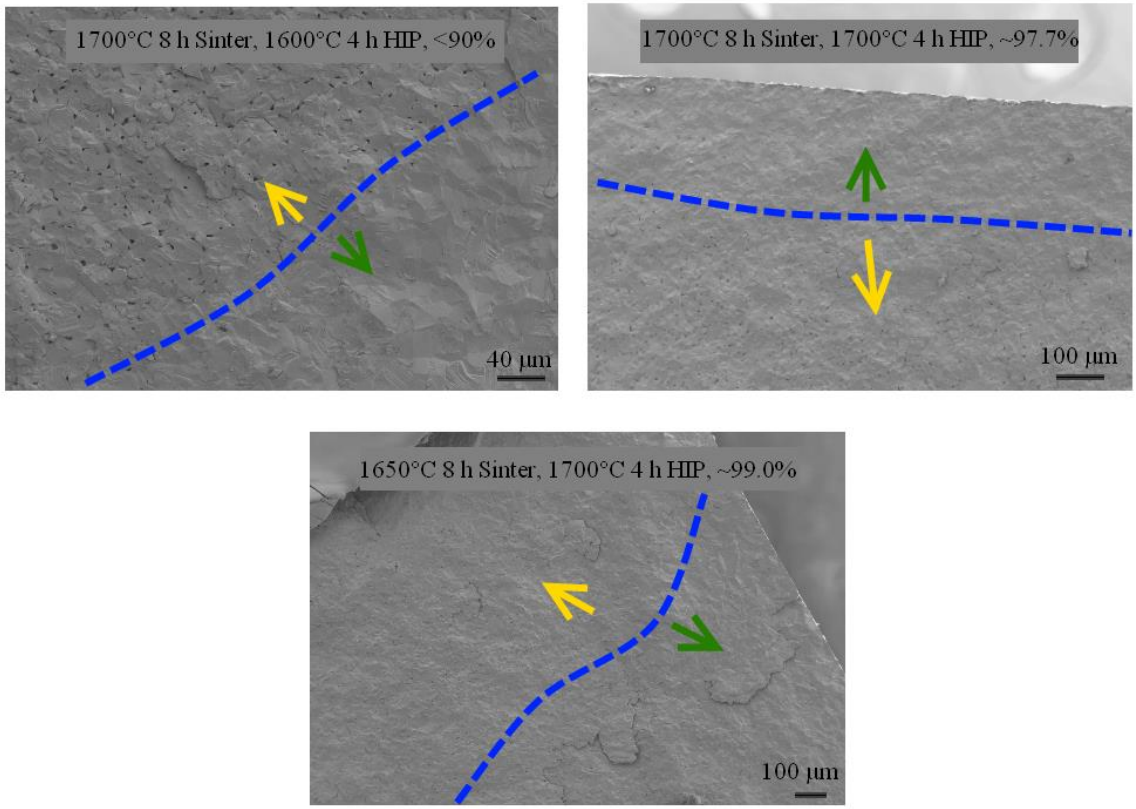

Figure 111: Low magnification micrographs of samples HIPed after being buried in loose powder, showing different porosity profiles at sample surface and centers.

In the figure above, green points to nearly pore-free regions generally located at the surfaces or edges of the samples, while yellow points to pore-containing regions in the bulk. The grinding off of the sample surfaces in the XRD data above resulting in broader peaks suggests that somehow, the sample surfaces were being more effectively HIPed than the interiors, resulting in larger grains (and narrower diffraction peaks) and a pore-free microstructure. This along with the general insensitivity of relative density on sintering parameters suggested that it is the HIP parameters needed to be adjusted in order to fully densify these samples to a theoretically dense state. To compare to the samples sintered

in the graphite element furnace, identically processed samples in both were fractured and imaged as shown in Figure 112.

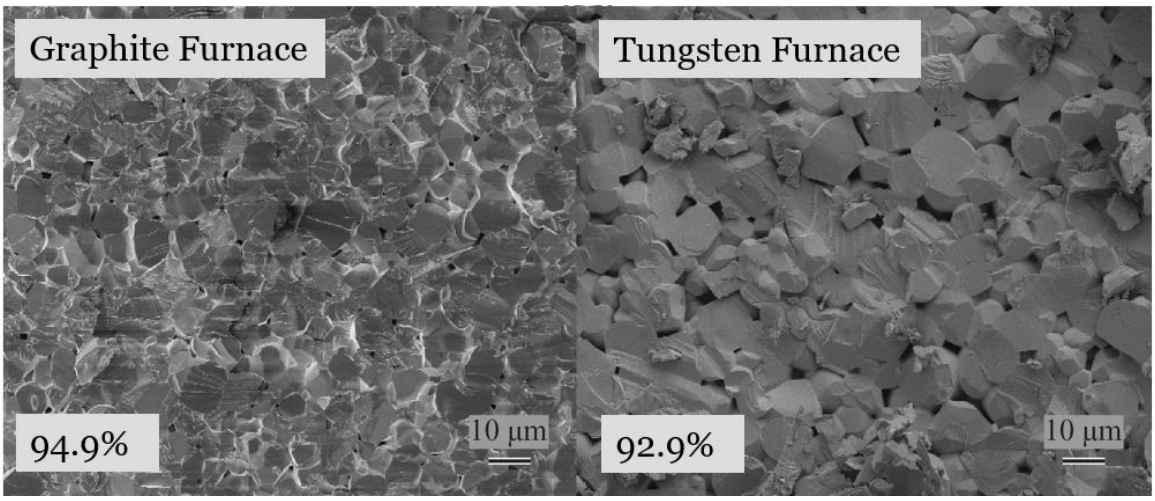

Figure 112: Comparison of 1600°C 8 h Lu_2O_3 samples sintered in graphite (left) and tungsten (right) furnaces. The tungsten furnace shows much larger and more numerous pores.

The comparison above shows that the graphite furnace samples sintered at this temperature have a microstructure more conducive to HIPing to high relative density due to a higher achieved sintered density as well as generally much smaller pores present at the grain boundaries. The presence of carbon in these samples seems to be acting as a grain growth inhibitor and prevents the grains and pores from coarsening to the extent seen in the tungsten furnace, where the samples are buried and do not interact with the furnace environment to the same extent. Because of this large degree of coarsening found in the samples produced in the tungsten furnace, many samples were unable to HIP to high relative density and maintained regions of high porosity.

These regions of remnant porosity also appear to be relatively sensitive to thermal treatment of HIPed samples, such as post-HIP annealing which had previously been

shown to have been a successful process to remove coloration and improve transparency. Opaque regions of HIPed samples appear to be most susceptible to damage by oxidation heat-treatment. In Figure 113, three distinct pore-containing regions of opacity show the highest extent of damage upon annealing, while the more pore-free and transparent regions of the specimen largely survive. Lastly, despite no coloration issues present from as-sintered samples retrieved from the tungsten element furnace, HIPed samples had the sample resulting black specks that were present from samples sintered in the graphite element furnace. This speckling is not improved with the annealing process.

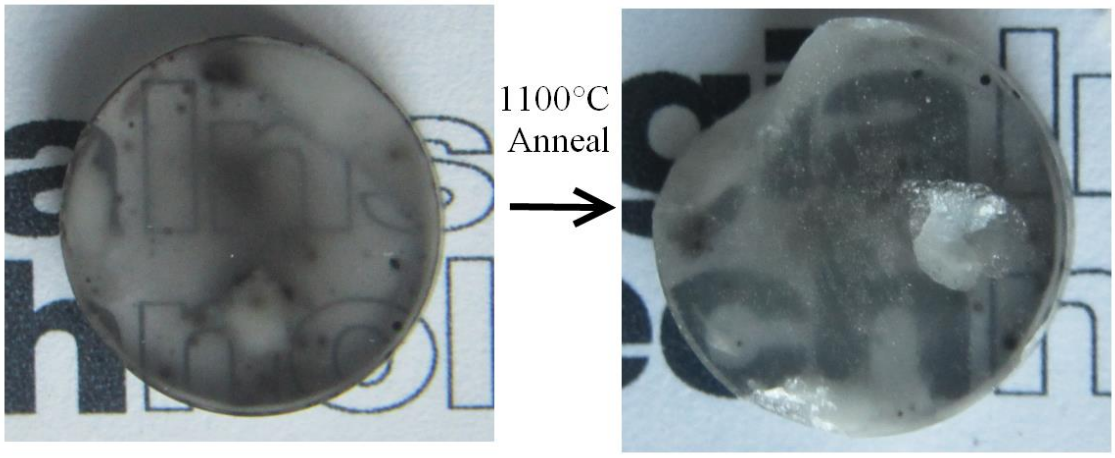

Figure 113: Images illustrating specimen damage of undensified regions upon annealing at 1100°C after HIPing.

Samples of less than ~99% relative density, without extended pore-free regions, showed a high tendency to break apart completely upon oxidation heat treatment, suggesting that the high degree of porosity dispersed throughout the sample would cause the whole specimen to fracture in the same manner as the isolated regions become damaged in the higher-density specimens. This phenomenon suggests that there is a remnant gas pressure within the pores of these samples, which breaks the specimens apart when the entrapped

argon pressurizes at elevated temperatures. The samples are able to maintain integrity during the HIPing process due to the externally applied pressure that remains present until the specimens return to room temperature. However, the pressurized remnant porosity resulted in thermally fragile ceramics, an issue since the samples' extent of thermal stability is a requirement for these to be used for laser operation; especially since they are expected to heat up as the laser active ions are pumped from a source, which generates heat through phonon production. It thus became clear that HIPing parameters needed to be adjusted such that the high pressure argon would not penetrate the pores and prevent densification and core formation. An identical set of specimens were produced and HIPed for both an extended duration of 8 h, as well as an elevated temperature of 1800°C for 4 h. The results of these adjustments is shown in Figure 114.

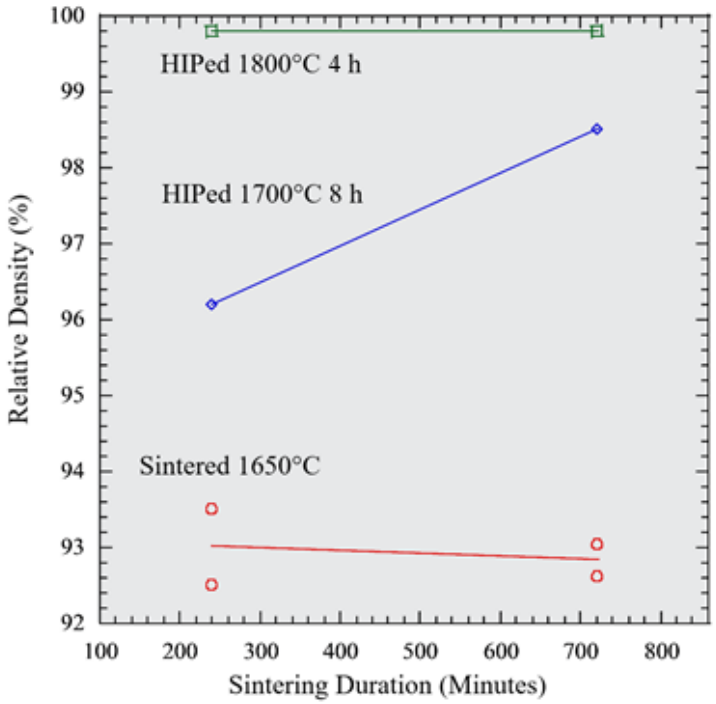

Figure 114: Sintered and HIPed densities of samples sintered tungsten element furnace at 1650°C.

The extended HIP duration to 8 h did not seem to improve HIP densities at all. However, samples sintered and HIPed at 1800°C did result in high relative densities and moderate transparency, though the elevated temperature did result in coloring of the ceramics. Since these samples were of higher relative density than those HIPed at 1700°C, the annealing process was much less damaging to the ceramic, as was successful at improving the optical quality. However, remnant black specks still remained, and were largely unaffected by the thermal treatment. Images of these samples pre and post-anneal are given in Figure 115.

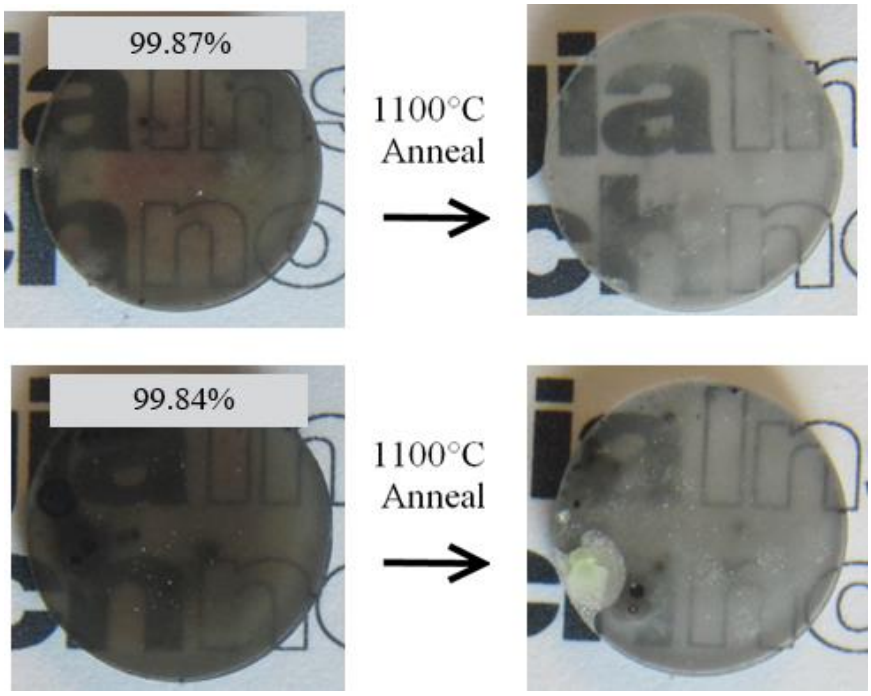

Figure 115: Indicated color change of graphite element samples HIPed to high relative density at 1800°C for 4 h. Samples retained evidence of cloudiness as well as black specks.

Once polished, these speckled samples again showed no trace of an impurity phase via x-ray diffraction, similar to the graphite element furnace samples as shown in Figure 107 (in red). To determine the elemental characteristic of the specks, EDS was revisited to determine the signature of the impurities. It was determine that a Mo based impurity was present in both the HIPed samples as well as in the Lu_2O_3 powder once spray dried. While not in a sufficiently high enough quantity to be detected by phase analysis, the Mo impurity was highly evident in the spray dried powder after also indicated on the HIPed samples. The EDS spectrum of the Mo impurities are given in Figure 116.

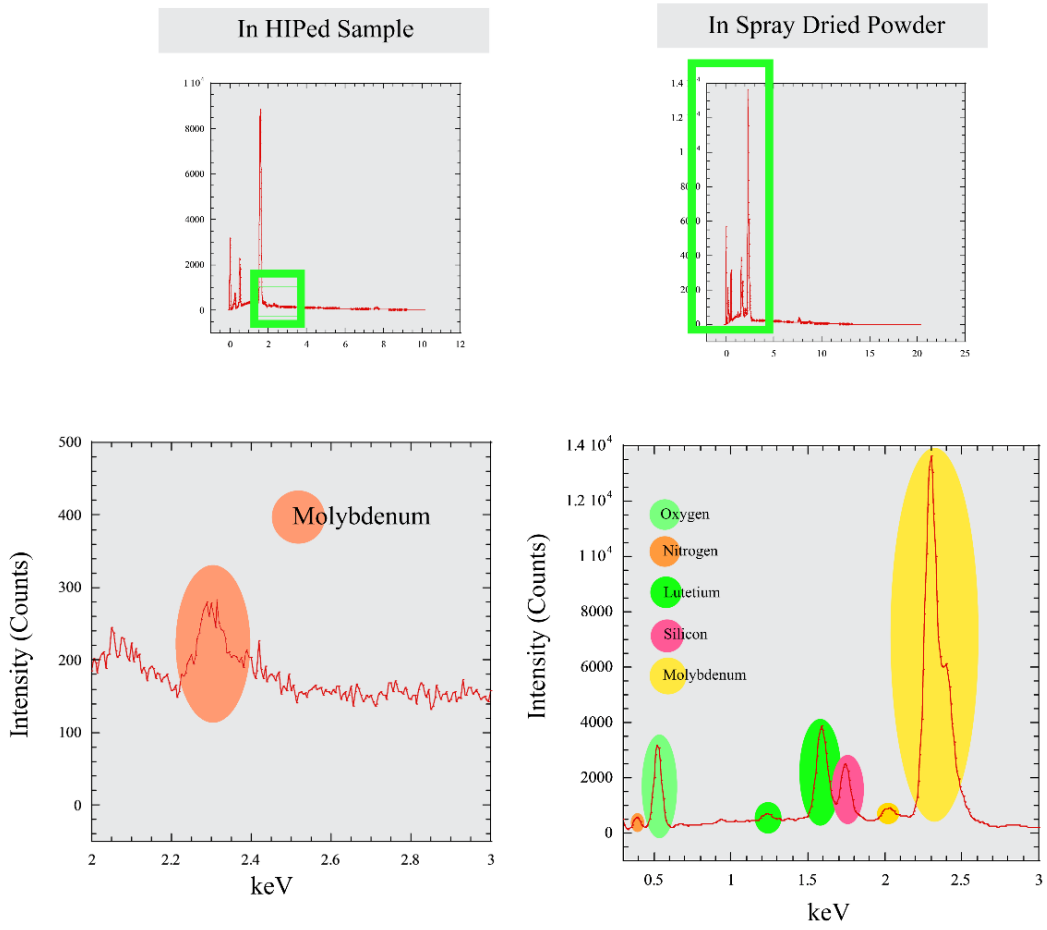

Figure 116: EDS spectra showing evidence of Mo impurities present in both a final HIPed sample (left) and in powder as-spray dried (right). Si and N presence is also detected.

The characteristic emissions for Mo: Ll (2.02 keV), Lα1 (2.29 keV) and Lβ1 (2.39 keV), Si: Kα (1.74 keV), and N: Kα (.393 keV) are obviously present in the spray dried powder before pressing into compacts. These impurities in the powder were able to be traced back to the previous application of the ultrasonic spray drying nozzle. While flushing the nozzle with the acetone solvent used was sufficient to not have obvious impurities present in the diffraction pattern(See Figures 87 and 88), or through visible inspection. The

remaining deposit in the nozzle bore was expelled with metal wire, and new batches were prepared. Subsequent EDS of these batches did not pick up any impurity presence.

4.2.6 Achieving Near 100% Relative Density with Pure Lu_2O_3 Ceramics

To continue investigation of HIP parameters with the new batch powder, samples sintered in both the graphite and tungsten element furnace were HIPed at various temperatures between 1600-1850°C at 1.5x the ultimate pressure of the typical HIPing process. This was investigated along with a lowering of the sintering temperature to see if high relative density could still be achieved. The results of this for a small set of samples sintered in the graphite furnace are given in Figure 117.

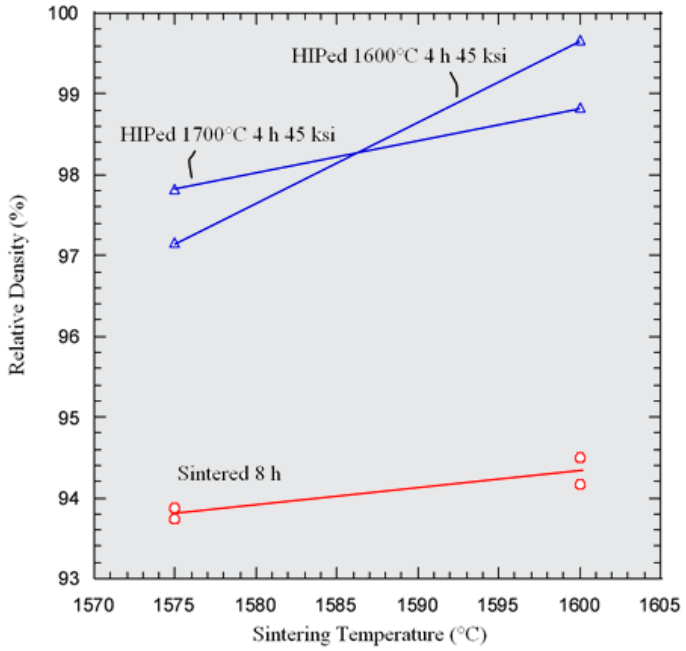

Figure 117: HIPed densities of graphite element sintered samples with an elevated pressure of 310 MPa.

For these samples any changes to the previously identified optimum sinter and HIP temperature (that is, away from 1600°C for both) resulted in samples of poorer relative density. Reducing the sintering temperature by even 25°C resulted in significantly lowered HIPed density, regardless of HIP temperature used. In addition to only achieving moderate translucency or sporadic transparency, the change in spray dry powder batches did not prevent the presence of black specks from appearing in the samples, even though Mo impurities were no longer picked up in the spray dried powder used to produce them. Images of the resulting samples HIPed at 1600°C are given in Figure 118.

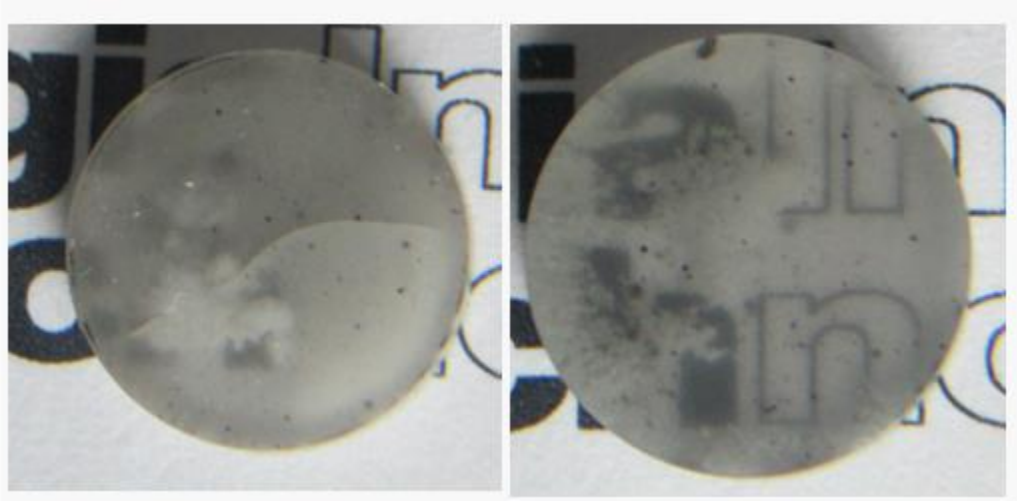

Figure 118: Samples sintered in graphite element furnace with clean powder and elevated pressure show both cloudiness and remaining black specks.

Thus, for samples sintered in the graphite element furnace, there was no improvement noticed for increasing the HIP pressure compared to the previous results shown in Figure 102. It also remains apparent that the phenomenon of black specks was not tied to the

presence of Mo and other impurities in the spray dried powder. Thus, the black speck presence is attributed to carbon impurities the agglomerate during sintering for samples sintered in the graphite furnace due to the high surface area of the spray dried particles formed from milled powder. For samples sintered in the tungsten element furnace, equivalent results are given in Figures 119 and 120.

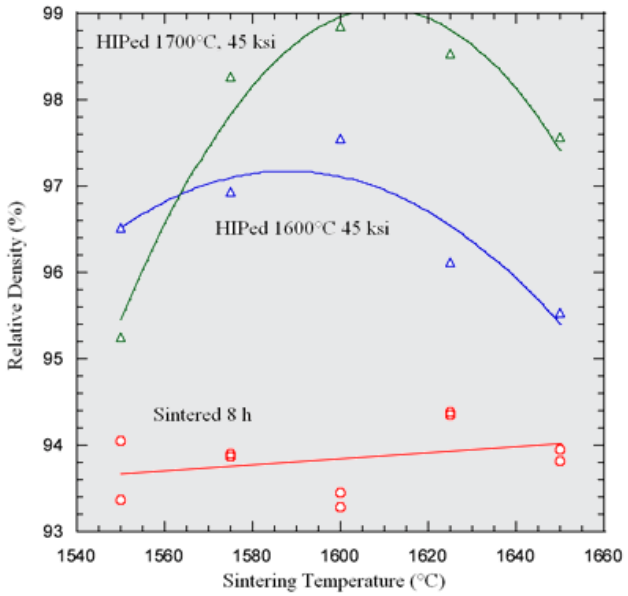

Figure 119: HIPed densities of tungsten element sintered samples (buried) with an elevated pressure of 310 MPa.

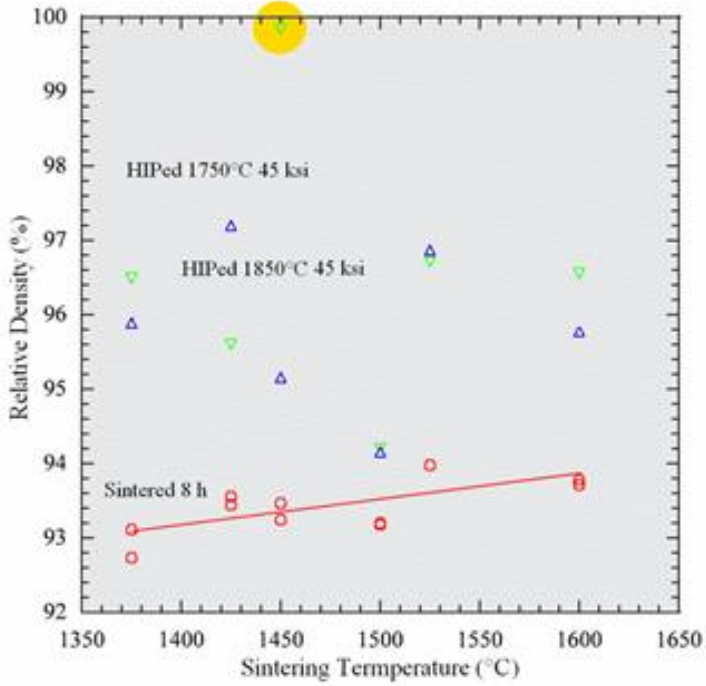

Figure 120: Sintered and HIPed densities of tungsten element sintered samples with an elevated HIP temperature and pressure.

Most all of these specimens did not HIP to > 99% relative density, suggesting that the pores were still being pressurized to a point where HIPing remained ineffective regardless of temperature or ultimate pressure. While moderate sintering temperature showed that a HIPing temperature of 1700°C was still more effective than 1600°C, low sintering temperatures showed no real trend with HIP result. A few samples did manage to achieve high relative density, though almost all samples sintered significantly below 1600°C proved to be the ineffectively HIPed. This is regardless of the sintered density showing only a moderate trend with sintered temperature in this range, and none of the samples showing any extent of open porosity during Archimedes density measurements showing no weight increase after boiling the samples in DI water. Despite the very high density of

the sample sintered at 1450°C and HIPed at 1750°C at 310 MPa, this specimen only remained translucent after polishing and maintained the presence of black specks. An image of this sample is given in Figure 121.

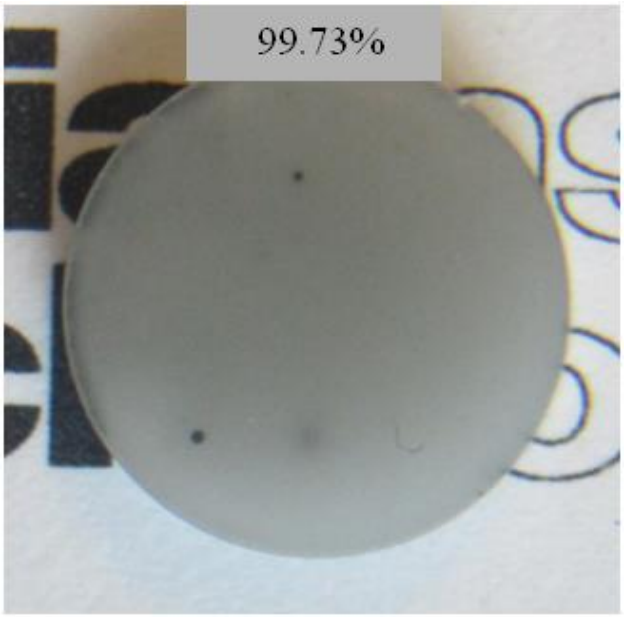

Figure 121: Near theoretically dense sample produced at 310 MPa still only achieves translucency, as well as maintains presence of black speck impurities.

The fact that this sample is of similar density to previous samples that showed a much greater extent of clarity suggests that this process is producing a microstructure not suited for an optical material, even if the porosity is nearly entirely eliminated. Samples sintered and HIPed in a similar manner in the graphite element furnace generally show a much higher degree of transparency. In addition to that, the black specks becoming present on these HIPed samples despite not being present in the powder or in the samples as-sintered (refer to Figure 106.) These black specks seem to be present in either set of samples from either furnace once HIPed, but only for samples that have undergone spray drying, which

suggests that the HIPing environment in combination with the spray drying methodology is the commonality in their presence.

To determine the cause of the translucency present, the above specimen was thermally etched at ~100°C below the sintering temperature for 2 h after it was polished to a finish of 1 μm, and then it was imaged via FE-SEM. While some polishing scratches are also present on the surface the sample, it is obvious that a high pore presence at both the grain boundaries and grain interiors is preventing the sample from being more transparent (Figure 121). Grain sizes of 10-30 μm are identified, and though the pore volume for the sample is low, the large grains suggests that the elevating HIPing temperature and pressure used to achieve this density adversely affected the microstructure with respect to desired optical quality.

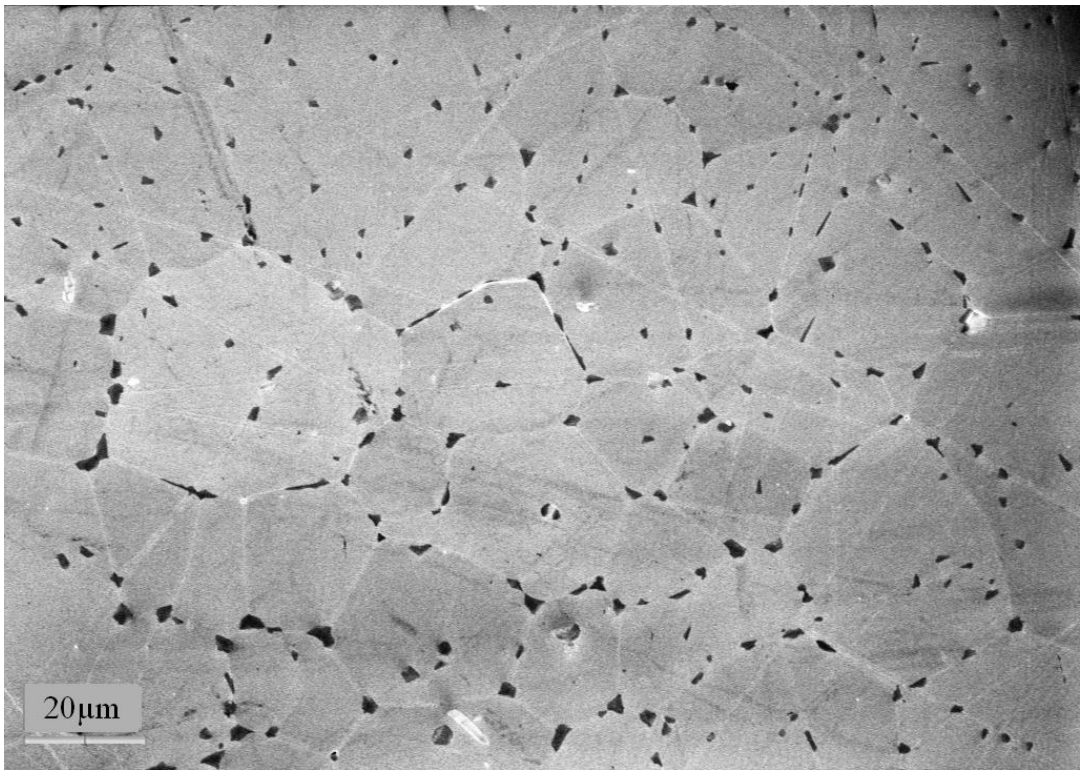

Figure 122: SEM Micrograph of thermally etched sample HIPed at 1750°C and 310 MPa. Many pores are seen both at the grain boundaries and grain interiors.

This shows that the more aggressive HIPing parameters undoes the precautions taken during sintering, and grows the grains such that pores become trapped within the bulks, and prevents their elimination. While the grain size here is not comparatively large compared to vacuum sintered samples in the literature, the size compared to the submicron particles contained within the spray dried granules suggests that the extent of grain growth was too rapid for the resulting microstructure to be favorable to optical transparency, even if the relative density of the sample is a close match to those produced by commercial powders earlier in this work.

The primary limitation of sintering in the tungsten furnace environment seemed to be the lack of any sort of grain growth inhibitor within the bulks of these samples. While a sintering temperature of 1600-1700°C produced samples in the near equivalent relative density range of samples produced in the graphite sintering furnace, the higher degree of HIP temperatures and pressures needed to fully densify these samples does not adequately remove the coarsened porosity. Samples produced from spray dried powders in the graphite sintering furnace were found to repeatedly sinter and HIP to high relative density, only the presence of carbon interaction that limited the pore and grain sizes shown in these samples also results in agglomerated black specks when the green compact is formed from samples with sufficiently high surface area compared to samples formed from commercial powder which do not exhibit this behavior.

V. CONCLUSIONS AND RECOMMENDATIONS

Continuing developments have led to high power output from polycrystalline ceramic lasers, where the work performed for this project has evaluated the possible production methods of forming Yb:Lu_2O_3 ceramics as a desirable candidate material for high powered lasing applications, as well as identifying a similar production method for forming potential substrate ceramic materials such as transparent Y_2O_3. This work has also provided an analysis of the production of the material and offers a starting blueprint for eventually producing laser quality specimens. Sinter, HIP, and annealing parameters were determined for vacuum sintering various commercial powders to moderate transparency with no precursor synthesis. Greater transparency and lower concentrations of isolated defect phases were observed at lower sintering soak temperatures, with high relative density achieved for commercial Yb:Lu_2O_3 over a dopant range of 0-8 mol %. A maximum of ~70% transmittance achieved for low (2 mol %) doping. Emission characteristics for samples produced with commercial powder show experimental threshold at 6 to 8 mol% dopant.

Processing methods and parameters such as sonication and chemical co-precipitation were evaluated, with YSZ based ball milling and atomization-based spray drying proving successful at reducing particle size and limiting sinter and HIP temperatures and still achieve >99.5% relative density. For the milled oxide slurries, optimum organic additive parameters for binder and plasticizer concentrations were determined to maximize sintered density, and this was studied for both Lu_2O_3 and Y_2O_3 based ceramics. A thorough

investigation was provided for comparing graphite and tungsten based vacuum sintering environments each evaluated for multiple production methods and parameters.

Ongoing investigation of expanding the dopant solubility limit with respect to fabrication methodologies is necessary in order to fully realize the potential of these materials, including considerations for producing them in an economically feasible manner with limited impurity presence. The solubility limit between 8-10 mol% Yb_2O_3 for optical Lu_2O_3 ceramics produced through vacuum sintering must be further investigated. Ceramics containing a higher concentration of additive would need to be synthesized and studied with respect to processing and sintering parameters to investigate if the limit could be extended past the 8 mol % identified for commercial powders. Parameters such as elevated thermolysis or annealing temperatures as well as improved vacuum level (through means such as a cryogenic pump) should also be studied and evaluated further with respect to the quality of the final ceramics Quench rate, milling setup and duration, as spray dry process parameters are potential other studies that could merit investigation.

The introduction of carbon or tungsten into samples is believed to be via formation or Lu_2O_3 (or suboxide Lu_2O_2) vapors at the elevating sintering temperatures reacting with hot furnace materials, which forms a gas which is soluble in sintering compact. Unfortunately, the thermodynamic data need to calculate vapor pressures of Lu_2O_3 and Y_2O_3 is not reliably available. However, the lower concentration of defects in post-HIPed Y_2O_3, with identically processed granules and still sintered in the graphite furnace points toward a lower vapor pressure for this compound relative to Lu_2O_3. From the graphite furnace, black dots are interpreted as agglomeration of deposited graphite or carbon containing compound. While the graphite presence is interpreted to act as a grain growth inhibitor,

facilitating sintering to closed porosity without sweeping pores into grains as indicated by comparing fracture surfaces. The lack of any grain growth inhibitor with the tungsten furnace permits grain growth and pore coarsening to the point in which post-HIPing is either ineffective or only effective at achieving high density at the cost of all remaining pores being swept into grain interiors.

A non-vacuum sintering atmospheres could be compared to the vacuum sintering results provided in this work: literature suggests that a flowing hydrogen environment for sintering could be implemented, where the positive pressure of gas present could prevent oxygen vacancies from forming. This would circumvent any high temperature vapor pressures of the ceramic or crucible material from forming as in a vacuum environment, which could be paired with a tungsten element furnace to produce clean sintered samples of high density without the presence of carbon or any other oxide eliminating the need for oxygen annealing. These could also be investigated to prevent the agglomeration of carbon phases within the bulks of the optical ceramics. For laser host materials specifically, instead of being produced as bulk ceramic disks or blocks, the high surface area of a fibrous gain medium would allow ceramics produced in that fashion to utilize radiative cooling as a means of combating heat generation during laser operation in addition to inherent thermal conductivity. A review of the literature suggests that fibers could be produced by utilizing an aqueous-based paste[52] with a methyl-cellulose binder, or by using a polymerizing polyacrylate binder, in which fibers are exposed to UW radiation as they emerge from an extrusion syringe[109]. In either method, the extruded fibers would then be exposed to thermolysis and sintering heat treatments and similarly studied, with literature suggesting oil-immersion observation over text as a qualitative measure of their

transparency[110, 111]. The work provided here involving powder and slurry processing, including YSZ based ball milling and plasticizer could be used as a baseline and applied to the processing of a slurry used to produce high quality ceramic fibers. Whether as fibers or disks, any ceramics produced would need to be thoroughly inspected for impurity presence and processed to achieve a pore-free microstructure, as this work has shown.

REFERENCES

[1] R.C. Powell, Physics of Solid-State Laser Materials, Springer-Verlag/AIP Press, New York, 1998.

[2] A. Ikesue, Y.L. Aung, Nature Photonics, 2 (2008) 721-727.

[3] A. Ikesue, Y.L. Aung, T. Taira, T. Kamimura, K. Yoshida, G.L. Messing, Annu Rev Mater Res, 36 (2006) 397-429.

[4] U. Griebner, V. Petrov, K. Petermann, V. Peters, Opt. Express, 12 (2004) 3125-3130.

[5] A. Ikesue, T. Kinoshita, K. Kamata, K. Yoshida, J Am Ceram Soc, 78 (1995) 1033-1040.

[6] W. Kim, C. Baker, G. Villalobos, J. Frantz, B. Shaw, A. Lutz, B. Sadowski, F. Kung, M. Hunt, J. Sanghera, I. Aggarwal, J Am Ceram Soc, 94 (2011) 3001-3005.

[7] J. Sanghera, W. Kim, C. Baker, G. Villalobos, J. Frantz, B. Shaw, A. Lutz, B. Sadowski, R. Miklos, M. Hunt, F. Kung, I. Aggarwal, Optical Materials, 33 (2011) 670-674.

[8] B.Y. Kokuoz, K. Serivalsatit, B. Kokuoz, O. Geiculescu, E. McCormick, J. Ballato, J Am Ceram Soc, 92 (2009) 2247-2253.

[9] N.A. Dulina, Y.V. Yermolayeva, A.V. Tolmachev, Z.P. Sergienko, O.M. Vovk, E.A. Vovk, N.A. Matveevskaya, P.V. Mateychenko, Journal of the European Ceramic Society, 30 (2010) 1717-1724.

[10] K. Zhang, A.K. Pradhan, G.B. Loutts, U.N. Roy, Y. Cui, A. Burger, Journal of Materials Research, 19 (2011) 2714-2718.

[11] E. Zych, D. Hreniak, W. Strek, Journal of Alloys and Compounds, 341 (2002) 385-390.

[12] E. Zych, D. Hreniak, W. Strek, L. Kepinski, K. Domagala, Journal of Alloys and Compounds, 341 (2002) 391-394.

[13] Z.M. Seeley, Z.R. Dai, J.D. Kuntz, N.J. Cherepy, S.A. Payne, Optical Materials, 35 (2012) 74-78.

[14] Q.W. Chen, Y. Shi, L.Q. An, J.Y. Chen, J.L. Shi, J Am Ceram Soc, 89 (2006) 2038-2042.

[15] M. Dubinskii, J. Ballato, K. Serivalsatit, S.G. Post, Proc. of SPIE, 8039 (2011).

[16] J. Lu, J.F. Bisson, K. Takaichi, T. Uematsu, A. Shirakawa, M. Musha, K. Ueda, H. Yagi, T. Yanagitani, A.A. Kaminskii, Applied Physics Letters, 83 (2003) 1101.

[17] J. Lu, K. Takaichi, T. Uematsu, A. Shirakawa, M. Musha, K. Ueda, H. Yagi, T. Yanagitani, A.A. Kaminskii, Applied Physics Letters, 81 (2002) 4324.

[18] K. Serivalsatit, J. Ballato, J Am Ceram Soc, 93 (2010) 3657-3662.

[19] K. Serivalsatit, B. Kokuoz, B. Yazgan-Kokuoz, M. Kennedy, J. Ballato, J Am Ceram Soc, (2010).

[20] Y. Shi, Q.W. Chen, J.L. Shi, Optical Materials, 31 (2009) 729-733.

[21] D. Zhou, Y. Shi, J. Xie, Y. Ren, P. Yun, J Am Ceram Soc, 92 (2009) 2182-2187.

[22] J. Sanghera, S. Bayya, G. Villalobos, W. Kim, J. Frantz, B. Shaw, B. Sadowski, R. Miklos, C. Baker, M. Hunt, I. Aggarwal, F. Kung, D. Reicher, S. Peplinski, A. Ogloza, P. Langston, C. Lamar, P. Varmette, M. Dubinskiy, L. DeSandre, Optical Materials, 33 (2011) 511-518.

[23] J. Sanghera, J. Frantz, W. Kim, G. Villalobos, C. Baker, B. Shaw, B. Sadowski, M. Hunt, F. Miklos, A. Lutz, I. Aggarwal, Opt Lett, 36 (2011) 576-578.

[24] L. An, A. Ito, T. Goto, Journal of the European Ceramic Society, 31 (2011) 1597-1602.

[25] T.C.d. Oliveira, M.S.d. Silva, L.M.d. Jesus, D.V. Sampaio, J.C.A.d. Santos, N.R.d.S. Souza, R.S.d. Silva, Ceramics International, 40 (2014) 16209-16212.

[26] I. Yamada, K. Fukumi, J. Nishii, M. Saito, Opt Lett, 35 (2010) 3111-3113.

[27] L. Jin, G. Zhou, S. Shimai, J. Zhang, S. Wang, Journal of the European Ceramic Society, 30 (2010) 2139-2143.

[28] K. Serivalsatit, T. Wasanapiarnpong, C. Kucera, J. Ballato, Optical Materials, 35 (2013) 1426-1430.

[29] R.J. Gaboriaud, M. Boisson, Le Journal de Physique Colloques, 41 (1980) C6-171-C176-174.

[30] L. Marsella, V. Fiorentini, Physical Review B, 69 (2004).

[31] J. Emsley, Nature's Building Blocks: An A-Z Guide to the Elements, Oxford University Press, 2001.

[32] M. Guzik, J. Pejchal, A. Yoshikawa, A. Ito, T. Goto, M. Siczek, T. Lis, G. Boulon, Crystal Growth & Design, 14 (2014) 3327-3334.

[33] M. Tokurakawa, K. Takaichi, A. Shirakawa, K. Ueda, H. Yagi, S. Hosokawa, T. Yanagitani, A.A. Kaminskii, Opt. Express, 14 (2006) 12832.

[34] M. Dubinskii, J. Sanghera, W. Kim, G. Villalobos, C. Baker, J. Frantz, B. Shaw, S. Bayya, B. Sadowski, M. Hunt, I. Aggarwal, S.G. Post, Proc. of SPIE, 8039 (2011).

[35] M. Surez, A. Fernndez, R. Torrecillas, J. L, (2012).

[36] H. Yanagida, K. Kōmoto, M. Miyayama, The chemistry of ceramics, Wiley, 1996.

[37] R.S. Quimby, Photonics and Lasers: An Introduction, John Wiley & Sons, Inc., 2006.

[38] W. Koechner, Solid-state Laser Engineering, Springer, 2006.

[39] R. Paschotta, Encyclopedia of Laser Physics and Technology, Wiley, 2008.

[40] B. Fain, P.W. Milonni, Journal of the Optical Society of America B, 4 (1987) 78.

[41] R.C. Hilborn, American Journal of Physics, 50 (1982) 982.

[42] W.L. Barnes, R.I. Laming, E.J. Tarbox, P.R. Morkel, IEEE Journal of Quantum Electronics, 27 (1991) 1004-1010.

[43] G. Liu, B. Jacquier, Spectroscopic Properties of Rare Earths in Optical Materials, Springer Berlin Heidelberg, 2006.

[44] C. Dang, J. Lee, C. Breen, J.S. Steckel, S. Coe-Sullivan, A. Nurmikko, Nature nanotechnology, 7 (2012) 335-339.

[45] L.D. DeLoach, S.A. Payne, L.L. Chase, L.K. Smith, W.L. Kway, W.F. Krupke, IEEE Journal of Quantum Electronics, 29 (1993) 1179-1191.

[46] L. Berger, U. Brauch, A. Giesen, H. Hugel, H. Opower, M. Schubert, K. Wittig, Coherent fiber coupling of laser diodes, Spie - Int Soc Optical Engineering, Bellingham, 1996.

[47] A. Collombet, Y. Guyot, M.F. Joubert, J. Margerie, R. Moncorgé, Optical Materials, 24 (2003) 215-219.

[48] A. Brenier, G. Boulon, Europhysics Letters (EPL), 55 (2001) 647-652.

[49] G.L. Miessler, Inorganic Chemistry, Pearson Education, 2008.

[50] A. Ikesue, Y.L. Aung, V. Lupei, Ceramic Lasers, Cambridge University Press, 2013.

[51] H. Zhang, Q. Yang, S. Lu, Z. Shi, Optical Materials, 34 (2012) 969-972.

[52] J.S. Reed, Principles of Ceramics Processing, Wiley, 1995.

[53] S.J.L. Kang, Sintering: Densification, Grain Growth and Microstructure, Elsevier Science, 2004.

[54] W.D. Kingery, Introduction to ceramics, Wiley, 1960.

[55] R.D. Carneim, G.L. Messing, Powder Technology, 115 (2001) 131-138.

[56] R.M. German, Sintering Theory and Practice, Wiley, 1996.

[57] I.M. Kolthoff, The Journal of Physical Chemistry, 36 (1931) 860-881.

[58] P.N. Sharratt, Crystallization : Meeting the environmental challenge, Elsevier, Amsterdam, PAYS-BAS, 1996.

[59] W. Kim, C. Baker, G. Villalobos, J. Frantz, B. Shaw, B. Sadowski, M. Hunt, I. Aggarwal, J. Sanghera, Optical Materials Express, 4 (2014) 2497.

[60] D.J. Scott, S.E. Harding, A.J. Rowe, R.S.o. Chemistry, Analytical Ultracentrifugation: Techniques and Methods, RSC Publishing, 2005.

[61] A. Van Nieuwenhuijzen, J. Van der Graaf, Handbook on Particle Separation Processes, IWA Publishing, 2011.

[62] A.S. Peshkovsky, S.L. Peshkovsky, S. Bystryak, Chemical Engineering and Processing: Process Intensification, 69 (2013) 77-82.

[63] C. Washington, S.S. Davis, International Journal of Pharmaceutics, 44 (1988) 169-176.

[64] D.A. Miller, M. Gil, 3 (2012) 363-442.

[65] H.L. Berger, Ultrasonic Liquid Atomization: Theory and Application, Partridge Hill Publishers, 1998.

[66] A. Ikesue, Y.L. Aung, J Am Ceram Soc, 89 (2006) 1936-1944.

[67] W. Liu, W. Zhang, J. Li, H. Kou, D. Zhang, Y. Pan, Journal of the European Ceramic Society, 31 (2011) 653-657.

[68] S. Arabgari, R. Malekfar, K. Motamedi, Journal of Nanoparticle Research, 13 (2010) 597-611.

[69] A. Ikesue, K. Kamata, Journal of the Ceramic Society of Japan, 103 (1995) 489-493.

[70] W. Zhang, T. Lu, N. Wei, B. Ma, F. Li, Z. Lu, J. Qi, Optical Materials, 34 (2012) 685-690.

[71] B. Liu, M. Gu, X. Liu, S. Huang, C. Ni, Applied Physics Letters, 94 (2009) 121910.

[72] Y. Fu, J. Li, Y. Liu, L. Liu, H. Zhao, Y. Pan, Optical Materials Express, 4 (2014) 2108.

[73] W. Zhang, T. Lu, B. Ma, N. Wei, Z. Lu, F. Li, Y. Guan, X. Chen, W. Liu, L. Qi, Optical Materials, 35 (2013) 2405-2410.

[74] L. Chrétien, R. Boulesteix, A. Maître, C. Sallé, Y. Reignoux, Optical Materials Express, 4 (2014) 2166.

[75] R. Boulesteix, A. Maître, L. Chrétien, Y. Rabinovitch, C. Sallé, H.J. Kleebe, J Am Ceram Soc, 96 (2013) 1724-1731.

[76] G.B. Tel'nova, A.A. Konovalov, I.V. Dudenkov, V.I. Burkov, K.A. Solntsev, Russian Journal of Inorganic Chemistry, 58 (2013) 1335-1340.

[77] S.N. Bagayev, V.V. Osipov, V.A. Shitov, E.V. Pestryakov, V.S. Kijko, R.N. Maksimov, K.E. Lukyashin, A.N. Orlov, K.V. Polyakov, V.V. Petrov, Journal of the European Ceramic Society, 32 (2012) 4257-4262.

[78] V.V. Osipov, Y.A. Kotov, M.G. Ivanov, O.M. Samatov, V.V. Lisenkov, V.V. Platonov, A.M. Murzakaev, A.I. Medvedev, E.I. Azarkevich, Laser Physics, 16 (2006) 116-125.

[79] N.G. Basov, V.V. Bashenko, E.P. Glotov, S.G. Gornyi, V.A. Danilychev, G.N. Karpov, V.A. Lopota, M.M. Malysh, I.G. Rudoi, V.A. Saburov, A.M. Soroka, Izvestiya Akademii Nauk Sssr Seriya Fizicheskaya, 48 (1984) 2310-2320.

[80] M.G. Ivanov, Y.L. Kopylov, V.B. Kravchenko, K.V. Lopukhin, V.V. Shemet, Inorganic Materials, 50 (2014) 951-959.

[81] J. Luo, Z. Zhong, J. Xu, Materials Research Bulletin, 47 (2012) 4283-4285.

[82] M. Oghbaei, O. Mirzaee, Journal of Alloys and Compounds, 494 (2010) 175-189.

[83] J. Liu, Z. Fu, W. Wang, J. Zhang, H. Wang, Y. Wang, S.W. Lee, K. Niihara, Journal of the European Ceramic Society, 34 (2014) 2475-2482.

[84] R. Boulesteix, R. Epherre, S. Noyau, M. Vandenhende, A. Maître, C. Sallé, G. Alombert-Goget, Y. Guyot, A. Brenier, Scripta Materialia, 75 (2014) 54-57.

[85] M. Prakasam, O. Viraphong, D. Michau, P. Veber, M. Velázquez, K. Shimamura, A. Largeteau, Ceramics International, 39 (2013) 1307-1313.

[86] C. Wang, Z. Zhao, Scripta Materialia, 61 (2009) 193-196.

[87] Z.A. Munir, U. Anselmi-Tamburini, M. Ohyanagi, Journal of Materials Science, 41 (2006) 763-777.

[88] M.N. Rahaman, Ceramic Processing and Sintering, Taylor & Francis, 2003.

[89] M. Prakasam, O. Viraphong, D. Michau, A. Largeteau, Ceramics International, 40 (2014) 1859-1864.

[90] Y. Futami, T. Yanagida, Y. Fujimoto, J. Pejchal, M. Sugiyama, S. Kurosawa, Y. Yokota, A. Ito, A. Yoshikawa, T. Goto, Radiation Measurements, 55 (2013) 136-140.

[91] D. Zhou, Y. Ren, J. Xu, Y. Shi, G. Jiang, Z. Zhao, Journal of the European Ceramic Society, 34 (2014) 2035-2039.

[92] H. Rétot, S. Blahuta, A. Bessière, B. Viana, B. LaCourse, E. Mattmann, Journal of Physics D: Applied Physics, 44 (2011) 235101.

[93] Y.T. Wu, L.S. Qin, H.S. Shi, Y. Zhang, Y.X. Yang, K.Y. Shu, IEEE Transactions on Nuclear Science, 57 (2010) 1343-1347.

[94] I. Razdobreev, L. Bigot, V. Pureur, A. Favre, G. Bouwmans, M. Douay, Applied Physics Letters, 90 (2007) 031103.

[95] H.W. Bruesselbach, D.S. Sumida, R.A. Reeder, R.W. Byren, IEEE Journal of Selected Topics in Quantum Electronics, 3 (1997) 105-116.

[96] K. Takaichi, H. Yagi, A. Shirakawa, K. Ueda, S. Hosokawa, T. Yanagitani, A.A. Kaminskii, physica status solidi (a), 202 (2005) R1-R3.

[97] N.-L. Wang, X.-Y. Zhang, P.-H. Wang, Materials Letters, 94 (2013) 5-7.

[98] N. Wang, X. Zhang, H. Jiang, T. Dong, D. Yang, Materials Chemistry and Physics, 135 (2012) 709-713.

[99] X. Zhao, Z. Wu, S. Ning, S. Liang, D. Wang, X. Hou, Opt Express, 19 (2011) 16126-16131.

[100] J.W. Kim, J.I. Mackenzie, W.A. Clarkson, Opt. Express, 17 (2009) 11935.

[101] L. Laversenne, Y. Guyot, C. Goutaudier, M.T. Cohen-Adad, G. Boulon, Optical Materials, 16 (2001) 475-483.

[102] K. Petermann, D. Fagundes-Peters, J. Johannsen, M. Mond, V. Peters, J.J. Romero, S. Kutovoi, J. Speiser, A. Giesen, Journal of Crystal Growth, 275 (2005) 135-140.

[103] R. Peters, C. Kränkel, K. Petermann, G. Huber, Journal of Crystal Growth, 310 (2008) 1934-1938.

[104] M.R. Middlemas, G.I.o. Technology, Fabrication, Strength and Oxidation of Molybdenum-silicon-boron Alloys from Reaction Synthesis, Georgia Institute of Technology, 2009.

[105] H. Duan, L. Zhang, G. Chen, Journal of chromatography. A, 1217 (2010) 160-166.

[106] S. Rajendran, T. Uma, T. Mahalingam, European Polymer Journal, 36 (2000) 2617-2620.

[107] J.A. Bearden, Reviews of Modern Physics, 39 (1967) 78-124.

[108] M.O. Krause, J.H. Oliver, Natural Widths of Atomic K and L Levels, K[alpha] X-ray Lines and Several KLL Auger Lines, American Chemical Society and the American Institute of Physics for the National Bureau of Standards, 1979.

[109] Y. De Hazan, M. Wozniak, J. Heinecke, G. Müller, T. Graule, J Am Ceram Soc, 93 (2010) 2456-2459.

[110] W.A. Clarkson, H.J. Kim, G. Fair, H. Lee, K. Keller, T.A. Parthasarathy, R. Hay, N. Hodgson, R. Shori, 7912 (2011) 79121T-79121T-79127.

[111] M. Dubinskii, G.E. Fair, H.J. Kim, H. Lee, T.A. Parthasarathy, K.A. Keller, Z.D. Miller, S.G. Post, 8039 (2011) 80390X-80390X-80399.

VITA

Bryan Joseph Vitale was born May 31st, 1989, in Cedar Rapids, Iowa on the date of the third wedding anniversary of his parents, Stephen and Gail Vitale. He graduated from Kennedy High School in Cedar Rapids in May of 2007 as a Valedictorian and that fall began his undergraduate studies at nearby Coe College to pursue a degree in Physics and Mathematics. In May of 2011, he earned his B.A. with many honors. He spent time in his undergraduate years working both in the labs of Coe as an undergraduate research assistant as well interning at a local engineering company, Rockwell Collins. These activities sparked an interest in materials which led him to pursue a graduate degree at the Georgia Institute of Technology in Materials Science and Engineering. In August of 2011, he began his graduate studies under Professor Robert Speyer, which would eventually lead to this dissertation.